PEERING INTO THE HEART OF GALACTIC STAR FORMATION: A DETAILED CHARACTERIZATION OF INFRARED-DARK CLOUDS

by

Sarah E. Ragan

A dissertation submitted in partial fulfillment
of the requirements for the degree of
Doctor of Philosophy
(Astronomy and Astrophysics)
in The University of Michigan
2009

Doctoral Committee:

Associate Professor Edwin A. Bergin, Chair
Professor Fred C. Adams
Professor Lee William Hartmann
David J. Wilner, Smithsonian Astrophysical Observatory

For Mom

ACKNOWLEDGMENTS

Foremost thanks go to my thesis committee, and especially to my advisor, Ted Bergin. His knowledge, guidance, and patience helped me to be successful as a student and most importantly an independent thinker and researcher. From the beginning his generosity and collaborative philosophy have shaped my attitude that will continue to serve me will in my career and life. Lori Allen and David Wilner brought their invaluable observational expertise to this project, and Lee Hartmann and Fred Adams provided guidance that helped connect this work to its broader astronomical context. All of this help immensely improved this work and honed my abilities as a scientist.

Many others have aided in my progress, starting with my undergraduate instructors at Drake University, Lawrence Staunton, Athan Petridis, Charles Nelson, and Robert Lutz, who prepared me well for my graduate studies, giving me the confidence early to stand on my own two feet. Several others had a hand in my success providing guidance in data reduction, explaining simulations, or lending other scientific expertise. These individuals include, but are not limited to, João Alves, John Carpenter, Claire Chandler, Paul Clark, James Di Francesco, Rachel Friesen, Rob Gutermuth, Fabian Heitsch, Doug Johnstone, Charlie Lada, Sébastien Maret, John Monnier, Rene Plume, and Shiya Wang. Thank you for saving me from reinventing the wheel – several times.

Thank you to the graduate students at the University of Michigan for helping to make my time here bearable, and sometimes downright fun. In particular, thank you to Matt Walker for helping me endure years of mediocre baseball. Thanks to my dear friends Jessica Krick, Becky Stanek, and Tom Brink for introducing me to Michigan Hockey. Thank you Jessica Werk for her support and companionship over the years, which helped me to be my best and preserve my humor through it all. Thank you

to Jeremy Browe, who entered my life at a difficult time, and stuck with me anyway. Finally, thank you to Javier Alonso, Patrick Bellmore, Ed Cackett, Janet Colucci, Oleg Gnedin, Kayhan Gultekin, Laura Ingleby, Eric and Michelle Miller, Jon Miller, Eli Rykoff and Rob Snyder for being kind and supportive friends throughout time in Michigan and beyond.

Finally, thank you to my family for their unrelenting support and understanding of my academic ambitions. While it has more difficult than I can express to spend my days away from you, your love and support has made me a far richer person than any part of my education. My deepest gratitude is owed to my mother, Leslie Ragan, and my sister, Amanda Ragan, for inspiring me everyday.

CONTENTS

DEDICATION ii
ACKNOWLEDGMENTS iii
LIST OF FIGURES ix
LIST OF TABLES xii
LIST OF APPENDICES xiii
ABSTRACT xiv

CHAPTER

1 **INTRODUCTION** 1
1.1 Quantification of Initial Conditions to Star Formation 2
1.2 Infrared-dark Clouds 5
1.2.1 Where are IRDCs? 5
1.2.2 Star Formation in IRDCs 6
1.2.3 Molecules in IRDCs 7
1.2.4 IRDC structure 8
1.3 Goals of Thesis 9
2 **MOLECULAR LINE OBSERVATIONS OF INFRARED-DARK CLOUDS** 11
2.1 Background 11
2.2 Source Selection & Observations 12
2.3 Results 13
2.3.1 Molecular Line Fits 13
2.3.2 Molecular Emission Morphologies 25
2.3.3 Distance Estimates 26

2.3.4 Column Densities and Densities . . . 29
2.3.5 Masses . . . 30
2.3.6 Velocity Dispersion . . . 35
2.4 Summary . . . 37
3 **THE YOUNG STELLAR POPULATION AND ENVIRONMENT OF IRDCs** . . . 39
3.1 Star Formation in IRDCs . . . 39
3.2 *Spitzer* Observations & Data Reduction . . . 40
3.2.1 Targets . . . 40
3.2.2 Data Processing . . . 42
3.3 Stellar Content . . . 43
3.3.1 Young Stellar Object Identification & Classification . . . 43
3.4 IRDC Environment . . . 67
3.4.1 Nebulosity at 8 and 24 μm . . . 67
3.4.2 The Spatial Extent of IRDCs . . . 68
3.5 Summary . . . 69
4 **USING SPITZER TO PROBE IRDC STRUCTURE** . . . 71
4.1 Background . . . 71
4.2 Tracing mass with dust absorption at 8 μm . . . 74
4.2.1 Modeling the Foreground and Background . . . 74
4.2.2 Identification of Structure . . . 78
4.2.3 Resolving Inaccuracy in Clump Mass Calculation . . . 83
4.2.4 Validating 8 μm absorption as a Tracer of Mass . . . 84
4.3 Mass Function . . . 92
4.4 Clump Mass Function of IRDCs . . . 92
4.4.1 The Contribution from the IRDC Envelope . . . 98
4.4.2 Mass-Radius Relation . . . 103
4.5 Summary . . . 104
5 **HIGH RESOLUTION NH_3 OBSERVATIONS IN IRDCs** . . . 107
5.1 Molecular Observations in IRDCs . . . 107

5.2 Observations & Data Reduction . . . 109
5.2.1 Green Bank Telescope . . . 109
5.2.2 Very Large Array . . . 110
5.2.3 Single-dish and Interferometer Data Combination . . . 111
5.3 Analysis & Results . . . 111
5.3.1 Optical Depth . . . 112
5.3.2 Spectral Moments . . . 112
5.3.3 Trends in Centroid Velocity . . . 120
5.3.4 Linewidths . . . 125
5.3.5 Column Density . . . 125
5.3.6 Temperature . . . 127
5.4 Discussion . . . 130
5.4.1 Organized Cloud Motions . . . 130
5.4.2 Thermal / Non-thermal Support . . . 137
5.4.3 IRDC Virial Mass . . . 138
5.4.4 Associated Star Formation . . . 138
5.4.5 Temperature Structure . . . 139
5.4.6 Chemical Abundance of NH_3 in IRDCs . . . 140
5.5 Summary . . . 142
6 **CONCLUSIONS AND FUTURE PROSPECTUS** . . . 143
6.1 Summary . . . 143
6.1.1 Molecules in Infrared-dark Clouds . . . 143
6.1.2 Young Stars in IRDCs . . . 143
6.1.3 IRDC Environment . . . 144
6.1.4 Probing Mass with Absorption in IRDCs . . . 145
6.1.5 IRDC Clump Mass Function . . . 145
6.1.6 High-resolution Ammonia Observations in IRDCs . . . 147
6.2 Understanding Galactic Star Formation . . . 147
6.3 Outlook . . . 148
6.3.1 IRDC Chemistry . . . 149

6.3.2 Star Formation in IRDCs 149
6.3.3 Physics of IRDC Fragmentation 150
6.3.4 The Future of IRDC Studies 151

APPENDICES 154
BIBLIOGRAPHY 190

LIST OF FIGURES

Figure

2.1 MSX images of IRDCs G005.85−0.23, G006.26−0.51, G009.16+0.06, and G009.21−0.22 with FCRAO contours 14

2.2 MSX images of IRDCs G009.28 −0.15, G009.86−0.04, G009.88 −0.11, and G010.59−0.31 with FCRAO contours 15

2.3 MSX images of IRDCs G010.70−0.33, G010.99−0.09, G012.22+0.14, and G012.50−0.22 with FCRAO contours 16

2.4 MSX images of IRDCs G014.33−0.57, G019.37−0.03, G019.40−0.01, and G023.37−0.29 with FCRAO contours 17

2.5 MSX images of IRDCs G023.48 −0.53, G024.05−0.22, G024.16+0.08, and G025.99−0.06 with FCRAO contours 18

2.6 MSX images of IRDCs G030.14−0.07, G030.53−0.27, G030.89+0.14, and G030.98 −0.15 with FCRAO contours 19

2.7 MSX images of IRDCs G031.02−0.12, G032.01+0.05, G033.82−0.22, and G034.63−1.03 with FCRAO contours 20

2.8 MSX images of IRDCs G034.74−0.12, G034.78 −0.80, G035.20−0.72, G037.44+0.14 and with FCRAO contours 21

2.9 MSX images of IRDCs G037.89−0.15 and G050.07+0.06 with FCRAO contours 22

2.10 IRDC mass histogram - N_2H^+ 31

2.11 IRDC mass histogram - $C^{18}O$ 33

2.12 Linewidth Histogram 36

3.1 *Spitzer* images of IRDC G005.85−0.23 46

3.2 *Spitzer* images of IRDC G006.26−0.51 47
3.3 *Spitzer* images of IRDC G009.16+0.06 48
3.4 *Spitzer* images of IRDC G009.28−0.15 49
3.5 *Spitzer* images of IRDC G009.86−0.04 50
3.6 *Spitzer* images of IRDC G012.50−0.22 51
3.7 *Spitzer* images of IRDC G023.37−0.29 52
3.8 *Spitzer* images of IRDC G023.48−0.53 53
3.9 *Spitzer* images of IRDC G024.05−0.22 54
3.10 *Spitzer* images of IRDC G034.74−0.12 55
3.11 *Spitzer* images of IRDC G037.44+0.14 56
3.12 A_K histogram of candidate YSOs 57
3.13 YSOs in IRDC G005.85−0.23 57
3.14 YSOs in IRDC G006.26−0.51 58
3.15 YSOs in IRDC G009.16+0.06 58
3.16 YSOs in IRDC G009.28−0.15 59
3.17 YSOs in IRDC G009.86−0.04 59
3.18 YSOs in IRDC G012.50−0.22 60
3.19 YSOs in IRDC G023.37−0.29 60
3.20 YSOs in IRDC G023.48−0.53 61
3.21 YSOs in IRDC G024.05−0.22 61
3.22 YSOs in IRDC G034.74−0.12 62
3.23 YSOs in IRDC G037.44+0.14 62
3.24 IRAC four color plot of Spitzer YSOs 64
3.25 FCRAO contours of G012.50−0.22 68

4.1 Background calculation illustration 75
4.2 Background calibration with SCUBA 78
4.3 G024.05−0.22 8 μm optical depth 82
4.4 `clumpfind` results on G024.05−0.22 8μm image 82
4.5 Wavelet analysis of G024.05−0.22 83

4.6 N_2H^+(1-0) BIMA contours of G012.50−0.22 87
4.7 N_2H^+(1-0) BIMA vs. 8μm optical depth 87
4.8 Clump mass vs. Mass derived by N_2H^+ 88
4.9 Mass and size sensitivity vs. distance 93
4.10 IRDC clump differential mass function 94
4.11 Differential Mass Function Comparison with Literature 99
4.12 IRDC clump mass-radius relation 100
4.13 IRDC clump mass-radius relation comparison with literature 101

5.1 Spectral moments in G005.85−0.23 113
5.2 Spectral moments in G009.28−0.15 114
5.3 Spectral moments in G009.86−0.04 115
5.4 Spectral moments in G023.37−0.29 116
5.5 Spectral moments in G024.05−0.22 117
5.6 Spectral moments in G034.74−0.12 118
5.7 VLA and GBT linewidth maps of G009.28−0.15 123
5.8 VLA and GBT linewidth maps of G023.37−0.29 124
5.9 Linewidth vs. IRDC distance 126
5.10 Kinetic Temperature map of G005.85−0.23 131
5.11 Kinetic Temperature map of G009.28−0.15 132
5.12 Kinetic Temperature map of G009.86−0.04 133
5.13 Kinetic Temperature map of G023.37−0.29 134
5.14 Kinetic Temperature map of G024.05−0.22 135
5.15 Kinetic Temperature map of G034.74−0.12 136
5.16 NH_3 (1,1) Integrated Intensity vs. $\tau_{8\mu m}$ with abundance 141

6.1 Mass Function Evolution 148
6.2 Modeled spectral energy distribution of a massive embedded protostar 149
6.3 Carbon chemistry as a function of A_V 152

LIST OF TABLES

Table

2.1 FCRAO Molecular Line Observations 23
2.2 Kinematic distances to IRDCs 27
2.3 Molecular Abundances and Cloud Masses 32

3.1 Spitzer Target Table 41
3.2 Summary of Young Stellar Objects 63
3.3 Spitzer-identified Embedded Protostars: Flux and Luminosity Estimates 65

4.1 `clumpfind` Parameter Summary 79

5.1 GBT Observation Summary 110
5.2 VLA Observation Summary 111
5.3 Summary of IRDC Moment Analysis 119
5.4 Summary of Physical Characteristics at $\int Tdv$ peaks 129

A.1 MSX properties of IRDCs and FCRAO observational parameters 155

C.1 YSO Photometry 162

D.1 `clumpfind` Results 176

LIST OF APPENDICES

Appendix

A Basic Properties of Target MSX IRDCs 155

B Sources Coincident with FCRAO IRDCs 159

C Spitzer Identified Young Stellar Objects: Photometry 161

D Clump Structure in IRDCs: `clumpfind` Results 176

ABSTRACT

Everything we know about star formation in other galaxies is based on light from massive stars. Yet, in our own Galaxy, it's the formation of massive stars that is the *least* understood. Most of what we know about star formation is based on studies of nearby, isolated, low-mass star formation regions. However, massive stars and clusters form primarily in the inner-Galaxy, where the bulk of the molecular gas resides. In particular, dense condensations within large molecular cloud complexes, called infrared-dark clouds (IRDCs) are the precursors to massive stars and clusters. These objects are key to understanding the initial conditions of massive star formation.

We present the results of a high-resolution multi-wavelength observational study of infrared-dark clouds. We mapped 41 IRDCs in the N_2H^+ $1 \rightarrow 0$, CS $2 \rightarrow 1$ and $C^{18}O$ $1 \rightarrow 0$ transitions using the Five College Radio Astronomy Observatory. With the centroid velocity, we infer accurate distances to the IRDCs and use the maps to deduce chemical abundances, physical structure and dynamical state of each cloud. The average total mass derived from N_2H^+ is $\approx 2500\ M_\odot$, and the overall linewidths of IRDCs are 2.0 - 2.9 km s^{-1}. Given these results, and that the clouds appear dark at 8 μm, we suggest that these clouds are the *precursor* sites of intermediate and high mass cluster formation.

We survey 11 IRDCs with *Spitzer Space Telescope* to examine their stellar content, environs, and mass distribution of absorbing material. Young stars are present in the vicinity of IRDCs, but the bulk of the absorbing material is devoid of any signs of star formation. The IRDCs in this sample are comprised of tens of clumps, ranging in sizes from 0.02 to 0.3 pc in diameter and masses from 0.5 to a few $10^3 M_\odot$, the broadest dynamic range in any mass spectrum study to date. We construct an IRDC clump mass spectrum, which has a slope of α=1.76$\pm$0.05 for clump masses from

$30M_{\odot}$ to $3000M_{\odot}$, which is consistent with starless clumps in massive star forming regions. We assert that the shape of the mass function is an intrinsic and universal feature of massive star and cluster formation regions. As these clouds evolve and their constituent clumps fragment, the mass spectrum will steepen and eventually assume the form of the core mass function that is observed locally.

We observe the NH_3 (1,1) and (2,2) inversion transitions in seven IRDCs using the Very Large Array at high spatial resolution ($\sim$ 5 $''$). We find two types of velocity structure in the observed sample: IRDCs that exhibit smooth gradients and those with clumpy velocity structure, where the latter group tends to be coincident with the presence of 24 μm point sources, indicating embedded star formation. The magnitude of the velocity gradients is less than the typical line widths of 2 - 3 km s^{-1}. The ratio of the (1,1) and (2,2) main line intensities allows for measurement of the gas temperature, which ranges from 8 to 16 K.

Using high-resolution observations, we have quantified the structure, star formation, kinematics, and chemistry of infrared-dark clouds. Our study of sub-structure in particular shows that IRDCs are undergoing fragmentation and are the precursors to star clusters, and thus we have placed IRDCs in context with Galactic star formation. The characterization presented here offers new constraints on theories of molecular cloud fragmentation and clustered star formation.

CHAPTER 1

INTRODUCTION

The formation of stars has been the focus of volumes of work over the past several decades, and as such, the underlying questions have helped shape the direction of astronomy. The discovery that young stars and pre-stellar objects emit a large fraction of their light longward of the accessible near-infrared wavelengths (Beichman et al., 1986) helped spur the design of modern instruments, such as the *Spitzer Space Telescope*, to understand the origin of their unique spectral energy distribution. Indeed, mainly in local regions, *Spitzer* has led to important progress on many fronts in star formation, including the photometric properties of young stellar objects (e.g. Allen et al., 2004), the character and evolution of disks around young stars (e.g. Espaillat et al., 2007), and the effects of dust on mid-infrared light in extinction and reddening at mid-infrared wavelengths in star-forming regions (e.g. Flaherty et al., 2007), to name some important examples. These studies were successful in part because the "laboratories" to observe the these processes in action are all available in local, low-mass star-forming regions, within a kiloparsec. The same cannot be said for the equally pressing question of how massive stars form. Our situation in the outskirts of the Milky Way puts us at a resolution disadvantage because massive star formation primarily takes place in the central part of the Galaxy, several kiloparsecs away, making all aspects of the process more challenging to observe.

Key to the progress in understanding low-mass star formation has been the identification and characterization the phases of the process, the earliest of which are the so called "pre-stellar cores." The isolation of such objects has allowed us to probe the earliest initial stages of star formation (André et al., 2000; Alves et al., 2001). The traditional method of locating low-mass cores has been to examine optical plates for

regions of obscured starlight and then to pursue follow up molecular line observations (Myers & Benson, 1983; Lee & Myers, 1999). A comparison with the IRAS point source catalog then denotes whether these cores are associated with newly formed stars (Beichman et al., 1986). This method cannot be applied to massive star forming regions since the greater distances makes isolating individual objects difficult. Moreover, the size and high column densities of Giant Molecular Clouds (GMCs) makes it impossible to use optical plates to find individual objects. An analogous method of searching for molecular cores is to search for obscured regions in galactic mid-infrared background. However, due to atmospheric constraints, ground-based observations in the mid-IR are difficult to obtain. The ISOCAM instrument on the Infrared Space Observatory was used in this fashion, but only with pointed observations towards previously identified cores (Bacmann et al., 2000). We are now better equipped to use the lessons from local studies and apply them to more distant regions to learn more about star formation in the Galaxy.

1.1 Quantification of Initial Conditions to Star Formation

The most fundamental property of a star is its mass, thus understanding the origin of that mass is the motivation of many star formation studies. To this end, efforts have focused on the characterization of the precursors to stars and clusters and how this distribution relates to the star(s) that will ultimately be produced. A typical quantification used in this arena is the mass function, which accounts for how much mass resides in independent objects, from the least massive to the most massive. Within molecular clouds (tens of parsecs (pc) in size, containing 10^4-10^5 times the mass of the sun, $M_\odot$), we adopt the nomenclature used by Bergin & Tafalla (2007) distinguishing "clouds" ($10^3 - 10^4$ $M_\odot$, $10^0 - 10^1$ pc), "clumps" (10-10^3 $M_\odot$, 10^{-1}-10^0 pc), and "cores" (10^{-1}-10^1 $M_\odot$, 10^{-2}-10^{-1} pc). This hierarchy of structure in itself instills a fundamental curiosity in not only its origin but its interconnection. Indeed, the connection between GMCs down to cores is an area of tremendous interest and debate in the theoretical realm of star formation studies (e.g. Bonnell et al., 1997; Krumholz et al., 2005) and is still in need of observational support. More

challenging yet is the understanding of this the assemblage of mass on very large scales, particularly in massive star-forming regions, as the very nature of such regions is very crowded and confused, making it difficult to detect individual objects, so observations set only weak limits on the details of the process.

Because molecular hydrogen (H_2), the primary constituent of star formation regions, does not radiate, reliable proxies are needed to trace the structure of material. Other, less abundant molecules trace these regions, but their abundances, which often change depend on the environment, are not ideal for such a task. Over the past ten years, sub-millimeter instruments have produced the high quality data that most sensitively probes local star-forming regions (e.g. Johnstone et al., 2000a). In low-mass regions within a few hundred parsecs, single-dish observations are capable of resolving individual pre-stellar cores and therefore one can study their properties. With more efficient mapping becoming possible over the past decade, entire regions can be mapped and the character of the ensemble of cores can be explored (e.g. Johnstone et al., 2000b). With interferometers, small-scale sub-core processes are observable (Friesen et al., 2009), and we come closer to a full understanding of the stages leading up to low-mass star formation. The same techniques that were successful in nearby regions have been used to determine the fundamental properties of Orion (e.g. Li et al., 2007; Johnstone et al., 2001), the nearest ($\sim$400 pc) and best-studied region producing high-mass stars, though with greater distance comes a higher degree of uncertainty and incompleteness at the low-mass end. In a number of these studies, the pre-stellar core mass function is remarkably similar to the mass function of stars in clusters, which has led some to suggest that the stellar mass function is set by the core mass function. In high-mass regions, the direct link in mass functions of pre-stellar clumps and the stars they will produce is not so clear. I aim to address this issue in this thesis.

The molecular hydrogen distribution in the Milky Way is not uniform; the primary reservoir is in the Molecular Ring (Burton et al., 1975), which resides at 4 - 5 kpc from the Galactic Center and contains $\sim$70% of the molecular gas inside the solar circle (Clemens et al., 1988; Jackson et al., 2006). Because the H_2 distribution is non-

uniform, one expects that star formation also would be non-uniform across the Galaxy, i.e. where there is a higher concentration of molecular gas, there will be more star formation. Indeed, Robinson et al. (1984) show that the peak of Galactic far-infrared emission, which is principally radiation from young stars (Beichman et al., 1986), originates from the Molecular Ring. Other star formation signposts, such as HII regions and diffuse ionized gas (Burton, 1976; Robinson et al., 1984), are ubiquitous in this region. Put together, the clear conclusion is that the Molecular Ring is the heart of Galactic star formation, where most stars and clusters form. Given the very clustered nature of star formation (Zinnecker et al., 1993), most studies are hampered by confusion. Also, massive stars in particular are believed to form on relatively short timescales, so examples at a given state of the process are intrinsically rare. As a result, the objects in the earliest phases – the "pre-stellar massive cores" – have been difficult to identify. As a result, our understanding of star formation in the Molecular Ring is less advanced than that of local regions. Until star formation in the Molecular Ring is understood, we will not have a complete picture of star formation in the Galaxy.

Star formation by nature is a dynamical process, therefore understanding he dynamical state of a prestellar core or clump is an important piece to the star formation puzzle. The width of spectral lines is a useful tool in measuring the internal energy in cores. In the well-studied local Bok globule, Barnard 68, for example, the velocity structure has been mapped extensively to determine the relative importance of thermal support versus non-thermal effects, including such things as inflow, outflow, collapse, or turbulence (Lada et al., 2003). In this case, the core is thermally supported. In more clustered environments, however, linewidths tend to be broader than thermal, indicating that other forces such as systematic core motions or turbulence is at play. Projecting these ideas into the clustered and dynamic environment of massive star formation regions, it is no surprise that non-thermal effects dominate to an even higher degree (Harju et al., 1993). In this thesis, I demonstrate a few of the many ways that massive star forming regions are dynamically distinct from local star forming regions.

1.2 Infrared-dark Clouds

Infrared-dark clouds are named for the qualitative way in which they were discovered. They were first recognized as dark patches or filaments in mid-infrared images from the Infrared Space Observatory (ISO) (Hennebelle et al., 2001) and Midcourse Space Experiment (MSX) (Egan et al., 1998). The MSX survey of the Galactic plane from 6 to 25 μm produced the first census of IRDCs (Egan et al., 1998), in which $\sim$2000 compact objects absorbing against the bright Galactic background mid-infrared emission were observed. The initial studies of IRDCs (e.g. Carey et al., 1998) demonstrated that these objects, termed infrared-dark clouds (IRDCs), are dense (n(H_2) $> 10^5$ cm^{-3}), cold (T $<$ 20K) concentrations of 10^3 - 10^5 $M_\odot$ of molecular gas. Since their discovery, further studies of infrared-dark clouds have established them as the precursors to clusters and key to the production of the star clusters that dominate star formation in the Galaxy.

1.2.1 Where are IRDCs?

Simon et al. (2006a) compiled a more complete catalog of IRDCs in the first and fourth quadrant of the Galaxy based on MSX data, in which they found 10,931 candidate IRDCs in absorption at 8 μm. To confirm the presence of the IRDC, follow up observations of molecular lines are needed. The most common tracer used in this study is carbon monoxide (CO), and the characteristic velocity (v_{lsr}) of the spectral line, when combined with rotation models of the Milky Way (Fich et al., 1989), is a way of determining the kinematical distance to the IRDC (see Chapter 2). In this way, the presence of an IRDC can be confirmed and its kinematic distance determined, and this has been done for hundreds of IRDCs, primarily in the first quadrant of the Galaxy ($(0^\circ < l < 90^\circ)$ Simon et al., 2006b; Sakai et al., 2008; Du & Yang, 2008). Since CO is abundant along the line of sight, multiple velocity components are common, which means that multiple distance solutions exist. Thus, emission maps are needed to confirm morphological similarity to the absorption at 8 μm, bolstering confidence of association. Less abundant molecular tracers, those that require a much higher H_2 density to show appreciable signal, are better distance

determinants for IRDCs because there are fewer velocity components along a given line of sight. I show in Chapter 2, for example, that N_2H^+, much less abundant than CO, more closely matches the dense, absorbing material than CS or $C^{18}O$, giving us a more reliable indicator of where the dense gas is along the line of sight.

With a significant number of reliable distance determinations available in the literature, Jackson et al. (2008) supplemented the sample with CS (2-1) observations of IRDCs from Simon et al. (2006a) in the Galaxy's fourth quadrant ($270° < l < 360°$). They found that the IRDC distribution, at least toward the central part of the Galaxy, appears to delineate the Molecular Ring of the Galaxy (Burton et al., 1975). Closer examination with a larger sample reveals that the distribution of IRDCs may not be symmetric to a ring-like structure, but instead skewed somewhat, which led Jackson et al. (2008) to assert that IRDCs could trace a spiral arm more closely than the Molecular Ring. This discrepancy is still under investigation, and as the sample of IRDCs builds in the literature, the distribution will become better understood.

The assertion that infrared-dark clouds are objects associated with star formation based only on their correlation with the Molecular Ring and/or Galactic spiral arm is not one without caveats, due to the observational bias to which their very definition subjects us. In order to be seen as "infrared-dark" an IRDC must have bright background emission – generally produced in the inner Galaxy – against which to absorb, thus dark clouds with identical properties to the IRDCs we discuss here may very well exist in the outer Galaxy, but cannot be detected in absorption; however, but they could be observed in dust emission. Indeed large-scale surveys of molecular gas are necessary to understand the galactic distribution fully.

1.2.2 Star Formation in IRDCs

A number of studies have detected the presence of deeply embedded massive protostars using sub-millimeter probes (Beuther & Steinacker, 2007; Rathborne et al., 2005, 2007; Pillai et al., 2006b) in isolated regions of IRDCs. Deep sub-millimeter observations are needed to detect such embedded objects, as we currently have limited access the spectral region where embedded massive protostars would be their

brightest – the far-infrared. Still, the objects that have been found are modeled to be tens to hundreds of solar luminosities. This affirms that IRDCs are the birth-sites of massive stars and clusters, yet to date there is no unambiguous identification of the *precursor*: a truly dark IRDC or an elusive "massive prestellar core."

Detailed molecular surveys show that molecules such as NH_3 and N_2H^+ trace the dense gas extremely well (Ragan et al., 2006; Pillai et al., 2006a), as seen in local dense prestellar cores (Bergin et al., 2002). Furthermore, the molecular emission corresponding to the absorbing structure of infrared-dark clouds universally exhibit non-thermal linewidths on par with massive star formation regions. Other studies have uncovered the presence of masers (Beuther et al., 2002; Wang et al., 2007) and outflows (Beuther & Sridharan, 2007), known indicators of ongoing embedded star formation. Already, the evidence shows that these are the sites where massive stars and star clusters will form or are already forming. It is clear that in order to understand massive star formation, and thus Galactic star formation, it is crucial to understand the structure and evolution of IRDCs.

Chambers et al. (2009) and Cyganowski et al. (2009) have conducted large surveys, mining the *Spitzer* archives and conducting supplemental observations, to identify candidate massive protostars and candidate massive starless cores. Targeting IRDCs, the authors search for indirect signposts of star formation, shock emission and masers respectively, to place an IRDC in a rudimentary evolutionary sequence – embedded protostar or no embedded protostar. These efforts and others have been extremely useful pathfinders for the more detailed studies like the ones mentioned above.

1.2.3 Molecules in IRDCs

Molecular surveys have been very useful in determining distances as well as the basic physical conditions of infrared-dark clouds. A molecule of particular interest in studying IRDCs is ammonia because of its unique utility in quantifying several physical properties of the gas up to very high densities, where most other molecules would be depleted. Already, IRDCs have been observed in ammonia (NH_3) (e.g. Pillai et al., 2006a,b), but only one high-resolution study of one IRDC is in the literature (Wang

et al., 2007).

Rathborne et al. (2008) and Beuther et al. (2009) have undertaken more detailed chemical studies in IRDCs, though they have mainly focused on chemistry in hot cores where star formation is ongoing. In the hot cores, the chemistry is extremely rich, and the current effort is to try to understand the evolutionary sequence based on careful examination of the spectra.

1.2.4 IRDC structure

IRDCs are truly remarkable star formation environments unlike any other we know. One of the most extraordinary features is the large amount of mass that occupies a relatively small volume of space, thereby increasing the difficulty in resolving individual structures. Applying tried and true methods for studying nearby star formation regions, IRDCs have been mapped in the millimeter (Carey et al., 1998; Johnstone et al., 2003; Parsons et al., 2009), though single-dish studies do not have the resolution to resolve the small structures. The seminal work on IRDC structure, Rathborne et al. (2006), maps 38 IRDCs at 1.2mm ($11''$ resolution = 0.2 pc 4 kpc) and finds that there are hundreds to thousands of solar masses confined to a few parsecs. These observations showed that IRDCs exhibit structure with median size of $\sim$0.5 pc. Recently, IRDC studies have turned to the *Spitzer Space Telescope* to study their structure (Ragan et al., 2009; Butler & Tan, 2009), taking advantage of the superior spatial resolution. The GLIMPE survey (Churchwell et al., 2009) has been especially important in providing a straightforward way of finding IRDCs. I will show in Chapter 4 that IRDCs exhibit structure on smaller scales when viewed with the *Spitzer Space Telescope*. In addition, I compare the structure of IRDCs to the structure in various star-formation regions. I also discuss the uncertainties in mass determination from different methods, and explore the strengths and weaknesses of structure identification methods.

1.3 Goals of Thesis

Infrared-dark clouds are coming more into focus as an important piece of the massive cluster formation puzzle. We have learned a great deal over the past decade by both galaxy-wide surveys, which have helped place IRDCs in their appropriate context as key players in Galactic star formation, and pointed observations, which uncover the detailed processes that govern their evolution. The aim of this thesis is in some sense to bridge this gap, by applying high-resolution observations to a broad sample of IRDCs, in hopes to understand their characteristics and place along the evolutionary track. In Chapter 2, I describe a single-dish molecular mapping survey that we undertook to examine the gross properties of a sizable sample of IRDCs. From this study, in addition to finding accurate distances to each IRDC, I calculate total IRDC masses, velocity dispersion and chemical abundances. This chapter is based primarily on work published in Ragan et al. (2006).

Chapter 3 discusses a *Spitzer Space Telescope* survey of a smaller sample of IRDCs, and I use these deep observations to study the young stellar content of the clouds. This complements the work in the literature that has explored embedded protostars in IRDCs, as it profiles any star formation in the vicinity that is occurring. Also, I describe the environment of IRDCs, incorporating molecular maps to determine the spatial extent of these regions. As I mentioned above, large-scale surveys of molecular gas (e.g. the Galactic Ring Survey) have given a broad picture of where IRDCs reside in the Galaxy, but little has been done to relate IRDCs to their place in the hierarchy of molecular cloud structure. Using multiple molecular line tracers, known to probe different density regimes in the gas, it is clear that IRDCs are the unique nurseries where massive clusters originate.

Chapter 4 uses the *Spitzer* observations, but here taking advantage of the sensitivity to absorbing structures against the mid-infrared Galactic background (analogous to the MSX surveys mentioned above) to probe the mass distribution of IRDCs. Armed with *Spitzer's* high angular resolution at 8 μm, I am able to resolve small, "clump" and "core"-sized structures in all of the observed IRDCs. I describe a tech-

nique to use the absorption as a mass probe, then conduct a study of the IRDC clump mass function. This is a key quantification for IRDCs, in that it can readily be compared with the local core mass function, cluster mass functions and the stellar mass function. Both Chapters 3 and 4 are based on work published in Ragan et al. (2009).

In Chapter 5, I present VLA observations of NH_3 (1,1) and (2,2) inversion transitions, which enables me to probe the temperature and velocity structure of IRDCs at high spatial resolution. While the ammonia traces the 8 μm absorption extremely well, there is tremendous diversity in the velocity structure of the clouds. This portion of the thesis is in preparation for publication.

I conclude with Chapter 6, where I summarize my results and discuss the much more detailed picture of IRDCs we've been able to paint with this thesis research. Many questions about the nature of the IRDCs remain open, but we've laid an excellent foundation from which we can learn how best to direct our future studies.

CHAPTER 2

MOLECULAR LINE OBSERVATIONS OF INFRARED-DARK CLOUDS

2.1 Background

The Midcourse Space Experiment (MSX) surveyed the galactic plane in mid-infrared bands spanning from 7 to 25 μm. This survey revealed a large population of dark clouds, predominantly located toward the inner galaxy (Egan et al., 1998). Follow-up molecular studies of a few objects confirmed that the obscured regions represent a new population of dense, $n(H_2) > 10^5$ cm^{-3}, and cold, T $<$ 20 K, molecular clouds (Carey et al., 1998). Further comparison to IRAS images demonstrated that most of these clouds are dark from 7–100 μm, presumably because these objects either do not contain newly formed stars, or any newly formed stars are very deeply embedded. As such, a sub-sample of these objects may trace massive pre-stellar cores. There has been substantial activity in this field recently, with numerous groups analyzing various samples of infrared dark clouds (IRDCs). These studies have shown that it is likely that IRDCs are the birth-sites of high-mass stars and stellar clusters (Sridharan et al., 2005; Menten et al., 2005; Rathborne et al., 2006; Pillai et al., 2006a).

We have identified a sample of infrared-dark clouds and searched them for emission from the N_2H^+ $1 \rightarrow 0$, CS $2 \rightarrow 1$ and $C^{18}O$ $1 \rightarrow 0$ transitions. In most cases, we find that the emission closely corresponds to the MSX dark regions. Using a gas temperature of T=15 K based on CO $1 \rightarrow 0$ data, we deduce several properties of the dark clouds including column density and mass.

2.2 Source Selection & Observations

To search for pre-stellar massive cores we have compiled a catalog of MSX dark clouds. This catalog is biased, as we have only searched the released MSX band A (centered at 8.8 μm) images for infrared dark clouds in the vicinity of known ultra-compact (UC) HII regions from the Wood & Churchwell (1989) catalog. More specifically, we searched for absorbing clouds within a square degree centered on a given UC HII region. This strategy takes advantage of the fact that young stars generally form in clusters, and, therefore, a good place to search for the pre-cursors to massive stars is in the vicinity of regions with current massive star formation evidenced by the UC HII regions. In this fashion we have isolated 114 infrared dark clouds, of which only a small fraction (15%) have known associations with radio sources or masers. From this catalog of 114 infrared dark clouds we selected a sub-sample of the 41 most compact and most opaque ($\tau_{8.8\mu m} \gtrsim 0.4$) cores and targeted these for molecular line observations.

We mapped 41 of the sample of MSX dark clouds in emission from $C^{18}O$ $J = 1 \rightarrow 0$ ($\nu = 109.782$ GHz), CS $J = 2 \rightarrow 1$ ($\nu = 97.981$ GHz), and N_2H^+ $J = 1 \rightarrow 0$ ($\nu = 93.173$ GHz) using the 14m Five College Radio Astronomy Observatory (FCRAO). The observations were made in 2002 February, May & December using the 16 element focal plane array receiver SEQUOIA. Each $2.5' \times 2.5'$ region was mapped with the $50''$ beam, with typical rms noise levels of $\sim 0.05 - 0.1$ K. We used the Narrow Band Correlator backend configured to a velocity resolution of ~ 0.13 km s^{-1}. Typical system temperatures (T_{sys}) were $200 - 300K$. Main beam efficiencies (η_{mb}) were approximated at 50% from the standard FCRAO values. This is accurate within a few percent for each transition. For each spectrum, a first-order, linear baseline was fit to remove instrumental and continuum offsets and drift.

This selection of species is motivated by studies of low-mass pre-stellar clouds. N_2H^+ is unlikely to significantly suffer from the effects of depletion as the core condenses, and this species is a good tracer of the dense centers of starless cores (Bergin & Langer, 1997; Tafalla et al., 2002). Conversely, $C^{18}O$ and CS emission can be

used to trace the outer layers. The table in Appendix A lists some basic dark cloud properties such as the name of the nearby HII region, the coordinates, the size, and the center-to-edge brightness contrast. The brightness contrast was obtained by comparing the brightness in the band centered at 8.8 μm at the center of the core with the average background brightness, estimated from an average of the intensities in a vertical and horizontal slit across the dark region. If the dark cloud was searched for molecular emission, we list the LSR velocity range which the observations probed.

2.3 Results

We detect emission from at least one and often multiple molecules in 34 of the 41 targets, 3 of which have two velocity components, and 7 targets we determine upper limits. Below we present the results of our observations, including a description of cloud morphologies, distances, densities, masses, and velocity dispersions.

2.3.1 Molecular Line Fits

Each line is fit with a Gaussian profile to determine the integrated intensity, line width, and the LSR velocity of the emitting material. Table 2.1 presents the results of the spectral line fitting. All parameters were extracted by standard Gaussian fitting methods in the CLASS package (Buisson et al. 2002); for N_2H^+, the seven main hyperfine components were fit together using the HFS routine. The reported line-center velocity corresponds to that of the strongest hyperfine component ($J = 1 \rightarrow 0$, $F_1, F = 2, 3 \rightarrow 1, 2$) at 93.1738 GHz.

Our observations were obtained with velocity resolution of 0.13 km s^{-1}, and to increase the signal to noise, we on occasion smoothed the line profiles by a factor of 2. As such, we had little sensitivity to structure within the line. Within our sensitivity limits (see §2.2), we see no evidence for extended line wings, and all lines were well-fit by single Gaussians. We report here only basic line properties.

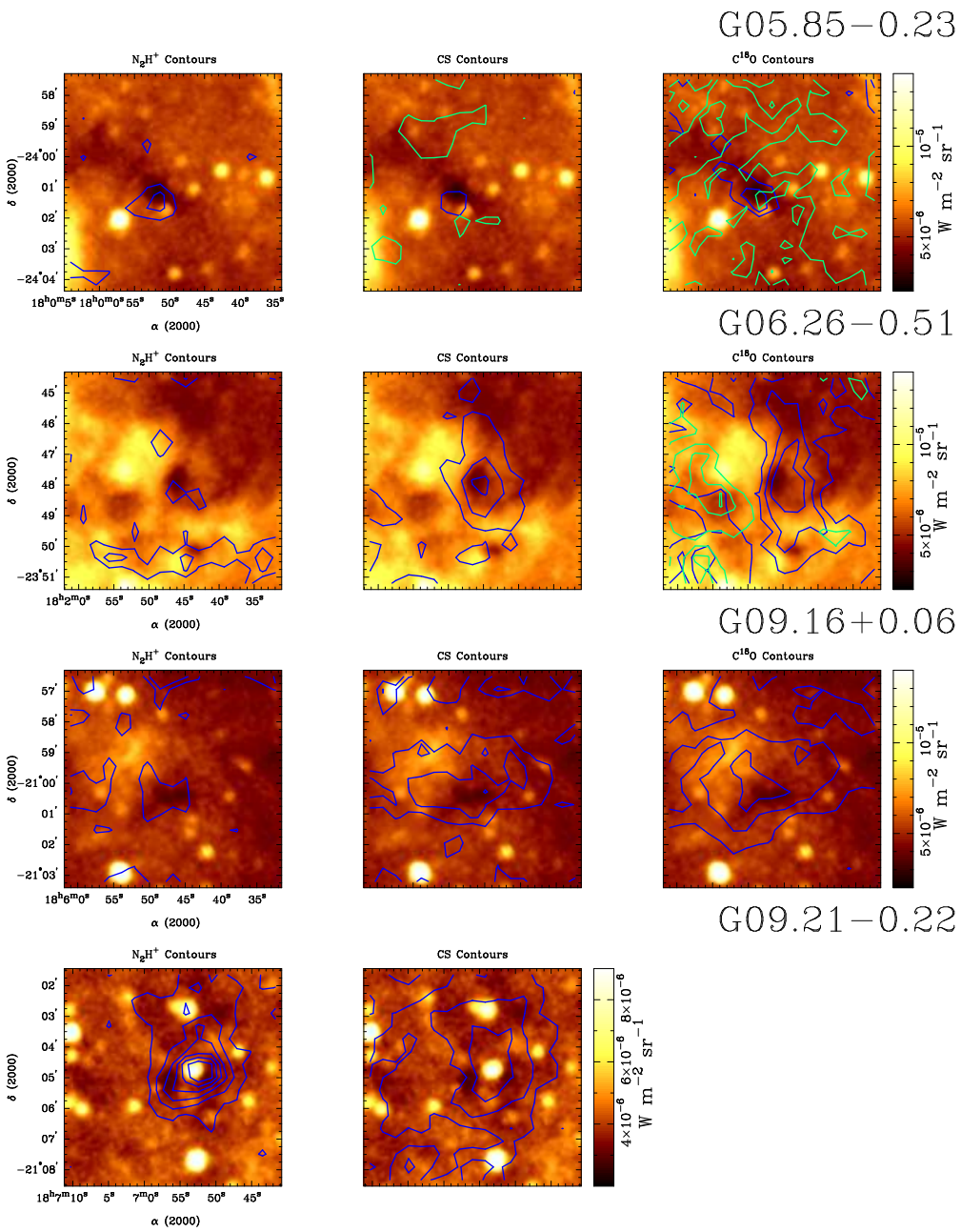

Figure 2.1. MSX images of IRDCs G005.85−0.23, G006.26−0.51, G009.16+0.06, and G009.21−0.22 with FCRAO contours *G005.85−0.23* - blue contours show emission at 17km s^{-1}; green contours: 9km s^{-1}. Levels: 1,2 K km s^{-1} for all plots. *G006.26−0.51* - blue contours : 23km s^{-1}; green contours : 17 km s^{-1}. Levels: N_2H^+ : 0.5, 1 K km s^{-1}. CS : 1,2,3,4 K km s^{-1}. $C^{18}O$: 1,2,3 K km s^{-1} for both velocities. *G009.16+0.06* - blue contours : 31km s^{-1}. Levels: N_2H^+ : 1,2 K km s^{-1}. CS : 0.5,1,1.5 K km s^{-1}. $C^{18}O$: 1,2,3 K km s^{-1}. *G009.21−0.22* - blue contours : 43km s^{-1}. Levels: N_2H^+ : 2,4,6,8,10,12 K km s^{-1}. CS: 1,2,3 K km s^{-1}.

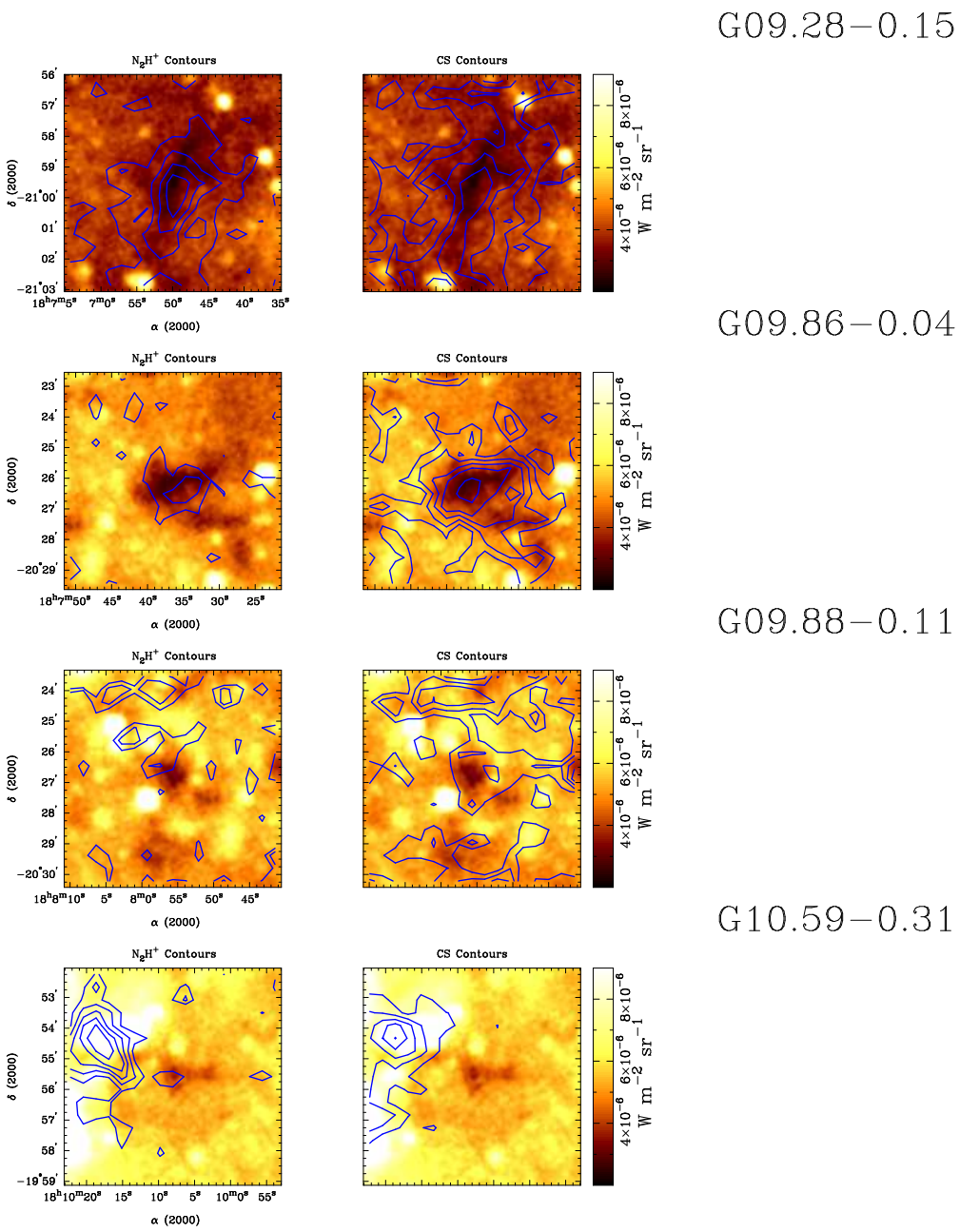

Figure 2.2. MSX images of IRDCs G009.28 −0.15, G009.86−0.04, G009.88 −0.11, and G010.59−0.31 with FCRAO contours *G009.28 −0.15* - blue contours : 42km s^{-1}. Levels: N_2H^+ : 1.5,3,4.5,6,7.5 K km s^{-1}. CS: 0.5,1,1.5,2,3 K km s^{-1}. *G009.86−0.04* - blue contours : 18km s^{-1}. Levels: N_2H^+ : 1.5,3,4.5,6,7.5 K km s^{-1}. CS: 0.5,1,1.5,2,3 K km s^{-1}. *G009.88 −0.11* - blue contours : 17km s^{-1}. Levels: N_2H^+ : 1,2 K km s^{-1}. CS: 0.5,1,1.5,2,3 K km s^{-1}. *G010.59−0.31* - blue contours : 17km s^{-1}. Levels: 3,5,7,9,11 K km s^{-1} for both molecules.

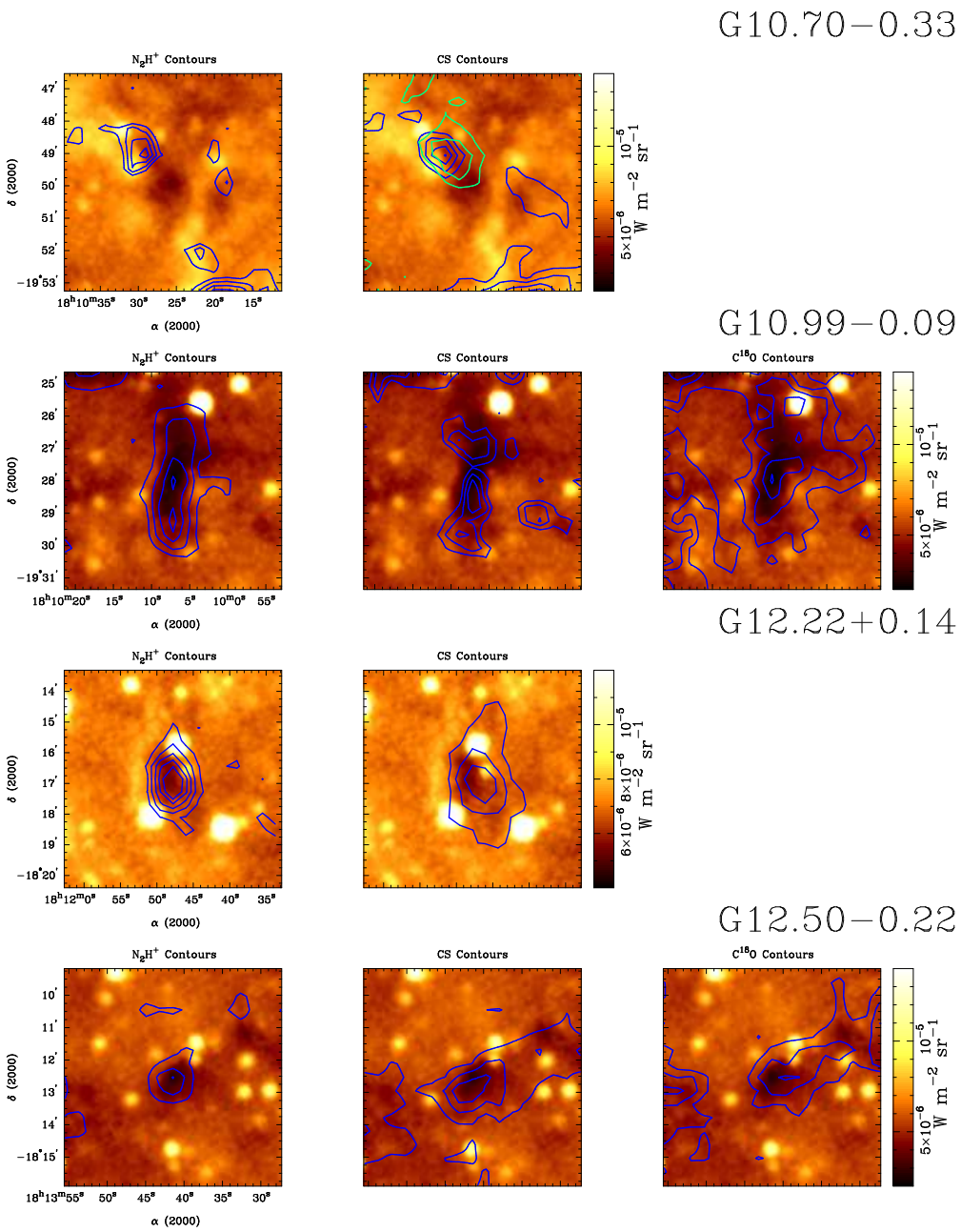

Figure 2.3. MSX images of IRDCs G010.70−0.33, G010.99−0.09, G012.22+0.14, and G012.50−0.22 with FCRAO contours *G010.70−0.33* - blue contours : 0km s^{-1}; green contours : 33km s^{-1}. Levels: 2,3,4,5 K km s^{-1} for both molecules/velocities. *G010.99−0.09* - blue contours : 30km s^{-1}. Levels: N_2H^+ : 2,4,6,8,10 K km s^{-1}. CS: 1,1.5,2 K km s^{-1}. $C^{18}O$: 2,3,4,5 K km s^{-1}. *G012.22+0.14* - blue contours : 40 km s^{-1}. Levels: 1,2,3,4,5 K km s^{-1} for each molecule. *G012.50−0.22* - blue contours : 36 km s^{-1}. Levels: N_2H^+ : 2,4,6,8,10 K km s^{-1}. CS: 1,2,3,4 K km s^{-1}. $C^{18}O$: 1,2,3 K km s^{-1}.

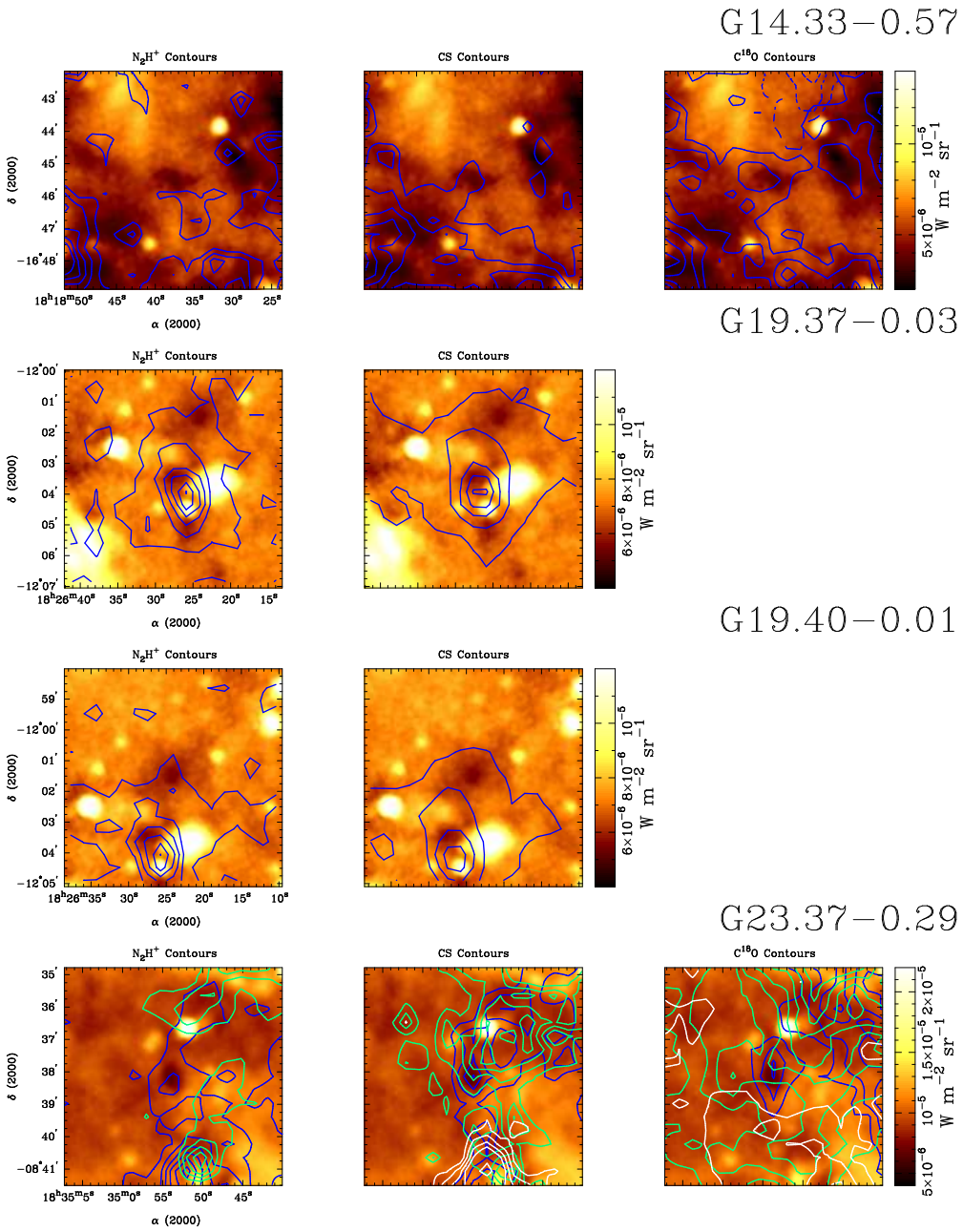

Figure 2.4. MSX images of IRDCs G014.33−0.57, G019.37−0.03, G019.40−0.01, and G023.37−0.29 with FCRAO contours *G014.33−0.57* - blue contours : 19km s^{-1} (solid (a)), 20km s−1 (dashed (b)) Levels: N_2H^+: 2,4,6,8,10 K km s^{-1}. CS : 2,3,4,5,6,7 K km s^{-1}. $C^{18}O$: 4,5,6,7,8,9 K km s^{-1} (a); 2,3,4 K km s^{-1} (b). *G019.37−0.03* - blue contours : 27km s^{-1}. Levels: N_2H^+ : 1,3,5,7,9,11 K km s^{-1}. CS : 1,2.5,4,5.5,7 K km s^{-1}. *G019.40−0.01* - blue contours : 27km s^{-1}. Levels: N_2H^+ : 1,3,5,7,9,11 K km s^{-1}. CS : 1,2.5,4,5.5,7 K km s^{-1}. *G023.37−0.29* - blue contours : 78km s^{-1}; green contours : 103km s^{-1}; white contours : 65km s^{-1}. Levels: N_2H^+ : 3,6,9,12,15,18 K km s^{-1} (78km s^{-1} component); 4,6,8,10 K km s^{-1} (103km s^{-1}). CS : 3,4,5,6,7 K km s^{-1} (78km s^{-1}); 3,4,5,6 K km s^{-1} (103km s^{-1}); 3,4,5,6,9 K km s^{-1} (65km s^{-1}). $C^{18}O$: 5,7,9,11 K km s^{-1} (78km s^{-1}); 3,6,9,12,15,18,21,24 K km s^{-1} (103km s^{-1}); 3,6,9 K km s^{-1} (65km s^{-1}).

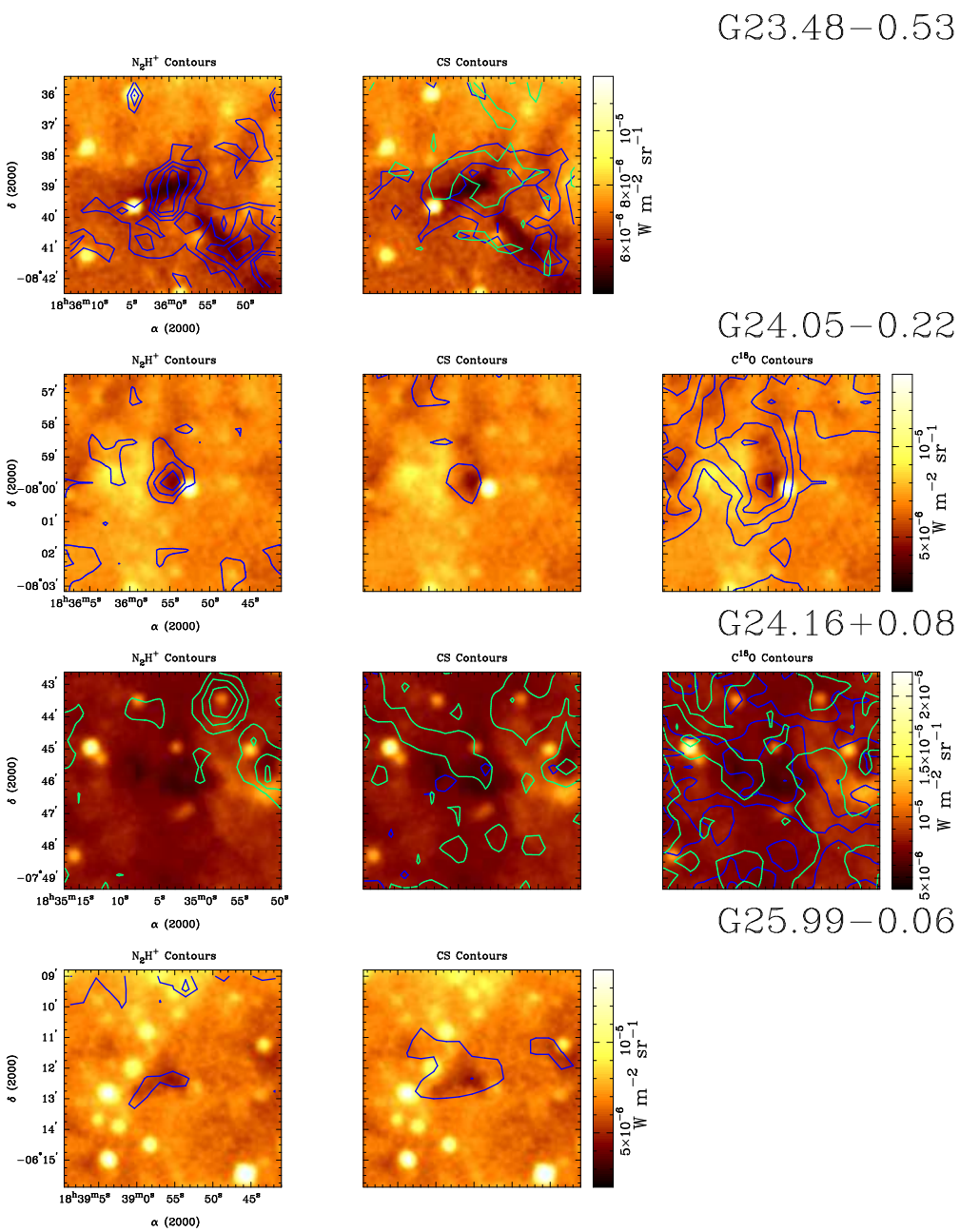

Figure 2.5. MSX images of IRDCs G023.48 −0.53, G024.05−0.22, G024.16+0.08, and G025.99−0.06 with FCRAO contours *G023.48 −0.53* - blue contours : 64km s^{-1}; green contours : 76km s^{-1}. Levels: 1,1.5,2,2.5 K km s^{-1} both molecules/velocities. *G024.05−0.22* - blue contours : 82km s^{-1}. Levels: N_2H^+ : 1,2,3 K km s^{-1}. CS : 1,2,3,4 K km s^{-1}. $C^{18}O$: 1,2,3,4,5 K km s^{-1}. *G024.16+0.08* - blue contours : 53km s^{-1}; green contours : 113km s^{-1}. Levels: N_2H^+ : 1,2,3 K km s^{-1} (113km s^{-1} component). CS : 1,2,3 K km s^{-1} in both velocities. $C^{18}O$: 1,2,3 K km s^{-1} (53km s^{-1}); 2,4,6 K km s^{-1} (113km s^{-1}). *G025.99−0.06* - blue contours : 90km s^{-1}. Levels: N_2H^+ : 1,2,3 K km s^{-1}. CS : 1,2 K km s^{-1}.

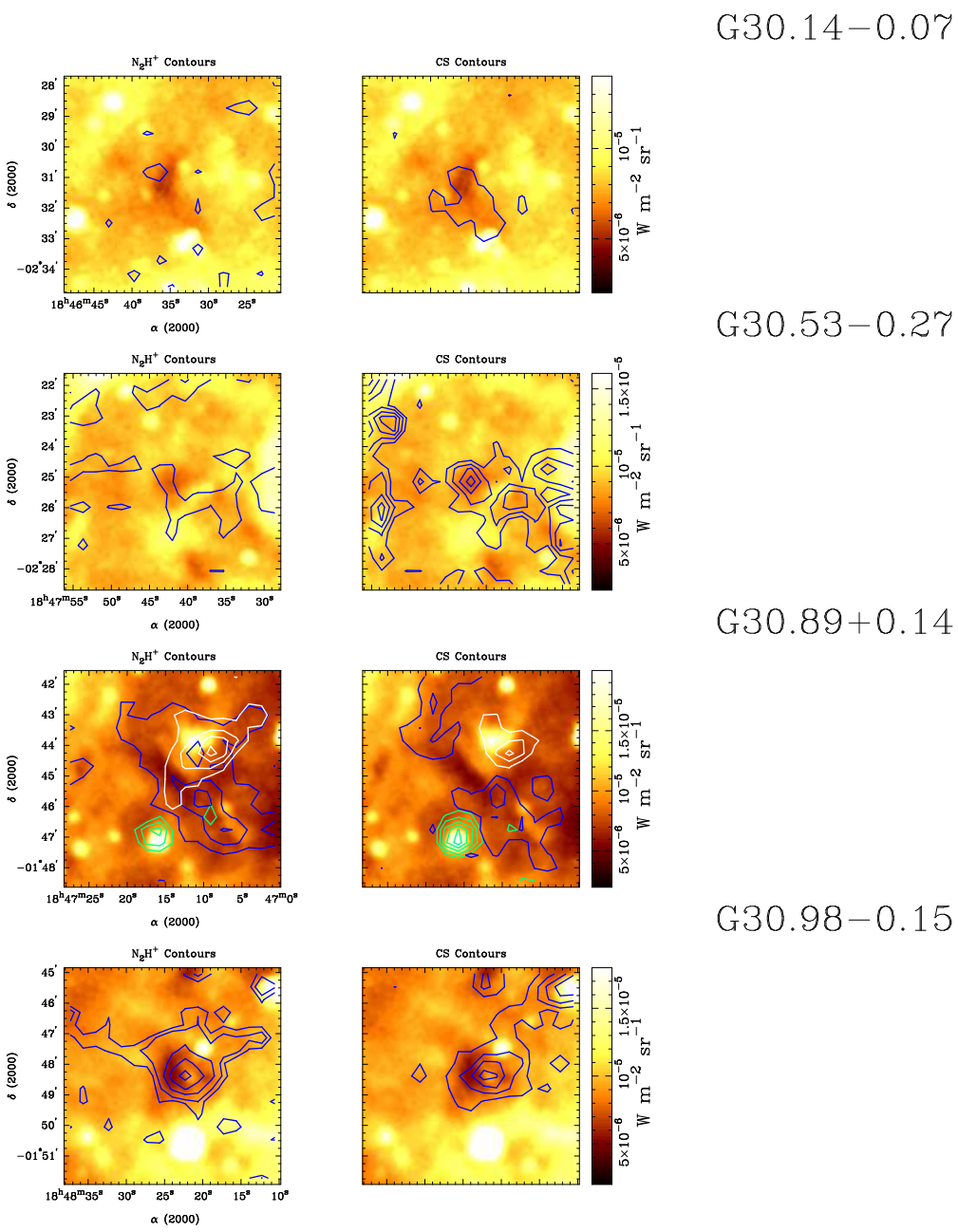

Figure 2.6. MSX images of IRDCs G030.14−0.07, G030.53−0.27, G030.89+0.14, and G030.98 −0.15 with FCRAO contours *G030.14−0.07* - blue contours : 87km s^{-1}. Levels: 0.5 for both molecules. *G030.53−0.27* - blue contours : 103km s^{-1}. Levels: N_2H^+ : 0.5 K km s^{-1}. CS : 1,1.5,2,2.5 K km s^{-1}. *G030.89+0.14* - blue contours : 96km s^{-1}; green contours : 40km s^{-1}; white contours : 108km s^{-1}. Levels: N_2H^+ : 2,3,4 K km s^{-1} (96km s^{-1} component); 2,4,6,8,10 K km s^{-1} (40km s^{-1}); 2,4,6,8,10 K km s^{-1} (108km s^{-1}). CS : 3,4,5,6,7 K km s^{-1} (96km s^{-1}); 2,3,4 K km s^{-1} (40km s^{-1} and 108km s^{-1} components). *G030.98 −0.15* - blue contours : 78km s^{-1}. Levels: N_2H^+ : 1,2,4,6,8 K km s^{-1}. CS : 1,2,3,4 K km s^{-1}.

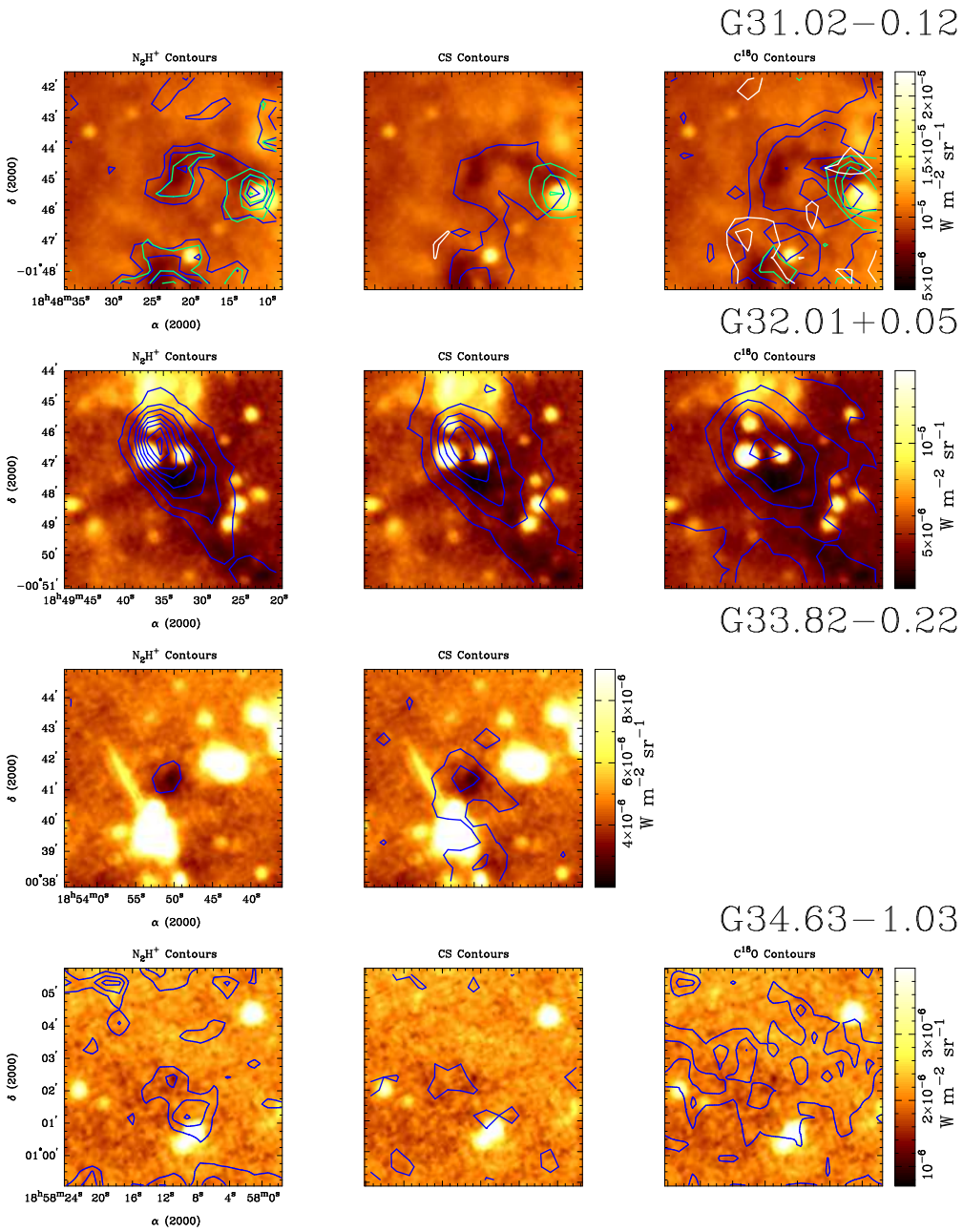

Figure 2.7. MSX images of IRDCs G031.02−0.12, G032.01+0.05, G033.82−0.22, and G034.63−1.03 with FCRAO contours *G031.02−0.12* - blue contours : 76km s^{-1}; green contours : 83km s^{-1}; white contours : 92km s^{-1}. Levels: N_2H^+ : 1,2,3,4 K km s^{-1} (76km s^{-1} and 83km s^{-1} components); 2,4,6,8,10 K km s^{-1} (92km s^{-1}). CS : 1,2,3,4,5,6,7 K km s^{-1} (76km s^{-1}); 1,2,3,4,5,6 K km s^{-1} (83km s^{-1}); 1,2,3,4,5,6,9 K km s^{-1} (92km s^{-1}). $C^{18}O$: 1,2,3,4,5,6,7,8,9 K km s^{-1} (76km s^{-1}); 1,2,3,6,9,12,15,18,21,24 K km s^{-1} (83km s^{-1}); 1,2,3 K km s^{-1} (92km s^{-1}) *G032.01+0.05* - blue contours : 95km s^{-1}. Levels: N_2H^+ : 3,6,9,12,15,18,21,24 K km s^{-1}. CS : 2,4,6,8,10 K km s^{-1}. $C^{18}O$: 2,4,6,8,10 K km s^{-1}. *G033.82−0.22* - blue contours : 11km s^{-1}. Levels: N_2H^+ : 1,2,3 K km s^{-1}. CS : 0.5,1 K km s^{-1}. *G034.63−1.03* - blue contours : 14km s^{-1}. Levels: N_2H^+ : 1,2,3 K km s^{-1}. CS : 0.5,1.0 K km s^{-1}. $C^{18}O$: 0.5,1,1.5 K km s^{-1}.

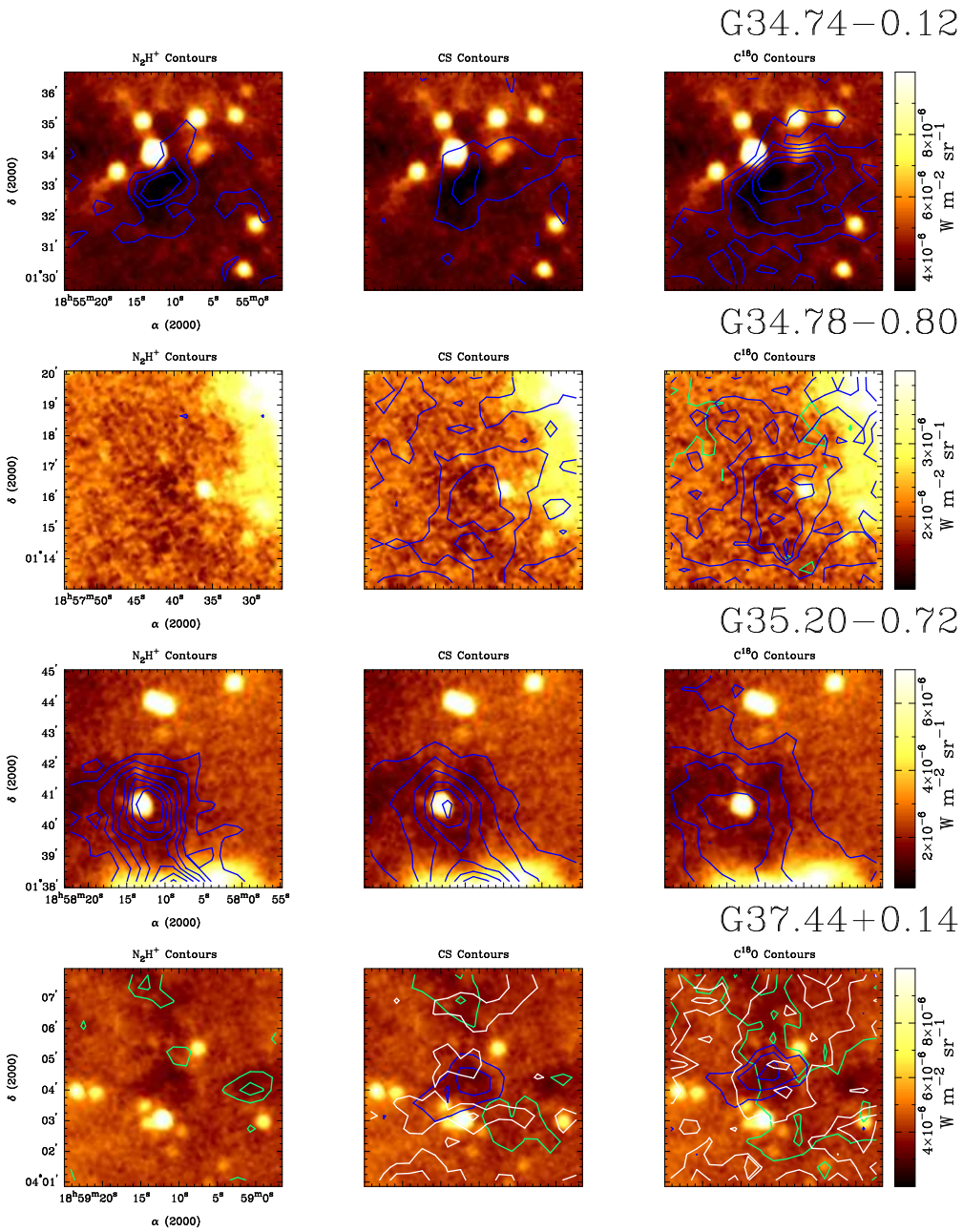

Figure 2.8. MSX images of IRDCs G034.74−0.12, G034.78 −0.80, G035.20−0.72, G037.44+0.14 and with FCRAO contours *G034.74−0.12* - blue contours : 79km s^{-1}. Levels: N_2H^+ : 1,2,3 K km s^{-1}. CS : 1,2,3,4 K km s^{-1}. $C^{18}O$: 1,2,3,4,5 K km s^{-1}. *G034.78 −0.80* - blue contours : 44km s^{-1}; green contours : 37km s^{-1}. Levels: N_2H^+ : 1,2,3,4 K km s^{-1} for both velocities. CS : 1,2,3 K km s^{-1} for both velocities. $C^{18}O$: 1,2,3 K km s^{-1} (44km s^{-1} component); 1,2,3,4,5,6 K km s^{-1} (37km s^{-1}). *G035.20−0.72* - blue contours : 33km s^{-1}. Levels: N_2H^+ : 2,4,6,8,10,12,14 K km s^{-1}. CS : 2,4,6,8,10,12 K km s^{-1}. $C^{18}O$: 2,4,6,8,10,12,14 K km s^{-1}. *G037.44+0.14* - blue contours : 40 km s^{-1}; green contours : 18km s^{-1}; white contours : 86km s^{-1}. Levels: 0.5,1,2,3 K km s^{-1} for all molecules/velocities.

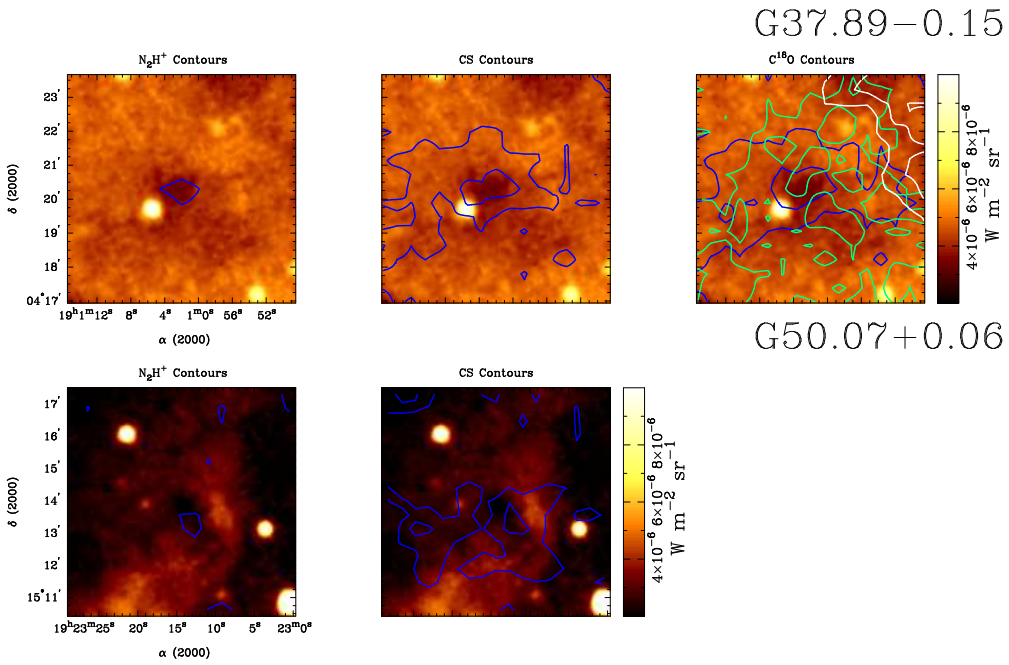

Figure 2.9. MSX images of IRDCs G037.89−0.15 and G050.07+0.06 with FCRAO contours. *G037.89−0.15* - blue contours : 13km s^{-1}; green contours : 65km s^{-1}; white contours : 86km s^{-1}. Levels: N_2H^+ : 0.5.1,2,3 K km s^{-1} (13km s^{-1} component). CS : 0.5.1,2,3 K km s^{-1} (13km s^{-1}). $C^{18}O$: 0.5,1,2,3 K km s^{-1} (13km s^{-1} and 65km s^{-1}); 2,3 K km s^{-1} (86km s^{-1}). *G050.07+0.06* - blue contours 55km s^{-1}. Levels: 0.5,1 K km s^{-1} for both molecules.

Table 2.1: FCRAO Molecular Line Observations.

			N_2H^+ J=1–0			$C^{18}O$ J=1–0			CS J=2–1		
Source	$\Delta\alpha$	$\Delta\delta$	$\int T_A^* dv$	V	Δv	$\int T_A^* dv$	V	Δv	$\int T_A^* dv$	V	Δv
	($'$)	($'$)	(K km s^{-1})	(km s^{-1})	(km s^{-1})	(K km s^{-1})	(km s^{-1})	(km s^{-1})	(K km s^{-1})	(km s^{-1})	(km s^{-1})
G005.85−0.23	0.4	−0.4	1.21(0.15)	17.2(0.1)	0.8(0.1)	1.44(0.17)	17.0(0.1)	1.7(0.2)	0.47(0.10)	16.9(0.2)	2.2(0.3)
G006.26−0.51	0.0	0.0	(<0.15)	···	···	1.69(0.11)	22.7(0.1)	2.3(0.2)	1.64(0.15)	23.2(0.2)	4.2(0.5)
G009.16+0.06	0.0	0.0	(<0.12)	···	···	1.39(0.09)	31.3(0.1)	1.7(0.1)	0.40(0.07)	31.3(0.1)	1.2(0.3)
G009.21−0.22	0.0	0.0	3.59(0.15)	42.8(0.1)	1.8(0.2)	···	···	···	1.29(0.11)	42.7(0.1)	2.8(0.3)
G009.28−0.15	0.0	0.0	3.66(0.10)	41.4(0.1)	1.9(0.4)	···	···	···	1.27(0.12)	41.3(0.1)	2.6(0.3)
G009.86−0.04	0.0	0.0	0.87(0.11)	18.1(0.1)	1.1(0.2)	···	···	···	1.52(0.14)	17.8(0.1)	2.3(0.2)
G009.88−0.11	0.0	0.0	(<0.13)	···	···	···	···	···	0.54(0.15)	17.3(0.2)	1.8(0.6)
G010.59−0.31	0.0	0.0	(<0.40)	···	···	···	···	···	(<0.24)	···	···
G010.70−0.33	0.0	0.0	(<0.13)	···	···	···	···	···	(<0.13)	···	···
G010.99−0.09	0.0	0.0	4.24(0.11)	29.6(0.1)	2.4(0.2)	2.25(0.17)	29.5(0.1)	2.2(0.2)	1.00(0.12)	29.2(0.3)	4.2(0.5)
G012.22+0.14	0.0	0.0	3.60(0.08)	39.6(0.1)	1.7(0.1)	···	···	···	1.78(0.07)	36.7(0.1)	2.2(0.1)
G012.50−0.22	0.0	0.0	2.97(0.10)	35.8(0.1)	1.8(0.1)	1.60(0.13)	35.7(0.1)	1.8(0.2)	1.40(0.10)	35.6(0.1)	2.0(0.2)
G014.33−0.57a	0.0	0.0	(<0.14)	···	···	2.19(0.15)	19.3(0.1)	2.1(0.2)	1.25(0.13)	19.6(0.1)	2.4(0.3)
G014.33−0.57b	−1.7	0.8	1.42(0.14)	20.0(0.1)	1.1(0.2)	1.81(0.12)	19.9(0.1)	1.6(0.2)	0.84(0.10)	20.3(0.1)	1.4(0.2)
G019.28−0.39	0.0	0.0	(<0.17)	···	···	···	···	···	0.26(0.07)	54.0(0.1)	1.1(0.2)
G019.37−0.03	0.0	0.0	3.62(0.11)	27.3(0.1)	2.5(0.1)	···	···	···	3.02(0.07)	27.0(0.1)	3.8(0.1)
G019.40−0.01	0.0	0.0	0.95(0.11)	27.0(0.1)	1.2(0.3)	···	···	···	0.81(0.06)	26.5(0.1)	2.9(0.3)
G023.37−0.29	0.0	0.0	2.88(0.27)	78.5(0.1)	2.0(0.2)	3.97(0.21)	78.1(0.1)	2.7(0.2)	2.30(0.12)	77.8(0.1)	4.8(0.3)
G023.48−0.53a	0.0	0.0	1.45(0.12)	64.8(0.1)	2.5(0.4)	···	···	···	0.90(0.09)	63.9(0.3)	4.8(0.6)
G023.48−0.53b	-2.1	-2.1	1.24(0.12)	62.8(0.1)	2.9(0.4)	···	···	···	0.73(0.08)	62.7(0.3)	2.9(0.4)
G024.05−0.22	0.0	0.0	2.71(0.21)	81.4(0.1)	1.9(0.3)	2.30(0.10)	81.5(0.1)	2.0(0.1)	1.00(0.13)	82.0(0.2)	2.8(0.5)
G024.16+0.08	0.0	0.0	(<0.10)	···	···	1.64(0.16)	51.8(0.1)	1.9(0.2)	(<0.10)	···	···
G025.99−0.06	0.0	0.0	0.80(0.15)	89.9(0.3)	1.6(0.5)	···	···	···	1.05(0.11)	90.2(0.1)	2.4(0.3)
G030.14−0.07	0.0	0.0	(<0.12)	···	···	···	···	···	(<0.15)	86.8(0.2)[a]	2.7(0.5)[a]

G030.14−0.07	0.0	0.0	(<0.12)	···	···	···	···	···	(<0.15)	86.8(0.2)	2.7(0.5)
G030.49−0.39	1.2	−0.8	(<0.14)	···	···	···	···	···	0.62(0.12)	106.4(0.3)	3.0(0.9)
G030.53−0.27	0.0	0.0	(<0.12)	···	···	···	···	···	1.73(0.19)	102.9(0.4)	7.3(0.9)
G030.89+0.14	0.0	0.0	1.29(0.13)	96.5(0.2)	3.4(0.3)	···	···	···	0.56(0.10)	95.9(0.3)	3.0(0.5)
G030.98−0.15	-0.4	0.0	4.56(0.12)	77.9(0.1)	2.6(0.1)	···	···	···	2.27(0.11)	77.9(0.1)	4.3(0.2)
G031.02−0.12	0.0	0.0	1.57(0.07)	76.6(0.1)	2.2(0.2)	1.24(0.11)	76.2(0.1)	3.0(0.3)	0.66(0.08)	76.6(0.2)	3.3(0.4)
G032.01+0.05	0.0	0.0	7.18(0.10)	95.3(0.1)	3.9(0.1)	4.42(0.12)	97.2(0.1)	4.7(0.2)	4.03(0.09)	96.0(0.1)	6.8(0.2)
G033.82−0.22	0.0	0.0	1.03(0.11)	11.3(0.1)	1.0(0.3)	···	···	···	0.48(0.09)	11.5(0.1)	1.0(0.2)
G034.63−1.03	0.0	0.0	1.16(0.15)	13.6(0.2)	2.6(0.6)	0.58(0.08)	12.8(0.1)	1.1(0.2)	(<0.15)	···	···
G034.74−0.12	0.0	0.0	1.92(0.17)	79.1(0.1)	2.7(0.3)	3.51(0.14)	78.9(0.2)	2.1(0.1)	1.11(0.10)	78.9(0.2)	3.8(0.4)
G034.78−0.80	0.0	0.0	0.33(0.11)	43.2(0.4)	3.0(0.7)	2.25(0.10)	44.1(0.1)	3.3(0.1)	1.83(0.07)	43.5(0.1)	3.0(0.2)
G035.20−0.72	0.0	0.0	3.02(0.20)	33.1(0.1)	2.5(0.3)	2.04(0.12)	33.2(0.1)	1.9(0.1)	1.91(0.13)	33.2(0.1)	3.4(0.3)
G037.44+0.14a	0.0	0.0	(<0.10)	···	···	1.14(0.06)	40.0(0.1)	1.6(0.1)	0.77(0.04)	40.1(0.1)	1.4(0.1)
G037.44+0.14b	−2.5	−0.4	0.65(0.08)	17.8(0.1)	0.5(0.1)	0.52(0.04)	17.8(0.1)	0.7(0.1)	0.25(0.03)	17.7(0.1)	0.9(0.1)
G037.89−0.15	0.0	0.0	0.45(0.08)	12.9(0.1)	0.7(0.1)	0.63(0.04)	12.9(0.1)	0.7(0.1)	0.36(0.04)	13.0(0.1)	0.7(0.1)
G043.64−0.82	0.4	2.4	(<0.25)	···	···	···	···	···	0.25(0.05)	85.4(0.1)	0.5(0.1)
G043.78+0.05	0.0	0.0	(<0.17)	···	···	···	···	···	(<0.09)	···	···
G050.07+0.06	−0.8	−0.8	(<0.19)	···	···	···	···	···	0.73(0.08)	54.8(0.1)	1.5(0.2)
G053.88−0.18	0.0	0.0	(<0.21)	···	···	···	···	···	(<0.12)	···	···
G075.75+0.75	0.0	0.0	(<0.12)	···	···	···	···	···	(<0.07)	···	···
G076.38+0.63	0.0	0.0	(<0.15)	···	···	···	···	···	(<0.07)	···	···

[a]Non-detection of CS in single scan. Average of 25 scans detects a weak line at the 5σ level. The velocity and line width from this average are provided in the table.

2.3.2 Molecular Emission Morphologies

Figures 2.1 through 2.9 display the MSX 8.8 μm images of each dark cloud overlayed with the integrated intensity maps of molecular emission for all observed molecular transitions. The contour levels for each dark cloud are specified in the captions. In some cases, multiple velocity components are detected, and the different velocity components are given different colors. The blue contours always correspond to the molecular emission morphology that most closely corresponds to the distribution of 8 μm absorption seen in the MSX image, and, therefore, is most likely to be associated with the dark cloud. The line properties of the other velocity components (i.e. emission that is unassociated with the absorbing cloud) are not reported. There are three cases in which an a/b designation was assigned to distinguish two emission peaks. For G014.33−0.57 and G023.48−0.53, there are two spatially distinct and separate emission peaks at approximately the same characteristic velocity. This may suggest that in these cases, we were able to resolve spatially separated fragments of a cloud. In the case of G037.44+0.14, there are two velocity components that appear to correspond to absorbing regions (the 40km s^{-1} feature corresponding to the central absorbing cloud; the 18km s^{-1} feature correpsonding to absorption to the north and west). Based on our assumptions, this would indicate that there are two unassociated dark clouds apparent in the same region of the sky by chance.

The IRDCs observed here exhibit a wide variety of morphologies evident in Figures 2.1 - 2.9. Some maps show well defined cores in all three molecular tracers (e.g. G032.01+0.05). Other maps, like G006.26−0.51, show fairly well defined cores in $C^{18}O$ and CS, but nothing obvious is seen in N_2H^+. And others, like G009.21−0.22, show a strong centrally concentrated N_2H^+ core but CS that is much more diffuse. Finally, there are cores like G010.59−0.31 that show no real evidence for molecular emission centered on the dark cloud at all in any of the tracers. In this case, it is possible that any molecular emission directly associated with the dark cloud lies outside of the observed velocity band (see Appendix A).

These differences in the molecular emission maps may be the result of differences in the evolutionary states. It is well known that CS and $C^{18}O$ can form relatively

quickly in the gas phase whereas N_2H^+ takes significantly longer. However, as density enhances, the CS and $C^{18}O$ tend to deplete onto the surfaces of dust grains, whereas N_2H^+ will remain in the gas phase. Upon protostar formation, CS and $C^{18}O$ can be released from dust grain surfaces and N_2H^+ is destroyed (e.g. see models of Bergin & Langer, 1997) and Lee et al. (2004). Therefore, two scenarios can lead to the low abundance of N_2H^+ relative to CS or $C^{18}O$: the star forming core is at an early stage of condensation and the densities are low such that CS and $C^{18}O$ would be not affected by dust depletion, or the presence of a protostar has released the CS and $C^{18}O$ from dust grains, all the while the N_2H^+ abundance is essentially unchanged throughout the process. Another possible explanation of the differences seen in the maps is that some of the dark clouds may contain as yet undetected protostars, obscured by the high opacity apparent in the 8.8 μm MSX images. In Chapter 3, I discuss star formation in IRDCs, and I include Appendix B, which gives information on all known signposts of star formation (e.g. masers, IRAS sources, radio emission) within 1 arcminute of the MSX absorption peak.

2.3.3 Distance Estimates

The kinematic distance to each dark cloud is calculated using using the line center velocity and the Milky Way rotation curve model of Fich et al. (1989). The distance assignments are presented in Table 2.2 for dark clouds for which we estimated masses. (Sources to which we are unable to assign a distance or those that show no significant emission are not subject to further calculations.) For every position, there is both a "near" and "far" distance solution that corresponds to the characteristic velocity of the emission. In addition to this ambiguity, Fich et al. (1989) cite a $\pm$14% maximal deviation of the data from their rotation curve model; based on this consideration, we calculate errors in the distances and provide them in Table 2.2. In the cases where no error range (or an incomplete one) is given, no physical solution exists when calculating the distance with that error offset. For all subsequent calculations, we assume that the dark cloud is located at the "near" distance. We believe that this is a reasonable assumption since the clouds are seen in absorption against the

Galactic mid-infrared background and, therefore, are unlikely to reside at the "far" distance. Assuming the "near" kinematical distance, which is also listed in Table 2.2, a typical core has a diameter of ∼0.9 pc.

Interestingly, the kinematical distances for the velocity component associated with the absorption are seldom coincident with the distances estimated for the UC HII region that was the original search target. In most cases we detect molecular emission at a single velocity, and no possible distance solution from the galactic rotation curve is consistent with the distance to the UC HII region. However, in the cases where there are multiple velocity components, the distance to the UC HII region is often consistent with one of the kinematic distance solutions for a secondary velocity component. For

Table 2.2: Kinematic distances to IRDCs.

Source	Velocity Component (km s^{-1})	Near Distance (kpc)	Far Distance (kpc)	Adopted Distance (kpc)	UCHII region Distance (kpc)
G005.85−0.23	17	$3.14^{+0.66}_{-0.76}$	$13.78^{+0.75}_{-0.67}$	3.14	2.6
	9	$1.53^{+0.86}_{-0.96}$	$15.38^{+0.97}_{-0.86}$		
G006.26−0.51	23	$3.78^{+0.59}_{-0.67}$	$13.12^{+0.67}_{-0.60}$	3.78	2.6
	17	$3.01^{+0.68}_{-0.77}$	$13.89^{+0.77}_{-0.68}$		
G009.16+0.06	31	$3.81^{+0.61}_{-0.69}$	$12.97^{+0.69}_{-0.61}$	3.81	6.2
G009.21−0.22	43	$4.57^{+0.53}_{-0.59}$	$12.21^{+0.59}_{-0.53}$	4.57	6.2
G009.28−0.15	42	$4.48^{+0.54}_{-0.61}$	$12.30^{+0.61}_{-0.54}$	4.48	6.2
G009.86−0.04	18	$2.36^{+0.78}_{-0.88}$	$14.39^{+0.87}_{-0.78}$	2.36	6.0
G010.99−0.09	30	$3.31^{+0.69}_{-0.76}$	$13.37^{+0.77}_{-0.68}$	3.31	6.0
G012.22+0.14	40	$3.75^{+0.65}_{-0.72}$	$12.86^{+0.73}_{-0.65}$	3.75	5.2
G012.50−0.22	36	$3.55^{+0.67}_{-0.75}$	$13.05^{+0.75}_{-0.67}$	3.55	5.2
G014.33−0.57	19	$1.99^{+0.85}_{-0.95}$	$14.48^{+0.95}_{-0.85}$	1.99	2.1
	20	$2.04^{+0.85}_{-0.94}$	$14.43^{+0.94}_{-0.85}$	2.04	
G019.37−0.03	27	$2.26^{+0.88}_{-0.98}$	$13.78^{+0.97}_{-0.88}$	2.26	4.5
G019.40−0.01	27	$2.23^{+0.88}_{-0.98}$	$13.81^{+0.97}_{-0.89}$	2.23	4.5
G023.37−0.29	78	$4.70^{+0.90}_{-0.88}$	$10.91^{+0.88}_{-0.91}$	4.70	9.0
	103	$5.69^{+1.20}_{-0.91}$	$9.91^{+0.92}_{-1.20}$		
	65	$4.13^{+0.88}_{-0.89}$	$11.47^{+0.90}_{-0.87}$		
G023.48−0.53	64	$4.10^{+0.88}_{-0.90}$	$11.50^{+0.89}_{-0.89}$	4.10	9.0

	76	$4.60^{+0.91}_{-0.88}$	$10.99^{+0.88}_{-0.91}$		
G024.05−0.22	82	$4.82^{+0.96}_{-0.90}$	$10.70^{+0.91}_{-0.96}$	4.82	9.0
G024.16+0.08	53	$3.46^{+0.91}_{-0.94}$	$12.05^{+0.94}_{-0.91}$	3.46	9.0
	113	$6.13_{-1.03}$	9.38		
G025.99−0.06	90	$5.15^{+1.23}_{-0.99}$	$10.13^{+0.99}_{-1.23}$	5.15	14.0
G030.89+0.14	96	$5.65_{-1.38}$	8.93	5.65	8.5
	40	$2.62^{+1.14}_{-1.15}$	$11.97^{+1.15}_{-1.14}$		
	108	$6.65_{-1.84}$	7.94		
G030.98−0.15	78	$4.63^{+1.63}_{-1.19}$	$9.94^{+1.19}_{-1.62}$	4.63	8.5
G031.02−0.12	76	$4.56^{+1.56}_{-1.19}$	$10.01^{+1.19}_{-1.56}$	4.56	8.5
	83	$4.90_{-1.23}$	9.67		
	92	$5.41_{-1.33}$	9.16		
G032.01+0.05	95	$5.77_{-1.51}$	8.64	5.77	8.5
G034.63−1.03	14	$0.84^{+1.26}$	$13.14^{+1.32}_{-1.26}$	0.84	3.2
G034.74−0.12	79	$4.86_{-1.45}$	9.11	4.86	3.7
G034.78−0.80	44	$2.80^{+1.33}_{-1.26}$	$11.17^{+1.25}_{-1.33}$	2.80	3.2
	37	$2.41^{+1.28}_{-1.26}$	$11.56^{+1.26}_{-1.29}$		
G035.20−0.72	33	$2.17^{+1.29}_{-1.28}$	$11.73^{+1.27}_{-1.30}$	2.17	3.2
G037.44+0.14	40	$2.59^{+1.47}_{-1.34}$	$10.91^{+1.34}_{-1.47}$	2.59	12.0
	18	$1.16^{+1.34}$	$12.34^{+1.36}_{-1.34}$		
	86	$5.90_{-2.12}$	7.60		
G037.89−0.15	13	$0.82^{+1.35}$	$12.60^{+1.38}_{-1.35}$	0.82	12.0
	65	$4.16_{-1.51}$	9.26		
	86	$6.09_{-2.31}$	7.33		

example, G037.44+0.14 has a secondary detection of a component at 18 km s^{-1}, and the "far" distance associated with it (12.34 kpc) is very close to the distance to the UC HII region (12.0 kpc). In this case, it is likely that we are detecting two clouds along the same line of sight at different distances: one near the UC HII region and one nearer to us. Since the emission of the primary component corresponds so well to the absorbing dark cloud, we maintain that these lie at the "near" distances, though there is significant uncertainty in the distance calculation. Nonetheless, as we will show, these clouds are massive and are likely associated with the formation of intermediate

and high-mass stars and stellar clusters.

2.3.4 Column Densities and Densities

To determine the molecular abundances relative to molecular hydrogen, we also need a measure of the total H_2 column density. We estimate $N(H_2)$ from the MSX images convolved to match the FCRAO beam resolution and the simple relation

$$\tau_\lambda = \sigma_\lambda \cdot N(HI + H_2) \tag{2.1}$$

where τ_λ is the dust optical depth, σ_λ is the dust extinction cross section, and $N(H_2)$ is the column density of molecular hydrogen.

The behavior of the mid-infrared extinction law is an area of active research. The Indebetouw et al. (2005) extinction law results show agreement with Weingartner & Draine (2001) for $R_v = 5.5$, "case B," which corresponds to dense clouds. We therefore adopt a value for σ_λ at 8.8 μm of 2.3×10^{-23} cm^2, though this value can be considered reliable only within a factor of 2. The optical depth, τ_λ, is roughly estimated by examining the relative intensities of the average background ($I_{o,\lambda}$) and central core (I_λ), assuming that

$$I_\lambda \; = \; I_{o,\lambda} e^{-\tau_\lambda} \tag{2.2}$$

assuming there is no emission coming from the core itself. In this estimation, we are neglecting foreground emission. The ratio $I_\lambda / I_{o,\lambda}$ is related, but not identical, to the brightness contrast listed in Appendix A, as those values do not incorporate the convolution to the FCRAO beam, and are provided at the original MSX resolution.

The column densities of $C^{18}O$ and CS are estimated by assuming that the cores are in local thermodynamic equilibrium (LTE) at a temperature of 15 K (as estimated by Carey et al., 1998), and that the emission is optically thin. While the optically thin assumption is probably reasonable for $C^{18}O$, it probably does not hold for CS, which generally has optically thick emission in the interstellar medium. For N_2H^+, the fits to the hyperfine components generally suggest low optical depth, or $\tau \sim 1$.

However, its emission is likely not in LTE. At a density of 10^5 cm^{-3}, the fractional population will be underestimated by a factor of $\sim$1.7 relative to LTE; we therefore apply this correction factor.

We also estimate the gas density by assuming the cloud is spherical and dividing the H_2 column density by the diameter of the cloud (using the sizes listed in Appendix A and the distances in Table 2.2). This gives an average density of ≈ 5000 cm^{-3}. This is well below to the average densities found in other studies of regions of massive star formation using other tracers. For example, Plume et al. (1997) surveyed multiple transitions of CS in 150 H_2O masers (used as signposts of massive star formation) and found an average gas density of 7.9×10^5 cm^{-3}. An obvious explanation for the lower density in our sample is that the clouds are not spherical, as we have naively assumed, and may instead be clumpy on scales below our resolution. Moreover, these objects are likely at an earlier evolutionary state which is characterized by lower densities. A more detailed analysis of the density and column density is presented in (Gibson et al., 2009).

2.3.5 Masses

The total mass of each dark cloud is estimated using an assumed ("near") distance, an approximate size based on the extent of molecular emission, the molecular column densities and approximate abundance calculated at the peak of absorption. Table 2.3 lists the masses of the objects for which there is a significant detection of N_2H^+ or $C^{18}O$ (or both) and a distance could be assigned. Since some of the dark clouds have a different structure when viewed in different molecular tracers and may have different opacities, we have, for completeness, estimated the masses independently based on the abundances derived from both the N_2H^+ and $C^{18}O$ data. Our average mass is $\approx 2000 - 3000$ M$_\odot$ (depending on whether the N_2H^+ or $C^{18}O$ mass is used).

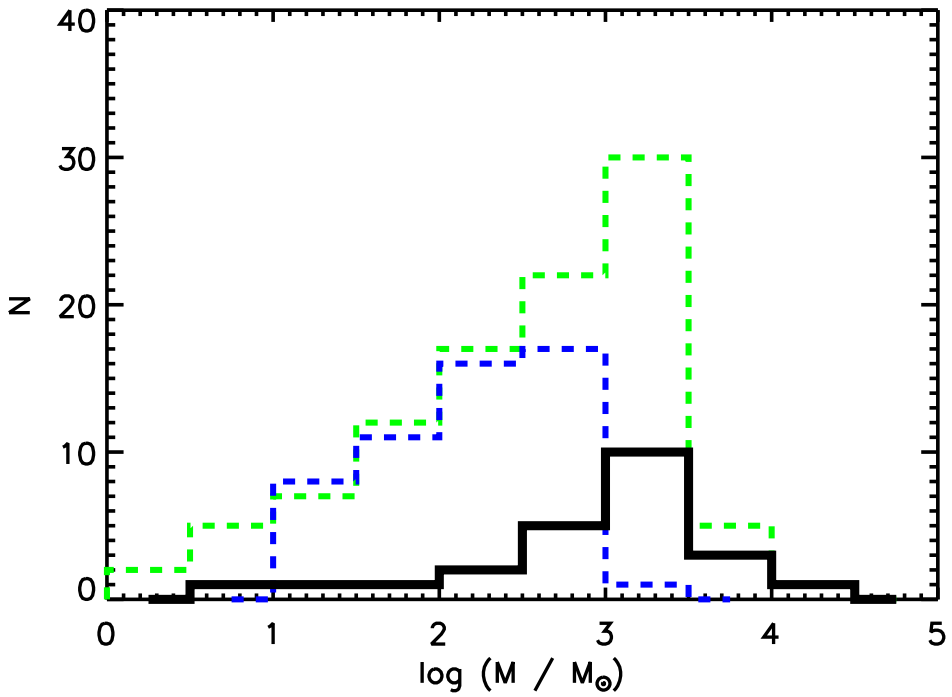

Figure 2.10. IRDC mass histogram - N_2H^+. The mass distribution for our sample of IRDCs as derived from N_2H^+ data plotted with samples from the literature. The black, solid-line histogram show the mass distribution for our sample of IRDCs. The green dashed histogram shows the distribution of masses of the Williams et al. (2004) cores (derived from 850 μm data) based on the near galactic distances. The blue dashed line represents the masses based on the far galactic distances.

Table 2.3: Molecular Abundances and Cloud Masses

Source	Distance	$N(H_2)$	Abundance Relative to H_2			Cloud Mass	
			N_2H^+	$C^{18}O$	CS	N_2H^+	$C^{18}O$
	(kpc)	($10^{21}cm^{-2}$)	(10^{-10})	(10^{-7})	(10^{-10})	($M_\odot$)	($M_\odot$)
G005.85−0.23	3.14	4.4 ± 0.9	2.9	3.5	5.0	2.6E+2	2.5E+2
G006.26−0.51	3.78	13.5 ± 1.2	···	1.3	5.6	···	6.2E+3
G009.16+0.06	3.81	4.4 ± 1.6	···	3.4	4.2	···	3.3E+3
G009.21−0.22	4.57	1.9 ± 1.2	20	···	32	1.4E+3	···
G009.28−0.15	4.48	7.5 ± 1.2	5.2	···	7.9	3.4E+3	···
G009.86−0.04	2.36	9.8 ± 1.0	0.94	···	7.2	1.5E+3	···
G010.99−0.09	3.32	8.1 ± 0.9	5.5	3.0	5.7	2.0E+3	4.3E+3
G012.22+0.14	3.75	2.8 ± 1.0	14	···	30	3.2E+2	···
G012.50−0.22	3.55	4.8 ± 1.7	6.5	3.6	14	5.4E+2	7.1E+3
G014.33−0.57a	1.99	4.1 ± 0.4	···	5.7	14	···	8.3E+2
G014.33−0.57b	2.05	3.4 ± 1.1	4.4	5.7	11	1.3E+3	1.2E+3
G019.37−0.03	2.26	2.2 ± 1.5	17	···	64	2.8E+2	···
G019.40−0.01	2.23	4.9 ± 1.0	2.1	···	7.7	2.1E+3	···
G023.37−0.20	4.70	3.4 ± 1.1	9.0	12	31	3.3E+3	4.1E+3
G023.48−0.53a	4.10	7.8 ± 3.3	2.0	···	5.4	2.7E+3	···
G023.48−0.53b	4.02	5.7 ± 1.4	2.3	···	6.0	2.0E+3	···
G024.05−0.22	4.82	2.7 ± 1.4	11	9.1	17	4.0E+2	2.1E+3
G024.16+0.08	3.46	4.0 ± 1.4	···	4.4	···	···	2.6E+3
G025.99−0.06	5.15	4.1 ± 1.5	2.1	···	12	6.8E+2	···
G030.89+0.14	5.65	4.2 ± 1.0	3.2	···	6.2	1.1E+4	···
G030.98−0.15	4.63	7.3 ± 2.7	6.6	···	14	1.9E+3	···
G031.02−0.12	4.56	4.3 ± 0.9	3.9	3.1	7.1	2.6E+3	4.7E+3
G032.01+0.05	5.77	7.3 ± 2.3	10	6.5	26	8.7E+3	1.3E+4
G034.63−1.03	0.84	3.6 ± 1.0	3.4	1.7	···	5.5E+1	6.0E+1
G034.74−0.12	4.86	5.1 ± 1.5	4.0	7.3	10	8.7E+2	2.4E+3
G034.78−0.80	2.80	6.1 ± 3.8	5.7	3.9	14	···	2.9E+3
G035.20−0.72	2.17	3.5 ± 2.5	9.2	6.2	25	1.0E+3	1.5E+3
G037.44+0.14a	2.59	3.0 ± 1.5	···	4.0	12	···	8.9E+1
G037.44+0.14b	1.16	2.6 ± 0.9	2.6	2.1	4.5	3.2E+1	1.1E+2
G037.89−0.15	0.82	3.2 ± 1.6	1.5	2.1	5.2	3.7E+0	5.4E+1

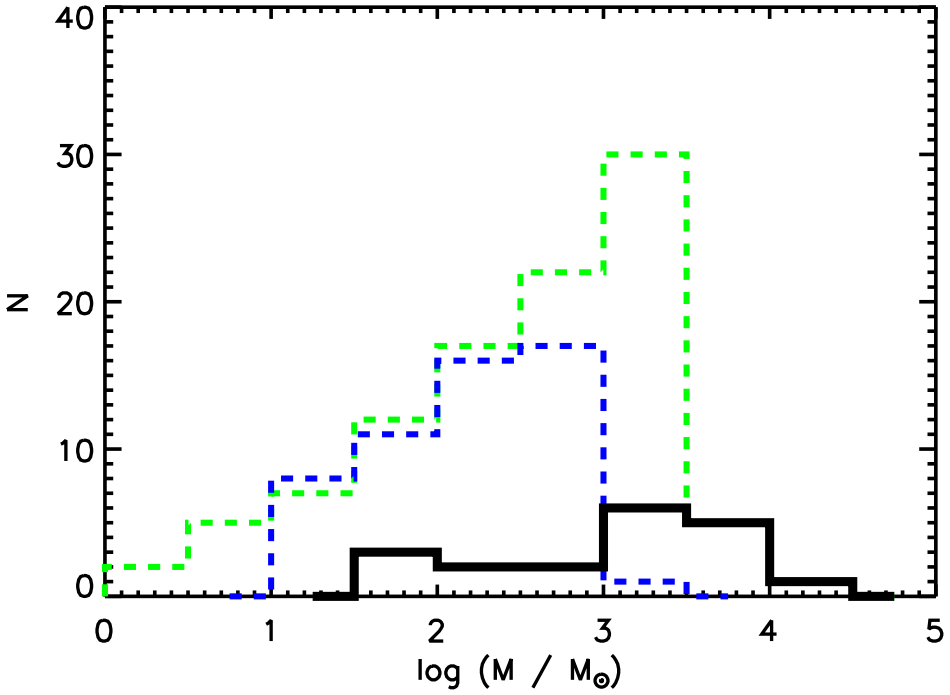

Figure 2.11. IRDC mass histogram - $C^{18}O$. The mass distribution for our sample of IRDCs as derived from $C^{18}O$ data plotted with samples from the literature. The black, solid-line histogram show the mass distribution for our sample of IRDCs. The green dashed histogram shows the distribution of masses of the Williams et al. (2004) cores (derived from 850 μm data) based on the near galactic distances. The blue dashed line represents the masses based on the far galactic distances.

Figures 2.10 and 2.11 show how the masses of our sample compare to the high-mass protostellar objects (HMPOs) presented in Williams et al. (2004), which were determined from submillimeter continuum emission. The masses for the HMPO sample are shown for both their "near" and "far" kinematic distances. Assuming that the sample encompasses objects at both the "near" and "far" kinematic distances, then the derived masses for HMPOs show a comparable range to our sources. One caveat with our comparison to the Williams et al. sample lies in the selection bias of our sample. As we will discuss below, our observations are only sensitive to relatively massive objects when the cores reside at such large distances. Furthermore, the HMPOs in the Williams et al. study also contain protostars which heat the surrounding environment and increase the dust emission. Therefore, in the warmer environments of the Williams et al. survey, lower mass cores would be easier to detect. The mass distributions shown in Figure 2.10 and 2.11 also show good agreement with that found by Shirley et al. (2003), who observed CS emission from a sample of massive star forming regions and found a mean mass of 920 $M_\odot$ with a large dispersion.

Mass Uncertainty

Several assumptions contribute to the uncertainty in the mass calculation, which is dominated by the error in the abundance calculation. We assume a constant temperature of 15 K, and a 5 K change in this value results in a $\sim$20% change in the abundance. The uncertainty in the dust opacity/column density relation contributes another factor of 2. Finally, we assume a constant abundance along the line of sight, which likely contributes an additional factor of 2 – 3 to the mass estimates.

We note that the typical distance to these clouds is $\sim$4 kpc, and with 50″ resolution, we are likely only sensitive to objects of some minimum mass. To examine this limit, we modeled the emission of a cloud assuming a constant density of $10^5 cm^{-3}$, a radius of 0.1pc, an N_2H^+ abundance of 5×10^{-10} using a Monte Carlo radiation transfer model (Ashby et al. 2000). We estimate that our observations are capable of detecting clouds of mass greater than 50-100 $M_\odot$ at a distance of 4 kpc with a 50″ beam.

Assuming that the "near" distance assumption is correct, the uncertainties mentioned above can account for up to a factor of $\sim 4-6$ in mass error, as the 14% error in translating the galactic rotation curve to kinematic distances only introduces a distance error of ∼20%. This accounting suggests that these objects are at least 100 $M_{\odot}$, and likely an order of magnitude more massive. Should the "near" distance assumption be incorrect and the dark clouds lie closer to the "far" kinematic distance, then the distance error dominates the calculation, and these clouds are substantially more massive.

2.3.6 Velocity Dispersion

The width of emission lines in star forming clouds serves as a useful diagnostic in determining the nature of a molecular region. According to Goldsmith (1987), the sites of massive star formation, GMCs, are characterized by large linewidths, while the isolated sites of low-mass star formation, dark clouds, have considerably smaller linewidths. We illustrate this range in Figure 2.12.

Caselli et al. (2002) derived linewidths for N_2H^+ for a sample of low-mass, dense clumps in dark clouds, a site in which we expect to find narrow lines. The average linewidth in the Caselli et al. study was 0.33 km s^{-1} for clumps in which no IRAS source is detected. Current chemical models and observations indicate that NH_3 and N_2H^+ are related because NH_3 likely forms via pathways linked N_2H^+ (Aikawa et al., 2005a). Therefore, we use the Harju et al. (1993) linewidths for NH_3 clumps in Orion and Cepheus, known to be large regions of clustered, high-mass star formation for comparison. In addition, we include a comparison with linewidths of a sample of ammonia cores presented in Molinari et al. (1996), though we only include only the "Low" sources, a sample they argue have less luminous IRAS source, more quiescent envelopes, and, therefore, are younger than their "High" counterparts.

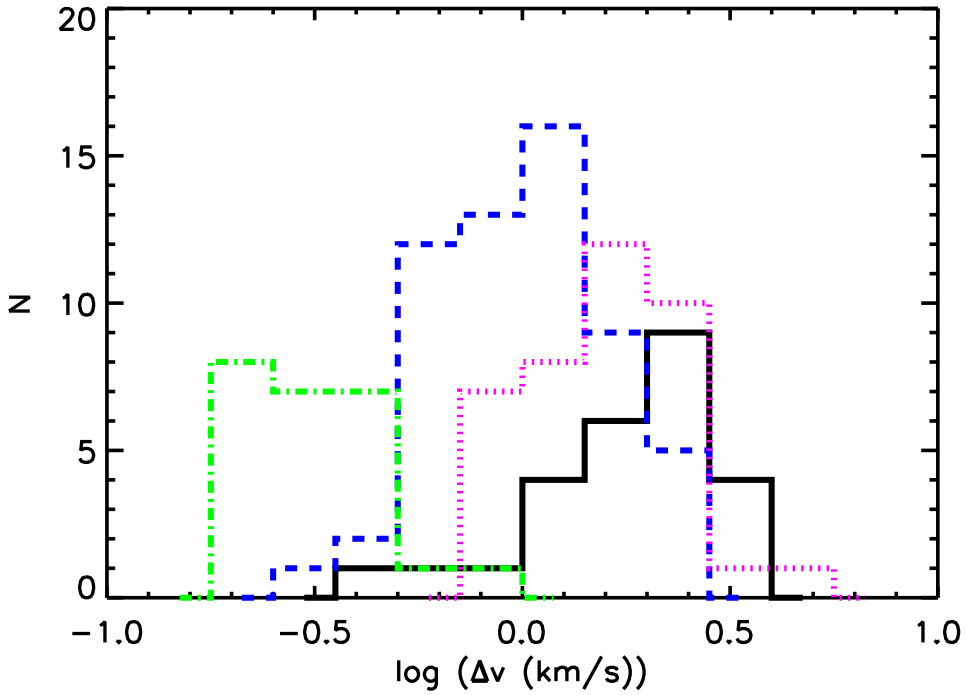

Figure 2.12. Linewidth Histogram. N_2H^+ linewidth of our sample (black, solid line) compared with N_2H^+ linewidth in Caselli et al. (2002) (green, dash-dotted histogram) and NH_3 linewidths from Harju et al. (1993) (blue, dashed histogram) and Molinari et al. (1996) (magenta, dotted histogram) studies.

We find average linewidths of 2.0 km s^{-1} for N_2H^+, 2.1 km s^{-1} for $C^{18}O$, and 2.9 km s^{-1} for CS. Though we see a broad range of line widths in the N_2H^+ observations of the dark clouds, the characteristic line widths presented here are generally higher than those of the Harju et al. study and, to a greater extent, the Caselli et al. study, which implies that the objects in this sample are likely not associated with low-mass star formation. However, we find good agreement with the Molinari et al. sample.

For the CS $J = 2 \rightarrow 1$ transition, the linewidths in the dark cloud sample are narrower than those observed by Plume et al. (1997) in survey of massive star forming regions, which averaged 4.2 km s^{-1} in this line. However, since Plume et al. surveyed regions known to have undergone massive star formation, it is possible that the current generation of massive stars are injecting additional turbulence into the surrounding environment. Similarly, the Shirley et al. (2003) study observed the CS $J = 5 \rightarrow 4$ transition in star-forming cores and found linewidths averaging 5.6 km s^{-1}. The narrower lines in the IRDCs indicates that they are still relatively quiescent and suggest that may, indeed, be pre-cursor sites of intermediate or massive star formation. As Gibson et al. (2009) show, the linewidths and sizes of IRDCs yield virial masses around $10^3 M_\odot$, which when compared with the mass derived from molecular emission, indicates that IRDCs are roughly in virial equilibrium and not transient objects.

2.4 Summary

We have identified 41 infrared-dark (at 8.8 μm) clouds that are opaque, compact, and associated with UC HII regions using MSX survey data. In order to determine some basic characteristics of these dark clouds, we have mapped emission from N_2H^+ $1 \rightarrow 0$, CS $2 \rightarrow 1$ and $C^{18}O$ $1 \rightarrow 0$ using the FCRAO and detect molecular emission in 34 of them. The morphology and relative strengths of these molecular lines varies dramatically, possibly indicating evolutionary differences and/or the presence of (an) undetected embedded protostar(s). Based on the derived kinematic distances and the simplifying assumption that the cores are optically thin, we have determined average properties: diameter $< D > \approx 0.9$ pc, density $< n > \approx 5000$ cm^{-3}, and mass

$< M > \approx 2500$ $M_\odot$. The low density estimate likely indicates that the dark clouds are clumpy rather than homogeneous. The derived masses, however, are comparable to those derived for a sample of HMPOs. The linewidths are larger than those seen in low-mass star forming cores and larger than in high-mass star forming cores in Orion and Cepheus. However, they are narrower than the CS linewidths seen in regions that are actively forming massive stars . These observations, taken together, suggest that the infrared-dark clouds may be the relatively quiescent pre-cursors to intermediate or massive star formation, the so-called "pre-protostellar cores." These data alone are not sufficient to determine the starlessness of the IRDCs, but deeper observations (see Chapter 3 & 4), and an examination of the clouds kinematics (see Chapter 5) go much further in understanding the true nature of these IRDCs.

CHAPTER 3

THE YOUNG STELLAR POPULATION AND ENVIRONMENT OF IRDCs

3.1 Star Formation in IRDCs

Viewed in the infrared, IRDCs appear to be "dark," quiescent clumps devoid of star formation activity, and initial follow-up observation in the sub-millimeter confirmed the low temperature, high density, "dark" nature of these objects (Egan et al., 1998). The presence of heating sources such as young stars would heat the gas and thus disrupt the cold condensation. However, more recent and detailed studies, such as Rathborne et al. (2005), Beuther & Steinacker (2007), and others have targeted IRDCs with very sensitive observations in an effort to detect deeply embedded protostars, else verify their starlessness. These studies have uncovered evidence of massive protstars obscured in early infrared observations, and models project them to be several hundreds of solar masses. This confirms the belief that IRDCs are the precursors to massive star clusters. To date, no IRDC has been unambiguously shown to be truly "dark," and the search for massive starless cores continues.

In hopes of finding good candidate massive starless cores, Chambers et al. (2009) has probed the IRDCs cataloged by Simon et al. (2006a) and identified IRDCs with and without an excess in the 4.5 μm band of IRAC aboard the *Spitzer Space Telescope*. Objects showing excess at 4.5 μm, known as Extended Green Objects (EGOs) or "green fuzzies," are believed to be sites of outflows which excite surrounding molecular gas (Neufeld & Yuan, 2008). The outflows are indirect signposts for star formation activity embedded within the dense gas. IRDC cores lacking the excess would then be good candidates for follow-up studies searching for "dark" cores. Cyganowski et al.

(2008) and Cyganowski et al. (2009) have also investigated EGOs and correlated them with CH_3OH masers in an effort to understand the evolution and outflow activity of massive young stellar objects. These studies are crucial in understanding to what infrared-dark clouds cores are precursors. However, studies of distributed young stellar population of IRDCs have been quite limited. van der Wiel & Shipman (2008) characterized young stars in IRDC G48.65 with *Spitzer*, finding 13 young stars ranging in mass from 0.1 to 8 $M_{\odot}$, though uncertainties are large because of the lack of constraining measurements at longer wavelengths. It is important to further the study the young stars in numerous IRDCs if we are to understand the clusters that IRDCs will ultimately form in addition to their most massive member.

IRDCs are known to have thousands of solar masses of material that will almost certainly become massive clusters (e.g. Rathborne et al., 2006; Butler & Tan, 2009; Ragan et al., 2009). We now see several examples of ongoing star formation taking place within IRDCs, but van der Wiel & Shipman (2008) and Ragan et al. (2009) were the first to characterize the young star population surrounding and on the surface of IRDCs. Here I present the first large scale survey of young stellar objects (YSOs) in IRDCs. I describe our deep, highly sensitive observations, the identification of candidate young stellar objects with them, and their association with the dense absorbing structure. I use complementary molecular data to examine the environment of IRDCs, including possible embedded young clusters of stars and the extent of the envelope gas. These observations give us additional clues to the evolutionary state of IRDCs and point to what will become of them as they evolve.

3.2 *Spitzer* Observations & Data Reduction

3.2.1 Targets

Searching in the vicinity of ultra-compact HII (UCHII) regions (Wood & Churchwell, 1989) for infrared-dark cloud candidates, Ragan et al. (2006) performed a survey of 114 candidates in N_2H^+(1-0), CS(2-1), and $C^{18}O$(1-0) with the FCRAO. In order to study substructure with *Spitzer*, we have selected a sample of targets from the Ragan

et al. (2006) sample which are compact, typically $2' \times 2'$ (or 2×2 pc at 4 kpc), and opaque, providing the starkest contrast at 8 μm (MSX Band A) with which to examine the absorbing structure. The selected objects also exhibit significant emission in transitions of CS and N_2H^+ that are known to trace high-density gas, based on their high critical densities. By selecting objects with strong emission in these lines, we ensure that their densities are $>10^4$ cm^{-3} and their temperatures are less than 20 K. Under these conditions in local clouds, N_2H^+ is strongest when CO is depleted in the pre-stellar phase (Bergin & Langer, 1997), hence a high N_2H^+/CO ratio guided our attempt to select the truly "starless" dark clouds in the IRDC sample. Our selection criteria are aimed to isolate earliest stages of star formation in local clouds and give us the best hope of detecting massive starless objects. The eleven IRDCs observed are listed in Table 3.1 with the distances derived in Ragan et al. (2006) using a Milky Way rotation curve model (Fich et al., 1989) assuming the "near" kinematic distance. The listed uncertainties in Table 3.1 arise from the $\pm$14% maximal deviation inherent in the rotation curve model.

Table 3.1. Spitzer target table.

IRDC	α (J2000)	δ (J2000)	distance (kpc)
G005.85−0.23	17:59:53	−24:00:10	$3.14^{+0.66}_{-0.76}$
G006.26−0.51	18:01:50	−23:47:11	$3.78^{+0.59}_{-0.67}$
G009.16+0.06	18:05:50	−20:59:12	$3.80^{+0.61}_{-0.69}$
G009.28−0.15	18:06:54	−20:58:51	$4.48^{+0.54}_{-0.61}$
G009.86−0.04	18:07:40	−20:25:25	$2.36^{+0.78}_{-0.88}$
G012.50−0.22	18:13:45	−18:11:53	$3.55^{+0.67}_{-0.75}$
G023.37−0.29	18:34:51	−08:38:58	$4.70^{+0.90}_{-0.88}$
G023.48−0.53	18:35:57	−08:39:46	$4.10^{+0.88}_{-0.90}$
G024.05−0.22	18:35:52	−08:00:38	$4.82^{+0.96}_{-0.90}$
G034.74−0.12	18:55:14	+01:33:42	$4.86_{-1.45}$
G037.44+0.14	18:59:08	+04:03:31	$2.59^{+1.47}_{-1.34}$

3.2.2 Data Processing

Observations of this sample of objects were made on 2005 May 7 – 9 and September 15 – 18 with IRAC centered on the coordinates listed in Table 3.1. Each region was observed 10 times with slightly offset single points in the 12s high dynamic range (HDR) mode. In addition, 0.4s images were obtained so that photometry could be done on bright sources. All four IRAC bands were observed over $7' \times 7'$ common field-of-view. MIPS observations were obtained on 2005 April 7 – 10 of the objects in this sample. Using the "large" field size, each region was observed in 3 cycles for 3s at 24 μm. MIPS observations cover smaller $5.5' \times 5.5'$ fields-of-view but big enough to contain the entire IRDC. Figures 3.1−3.11 show each IRDC field in all observed wavebands. The absorbing structures of the IRDCs are most prominent at 8 μm and 24 μm.

We used IRAC images processed by the Spitzer Science Center (SSC) using pipeline version S14.0.0 to create basic calibrated data (BCD) images. These calibrated data were corrected for bright source artifacts ("banding", "pulldown", and "muxbleed") and cleaned of cosmic ray hits using customized versions of the IRAC team pipeline scripts (Pipher et al., 2004; Hora et al., 2004). The images were made into mosaics using Gutermuth's WCS-based IRAC post-processing and mosaicking package which includes a frame-by-frame distortion correction, derotation, sub-pixel offsetting in a single transformation, and on-the-fly background matching (Gutermuth et al., 2008), all utilizing FITS images manipulated with Interactive Data Language (IDL) scripts from the Astronomy Users Library (Landsman, 1993).

Source finding and aperture photometry were performed using Gutermuth's PhotVis version 1.10 (Gutermuth et al., 2004). We used a $2.4''$ aperture radius and a sky annulus from $2.4''$ to $6''$ for the IRAC photometry. The photometric zero points for the [3.6], [4.5], [5.8], and [8.0] bands were 22.750, 21.995, 19.793, and 20.187 magnitudes, respectively. For the MIPS 24 μm photometry, we use a $7.6''$ aperture with $7.6''$ to $17.8''$ sky annuli radii and a photometric zero point of 15.646 magnitude. All photometric zero points are calibrated for image units of DN and are corrected for the adopted apertures.

To supplement the *Spitzer* photometry, we incorporate the source photometry from the Two-Micron All Sky Survey (2MASS) Point Source Catalog (PSC). Source lists are matched for a final catalog by first matching the four IRAC band catalogs using Gutermuth's WCSphotmatch utility, enforcing a $1''$ maximal tolerance for positive matches. Then, the 2MASS sources are matched with tolerance $1''$ to the mean positions from the first catalog using the same WCS-based utility. Finally, the MIPS 24 μm catalog is integrated with matching tolerance $1.5''$.

3.3 Stellar Content

Young stars are known to exhibit excess emission in the min-infrared spectral energy distributions (SEDs) (Allen et al., 2004) which originates mainly from their dusty circumstellar material. The tremendous sensitivity of *Spitzer* provides the best tool to date to characterize young stellar populations in detail. Before the *Spitzer* era, IRAS led the effort in identifying the brightest infrared point sources in the Galaxy. Only one object in this sample, G034.74−0.12 (Figure 3.10) has an IRAS point source (18526+0130) in the vicinity, thus, by previous standards, these objects would be considered starless. Here, with *Spitzer*, we have identified tens of young stellar objects (YSOs) in the field of each IRDC in the sample.

3.3.1 Young Stellar Object Identification & Classification

With this broad spectral coverage from 2MASS to IRAC to MIPS, we apply the robust critieria described in Gutermuth et al. (2008) to identify young stellar objects (YSOs) and classify them. This is a three phase approach that accounts for the conditions typical of star forming regions, using the most up-to-date extinction law information (see Indebetouw et al., 2005; Flaherty et al., 2007) and – at each stage – takes independent measures to eliminate extragalactic contaminants.

External galaxies and weak-line active galactic nuclei (AGN) have photometric properties that resemble that of YSOs. Using the prominent polycyclic aeromatic hydrocarbon (PAH) feature near 8 μm, which is dominant in galaxies and AGN, sources showing large excesses at in IRAC band 4 are filtered out. In addition,

background galaxies and AGN, as we would see them through the extincting molecular cloud dust, appear particularly dim as a result. Therefore, using the extinction at K band (A_K), the photometry is dereddened and color criteria applied. Finally, sources showing an excess at 4.5 μm, which likely arises from shocked H_2 line emission (Neufeld & Yuan, 2008), are removed. [1] In each case described here, the imperfect criteria will select both contaminants and true YSOs. To mitigate this over-filtering, these objects are checked for MIPS 24 μm emission.

Asymptotic giant branch (AGB) stars are another common contaminant in YSO studies (Robitaille et al., 2008), appearing here as very red (high A_K) sources. Extinction in the K-band, however, is not a good selector of AGB stars, as there is a degeneracy with the true, very deeply embedded young stars, as we show in Figure 3.12. To improve our source discrimination, we use the colors and magnitudes of AGB stars from a study of the stellar population in the Large Magellanic Clouds (LMC) (Meixner et al., 2006), we apply additional color criteria to select dusty, evolved AGB stars ([3.6] - [8.0] < -1.525([8.0] - [24]) + 7.025). Approximately 17% of the YSOs could also qualify as AGB stars under this criteria, although the criteria derived from LMC studies may not be strictly correct for the IRDCs, which lie in a very different environment and at a different vantage point than observed here. Further study of the stellar population's association with the IRDCs is needed to set firm limits on the level of AGB contamination.

Spitzer studies have shown that the extinction law flattens through 4.5 to 8.0 μm and rises in the 3.6 μm band (Indebetouw et al., 2005; Flaherty et al., 2007). So to not confuse differential extinction with intrinsic YSO differences, the first stage of the classification scheme relies on the [4.5] - [8.0] color to distinguish between Class I and Class II YSOs. Appendix C lists the J, H, K_s, 3.6, 4.5, 5.8, 8.0 and 24 μm photometry for all stars that met the YSO criteria, and we note the extinction at K and the classification as Class I Protostars (CI), Class II Pre-Main Sequence (PMS) stars (CII), embedded protostars (EP), or transition disk objects (TD). We

[1] While the shocked H_2 may indicate an outflow from a young star, the photometric colors do not reflect the true classification of the object, and therefore their inclusion would skew the populations.

note which objects have colors consistent with AGB colors. A color-color diagram displaying these various classes of YSOs in the entire sample (and excluding identified contaminants) is shown in Figure 3.24[2]. The extinction laws from both Flaherty et al. (2007) and Indebetouw et al. (2005) are plotted to show the effect of five magnitudes of visual extinction.

The objects associated with these IRDCs are a great distance from us and in the plane of the Galaxy, so they naturally suffer from a great deal of extinction, reddening, and foreground contamination. Furthermore, the reddening law used in this classification scheme and the measures taken to extricate extragalactic contaminants may be inaccurate due to the great distance to IRDCs, as the criteria were originally designed to suit local regions. This may result in misclassification of sources. For example, a highly reddened Class II object might appear as an embedded protostar. Nonetheless, if these objects are indeed protostars, it is likely that they are associated with the IRDC.

In Table 3.2, we summarize the number of each class of YSO in each IRDC field, and Figures 3.13-3.23 show the spatial distribution of the YSOs superposed on the 8 and 24 μm *Spitzer* images. In all, there are 308 YSOs under the Gutermuth et al. (2008) criteria. We note the number of these YSOs that are spatially coincident with the absorbing IRDC clumps (see §4.2.2). Only ∼13% of the YSOs are within or border the very dense gas considered a "clump" (see Chapter 4). The rest of the YSOs appear to be a distributed population of stars surrounding the IRDC. This may be because any star directly associated with the IRDC is too heavily obscured to be detected even with the deep Spitzer observations we undertook, or the presence of a hot young star may have disrupted the (formerly) infrared-dark clump and we see the star unassociated with absorption. Our observations are sensitive to 1-3 $M_{\odot}$, 1Myr-old pre-main sequence stars (Baraffe et al., 1998), or 1 $L_{\odot}$ Class 0 protostar at 4 kpc with no extinction (Whitney et al., 2003). With extinction, which can reach 1-2 magnitudes in the *Spitzer* bands, embedded YSOs up to 3-4 $M_{\odot}$ might be present, but hidden from our view.

[2]No embedded protostar was detected in all four IRAC bands, so none are plotted in Figure 3.24.

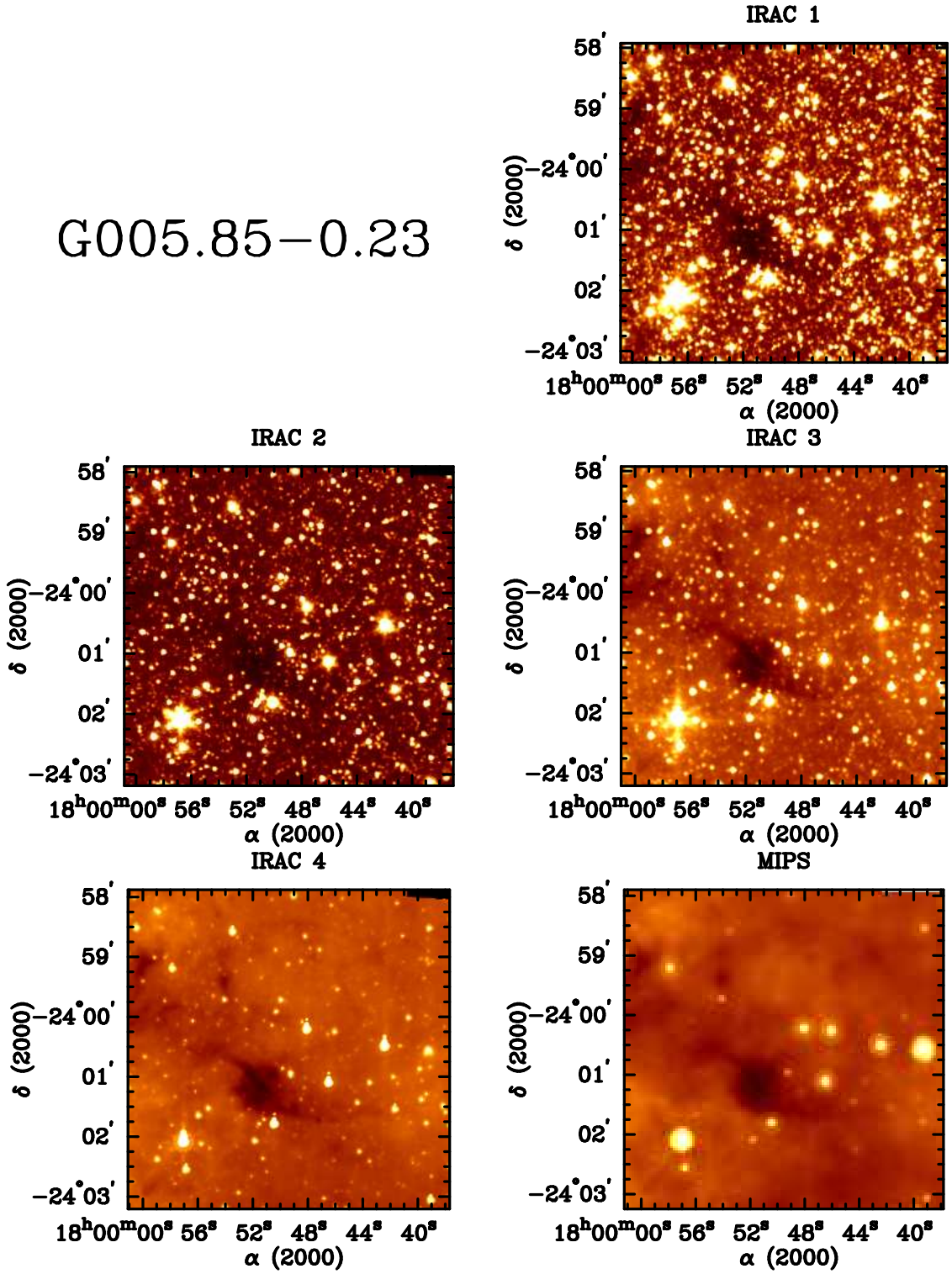

Figure 3.1. *Spitzer* images of IRDC G005.85−0.23: Top Row Right: 3.6μm. Middle Row Left: 4.5μm. Middle Row Right: 5.8μm. Bottom Row Left: 8μm. Bottom Row Right: 24μm.

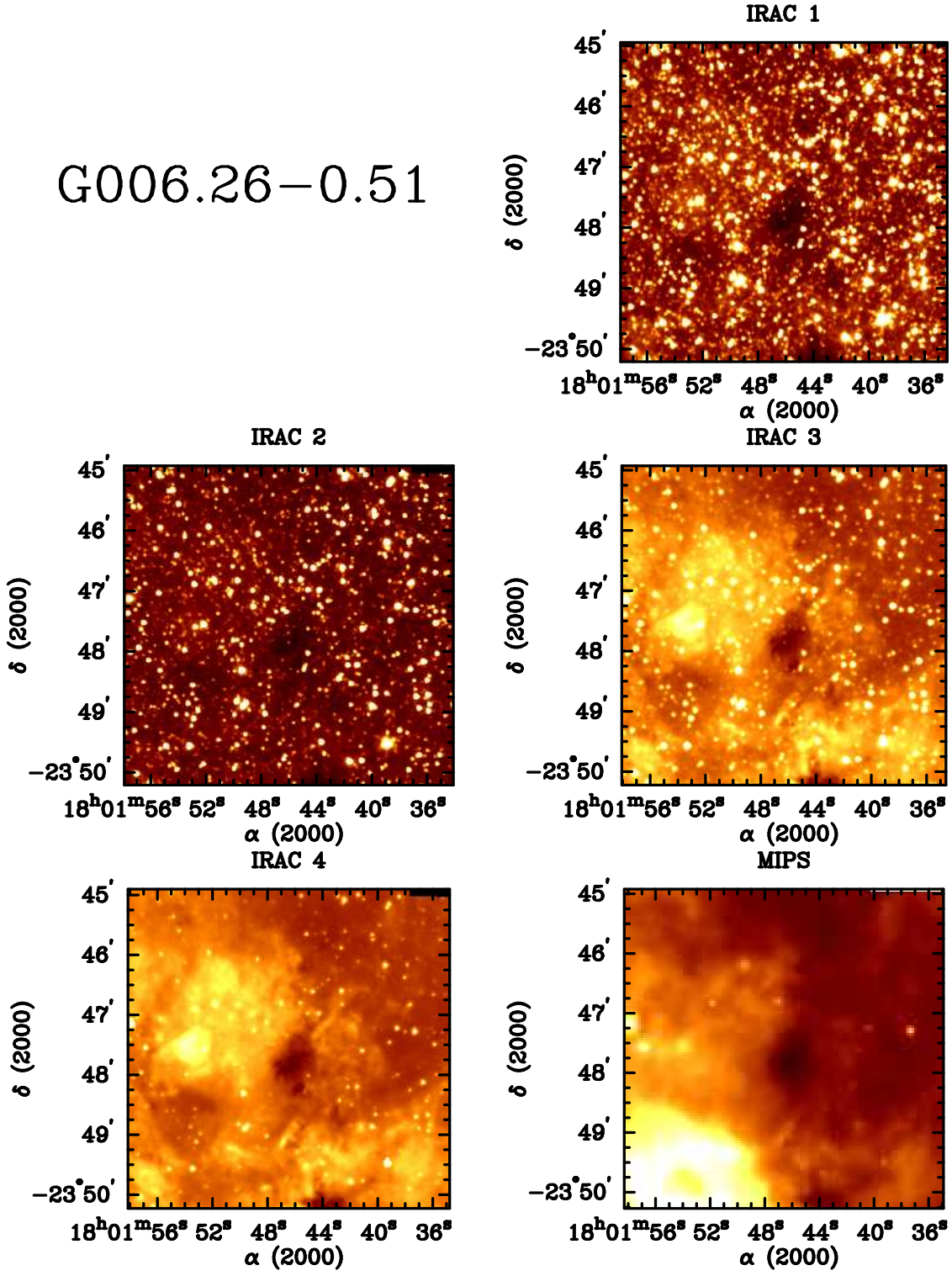

Figure 3.2. *Spitzer* images of IRDC G006.26−0.51: Wavelengths as noted in Figure 3.1.

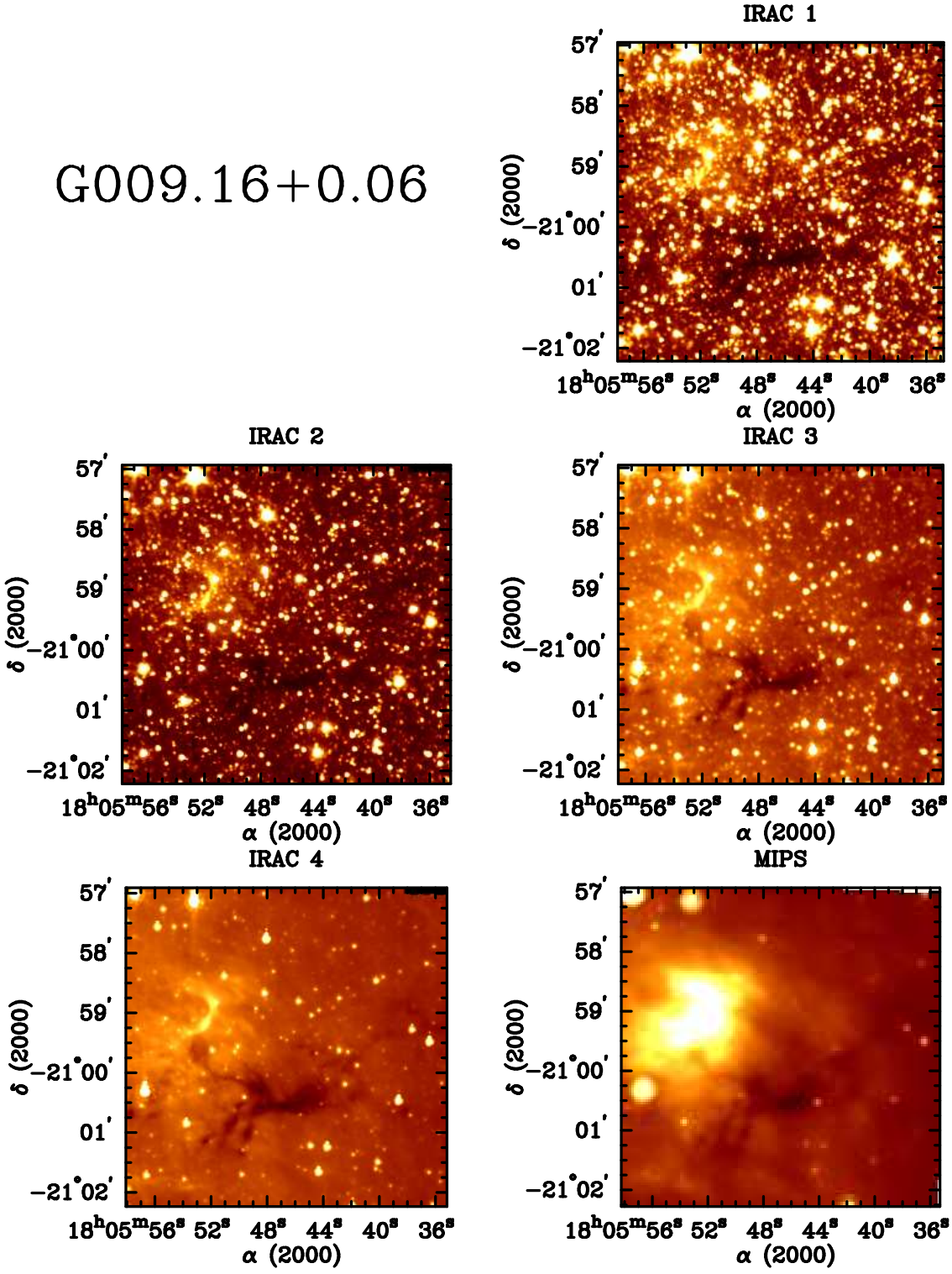

Figure 3.3. *Spitzer* images of IRDC G009.16+0.06: Wavelengths as noted in Figure 3.1.

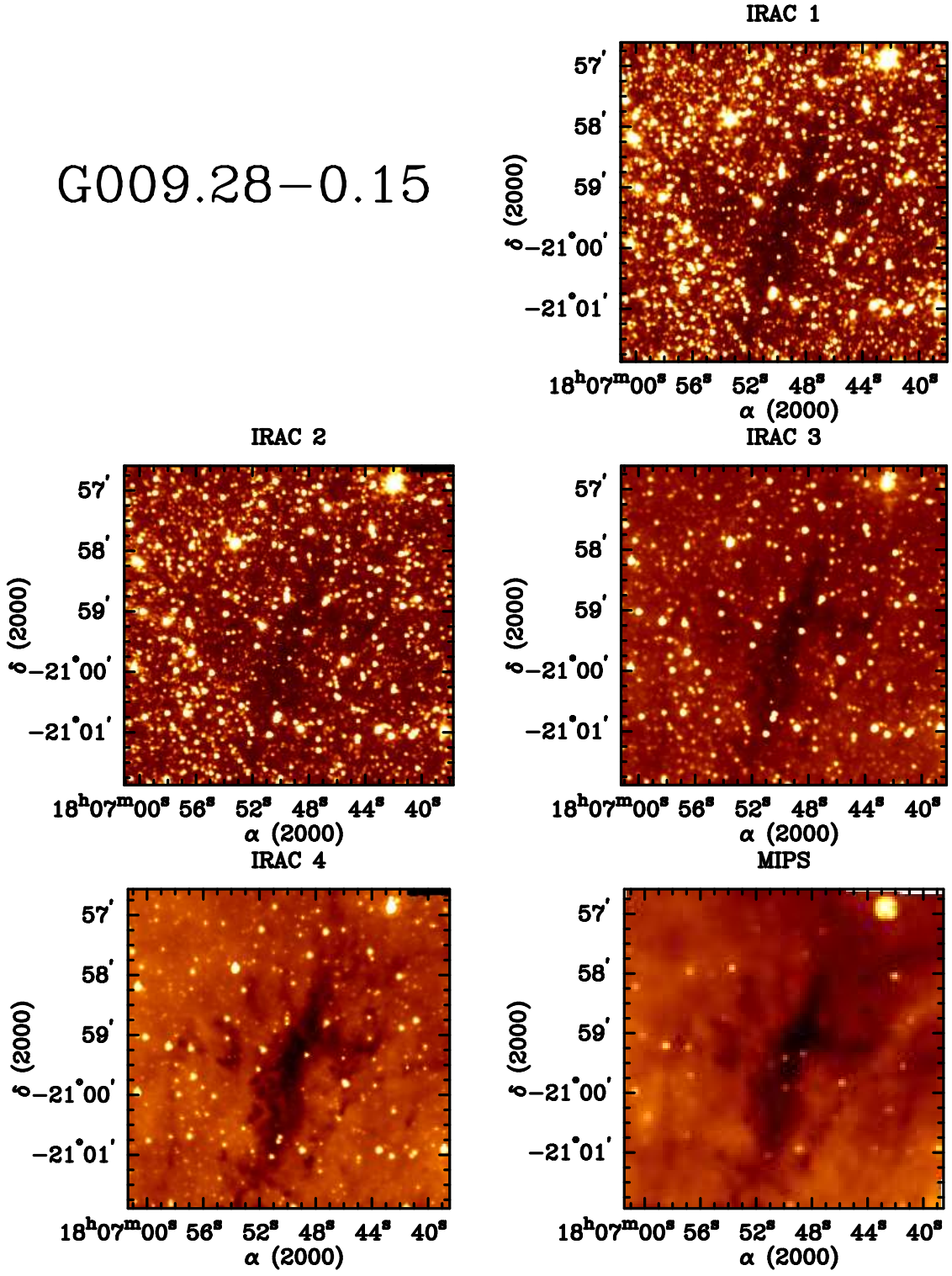

Figure 3.4. *Spitzer* images of IRDC G009.28−0.15: Wavelengths as noted in Figure 3.1.

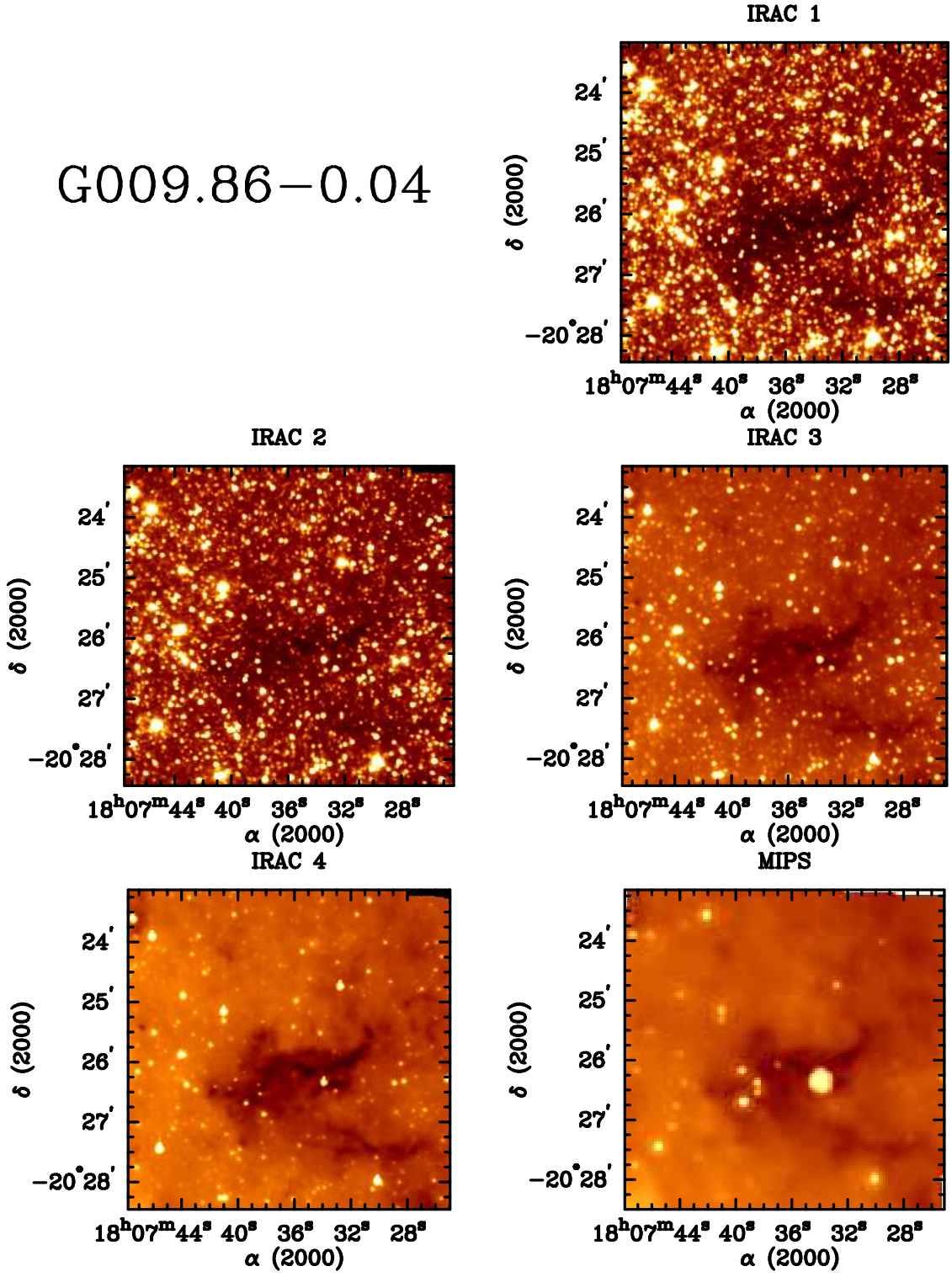

Figure 3.5. *Spitzer* images of IRDC G009.86−0.04: Wavelengths as noted in Figure 3.1.

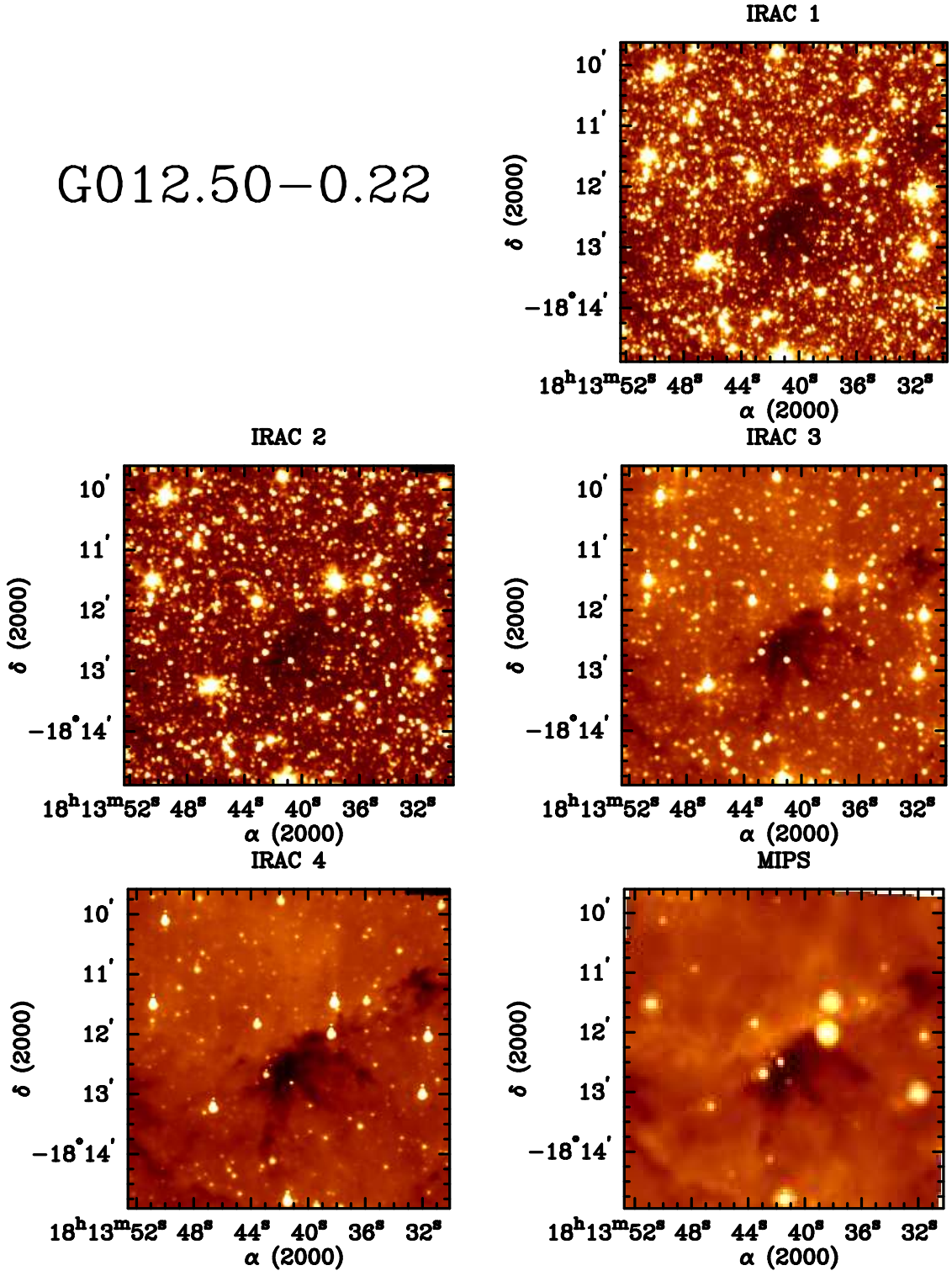

Figure 3.6. *Spitzer* images of IRDC G012.50−0.22: Wavelengths as noted in Figure 3.1.

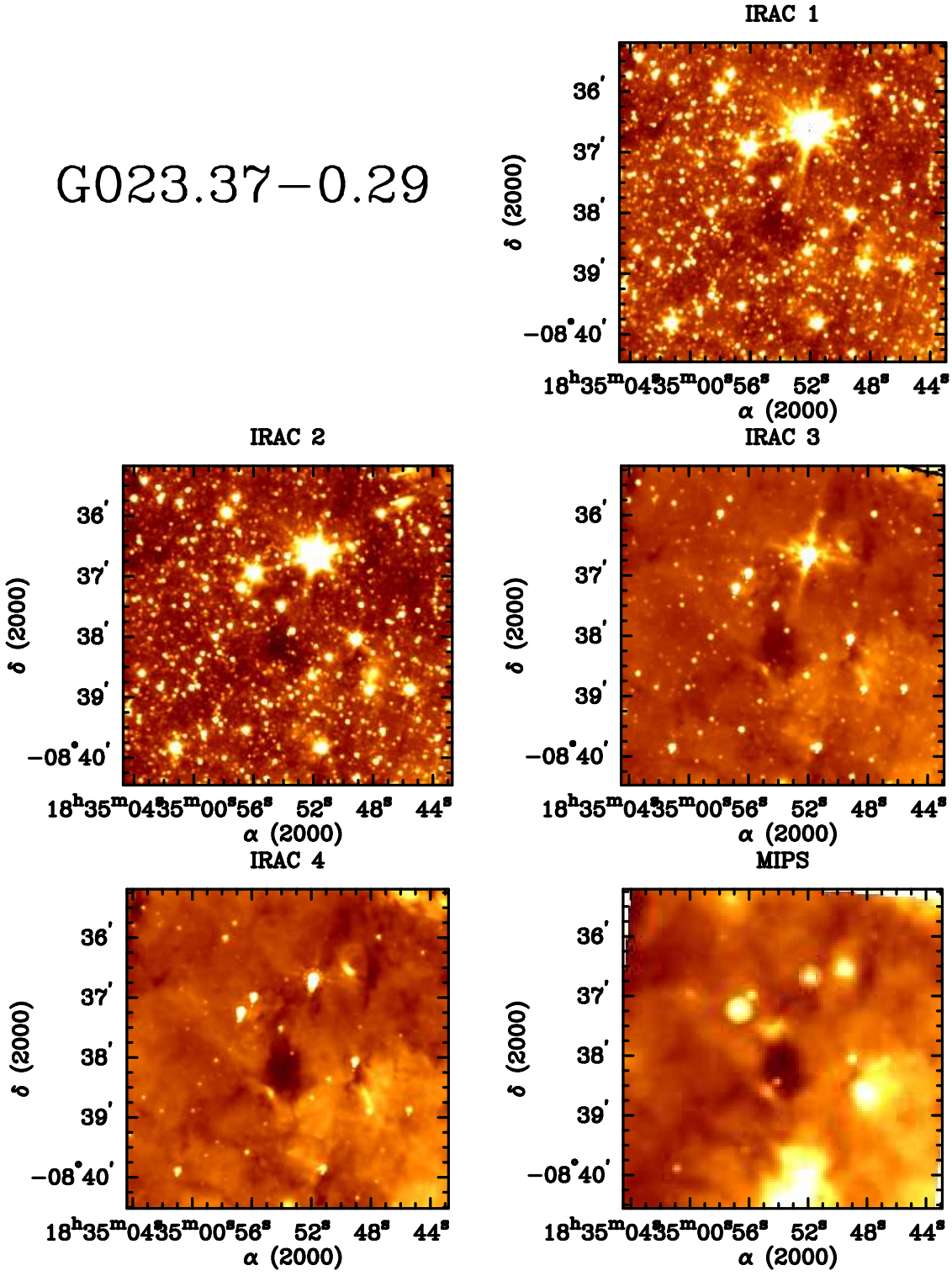

Figure 3.7. *Spitzer* images of IRDC G023.37−0.29: Wavelengths as noted in Figure 3.1.

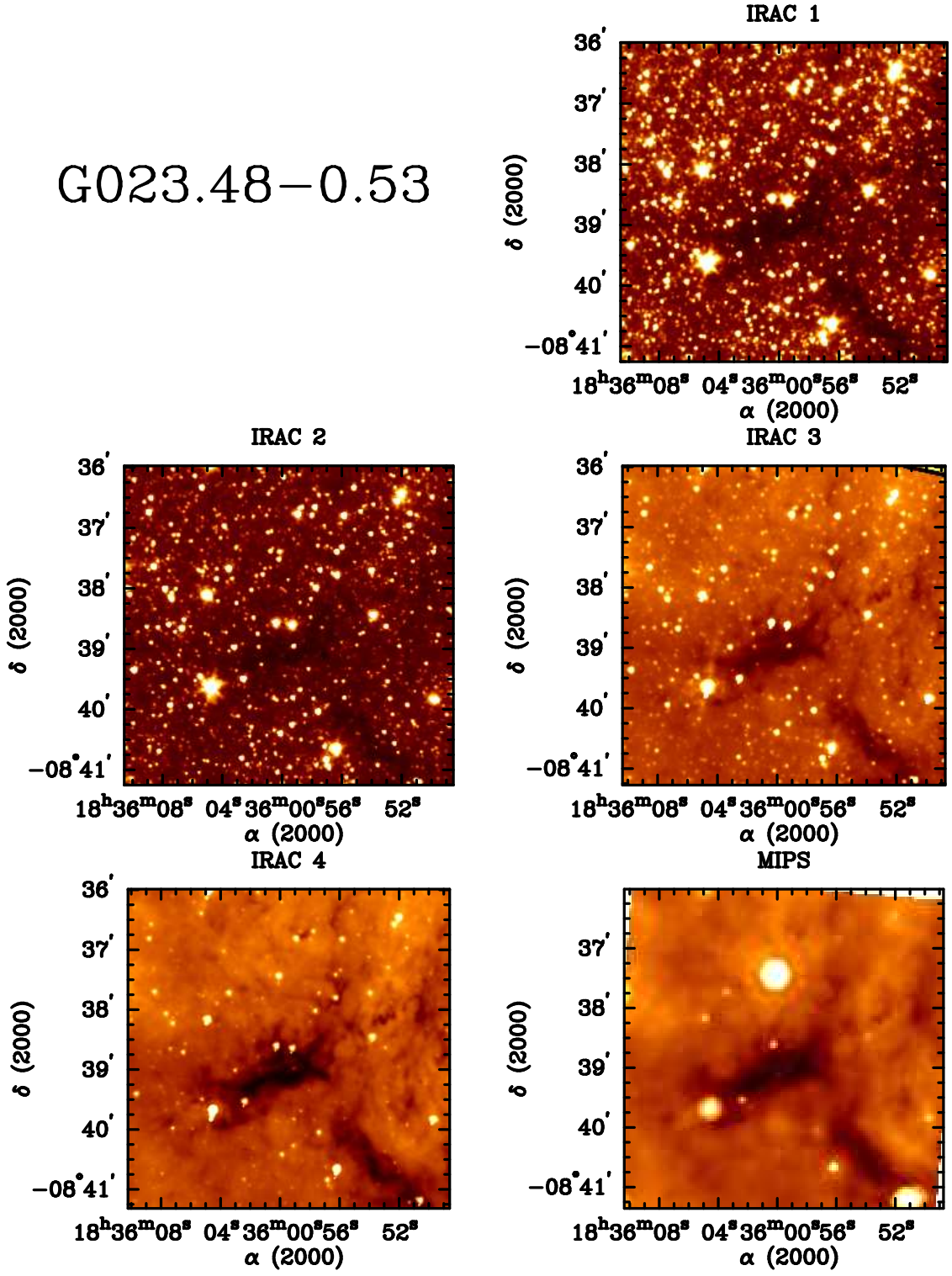

Figure 3.8. *Spitzer* images of IRDC G023.48−0.53: Wavelengths as noted in Figure 3.1.

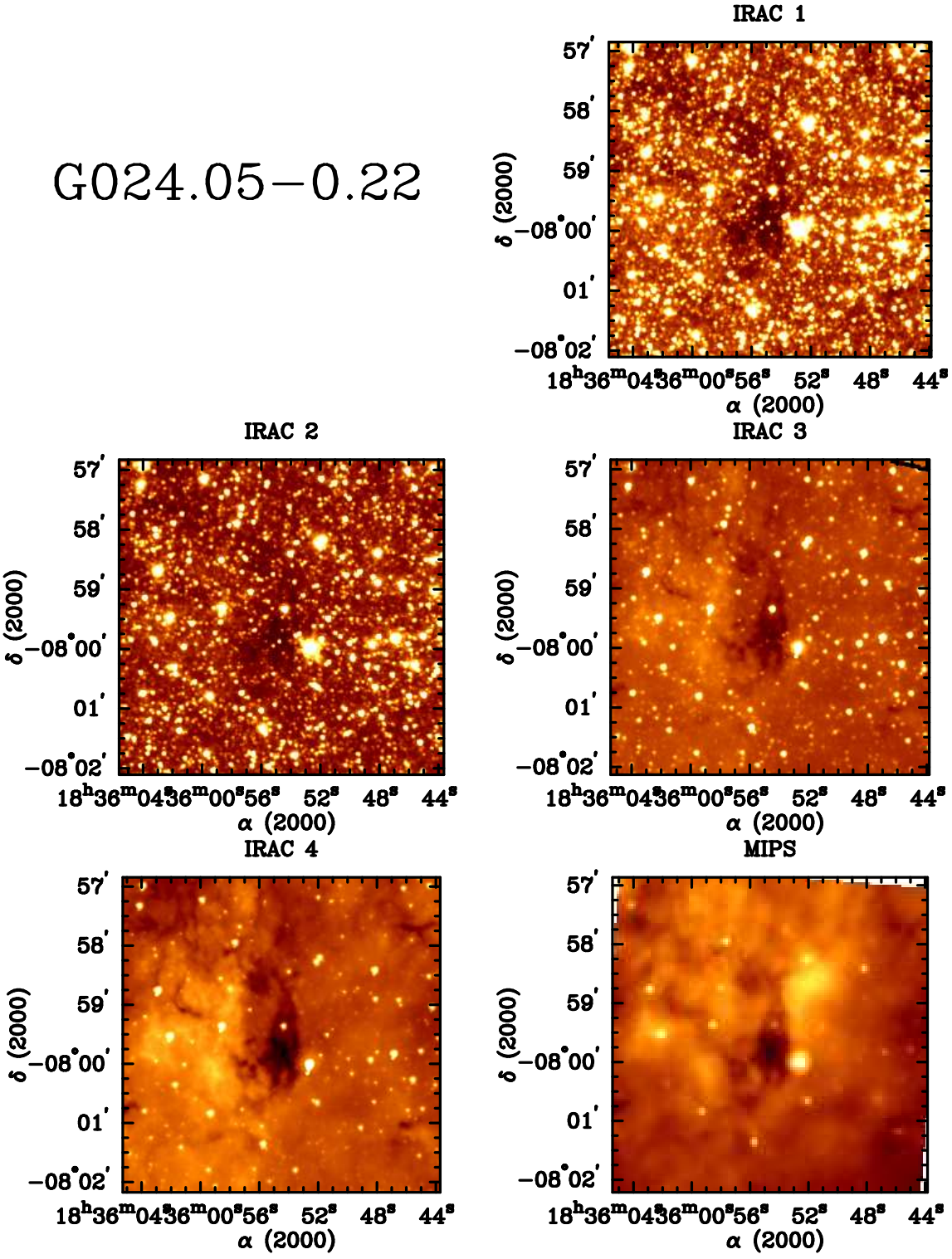

Figure 3.9. *Spitzer* images of IRDC G024.05−0.22: Wavelengths as noted in Figure 3.1.

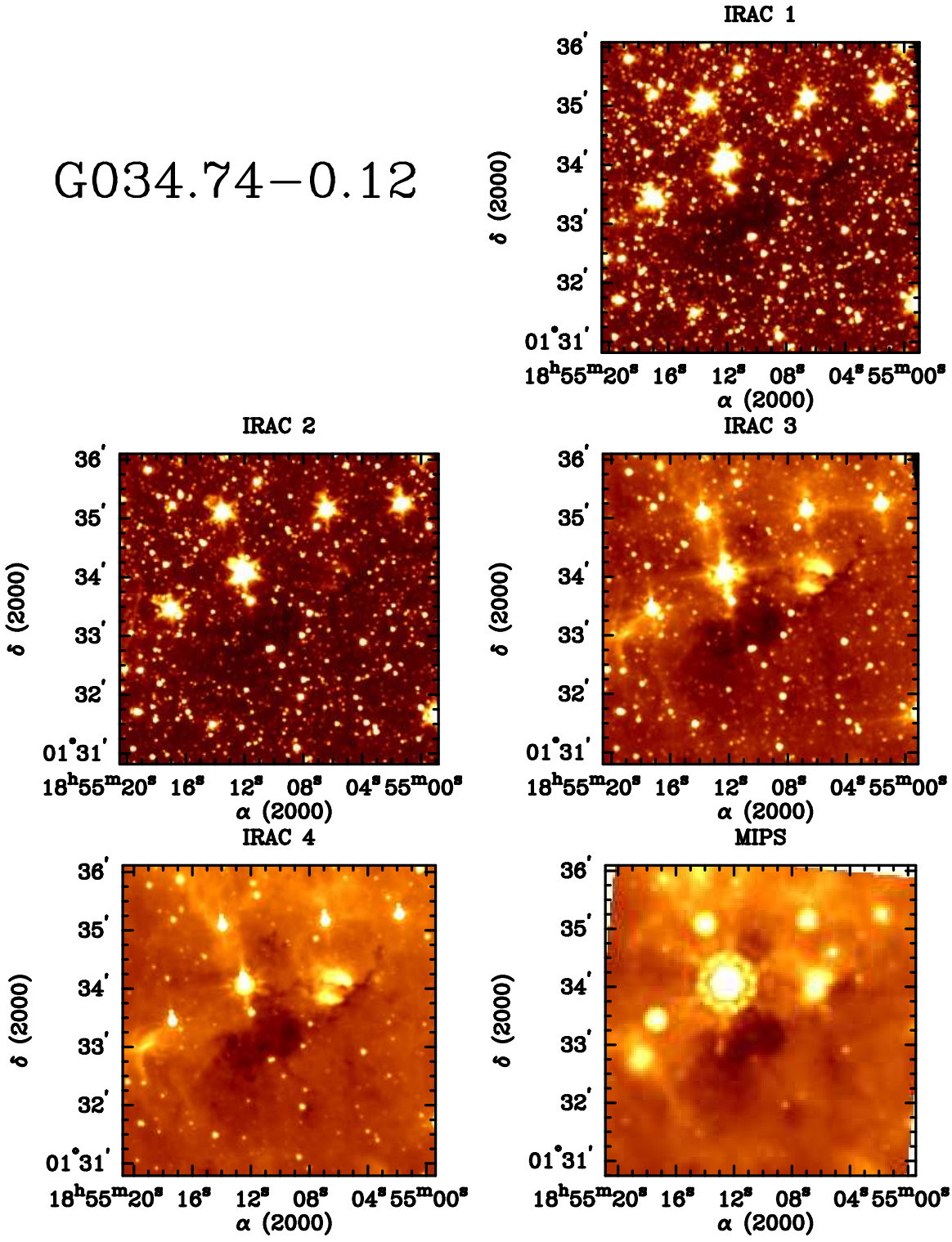

Figure 3.10. *Spitzer* images of IRDC G034.74−0.12: Wavelengths as noted in Figure 3.1.

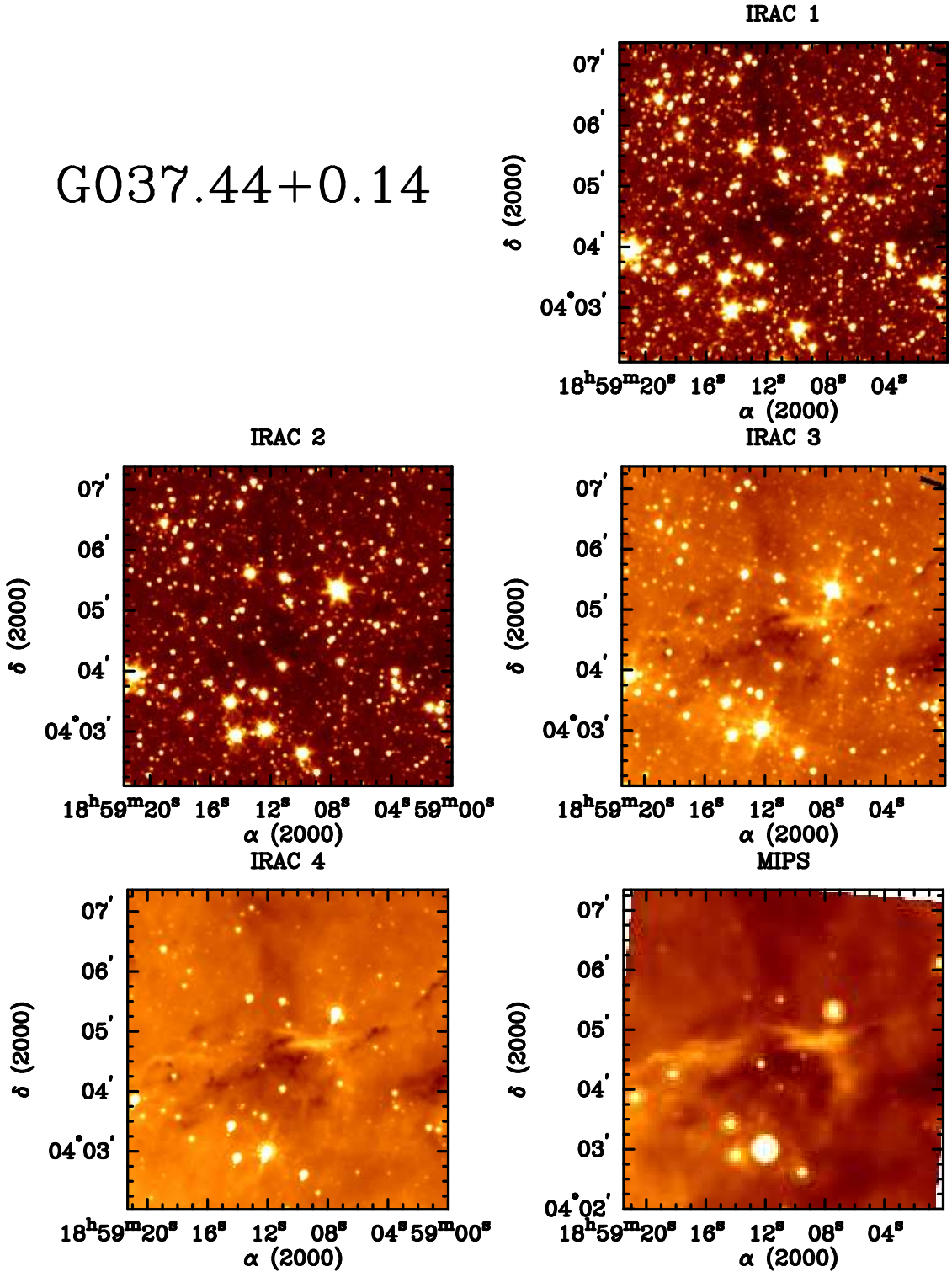

Figure 3.11. *Spitzer* images of IRDC G037.44+0.14: Wavelengths as noted in Figure 3.1.

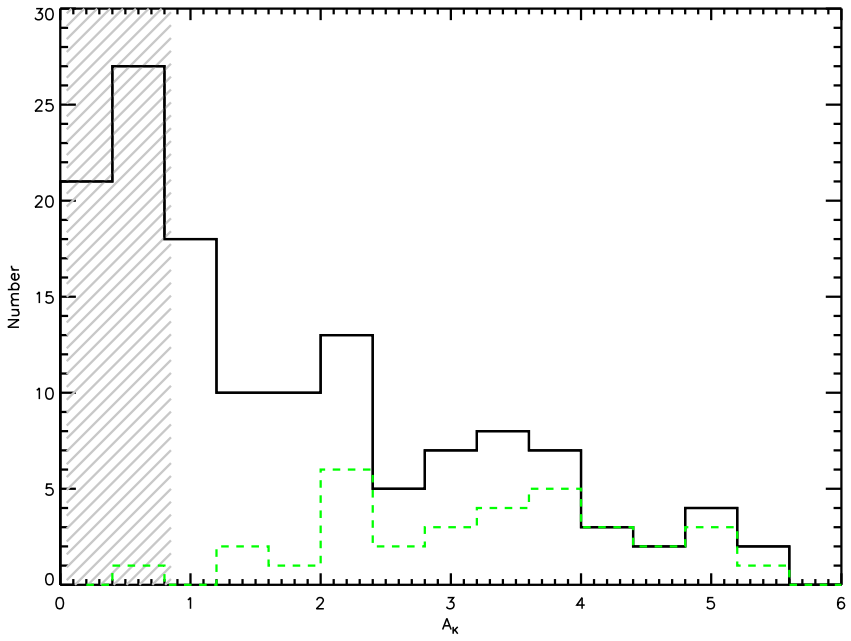

Figure 3.12. A_K histogram of candidate YSOs. The shaded region shows the range of extinction values typical of field stars up to the distance to IRDCs. Black histogram shows all 138 YSOs with a measurement of A_K (see Appendix C), 97 (71%) of which exhibit extinction greater than that typical of a field star at the distance of the IRDCs. Green dashed histogram shows possible AGB stars (Meixner et al., 2006).

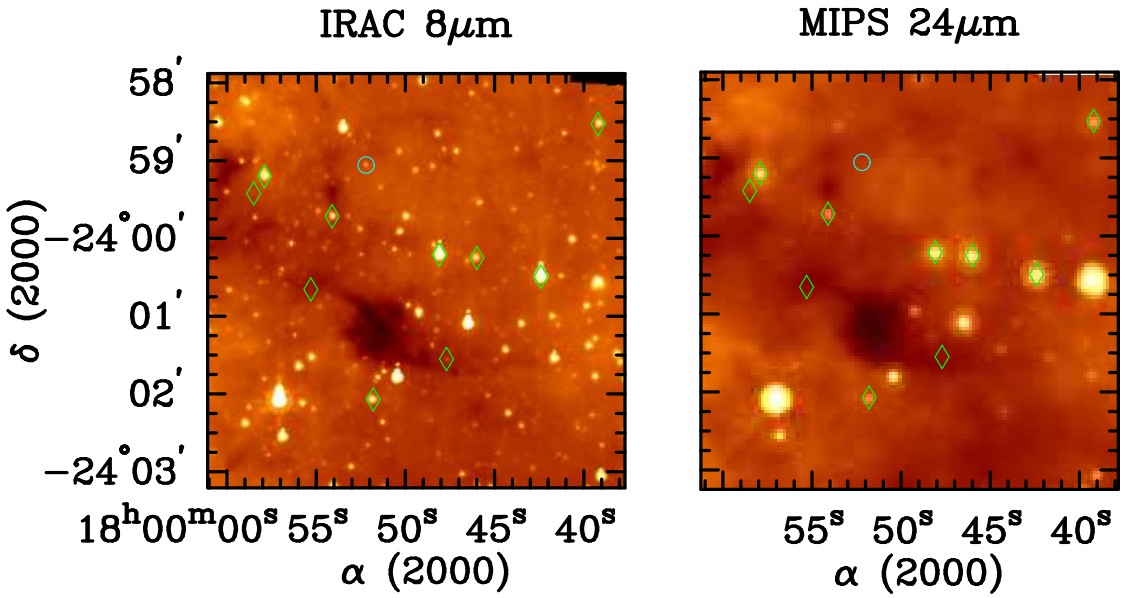

Figure 3.13. YSOs in IRDC G005.85−0.23: The 8μm (left) and 24μm (right) images of the IRDC fields, with the identified young stellar objects labeled to show association with the IRDC absorption. YSOs are indicated as follows: Class I protostars (blue diamonds), Class II pre-main sequence stars with disks (green diamonds), deeply embedded sources (red diamonds), and transition disk objects (cyan circles).

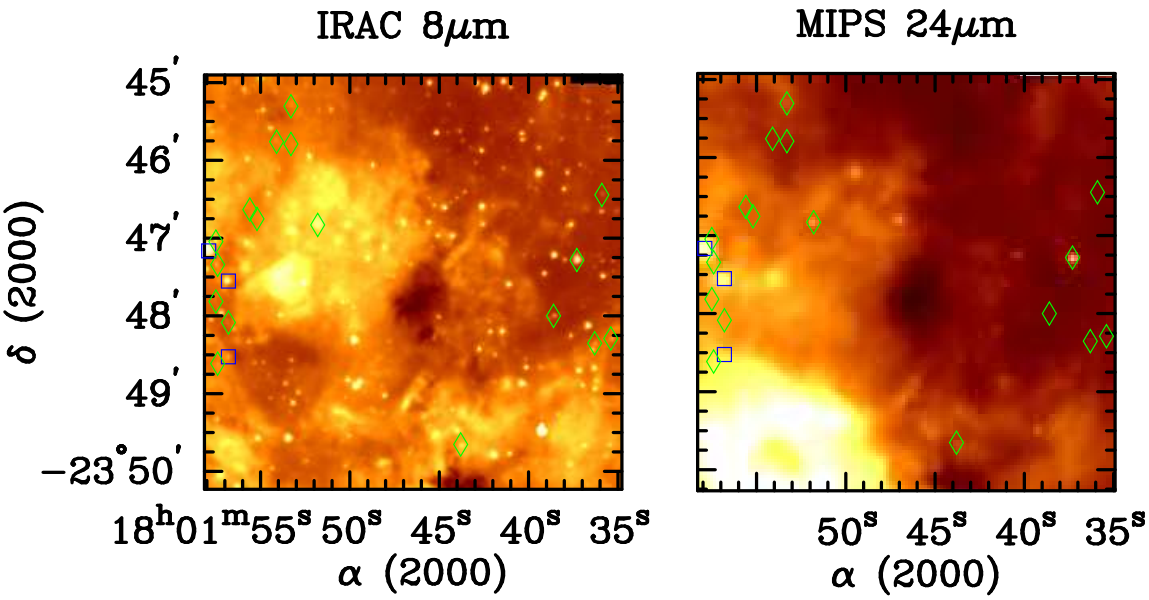

Figure 3.14. YSOs in IRDC G006.26−0.51: Labeling same as in Figure 3.13.

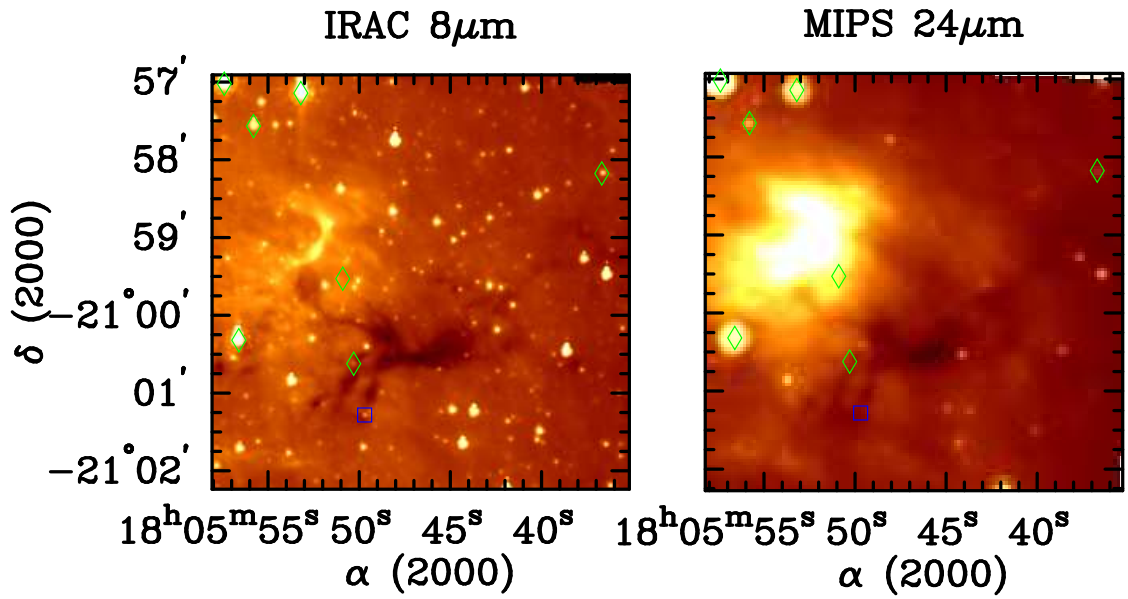

Figure 3.15. YSOs in IRDC G009.16+0.06: Labeling same as in Figure 3.13.

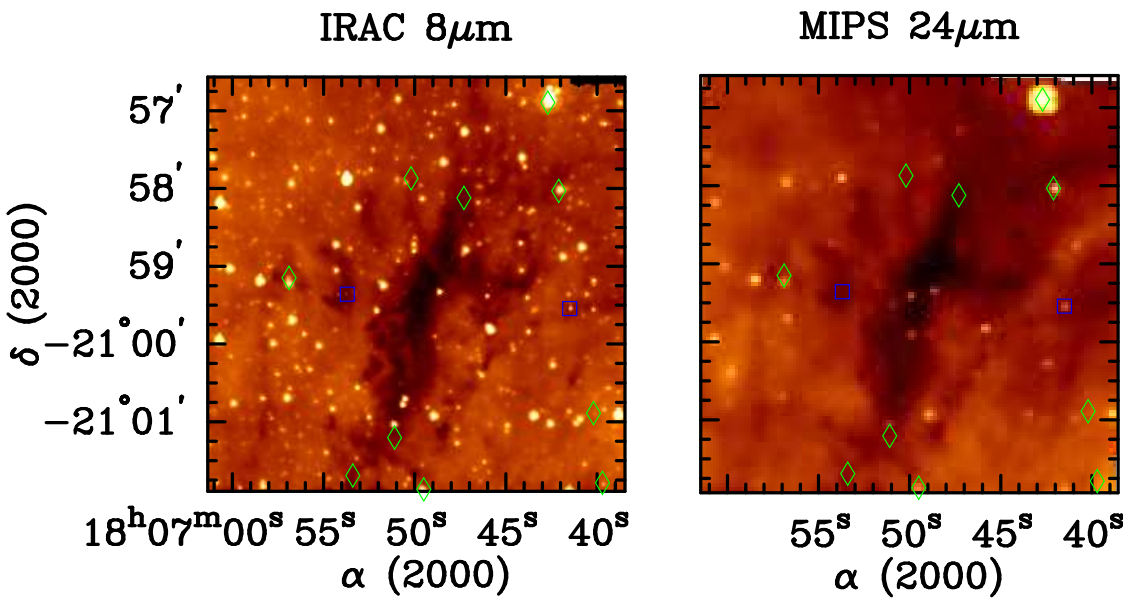

Figure 3.16. YSOs in IRDC G009.28−0.15: Labeling same as in Figure 3.13.

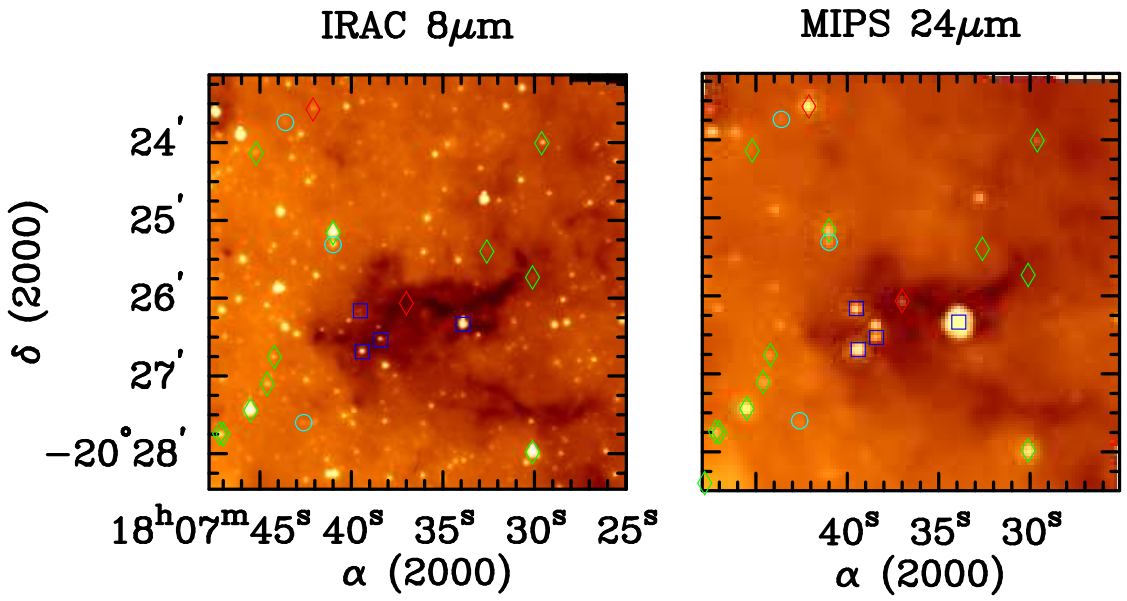

Figure 3.17. YSOs in IRDC G009.86−0.04: Labeling same as in Figure 3.13.

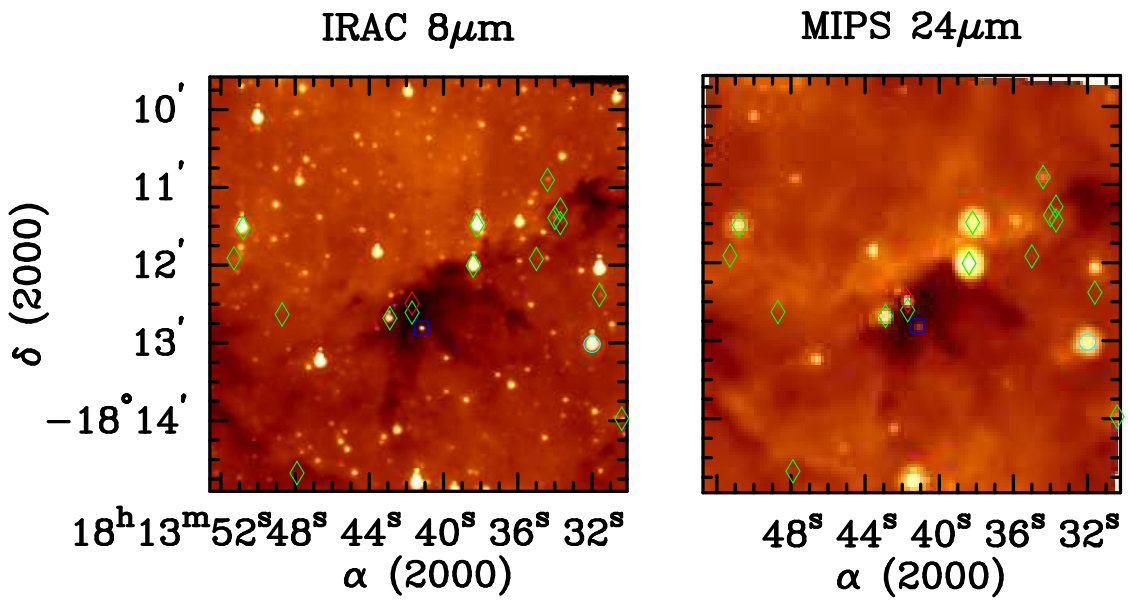

Figure 3.18. YSOs in IRDC G012.50−0.22: Labeling same as in Figure 3.13.

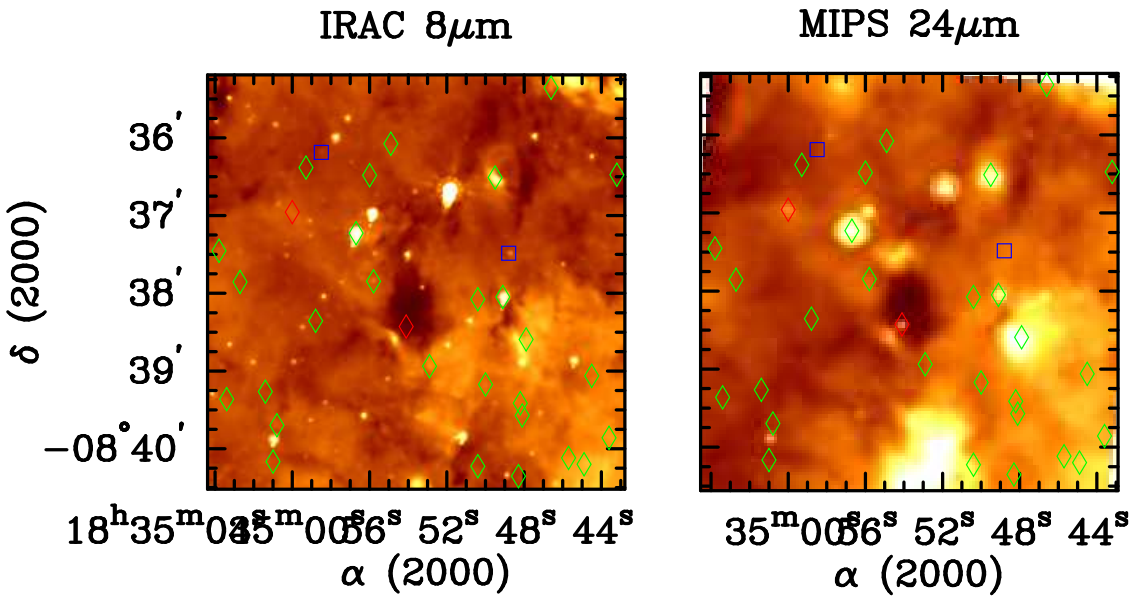

Figure 3.19. YSOs in IRDC G023.37−0.29: Labeling same as in Figure 3.13.

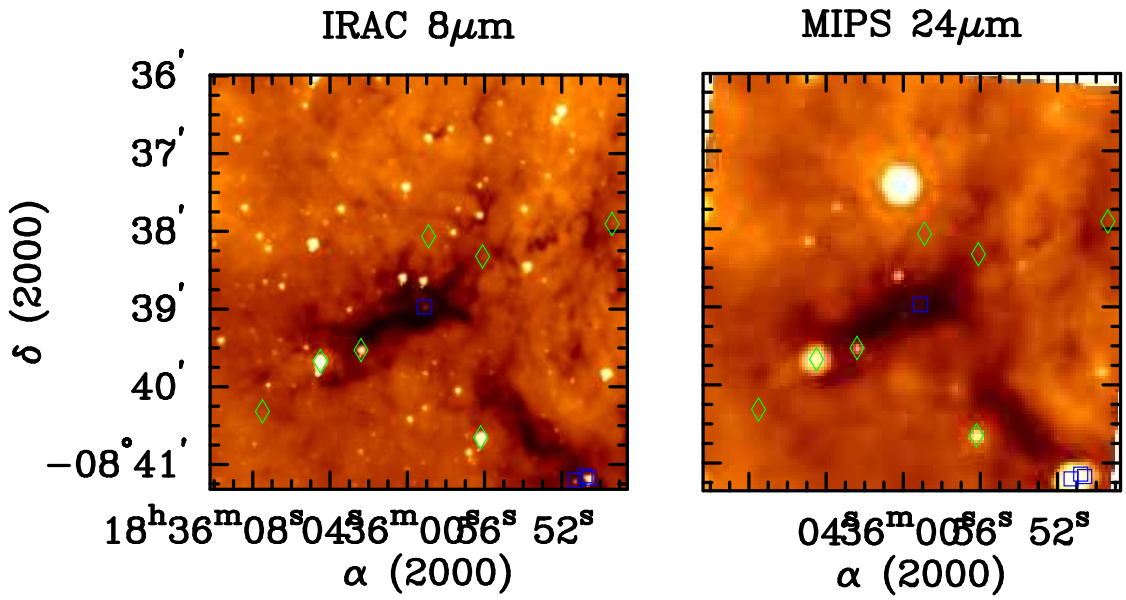

Figure 3.20. YSOs in IRDC G023.48−0.53: Labeling same as in Figure 3.13.

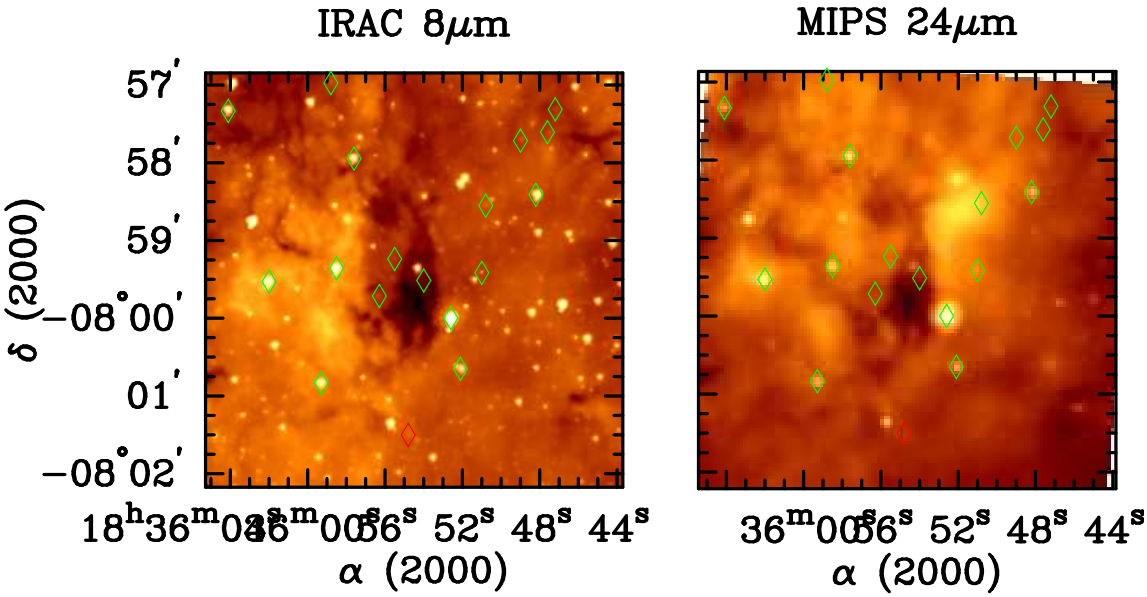

Figure 3.21. YSOs in IRDC G024.05−0.22: Labeling same as in Figure 3.13.

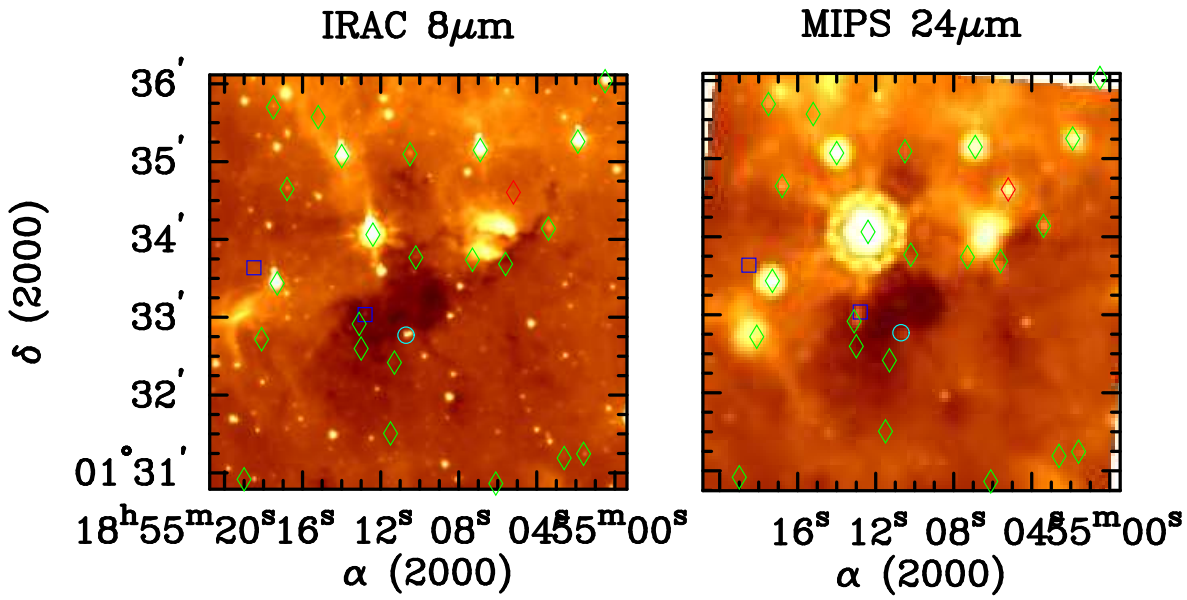

Figure 3.22. YSOs in IRDC G034.74−0.12: Labeling same as in Figure 3.13.

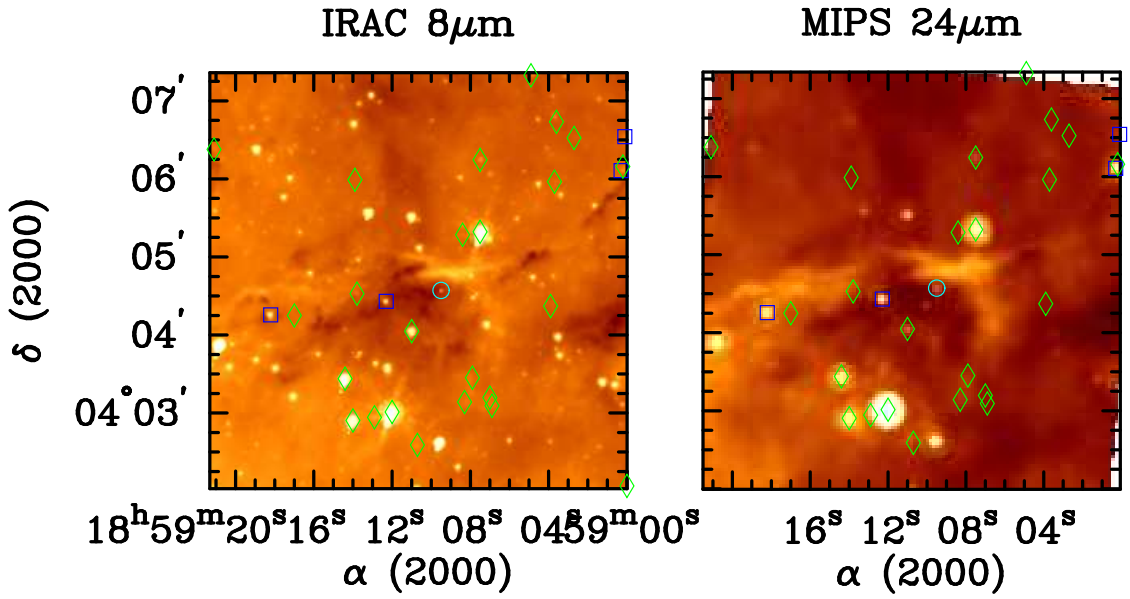

Figure 3.23. YSOs in IRDC G037.44+0.14: Labeling same as in Figure 3.13.

Table 3.2. Summary of Young Stellar Objects. In parentheses, we indicate the number from each classification that are associated with a "clump," which are determined in Chapter 4.

IRDC	Class I Protostars	Class II PMS stars	Transition Disks	Embedded Objects	Total Number
G005.85−0.23	0	22(2)	1	0	23(2)
G006.26−0.51	3(1)	26(4)	0	0	29(5)
G009.16+0.06	1	12(1)	0	0	13(1)
G009.28−0.15	2(1)	15(2)	0	0	17(3)
G009.86−0.04	5(3)	21(1)	3	2(1)	31(5)
G012.50−0.22	4(1)	22(1)	1	1(1)	28(3)
G023.37−0.29	8	36(2)	0	2(1)	46(3)
G023.48−0.53	5(4)	16	0	0	21(4)
G024.05−0.22	0	24(4)	0	1	25(4)
G034.74−0.12	4(1)	28(4)	2(1)	1	35(6)
G037.44+0.14	5(1)	33(1)	2(1)	0	40(3)
Total	37(12)	255(22)	9(2)	7(3)	308(39)

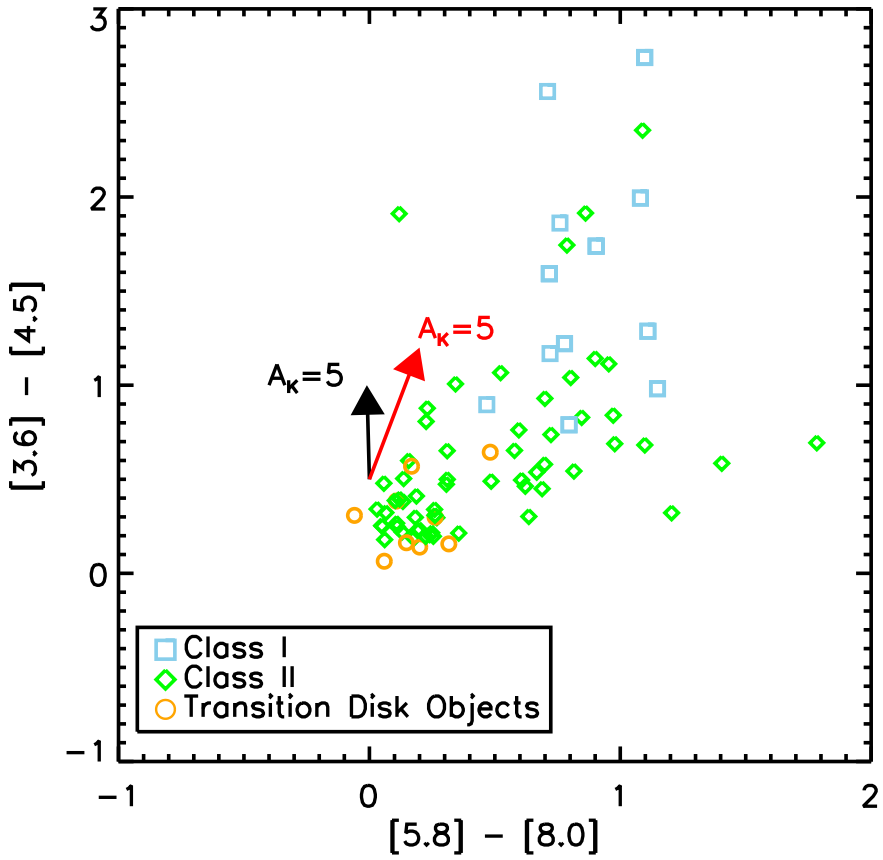

Figure 3.24. IRAC four color plot of Spitzer YSOs. Includes all objects that had photometry in all four IRDC bands with errors less than 0.2 magnitudes. Class I protostars are marked with blue squares, green diamonds mark the more-evolved Class II sources, and transition/debris disk objects are marked with orange circles. The deeply embedded objects identified with this analysis did not have sufficient detections in IRAC bands to appear on the color-color plots. The extinction law from Flaherty et al. (2007) indicated by the black arrow, and the extinction law from Indebetouw et al. (2005) is plotted as the red arrow.

Table 3.3. Spitzer-identified Embedded Protostars: Flux and Luminosity Estimates. The Index number corresponds to that reported in Table C.1.

IRDC	Index number	α (J2000)	δ (J2000)	3.6μm (mJy)	4.5μm (mJy)	5.8μm (mJy)	8μm (mJy)	24μm (mJy)	L_{MIR} ($L_\odot$)
G009.86−0.04	6	18:07:36.99	-20:26:03.9	···	···	···	···	7.00±2.47	>0.05
	7	18:07:42.12	-20:23:34.3	···	···	···	···	43.64±5.45	>0.33
G012.50−0.22	5	18:13:41.71	-18:12:29.6	···	0.02± 0.01	···	···	42.93±12.81	>2.1
G023.37−0.29	9	18:34:54.12	-08:38:25.5	···	···	···	···	33.94± 8.18	>1.0
	10	18:35:00.04	-08:36:57.4	0.02± 0.01	···	···	···	18.15±4.56	>1.5
G024.05−0.22	1	18:35:54.73	-08:01:30.2	···	···	···	···	5.88±1.27	>0.2
G034.74−0.12	5	18:55:05.20	+01:34:36.2	···	0.02± 0.01	···	···	36.13±4.84	>3.3

A test of whether these YSOs originate from the IRDC is to compare the A_K value measured toward the YSOs to that expected toward stars up to the distance to the IRDC. Presumably, stars born in the very dense IRDC environment would show residual high A_K values due to the surrounding material in the cloud. According to Binney & Merrifield (1998), A_K values between 0.4 and 0.9 are expected for the standard extinction through the plane of the Galaxy for objects at 2 to 5 kpc, so any A_K value in excess of these values is considered "enhanced." As shown in Figure 3.12, 70% of the YSOs with A_K measurements (97/138) exhibit A_K values in excess of this expectation, which implies there is additional dense gas and dust extincting the light of the YSOs. The 30% of all YSOs not showing excess extinction can either be on the surface of IRDCs, where all the extincting material is behind them, or they are in the field. The A_K measure, however, is also high for the AGB contaminants in this sample. We note in Appendix C which YSOs have colors consistent with AGB stars. Up to 35% (34/97) of the excess extinction objects might be AGB stars rather than associated YSOs. Thus, A_K is not the ideal proxy of stellar association, and we are currently developing a more robust discriminant for determining YSO association.

Table 3.3 lists all of the objects identified as embedded objects that are spatially coincident with an IRDC. We list the flux density at each Spitzer wavelength and an estimate of the mid-infrared luminosity derived from integrating the spectral energy distribution, which is dominated by emission at 24 μm. In the likely event that the embedded objects are extincted, these mid-infrared luminosities will be underestimated. Taking the average extinction estimations, which can be derived most reliably from the measurements of Class II objects, A_K ranges from 1 to 3, which, if the extinction law Flaherty et al. (2007) is applied, corresponds to A_{24} of 0.5 to 1.6. As a check, we use a second method to estimate the extinction: based on average values of the optical depth we measure in the IRDCs, we confirm that A_{24} $\sim$1 is typical in these objects. Given the uncertain extinction properties and the fact that a large portion of these embedded sources' luminosity will emerge at longer wavelengths not observed here, the luminosities presented in Table 3.3 are lower limits. Stars with luminosities in this range, according to Robitaille et al. (2006), arise from

stars ranging from 0.1 to 2 $M_{\odot}$, but are likely much greater.

3.4 IRDC Environment

3.4.1 Nebulosity at 8 and 24 μm

Four IRDCs in our sample (G006.26−0.51, Figure 3.2; G009.16+0.06, Figure 3.3; G023.37−0.29 Figure 3.7; G034.74−0.12, Figure 3.10) exhibit bright emission nebulosity in the IRDC field at 8 and 24 μm, and just at 24 μm in G024.05−0.22, Figure 3.9. These regions tend to be brightest in the thermal infrared (e.g. 24 μm) but show some emission at 8 μm, which suggests they are sites of high mass star cluster formation. To test whether the apparent active star formation is associated with the IRDC in question, or if it is in the vicinity, we correlate each instance of a bright emission with the molecular observations of the object obtained by Ragan et al. (2006). The molecular observations provide velocity information which, due to Galactic rotation, aid in estimating the distance to the mid-infrared emission (Fich et al., 1989). This distance compared with the distance to the IRDC enables us to discern whether the IRDC and young cluster are at the same distance or one is in the foreground or background.

In the case of G006.26−0.51 (Figure 3.2), we detect infrared emission at 24 μm east of the IRDC. This is spatially coincident and has similar morphology to $C^{18}O$ (1-0) emission emitting at a characteristic velocity of 17 km s^{-1} (Ragan et al., 2006), corresponding to a distance of about 3±0.5 kpc. The IRDC has a velocity of 23 km s^{-1}, which gives a distance of 3.8 kpc, but with an uncertainty of over 500 pc (see Table 1 and Ragan et al. (2006)). Given the errors inherent in the distance derivation from the Galactic rotation curve, we cannot conclusively confirm or rule out association.

G009.16+0.06 (Figure 3.3), has neither distinct velocity component evident in the molecular observations nor does the molecular emission associated with the IRDC overlap with the 24 μm emission. Embedded clusters should be associated with molecular emission especially $C^{18}O$ which is included in the FCRAO survey. Associated emission for this object likely lies outside the bandpass of the FCRAO observations

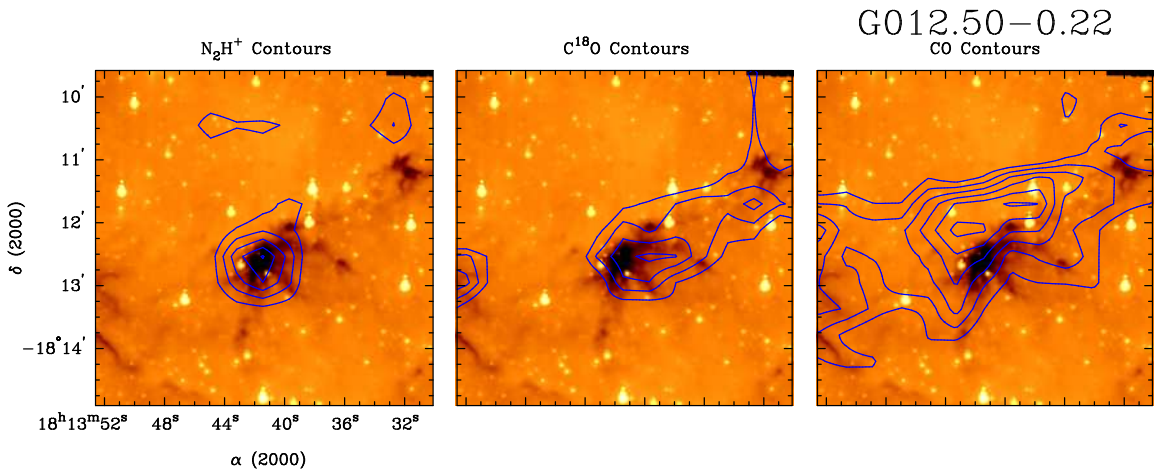

Figure 3.25. FCRAO contours of G012.50−0.22. N_2H^+ (1-0) contours (left), $C^{18}O$ (1-0) (center) and ^{12}CO (1-0) (right) plotted over the *Spitzer* 8 μm image of G012.50−0.22. Each tracer probes a different density regime, as the critical density of the molecular transition decreases from left to right.

and is at a greater or lesser distance than IRDC.

The 24 μm image of G023.37−0.29 (Figure 3.7) shows bright emission to the south of the IRDC and another region slightly south and west of the IRDC. This emission is not prominent in the IRAC images, suggesting that this is potentially an embedded star cluster. Molecular observations show strong emission peaks in both CS (2-1) and N_2H^+ (1-0) in the vicinity of the IRAC 8 μm and MIPS 24 μm emission. However, there are three distinct velocity components evident in the observed bandpass, none of which is more spatially coincident with the 24 μm emission than the others. Unfortunately, the spatial resolution of the FCRAO survey is insufficient for definitive correlation.

Finally, in G024.05−0.22 (Figure 3.9) and G034.74−0.12 (Figure 3.11), no molecular emission is distinctly associated with the nebulosity; the most likely scenario for this object is that the associated molecular emission lies outside the bandpass of the FCRAO observation and, therefore, is not associated.

3.4.2 The Spatial Extent of IRDCs

Most studies, including this thesis, focus primarily on the dense structures that comprise infrared-dark clouds, yet their connection to the surrounding environment has

not yet been discussed in the literature. While it is clear that some star formation is directly associated with the dense material, star formation is also occurring beyond the extent of the IRDC as it appears in absorption. Figure 3.25 shows molecular line contours from Ragan et al. (2006) over the *Spitzer* 8 μm image. N_2H^+, a molecule known to trace very dense gas, corresponds exclusively to the dark cloud. On the other hand, $C^{18}O$ and, to a greater extent ^{12}CO, show a much more extended structure, which demonstrates that the infrared-dark cloud resides within a greater molecular cloud complex.

For all of the objects in our sample, the ^{12}CO emission was present at the edge of the map (up to $2'$ away from the central position), so it is likely that the emission, and therefore the more diffuse cloud that it probes, extends beyond the mapped area. Thus, the full spatial extent of the surrounding cloud is not totally probed by our data.

3.5 Summary

We present new *Spitzer* IRAC and MIPS 24 μm photometric measurements supplemented with 2MASS J, H, K_s photometry of the distributed young stellar population observed in the Spitzer fields. Rigid color criteria are applied to identify candidate young stellar objects that are potentially associated with the infrared-dark clouds. In all, 308 young stellar objects are identified (see Appendix C). Most (70%) YSOs that have a A_K measurement have extinction in excess of a field star at the distance of the IRDCs, implying that most of these stars are indeed associated with the IRDC; asymptotic giant branch stars, however, are an important contaminant of this sample, and further work is needed to determine the extent of their significance. Seven of the YSOs are classified as embedded protostars. For those objects, we set lower limits on the infrared luminosities. One IRDC has an IRAS source in the field, which is the best candidate for an associated massive star. Otherwise, our observations provide no evidence for massive star formation in IRDCs, though sensitivity limitations do not rule out the presence of low mass stars and heavily extincted stars.

In this sample, half (5/11) of the sample shows no clear evidence for *embedded*

sources in the dense absorbing gas, and instead appear populated sparsely with young protostars, the photometric properties of which are given in Appendix C, and the overall IRDC star content is summarized in Table 3.2. Among those embedded objects correlated with the absorbing structure at 8 μm, which are summarized in Table 3.3, we find a marked lack of luminous sources (>5 $L_{\odot}$) at these wavelengths. There may be significant extinction at 24 μm, in which case we would underestimate their luminosity. Further, even in IRDCs with embedded protostars, most of the cloud core mass is not associated with an embedded source. It is our contention that based on these *Spitzer* most of the IRDC mass does not harbor significant massive star formation, and, hence IRDCs are in an early phase of cloud evolution.

Bright emission nebulosity is evident at 8 μm and 24 μm in four fields, possibly due to the presence of high mass stars or a cluster. If the IRDC were associated with the nebulosity, it would be a strong indication that the IRDCs have massive star formation occurring already in the vicinity. Molecular data give no definitive evidence that these bright nebulous regions are associated with the IRDCs.

CHAPTER 4

USING SPITZER TO PROBE IRDC STRUCTURE

A primary goal of my *Spitzer* study is to explore the mass function of clumps in infrared-dark clouds and compare it to that of massive star formation regions, local star formation regions, and the stellar IMF. We note that there is some ambiguity in the literature about the "clump" versus the "core" mass functions. In the following description, a "core" mass function refers to the mass spectrum objects with masses in the "core" regime (10^{-1}-10^{1} $M_{\odot}$, 10^{-2}-10^{-1} pc), and a "clump" mass function for objects in the "clump" regime (10-10^{3} $M_{\odot}$, 10^{-1}-10^{0} pc), as summarized in Bergin & Tafalla (2007). The mass function quantification is the most widely used measure of mass distribution in star-forming and pre-stellar regions, thus allowing for direct comparisons to be made between regions of various environments, scales, and evolutionary stages. Here we present the infrared-dark cloud clump mass function. We describe the relevance of this result in the context of Galactic star formation and discuss several methods we use to test its validity.

4.1 Background

A mass function (MF) is a common metric used to account for the breakdown in mass of objects in a given population. The initial mass function of stars (IMF), made famous by Salpeter (1955) and refined many times over (e.g. Kroupa, 2001), generally follows a power law trend. In the differential mass function (DMF) formalism, $dN/dM \propto M^{-\alpha}$, where N is the number of stars, M is the mass, and $\alpha = 2.35$ for the high-mass tail of stars. In other contexts, the mass function can be de-

scribed as a function of the logarithm of mass, which is conventionally presented as $dN/d(log\ m) \propto M^{\Gamma}$, in which case $\Gamma = -(\alpha - 1)$. In the results that follow, we present the slope of the clump mass function in terms of α.

The same construction can be applied to pre-stellar objects, and in local regions, several studies have found that the pre-stellar core mass function (CMF) that is similar in shape to the stellar initial mass function (e.g. Motte et al., 1998). This potentially suggests a one-to-one mapping between the CMF and IMF, perhaps scaled by a constant "efficiency" factor (e.g. Alves et al., 2007). However, resolution considerations, especially when looking at more distant regions, limit the robustness of these claims.

Mass distributions in nearby star forming regions have been probed in a variety of ways: most commonly, observation of dust thermal continuum emission. Cold dust emission is optically thin at millimeter and sub-millimeter wavelengths, and can therefore be used as a direct tracer of mass. A number of surveys of local clouds (e.g. Johnstone et al., 2000b; Motte et al., 1998) have been performed with single-dish telescopes covering large regions in an effort to get a complete picture of the mass distribution of low-mass clouds. This is an extremely powerful technique, but as Goodman et al. (2009) demonstrate, this technique suffers from some limitations, chief among them poor spatial resolution (in single-dish studies), required knowledge of dust temperatures (Pavlyuchenkov et al., 2007), and the insensitivity to diffuse extended structures.

Another technique that has been employed to map dust uses near-infrared extinction mapping (Alves et al., 2007; Lombardi et al., 2006), which is a way of measuring A_V due to dark clouds by probing the color excesses of background stars (Lombardi & Alves, 2001). This method is restricted to nearby regions of the Galaxy because of sensitivity limitations and the intervention of foreground stars, both of which worsen with greater distance. Also, the dynamic range of A_V in such studies is limited to $\sim$1-60 (Lombardi & Alves, 2001), while our technique probes from A_V of a few to $\sim$100.

Both the dust emission and near-infrared extinction mapping techniques are diffi-

cult to apply to regions such as infrared-dark clouds due to the much greater distance to IRDCs. As we show in §4.2.2, absorbing structure exists below the spatial resolution limit of single-dish surveys. Sensitivity limitations and foreground contamination preclude use of near infrared extinction mapping to probe IRDCs. As we show in the following section, extinction mapping in the mid-infrared is a powerful technique in probing IRDCs.

Structure in star-forming regions can also be probed with CO isotopologues, which find a somewhat different character to the distribution of mass in molecular clouds. Kramer et al. (1998) determined that the clump mass function in molecular clouds follows a power law with α between 1.4 and 1.8 ($-0.8 < \Gamma < -0.4$). This is significantly shallower than the Salpeter-like slope for clumps found in works using dust as a mass probe. This disagreement may be due to an erroneous assumption inherent in one (or both) of the techniques, or it may be that the techniques are finding information about how the fragmentation process takes place from large scale, probed by CO, to small scales, probed by dust. Another possible explanation is that most of the objects in Kramer et al. (1998) are massive star forming regions, and star formation in these regions may be intrinsically different than tyical regions studied in the local neighborhood (e.g. Taurus, Serpens).

Sub-millimeter observations of more distant, massive star-formation regions have been undertaken (e.g. Reid & Wilson, 2006; Li et al., 2007; Mookerjea et al., 2004; Rathborne et al., 2006) with a mixture of results regarding the mass function shape. Rathborne et al. (2006), for example, performed IRAM observations of a large sample of infrared-dark clouds. Each cloud in that sample is comprised of anywhere from 2 to 18 cores with masses ranging from 8 to $2000 M_{\odot}$. They find a Salpeter-like ($\alpha \sim 2.35$) mass function for IRDC cores. However, our Spitzer observations reveal significant structure below the spatial resolution scales of Rathborne et al. (2006). I show that the mass function within a fragmenting IRDC is shallower than Salpeter and closer to the mass function derived from CO emission.

Given the strong evidence for fragmentation, it is clear that IRDCs are the precursors to massive clusters. It is then natural to draw comparisons between the

characteristics of fragmenting IRDCs and the nearest region forming massive stars, Orion. At ∼500 pc, it is possible to resolve what are likely to be pre-stellar objects in Orion individually with current observational capabilities. With the high-resolution of our study, we can examine star formation regions (IRDCs) at a similar level of detail as single-dish telescopes can survey Orion. For example, we detect structures on the same size scale (∼0.03 pc) as the quiescent cores found by Li et al. (2007) in the Orion Molecular Cloud, however the most massive core in their study is ∼50 $M_{\odot}$. These cores account for only a small fraction of the total mass in Orion.

4.2 Tracing mass with dust absorption at 8 μm

Each infrared-dark cloud features distinct absorbing structures evident at all Spitzer wavelengths (see Figures 3.1 through 3.11), but they are most pronounced at 8 μm and 24 μm due to strong background emission from polycyclic aeromatic hydrocarbons (PAHs) and small dust grains in the respective bandpasses (Draine, 2003). The IRDCs in this sample exhibit a range of morphologies and surrounding environments (see Section 3.4). The IRDCs in this sample show a morphological mix of filamentary dark clouds (e.g. G037.44+0.14, Figure 3.11) and large "round" concentrations (e.g. G006.26−0.51, Figure 3.2). Remarkably, these detailed structures correspond almost identically between the 8 μm and 24 μm bands, despite the fact that the source of the background radiation arises from separate mechanisms. At 8 μm emission from PAHs dominate on average, and at 24 μm, the bright background is due to the thermal emission of dust in the Galactic plane. Considering this scenario, it is unlikely that we are mistaking random background fluctuations for dense, absorbing gas with the appropriate characteristics to give rise to massive star and cluster formation.

4.2.1 Modeling the Foreground and Background

In the Galactic plane, the 8 μm background emission varies. To accurately estimate structures seen in absorption, we account for these variations using a spatial median filtering technique, motivated by the methods used in Simon et al. (2006a). For each pixel in the IRAC image, we compute the median value of all pixels within a variable

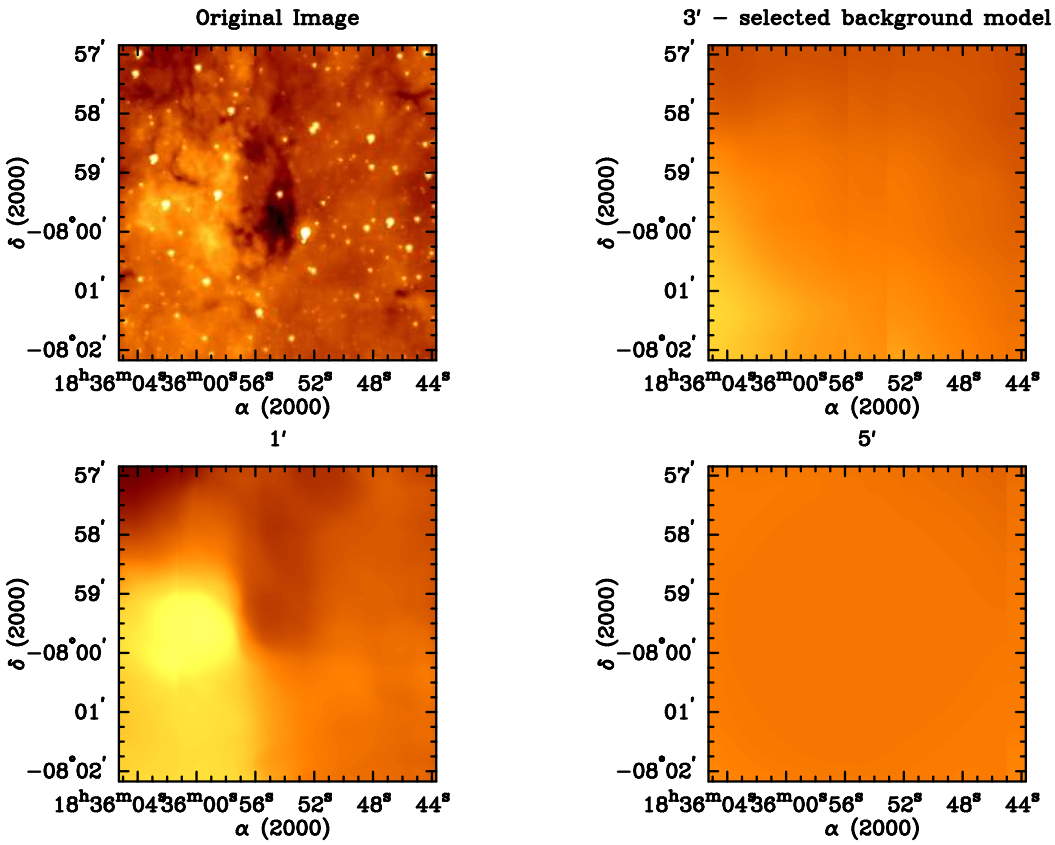

Figure 4.1. Background calculation illustration. *Upper left:* Original IRAC 8 μm image of G024.05-0.22. *Upper right:* Background model using the spatial median filtering technique with a 3′ radius. The dark cloud is virtually eliminated from the background, but still accounts for the large-scale variations. *Lower left:* Same as upper right panel, except that a 1′ radius is used, which models the dark cloud as part of the background. *Lower right:* Same as upper right and lower left panels, except that a 5′ radius is used, which misses the background variation and is almost a constant value.

radius and assign that value to the corresponding pixel in the background model. Figure 4.1 illustrates an example of several trials of this method, including models with $1'$, $3'$, and $5'$ radius of pixels included in a given pixel's median calculation. We select the size of the filter to be as small as possible such that the resulting map shows no absorption as background features. If the radius is too small, most of the included pixels will have low values with few representing the true background in the areas where absorption is concentrated (lower left panel of Figure 4.1). The background variations are also not well-represented if we select a radius too large (lower right panel of Figure 4.1). Based on our analysis, the best size for the filter is $3'$. The observed 8 μm emission is a combination of both background and foreground contributions;

$$\int I^{estimate} d\lambda = \int I_{BG}^{true} d\lambda + \int I_{FG} d\lambda \tag{4.1}$$

where $\int I^{estimate}\ d\lambda$ is the intensity that we measure from the method described above, $\int I_{BG}^{true}\ d\lambda$ is the true background intensity, which can only be observed in conjunction with $\int I_{FG}\ d\lambda$, the foreground intensity, all at 8 μm. The relative importance of the foreground emission is not well-known. For simplicity, we assume the foreground can be approximated by constant fraction, x, of the emission across each field.

$$\int I_{FG}\ d\lambda = x \int\ I_{BG}^{true}\ d\lambda \tag{4.2}$$

One way to estimate the foreground contribution has already been demonstrated by Johnstone et al. (2003). The authors compare observations of IRDC G011.11−0.12 with the *Midcourse Science Experiment (MSX)* at 8 μm and the Submillimeter Common-User Bolometer Array (SCUBA) on the James Clerk Maxwell Telescope (JCMT) at 850 μm (see their Figure 3) and use the point at which the 8 μm integrated flux is at its lowest at high values of 850 μm flux for the foreground estimate. The top panel Figure 4.2 shows a similar plot to Figure 3 in Johnstone et al. (2003), except our integrated 8 μm flux is measured with *Spitzer* and presented here in units of MJy/sr. SCUBA 850μm data for two of the IRDCs in this sample (G009.86−0.04

and G012.50−0.22) are available as part of the legacy data release (Di Francesco et al., 2008) and are included in this plot. Just as Johnstone et al. (2003) point out, we see a clear trend: where 8 μm emission is low along the filament, the 850μm flux is at its highest. In the case of G011.11−0.12, where the SCUBA data are of the highest quality, we take the minimum 8 μm flux density to be an estimate of the foreground contribution. Assuming this trend is valid for our sample of IRDCs, we use the 8 μm emission value measured at the dust opacity peak in each source as our estimation of the foreground level for that object (for the remainder of this paper, we will refer to this method as foreground estimation method "A"). Given these considerations, we find values for x to range between 2 and 5. Up to 20% of this foreground contamination is likely due to scattered light in the detector (S.T. Megeath, private communication). We assume constant foreground flux at this level. As an alternative foreground estimate, we also test a case in which we attribute half of the model flux to the background and half to the foreground. This is equivalent to choosing a value of x of 1, and based on Figure 4.2, is also a reasonable estimate. This method will be referred to as foreground estimation method "B." For most of the following figures and discussion, we use estimation method A and refer the results from method B in the text when applicable.

With an estimation of the foreground contribution, the absorption can be quantitatively linked to the optical depth of the cloud. The measured integrated flux, $\int I_m d\lambda$ at any point in the image, including contributions from both the foreground and background, can then be expressed as

$$\int I_m d\lambda = \int I_{BG}^{true} e^{-\tau_8} d\lambda + \int I_{FG} d\lambda \tag{4.3}$$

where τ_8 is the optical depth of the absorbing material. For the subsequent calculations, we use the average intensity, assuming uniform transmission over the IRAC channel 4 passband, and average over the extinction law of Weingartner & Draine (2001) in this wavelength region in order to convert the optical depth into a column density (see discussion in next section). We note that we make no attempt

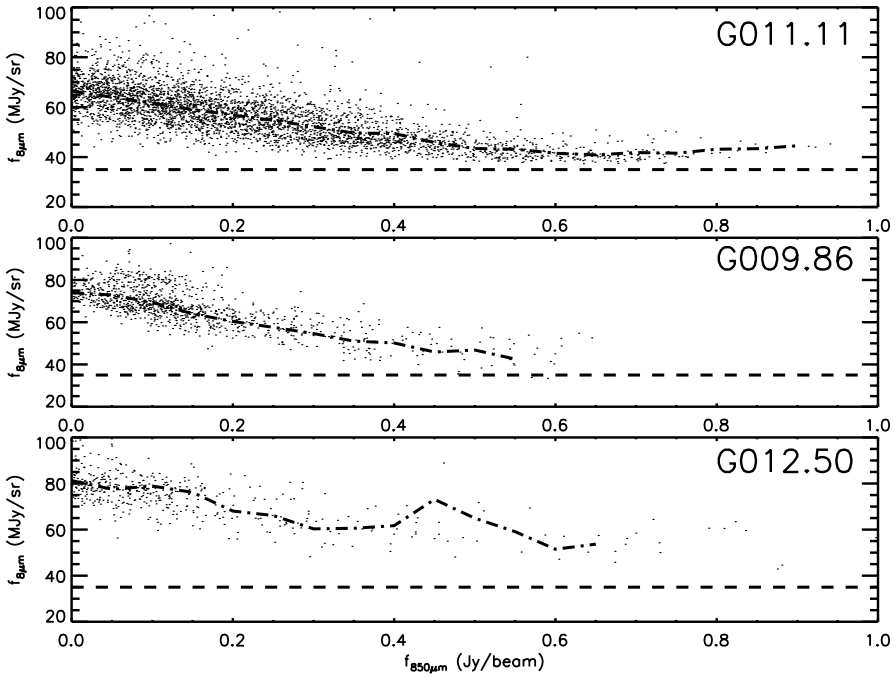

Figure 4.2. Background calibration with SCUBA. Spitzer 8 μm vs. SCUBA 850μm flux for IRDC G011.11−0.12, G009.86−0.04, and G012.50−0.22. The horizontal dashed line marks where the 8 μm flux density reaches a minimum in G011.11−0.12, which is also indicated for the two other IRDCs with available SCUBA data. This flux density serves as an estimate of the foreground emission at 8 μm. The dash-dotted line indicates the mean 8 μm emission.

to correct for the spectral shape of the the dominant PAH emission feature in the 8 μm Spitzer bandpass, which we assume dominates the background radiation. In addition, clumpy material that may be optically thick and is not resolved by these observations will cause us to underestimate the column density. These factors could introduce an uncertainty in the conversion of optical depth to column density. Still, we will show in Section 4.2.4 that dust models compare favorably to our estimation of the dust absorption cross section, lending credence to our use of τ as a tracer of column density.

4.2.2 Identification of Structure

Figure 4.3 shows a map of optical depth G024.05−0.22. This provides an example of the the absorbing substructure in one of the IRDCs in our sample. Owing to the

Table 4.1. `clumpfind` Parameter Summary

IRDC	Lower τ Threshold	$\Delta\tau$
G005.85−0.23	0.27	0.20
G006.26−0.51	0.27	0.11
G009.16+0.06	0.19	0.10
G009.28−0.15	0.35	0.06
G009.86−0.04	0.32	0.11
G012.50−0.22	0.31	0.16
G023.37−0.29	0.36	0.11
G023.48−0.53	0.39	0.09
G024.05−0.22	0.22	0.09
G034.74−0.12	0.27	0.07
G037.44+0.14	0.29	0.17

high spatial resolution of Spitzer at 8 μm (1 pixel = 0.01 pc at 4 kpc, accounting for oversampling), we see substructures down to very small scales ($\sim$0.03 pc) in *all* IRDCs in our sample.

In order to identify independent absorbing structures in the 8 μm optical depth map, we employed the `clumpfind` algorithm (Williams et al., 1994). In the two-dimensional version, `clfind2d`, the algorithm calculates the location, size, and the peak and total flux of structures based on specified contour levels. We use the Spitzer PET[1] to calculate the sensitivity of the observations, i.e. to what level the data permit us to discern true variations from noise fluctuations. At 8 μm, the observations are sensitive to 0.0934 MJy/sr which, on average, corresponds to an optical depth sensitivity (10-σ) of $\sim$0.02. While the clumps take on a variety of morphologies, since `clumpfind` makes no assumptions about the clump shapes, we approximate the clump "size" by its effective radius,

$$r_{eff} = \sqrt{\frac{n_{pix}\ A_{pix}}{\pi\ f_{os}}} \tag{4.4}$$

where n_{pix} is the number of pixels assigned to the clump by `clumpfind`, and A_{pix} is the area subtended by a single pixel. The correction factor for oversampling, f_{os} accounts for the fact that the *Spitzer Space Telescope* has an angular resolution of

[1]http://ssc.spitzer.caltech.edu/tools/senspet/

2.4″ at 8 μm, while the pixel scale on the IRAC chip is 1.2″, resulting in oversampling by a factor of 4.

The number and size of structures identified with `clumpfind` varies depending on the number of contouring levels between the fixed lower threshold, which is set by the sensitivity of the observations, and the highest level set by the deepest absorption. We set the lowest contour level to 10σ above the average background level. In general, increasing the number of contour levels serves to increase the number of clumps found. In all cases, we reach a number of levels where the addition of further contouring levels results in no additional structures. We therefore select the number of contour levels at which the number of clumps levels off, i.e. when the addition of more contour levels reveals no new clumps. We also remove those clumps found at the image edge or bordering a star, as the background estimation is likely inaccurate and/or at least a portion of the clump is probably obscured by the star, rendering any estimation of the optical depth inaccurate.

Using `clumpfind`, each IRDC broke down into tens of clumps, ranging in size from tens to hundreds of pixels per clump. The average clump size is 0.04 pc. Typically, there is one or two central most-massive clumps and multiple smaller clumps in close proximity. In some instances, clumps are strung along a filamentary structure, while in other cases, clumps are radially distributed about a highly-concentrated center. Figure 4.4 shows an example of how the clumps are distributed spatially in G024.05−0.22 as `clumpfind` identifies them.

With reliable identification of clumps, we next calculate individual clump masses. As described, `clumpfind` gives total optical depth measured at 8 μm, $\tau_{8,tot}$, within the clump boundary, its size and position. This can be directly transformed into $N(H)_{tot}$ via the relationship

$$N(H)_{tot} = \frac{\tau_{8,tot}}{\sigma_8 \ f_{os}} \tag{4.5}$$

where σ_8 is the dust absorption cross section at 8 μm. We derive an average value of σ_8 over the IRAC channel 4 bandpass using dust models that take into account

higher values of R_V corresponding to dense regions in the ISM. Using Weingartner & Draine (2001), we use $R_V = 5.5$, case B values, which agree with recent results from Indebetouw et al. (2005). We find the value of σ_8 to be $2.3\times10^{-23}\mathrm{cm}^2$.

The column density can then be used with the average clump size and the known distance to the IRDC, assuming all clumps are at approximately the IRDC distance, to find the clump mass. The mass of a clump is given as

$$M_{clump} = 1.16 m_H N(H)_{tot} A_{clump} \tag{4.6}$$

where m_H is the mass of hydrogen, $N(H)_{tot}$ is the total column density of hydrogen, the factor 1.16 is the correction for helium and A_{clump} is the area of the clump. Appendix D gives the location, calculated mass and size of all the clumps identified with `clumpfind`. We also note which clumps are in the vicinity of candidate young stellar objects (Appendix C) or foreground stars, thereby subjecting the given clump properties to greater uncertainty. On average (for foreground estimation method A), 25% of clumps border a field star, and these clumps are flagged and not used in the further analysis. In each infrared-dark cloud, we find between $3000 M_\odot$ and $10^4 M_\odot$ total mass in clumps, and typically $\sim$15% of that mass is found in the most massive clump.

We perform the same analysis on the maps produced with foreground estimation method B. The foreground assumption in this case leads to lower optical depths across the map. Due to the different dynamic range in the optical depth map, `clumpfind` does not reproduce the clumps that are found with method A exactly. The discrepancy arises in how `clumpfind` assigns pixels in crowded regions of the optical depth map, so while at large the same material is counted as a clump, the exact assignment of pixels to specific clumps varies somewhat. On average, the clumps found in the "method B" maps tend to have lower masses by a factor of 2, though the sizes do not differ appreciably from those found with foreground estimation method A.

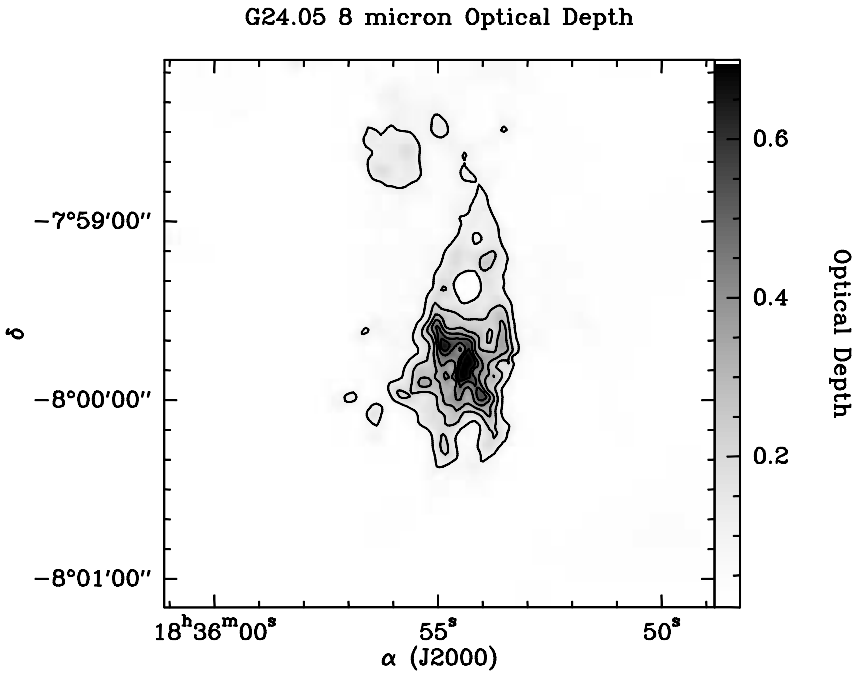

Figure 4.3. G024.05−0.22. 8 μm optical depth. Contours are from 0.1 to 0.7 in increments of 0.1.

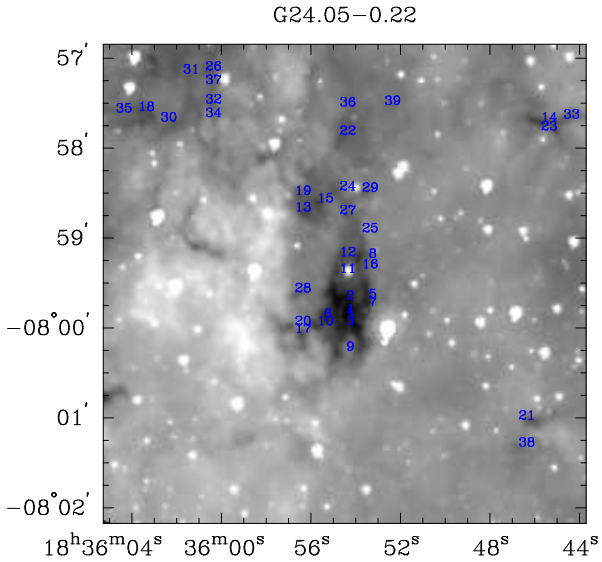

Figure 4.4. `clumpfind` results on G024.05−0.22 8μm image. Absorption identified as a "clump" is denoted by a number. The clumps are ordered in decreasing mass, with 1 being the most massive. See Appendix D.

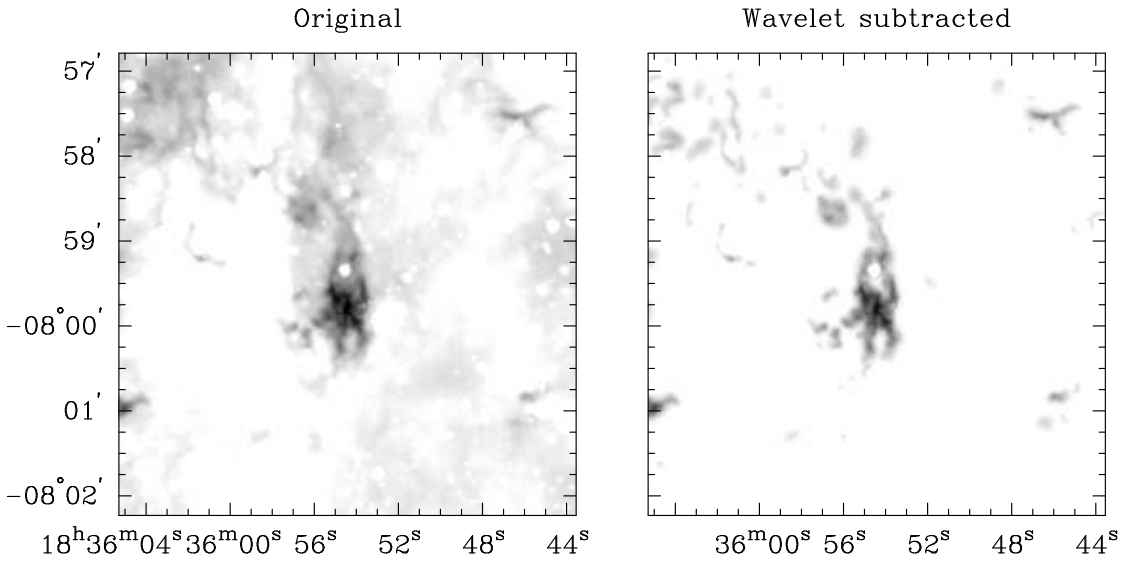

Figure 4.5. Wavelet analysis of G024.05−0.22. Original optical depth image of G024.05−0.22 (left) and the wavelet subtracted image (right) of the same region.

4.2.3 Resolving Inaccuracy in Clump Mass Calculation

The clumps identified in this fashion include a contribution from the material in the surrounding envelope. As a result, a portion of the low-mass clump population may not be detected, and the amount of material in a given clump may be overestimated. To examine this effect, we use the `gaussclumps` algorithm (Stutzki & Guesten, 1990) to identify clumps while accounting for the contribution from the cloud envelope. This method was designed to decompose three-dimensional molecular line observations by deconvoloving the data into clumps fit by Gaussians. To use the algorithm here without altering the code, we fabricated a data cube by essentially by mimicking a third (velocity) dimension, thus simulating three-dimensional clumps that were all centered in velocity on a single central plane. Mookerjea et al. (2004) and Motte et al. (2003) have used similar techniques to simulate a third dimension to their dust continuum data sets. The `gaussclumps` algorithm inherently accounts for an elevated baseline level, which can be used to approximate the envelope. Applied to our data set, `gaussclumps` finds that 15-50% of the material is in the envelope.

The `clumpfind` and `gaussclumps` methods result in nearly one-to-one clump identification in the central region of the IRDC. However, because the contribution from

the cloud envelope falls off further away from the central concentration of mass in the IRDC, `gaussclumps` fails to find low-mass clumps on the outskirts of IRDCs as successfully as `clumpfind`, despite being statistically valid relative to their local background. We conclude that `gaussclumps` is not suitable to identify of structure in the outskirts of the IRDCs where the envelope is below the central level.

Another method commonly employed in the literature to account for the extended structures in which dense cores reside is a "wavelet subtraction" technique, which is described in Alves et al. (2007). To address the varying levels of background across the optical depth map, we use the wavelet transform of the image to extract the dense cores. For one IRDC in our sample, G024.05−0.22, we (with the help of J. Alves, private communication) perform the wavelet analysis on the optical depth map. Figure 4.5 shows a comparison between the original optical depth map and the wavelet-subtracted map. With the removal of the "envelope" contribution in this fashion, the clumps are up to 90% less massive on average, and their average size decreases by 25%, or ∼0.02 pc.

Both using `gaussclumps` and applying wavelet subtraction methods to extract clumps show that the contribution of the cloud envelope is not yet well-constrained quantitatively. Not only is the cloud envelope more difficult to detect, its structure is likely not as simple as these first order techniques have assumed in modeling it. As such, for the remainder of the paper, we will not attempt to correct the clump masses on an individual basis, but rather focus our attention on the clump population properties as a whole. In §4.2.4, we employ several techniques to calibrate our mass estimation methods. We will show that the effect of the envelope is systematic and does not skew the derived relationships, such as the slope of the mass function.

4.2.4 Validating 8 μm absorption as a Tracer of Mass

In previous studies, molecular clouds have been predominantly probed with using the emission of warm dust at sub-millimeter wavelengths. While there are inherent uncertainties in the conversion of flux density to mass, the emission mechanism is well-understood. The method described above is a powerful way to trace mass in

molecular clouds. To understand the extent of its usefulness, here we validate dust absorption as a mass tracer by drawing comparisons between it and results using more established techniques. First, we relate the dust absorption to dust emission as probes of column density. Second, we use observations of molecular tracers of dense gas not only to further cement the validity of the absorbing structures, but also to place the IRDCs in context with their surroundings. Finally, we show that the sensitivity of the technique does not have a strong dependence on distance.

Probing Column Density at Various Wavelengths

As we discussed in §4.2.1, there is an excellent correlation between the 8 μm and 850 μm flux densities in IRDC G011.11-0.12. Figure 4.2 shows the point-to-point correlation between the SCUBA 850 μm flux density and Spitzer 8 μm flux density. This correspondence itself corroborates the use of absorption as a dust tracer. In addition, the fit to the correlation can confirm that the opacity ratio, κ_8 /κ_{850}, is consistent with dust behavior in high density environments. Relating the 8 μm flux density

$$f_8 = f_{bg} e^{-\kappa_8 \Sigma(x)} + f_{fg} \tag{4.7}$$

where κ_8 is the 8 μm dust opacity, $\Sigma(x)$ is the mass column density of emitting material, and f_{bg} and f_{fg} are the background and foreground flux density estimates, respectively (from §4.2.1), and the 850 μm flux density

$$f_{850} = B_{850}(T_d = 13K)\kappa_{850}\Sigma(x)\Omega \tag{4.8}$$

where B_{850} is the Planck function at 850 μm evaluated for a dust temperature of 13 K, κ_{850} is the dust opacity at 850 μm and Ω is the solid angle subtended by the JCMT beam at 850 μm, one can find a simple relation between the two by solving each for $\Sigma(x)$ and equating them. The opacity ratio, put in terms of the flux density measurements is as follows:

$$\frac{\kappa_8}{\kappa_{850}} = \frac{B_{850}\,\Omega}{f_{850}} ln\left(\frac{f_{bg}}{f_8 - f_{fg}}\right) \tag{4.9}$$

From our data, we confirm this ratio is considerably lower (∼500) in cold, high density environments than in the diffuse interstellar dust as found by Johnstone et al. (2003).

I perform another consistency check between our data and dust models. With maps at both 8 and 24 μm, both showing significant absorbing structure against the bright Galactic background (albeit at lower resolution at 24 μm), we can calculate the optical depth of at 24 μm in the same way we did in Section 4.2.1. The optical depth scales with the dust opacity by the inverse of the column density ($\tau_\lambda \propto \kappa_\lambda / N(H)$), so the ratio of optical depths is equal to the dust opacity ratio. We find that the typical ratio as measured by Spitzer in IRDCs is

$$\frac{\kappa_8}{\kappa_{24}} = \frac{\tau_8}{\tau_{24}} \sim 1.2 \tag{4.10}$$

which is comparable to 1.6, the Weingartner & Draine (2001) prediction (for R_V = 5.5, case B) and 1-1.2 predicted by Ossenkopf & Henning (1994) in the high-density case. We conclude that the dust properties we derive are consistent with the trends that emerge from models of dense environments typical of infrared-dark clouds.

Molecular Line Tracers

Molecular lines are useful probes of dense clouds, with particular molecules being suited for specific density ranges. For instance, chemical models show that N_2H^+ is an excellent tracer of dense gas in pre-stellar objects (Bergin & Langer, 1997). In support of these models, observations of low-mass dense cores (Tafalla et al., 2002; Bergin et al., 2002) demonstrate that N_2H^+ highlights regions of high central density (n∼10^6 cm^{-3}), while CO readily freezes out onto cold grains (when n > 10^4 cm^{-3}), rendering it undetectable in the central denser regions of the cores. CO is a major destroyer of N_2H^+, and its freeze-out leads to the rapid rise in N_2H^+ abundance in cold gas. When a star is born, the CO evaporates from grains and N_2H^+ is destroyed in the proximate gas (Lee et al., 2004). Thus, N_2H^+ is a preferential tracer of the

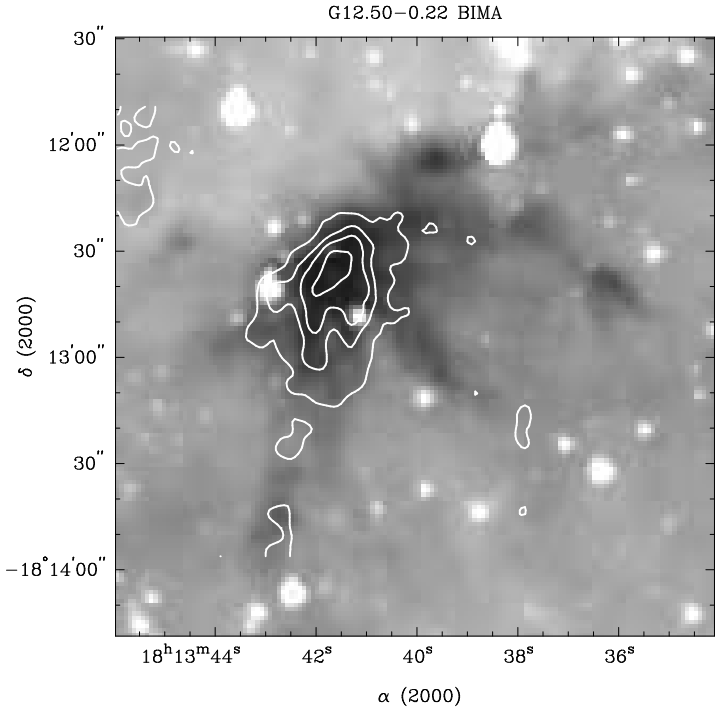

Figure 4.6. N_2H^+(1-0) BIMA contours of G012.50−0.22. Integrated intensity contours of N_2H^+ from 1.5 to 7.5 K km s^{-1} in 2 K km s^{-1} increments, plotted over the IRAC 8 μm image of IRDC G012.50−0.22.

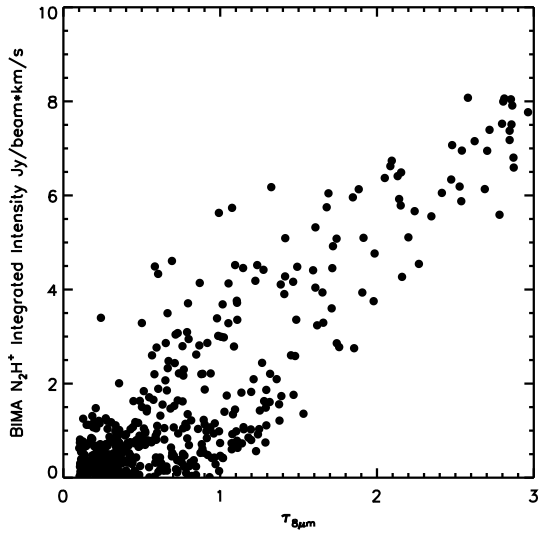

Figure 4.7. N_2H^+(1-0) BIMA vs. 8μm optical depth. Points with high integrated intensity but low optical depth correspond to stars, whose presence leads to the underestimation of optical depth in the vicinity.

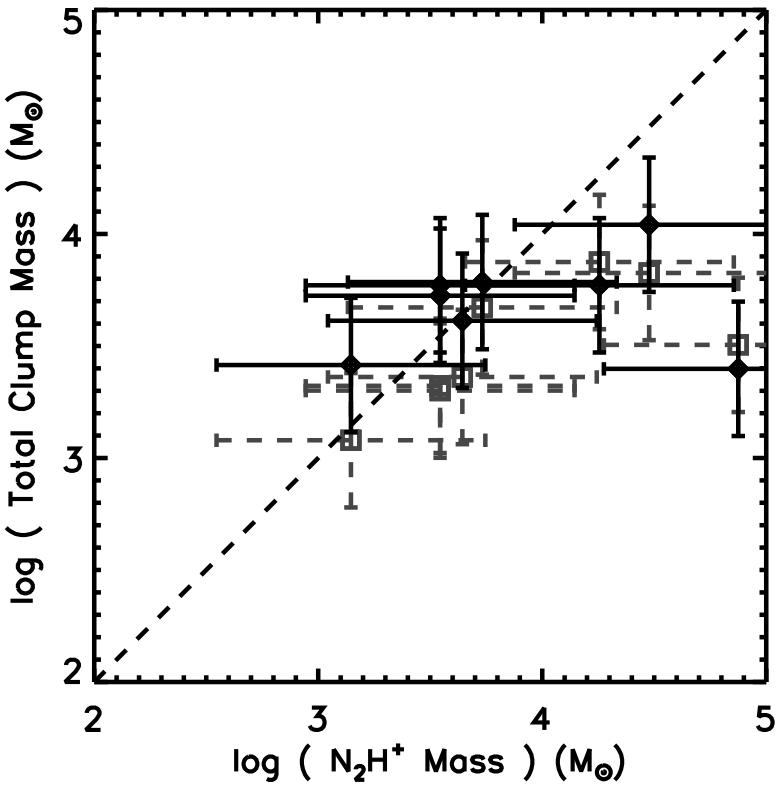

Figure 4.8. Clump mass vs. Mass derived by N_2H^+. Comparison of the total mass derived from N_2H^+ maps from Ragan et al. (2006) and total clump mass as derived from dust absorption at 8 μm, where the black diamonds represent the mass using foreground estimation method A and the grey squares show the masses derived using foreground estimation method B (see §4.2.1). Three of the IRDCs in the sample did not have adequate N_2H^+ detections. Error bars for 30% systematic errors in the mass are plotted for the clump mass estimates, and a factor of 5 uncertainty is plotted for the N_2H^+ mass estimates. The dashed line shows a one-to-one correspondence for reference.

densest gas that has not yet collapsed to form a star in low-mass pre-stellar cores.

While N_2H^+ has been used extensively as a probe of the innermost regions of local cores, where densities can reach $10^6 cm^{-3}$ (e.g. Tafalla et al., 2004), this chemical sequence has not yet been observationally proven in more massive star forming regions. Nonetheless recent surveys (e.g. Sakai et al., 2008; Ragan et al., 2006) confirm that N_2H^+ is prevalent in IRDCs, and mapping by Ragan et al. (2006) shows that N_2H^+ more closely follows the absorbing gas than CS or $C^{18}O$, which affirms that the density is sufficient for appreciable N_2H^+ emission. These single dish surveys do not have sufficient resolution to confirm the tracer's reliability on the clump or pre-stellar core scales in IRDCs. Interferometric observations will be needed to validate N_2H^+ as a probe of the chemistry and dynamics of individual clumps.

For one of the objects in our sample, G012.50−0.22, we had previous BIMA observations of N_2H^+ emission with $8'' \times 4.8''$ spatial resolution. The BIMA data were reduced using the standard MIRIAD pipeline reduction methods (Sault et al., 1995). As in nearby clouds, such as Walsh et al. (2004), the integrated intensity of N_2H^+ relates directly to the dust (measured here in absorption) in this IRDC. We demonstrate the quality of N_2H^+ as a tracer of dense gas in Figure 4.6, with contours of N_2H^+ integrated intensity from BIMA observations plotted over the 8 μm image, and in Figure 4.7, which plots the point-to-point correlation between BIMA integrated intensity and 8 μm optical depth.

Two trends are apparent in Figure 4.7. First, below $\tau < 0.25$ there is a lack of N_2H^+ emission. This suggests that the absorption may be picking up a contribution from a lower density extended envelope that is incapable of producing significant N_2H^+ emission. This issue is discussed in greater detail in §4.4.1. Alternatively, the interferometer may filter out extended N_2H^+ emission. The second trend evident in Figure 4.7 is that for $\tau > 0.25$, there is an excellent overall correlation, confirming that mid-infrared absorption in clouds at distances of 2 to 5 kpc is indeed tracing the column density of the *dense* gas likely dominated by pre-stellar clumps.

In addition to directly tracing the dense gas in IRDCs, molecular observations can be brought to bear on critical questions regarding the use of absorption against the

Galactic mid-infrared background and how best to calibrate the level of foreground emission. One way to approach this is to use the molecular emission as a tracer of the total core mass and compare this to the total mass estimated from 8 μm absorption with differing assumptions regarding the contributions of foreground and background (see § 4.2.1). In Ragan et al. (2006) we demonstrated that the distribution of N_2H^+ emission closely matches that of the mid-infrared absorption (see also § 4.2). This is similar to the close similarity of N_2H^+ and dust continuum emission in local pre-stellar cores (e.g. Bergin & Tafalla, 2007). Thus we can use the mass estimated from the rotational emission of N_2H^+ to set limits on viable models of the foreground. In Ragan et al. (2006) we directly computed a mass using an N_2H^+ abundance assuming local thermodynamic equilibrium (LTE) and using the H_2 column density derived from the MSX 8 μm optical depth. However, this estimate is highly uncertain as the optical depth was derived assuming no foreground emission, and the N_2H^+ emission may not be in LTE. Instead, here, we will use chemical theory and observations of clouds to set limits.

N_2H^+ appears strong in emission in dense pre-stellar gas due to the freeze-out of CO, its primary destruction route. Detailed theoretical models of this process in gas with densities in excess of 10^5 cm^{-3} (Aikawa et al., 2005b), as expected for IRDCs, suggest a typical abundance should be $\sim 10^{-10}$ with respect to H_2 (Maret et al., 2006; Aikawa et al., 2005b; Pagani et al., 2007). This value is consistent with that measured in dense gas in several starless cores (Tafalla et al., 2002; Maret et al., 2006). Using this value we now have a rough test of our foreground and background estimates. For example, in G024.05−0.22 we find a total mass of 4100 $M_\odot$ (foreground estimation method A). Using the data in Ragan et al. (2006), we find that the total mass traced by N_2H^+ is 4400 $M_\odot$, providing support for our assumptions. Figure 4.8 shows the relationship between the total clump mass derived from absorption and the total mass derived from our low-resolution maps of N_2H^+ for the eight IRDCs in our sample that were detected in N_2H^+. In general, there is good agreement. We plot a 30% systematic error in the total clump masses (abscissa) and a factor of 5 in for the total N_2H^+ mass estimate (ordinate). In the cases where the estimates

differ, the N_2H^+ mass estimate tends to be greater than the total mass derived from the dust absorption clumps. This discrepancy likely arises in large part from an under-estimation of N_2H^+ abundance and/or non-LTE conditions. All the same, the consistency of the mass estimates, together with the morphological correspondence, reaffirms that the we are probing the dense clumps in IRDCs and that our mass probe is reasonably calibrated.

We find no discernible difference between methods A and B of foreground estimation. However, we note that both are substantially better than assuming no foreground contribution. We therefore believe that method A is an appropriate estimate of the foreground contribution.

Effects of Distance on Sensitivity

Infrared-dark clouds are much more distant than the local, well-studied clouds such as Taurus or ρ Ophiuchus. As such, a clear concern is that the distance to IRDCs may preclude a well-defined census of the clump population. The most likely way in which the our survey is incomplete is the under-representation of low-mass objects due to their relatively small size, blending of clumps along the line of sight, or insensitivity to their absorption against the background. One observable consequence of this effect, assuming IRDCs are a structurally homogeneous class of objects, might be that more distant IRDCs should exhibit a greater number of massive clumps at the expense of the combination of multiple smaller clumps. Another possible effect is the greater the distance to the IRDC, the less sensitive we become to small clumps, and clumps should appear to blend together (i.e. neighboring clumps will appear as one giant clump). Due to this effect, we expect that the most massive clumps of the population will be over-represented. As a test, we examine the distribution of masses and sizes of clumps as a function of IRDC distance, which is shown in Figure 4.9. This sample, with IRDCs ranging in distance from 2.4 to 4.9 kpc away, does not show a strong trend of this nature. We show the detection limit for clumps to illustrate the very good sensitivity of this technique and that while it does impose a lower boundary on clump detectability, most clumps are not close to this value. We found no strong

dependence of clump mass or size on the distance to the IRDC and conclude that blending of clumps does not have a great effect on the mass sensitivity.

Typical low-mass star forming cores range in size from 0.03 to 0.1 pc (Bergin & Tafalla, 2007). If one were to observe such objects 4 kpc, they would only subtend a few arcseconds. For example, if L1544, a prototypical pre-stellar core, resided at the typical distance to the IRDCs in the sample, it would show sufficient absorption (based on reported column density measurements by Bacmann et al., 2000) against the Galactic background, but according to Williams et al. (2006), would subtend $3''$ in diameter at our fiducial 4 kpc distance, which is very close to our detection limit. In addition, very low mass clumps could blended into any extended low-density material that is included in our absorption measurement. These effects should limit our sensitivity to the very low-mass end of our clump mass function.

To first order, we have shown distance is not a major factor because the high-resolution offered by *Spitzer* improves our sensitivity to small structures. However, infrared-dark clouds are forming star clusters and by nature are highly structured and clustered. As such, we can not rule out significant line-of-sight structure. Since independent clumps along the line-of-sight might have distinct characteristic velocities, the addition of kinematical information from high-resolution molecular data (Ragan et al., in prep.) will help the disentanglement.

4.3 Mass Function

4.4 Clump Mass Function of IRDCs

We use the IRDC clump masses calculated in §4.2.2 (using `clumpfind` and foreground estimation method A) to construct an ensemble mass function in Figure 4.10. The mass function that results from using foreground estimation method B is shifted to lower masses by a factor of 2, but the shape is identical. Because IRDCs appear to be in a roughly uniform evolutionary state over the sample (i.e. they are all likely associated with the Molecular Ring, and they possess similar densities and temperatures), we merge all the clumps listed in Appendix D as ensemble and present

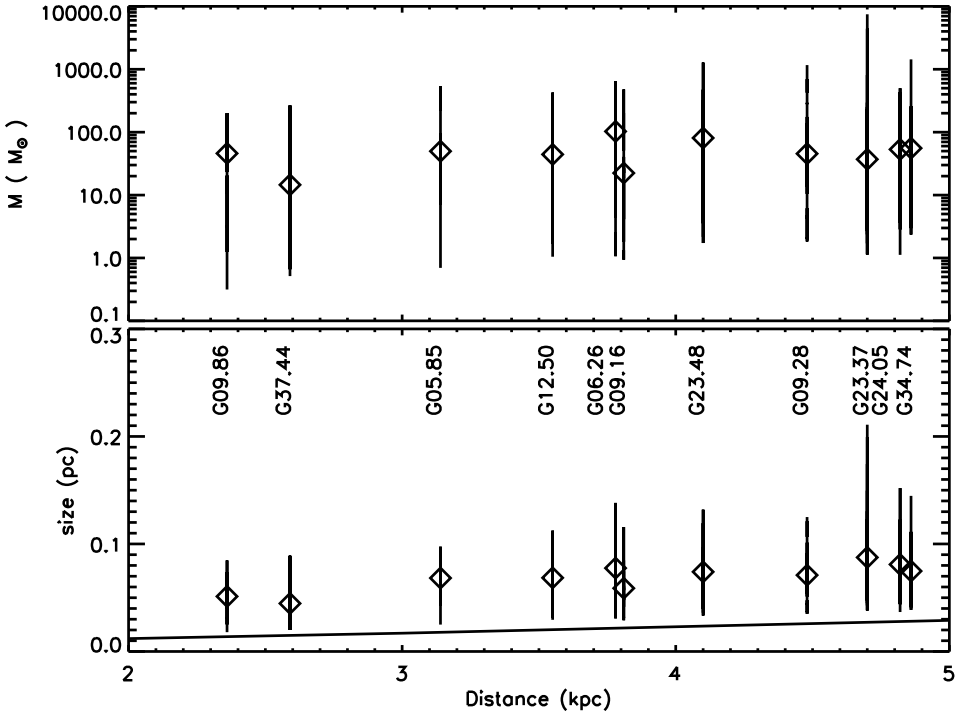

Figure 4.9. Mass and size sensitivity vs. distance. Top: The range in clump mass as a function of distance in kiloparsecs. The median clump mass for each IRDC in the sample is indicated with a diamond. Bottom: The range in clump size as a function of distance. The median clump size for each IRDC in the sample is indicated with a diamond. The resolution limit is plotted as a solid line, and it shows the boundary at which `clumpfind` defines a "clump" for an object at the distance of the indicated host IRDC.

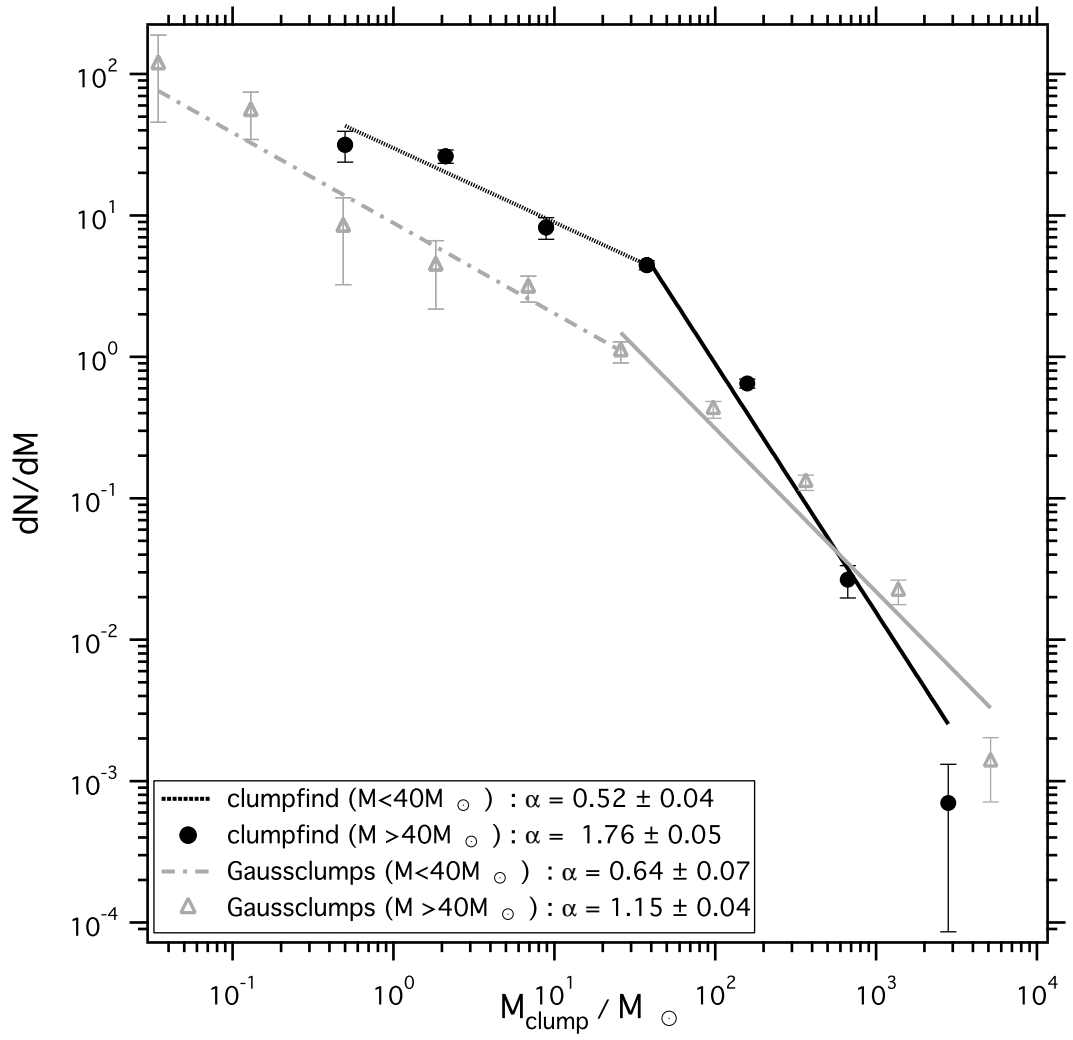

Figure 4.10. IRDC clump differential mass function. All clumps in the 11 IRDC sample are used. Black filled circles indicate results of the `clumpfind` technique, and the green open triangles denote the results of the `gaussclumps` clump-finding method. The fits are broken power laws. On the high-mass end, the slope of the `gaussclumps` method mass function ($\alpha = 1.15 \pm 0.04$) is shallower than the slope of hte `clumpfind` mass function ($\alpha = 1.76 \pm 0.05$).

a single mass function for all the objects at a range of distances. This assumes that the character of the mass function is independent of the distance to a given IRDC. Recall that we see no evidence (see Figure 4.9) for the mass distributions to vary significantly with distance.

For the calculation of the errors in the DMF we have separately accounted for the error in the mass calculation and the counting statistics. We used a method motivated by Reid & Wilson (2005) to calculate the mass error. We have assumed that the clump mass error is dominated by the systematic uncertainty of 30% in the optical depth to mass correction. For each clump we have randomly sampled a Guassian probability function within the 1σ envelope defined by the percentage error. With these new clump masses we have re-determined the differential mass function. This process is repeated 10^4 times, and the standard deviation of the DMF induced by the error in the mass is calculated from the original DMF. This error is added in quadrature to the error introduced by counting statistics. The provided errors are 1σ, with the caveat that the value assumed for the systematic uncertainty is open to debate. As a result, when there are large numbers in a given mass bin, the error is dominated by the mass uncertainty. Conversely, when there are few objects in a mass bin, the error is dominated by counting.

The IRDC clump mass function for this sample spans nearly four orders of magnitude in mass. We fit the mass function with a broken power law weighted by the uncertainties. At masses greater than $\sim 40 M_\odot$, the mass function is fit with a power law of slope α=1.76$\pm$0.05. Below $\sim 40 M_\odot$, the slope becomes much shallower, α=0.52$\pm$0.04. We also include in Figure 4.10 the mass function of clumps found with the `gaussclumps` algorithm, with errors calculated in the identical fashion. Performing fits in the equivalent mass regimes results in a shallower slope for masses greater than $40 M_\odot$ (α=1.15$\pm$0.04), while the behavior at low masses is similar. As discussed in §4.2.2, the clumps found with `clumpfind` and `gaussclumps` are in good agreement in the central region of each IRDC, but tend to disagree on the outskirts. This is a consequence of the failure of `gaussclumps` to model the varying background. Examination of the images reveals that the contribution of the diffuse material varies across

the image, thereby setting the background level too high for outer clumps (where the envelope contributes less) to be detected. In fact, these clumps appear to be preferentially in the 30 to $500M_{\odot}$ range, and a mass function constructed with the `gaussclumps` result is significantly shallower than derived with `clumpfind` (see Figure 4.10). We conclude that `gaussclumps` is not suitable to identify structure away from the central region of the IRDC where the envelope level is below the central level. This is further supported by the wavelet analysis which is capable of accounting for a variable envelope contribution. It is worth noting that for the one IRDC for which we have the wavelet analysis, that the slope of the derived mass function shows little appreciable change and agrees with the `clumpfind` result.

To put the mass function into context with known Galactic star formation, we plot the clump mass function of all clumps in our sample in Figure 4.11 along with the core/clump mass function of a number of other studies probing various mass ranges. We select four studies, each probing massive star forming regions at different wavelengths and resolutions including quiescent cores in Orion (Li et al., 2007), clumps in M17 (Reid & Wilson, 2006), clumps in RCW 106 (Mookerjea et al., 2004), and clumps in massive star formation region NGC 6334 (Muñoz et al., 2007). In their papers, each author presents the mass function in a different way, making it difficult to compare the results directly to one another. Here, we recompute the mass function for the published masses in each work uniformly (including the treatment of errors, see above). Each of the mass functions is fit with a power law. Figure 4.11 highlights the uniqueness of our study in that it spans over a much larger range in masses than any other study to date.

At the high-mass end, the mass function agrees well with the Mookerjea et al. (2004) and Muñoz et al. (2007) studies, which probed to lower mass limits of $30M_{\odot}$ and $4M_{\odot}$, respectively. The fall-off from the steep slope at the high mass end to a shallower slope at the low mass end immediately suggests that completeness, enhanced contribution from the envelope and/or clump blending become an issue. However, the slope at the low mass end compares favorably with Li et al. (2007) and Reid & Wilson (2006) which probe mass ranges 0.1 to $46M_{\odot}$ and 0.3 to $200M_{\odot}$, respectively.

In addition to the general DMF shape at both the high mass and low mass end, the "break" in the mass function falls in the $10M_{\odot}$ to $50M_{\odot}$ range for the ensemble of studies, including ours. If this is a real feature of the evolving mass spectrum, this can shed some light on the progression of the fragmentation process from large, massive objects to the numerous low-mass objects like we see in the local neighborhood. The characteristic "break" mass can also be a superficial artifact of differences in binning, mass determination technique, and observational sensitivity. Our study is the only one that spans both mass regimes, and further such work is needed to explore the authenticity of this feature. However, we speculate that this may be an intrinsic feature.

It is possible that the slope of the IRDC clump mass function might be an artifact of a limitation in our technique. With the great distances to these clouds, one would expect the effect of clump blending to play a role in the shape of their mass spectrum. We have shown in § 4.2.4 that distance does not dramatically hinder the detection of small clumps. Our study samples infrared-dark clouds from 2.4 kpc to 4.9 kpc, and we find that the number of clumps does not decrease with greater distance, nor does the median mass tend to be be significantly greater with distance. Furthermore, with the present analysis, we see no evidence that including clumps from IRDCs at various distances affects the shape of the mass function.

From past studies of local clouds there has been a disparity between mass function slope derived with dust emission and CO (e.g. compare Johnstone et al., 2001; Kramer et al., 1998). Our result suggests that massive star forming regions have mass functions with slope in good agreement with CO isotopologues, e.g. α=1.8. This is crucial because CO observations contain velocity information, which allow for the clumps to be decomposed along the line-of-sight. Still, the authors find a shallow slope in agreement with ours. We conclude that clump blending, while unavoidable to some extent, does not skew the shape of the mass function as derived from dust emission or absorption. A close look at Kramer et al. (1998) results finds that the majority of objects studied are massive star formation regions. Given the general agreement of the clump mass function of this sample of IRDCs with other studies of

massive star formation regions, we believe this result represents the true character of these objects, not an artifact of the observing technique.

Several studies of pre-stellar cores in the local neighborhood show a mass distribution that mimics the shape of the stellar IMF. That the slope of the mass function in infrared-dark clouds is considerably shallower than the stellar IMF should not be surprising. The masses we estimate for these clumps are unlikely to give rise to single stars. Instead, the clumps themselves must fragment further and eventually form a star cluster, likely containing multiple massive stars. Unlike Orion A, for example, which contains $\sim 10^4$ $M_\odot$ distributed over a 380 square parsec (6.2 square degrees at 450 pc) region (Carpenter, 2000), in IRDCs, a similar amount of mass is concentrated in clumps extending only a 1.5 square parsec area. Therefore, we posit that IRDCs are not distant analogues to Orion, but more compact complexes capable of star formation on a more massive scale.

Given the high masses estimated for infrared-dark clouds, yet the lack evidence for the massive stars they must form is perhaps indicating that we see them necessarily *because* we are capturing them just before the onset of star formation. Such a selection effect would mean that we preferentially observe these dark objects because massive stars have yet to disrupt their natal cloud drastically in the process of protostar formation.

4.4.1 The Contribution from the IRDC Envelope

Like nearby clouds, infrared-dark clouds are structured hierarchically, consisting of dense condensations embedded in a more diffuse envelope. Here we present various attempts to estimate the fraction of the total cloud mass resides in dense clumps compared to the extended clouds. First, we use archival ^{13}CO data to probe the diffuse gas and use it to estimate the envelope mass. To further explore the contribution of the envelope, we demonstrate that a wavelet analysis, a technique designed to remove extended structures from emission maps, gives a similar relationship between envelope and dense clump mass. Alternatively, applying the `gaussclumps` algorithm to the data provides an average threshold that describes the diffuse structure.

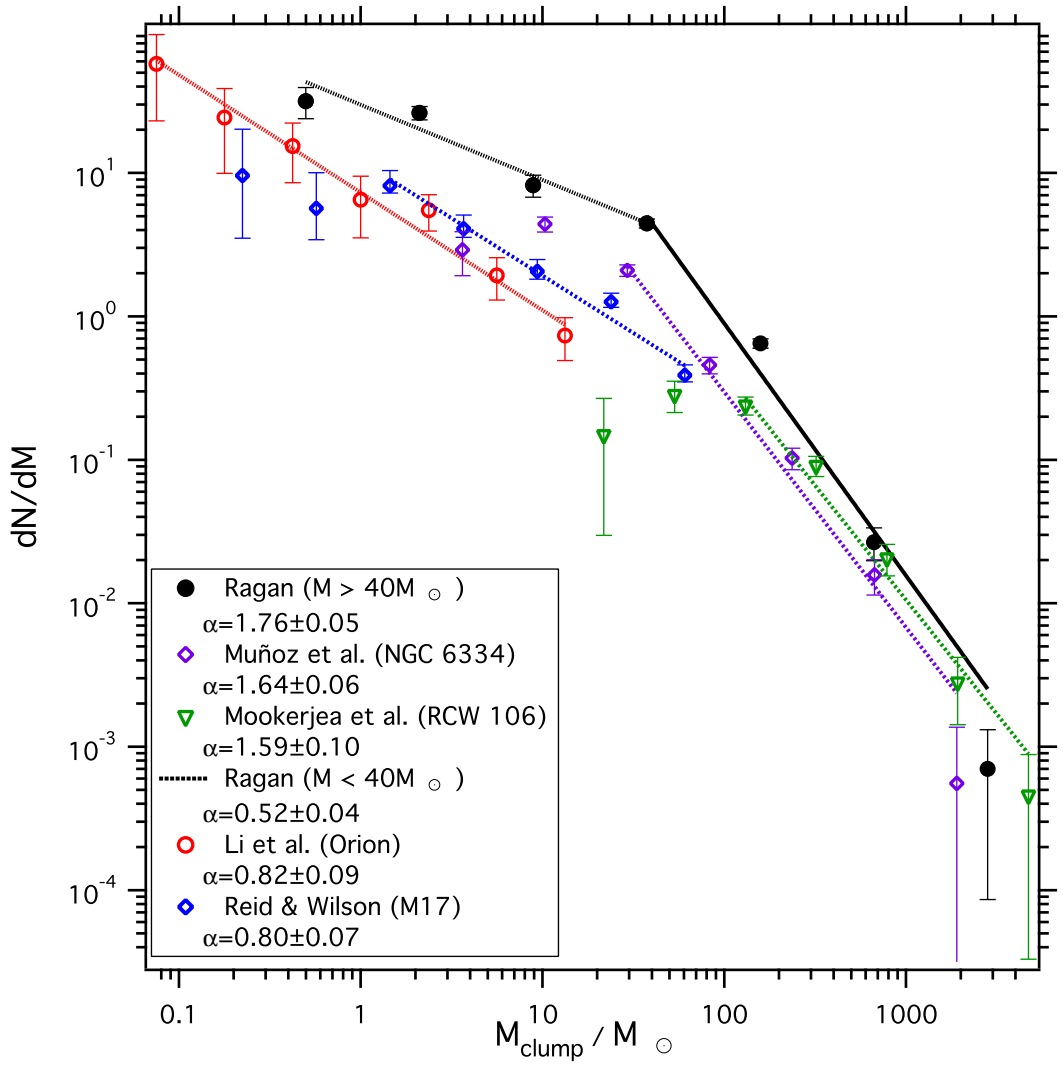

Figure 4.11. Differential Mass Function Comparison with Literature. This ensemble IRDC clump sample (black filled circles) fit with a single power-law for $M_{clump} > 30M_{\odot}$ ($\alpha = 1.76 \pm 0.05$) compared with various star formation regions in the high mass regime and their respective single power-law fit slopes. At the high mass end, our fit agrees well with that of other studies: *Open purple diamonds* from Muñoz et al. (2007) ($\alpha = 1.64 \pm 0.06$); *Open green inverted triangles* from Mookerjea et al. (2004) ($\alpha = 1.59 \pm 0.10$). At the low mass end, we fit a second power law for the bins with $M_{clump} < 30M_{\odot}$ ($\alpha = 0.52 \pm 0.04$), which agrees well with other studies in this mass regime: *Open blue diamonds* from Reid & Wilson (2006) ($\alpha = 0.80 \pm 0.07$); *Open red circles* from quiescent Orion cores from Li et al. (2007)($\alpha = 0.82 \pm 0.09$). Note that only this study spans the entire range of masses, so the reality of the apparent break at $\sim 30M_{\odot}$ is in question.

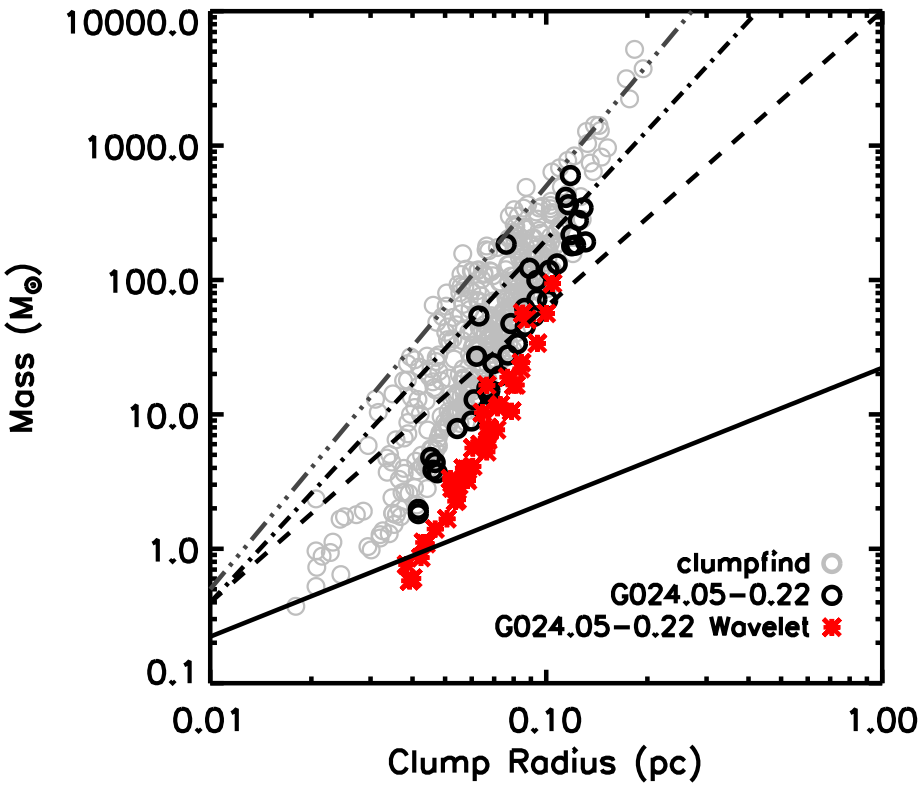

Figure 4.12. IRDC clump mass-radius relation. `clumpfind` clumps (foreground method A) in the entire sample of IRDCs (gray) plotted with the clumps found only in G024.05−0.22 highlighted in black, and the clumps found in the wavelet subtracted image (red). The solid line denotes the critical Bonnor-Ebert mass-radius relation for $T_{internal}$=15 K. The dashed line is the $M \propto R^{2.2}$ from the Kramer et al. (1996) CO multi-line study of Orion. The dash-dotted line is taken from Williams et al. (1994), which finds $M \propto R^{2.7}$, and the top-most dashed-three-dotted line is a constant density relation ($M \propto R^3$).

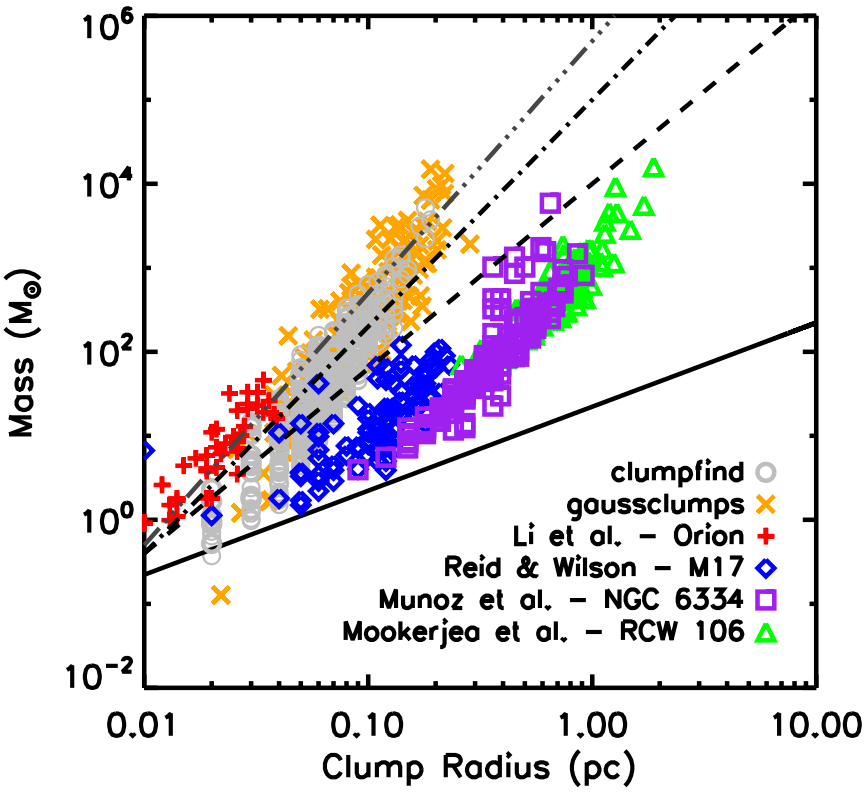

Figure 4.13. IRDC clump mass-radius relation comparison with literature. The same relationships are plotted with the lines described in Figure 4.12. We compare the IRDC mass-radius relation with all the studies of massive star forming regions included in Figure 4.11, with the same corresponding colors, indicated in the legend.

We use ^{13}CO (1-0) molecular line data from the Galactic Ring Survey (Jackson et al., 2006) in the area covered by our *Spitzer* observations of G024.05−0.22 to probe the diffuse material in the field. The ^{13}CO emission is widespread, covering the entire area in the IRAC field, thus we are not probing the entire cloud. Assuming local thermodynamic equilibrium (LTE) at a temperature of 15 K and a ^{13}CO abundance relative to H_2 of 4×10^{-6} (Goldsmith et al., 2008), we find that the the clump mass is ∼20% of the total cloud mass. This demonstrates that IRDCs are the densest regions of much larger molecular cloud complexes; however, the fraction of mass that we estimate the clumps comprise relative to the cloud is an upper limit because the full extent of the cloud is not probed with these data.

In §4.2.3, we discuss two ways in which we account for the envelope in the clump-finding process. First, the `gaussclumps` algorithm is an alternative method of identifying clumps, and in §4.4 we examine the effect this method has on the clump mass function. The algorithm is insensitive to clumps on the outskirts of the IRDC, thereby flattening the mass function. While `gaussclumps` may oversimplify the structure of the envelope for the purposes of identifying clumps, it does provide a envelope *threshold*, above which optical depth peaks fit as clumps and below which emission is subtracted. This threshold approximates the level of the envelope, and as a result, `gaussclumps` finds 15-50% of the optical depth level is from the diffuse envelope. The wavelet subtraction technique results in clumps that are on average 90% less massive and smaller in size by 25% (∼0.02 pc) than those extracted from the unaltered map.

These analyses of the IRDC envelope show us that our technique is only sampling 20-40% of the clouds total mass and, at the same time, the clump masses themselves include a contribution from the surrounding envelope. Because of these factors, the different methods for isolating "clumps" have varying levels of success. For example, using `gaussclumps` equips us to parametrically remove the envelope component to the clump, but due to the underlying assumption of the baseline level, it misses many clumps that `clumpfind` identifies successfully. The mass function that results from using the `gaussclumps` method is shallower than that from `clumpfind`, as `gaussclumps` fails to find clumps on the periphery of the dominant (often central)

concentration of clumps, where the envelope level is lower.

While both the `clumpfind` and `gaussclumps` methods have their drawbacks, it is clear that IRDCs have significant structure on a large range of scales. The relatively shallow mass function for IRDC clumps and other massive star forming regions shows that there is a great deal of mass in large objects, and future work is needed to understand the detailed relationship between the dense clumps and their surroundings.

4.4.2 Mass-Radius Relation

Next we investigate the relationship between the mass and size of the clumps found in IRDCs, which informs us of the overall stability of the clump structures. Figure 4.12 shows the mass-radius relationship of the `clumpfind`-identified clumps, highlighting the results for G024.05−0.22 and the wavelet-subtracted case. Indeed, the clumps extracted from the wavelet-subtracted map are shifted down in mass by 90% and down in size by 25%, but the relationship between the quantities does not change.

As a means of understanding the clump nature in this fashion, we plot a number of relations from the literature for comparison. First, we note that many of the clumps may lie at the density threshold of our observations, thus a constant density relationship ($M \propto R^3$) might hold. We also plot the relation of simple self-gravitating Bonnor-Ebert spheres ($M\ (R)\ =\ 2.4Ra^2/G$, where a is the sound speed and set to 0.2 km s^{-1}, solid line) and also the mass-radius relationship observed in a multi-line CO survey of Orion ($M \propto R^{2.2}$, Kramer et al., 1996, (dashed line)). For comparison, Figure 4.12 also shows these properties from the other studies of massive star formation regions. We note that the spatial resolution of the comparison studies is larger than the resolution of this study. The relationship for Orion (Li et al., 2007), M17 (Reid & Wilson, 2006), NGC 6334 (Muñoz et al., 2007) and RCW 106 (Mookerjea et al., 2004) all agree with the Kramer et al. (1996) relationship, which is consistent with the mass function agreement to CO studies (see §4.4).

The IRDC clumps are likely gravitationally unstable, showing higher densities than their local Bonnor-Ebert sphere counterparts and exhibiting large velocity dispersions (Chapter 5). The relationship for clumps in IRDCs shows a steeper trend,

one closer to the Williams et al. (1994) relationship, $M \propto R^{2.7}$. Also, dust extinction at 8 μm has greater sensitivity to high-densities than CO, which is known to freeze out at extreme densities. Hence, while the IRDC clumps are clearly Jeans unstable, the slope of the relation may be simply a reflection of the different mass probe used here.

4.5 Summary

The *Spitzer Space Telescope* affords us the ability to probe a spatial regime of massive clouds in the Galactic Ring at comparable resolution as has been applied to the numerous studies of local, low-mass star formation. In this way, we extend the frontier of detailed star formation studies to include regions the likes of which are not available in the solar neighborhood. This study demonstrates a powerful method for characterizing infrared-dark clouds, the precursors to massive stars and star clusters. IRDCs provide a unique look at the initial conditions of star formation in the Galactic Ring, the dominant mode of star formation in the Galaxy.

We present our method of probing mass in IRDCs using dust absorption as a direct tracer of column density. We perform the analysis using two different assumptions (methods A and B) for the foreground contribution to the 8 μm flux. The IRDC envelope contribution to the To validate our method in the context of others, we compare and find good agreement between the 8 μm absorption and other tracers of dust, such as sub-millimeter emission from dust grains measured with SCUBA and N_2H^+ molecular line emission measured with FCRAO and BIMA. We show that distance does not play a role in the effectiveness of the technique. The high resolution *Spitzer* observations allows us to probe the absorbing structures in infrared-dark clouds at sub-parsec spatial scales. We apply the `clumpfind` algorithm to identify independent absorbing structures and use the output to derive the mass and size of the clumps. Tens of clumps are detected in each IRDC, ranging in mass from 0.5 to a few $\times$ 10^3 $M_\odot$ with sizes from 0.02 to 0.3 pc in diameter. We also apply the `gaussclumps` algorithm to identify clumps. The structures in the central region of the IRDC correspond almost perfectly to the `clumpfind` result, but `gaussclumps` misses clumps

on the outskirts because it fails to account for a spatially variable background level.

On average, 25% of clumps are in the vicinity of stars and ∼10% are in near YSOs, which are the most likely sources to be associated with the infrared-dark cloud. Most of the mass is not associated with any indicator of star formation. This leads us to conclude that IRDCs are at in earlier stage than, say, the nearest example of massive star formation, the Orion Nebula, and these results are powerful clues to the initial conditions of star cluster formation. Further studies are needed, however, to fully characterize the stellar content of IRDCs.

Infrared-dark clouds exhibit significant substructure on scales from 0.5 $M_{\odot}$ to 10^3 $M_{\odot}$, which points to the fragmenting nature of these objects. The typical densities – in excess of 10^5 cm^{-3} – and temperatures – less than 20 K – place these objects in the regime of massive star formation regions, though they appear to be at a very early stage of this process. The IRDC clump mass function has a slope of $\alpha = 1.76 \pm 0.05$ for masses greater than ∼40 $M_{\odot}$, which is in agreement with studies of other massive star forming regions. Despite the similarity in slope, IRDCs are distinct from other massive star-forming regions, such as Orion or the larger complex W49, in that they contain many time the amount of mass in a fraction of the volume. At masses lower than 40 $M_{\odot}$, we find a shallower slope to the mass function ($\alpha = 0.52 \pm 0.04$), which may be due to incompleteness or it reflects a transition between clustered and more distributed star formation (Adams & Myers, 2001).

Just as in all surveys of IRDCs to date, this study is subject to the blending of clumps, which could alter the shape of the mass function to over-represent the most massive clumps at the expense of clumps of all masses and sizes. To the extent that this sample allows, we find that this does not drastically effect the shape of the mass function. Other studies of cloud fragmentation that have the advantage of a third dimension of information also find a shallower clump mass function slope (Kramer et al., 1998). We therefore conclude that this result is a true reflection of IRDC structure and nature of massive star formation. The massive clumps will eventually give rise to massive stars and clusters depending on the fragmentation mechanisms and sources of clump support. It is likely that the *most* massive clumps will fragment

further, which would effectively steepen the mass function. It is worth noting that the embedded cluster mass function (Lada & Lada, 2003) or that of star clusters in the Large and Small Magellanic Clouds (Hunter et al., 2003) has a slope of $\alpha \sim 2$, which supports the steepening mass function paradigm. Within clusters (on smaller scales) the clumps will fragment further, steepening the mass function even more, eventually resembling the core mass function seen locally (e.g. Alves et al., 2007).

CHAPTER 5

HIGH RESOLUTION NH_3 OBSERVATIONS IN IRDCs

We present observations of NH_3 (J, K) = (1,1) and (2,2) inversion transitions towards a sample of six infrared-dark clouds selected from our *Spitzer* observations. We conducted our survey using combined data from the Very Large Array (VLA) and Green Bank Telescope (GBT). The high-resolution of these observations allow detailed study of the the chemistry, kinematics and mass structure on the core size-scale. We find the distribution of ammonia follows the dust absorption structure seen in the *Spitzer* 8 μm band. These observations give a reliable measure of the gas temperature in IRDCs at very high-resolution such that the effects on small scales are not washed out by beam dilution, as would be the case in single-dish studies.

5.1 Molecular Observations in IRDCs

Molecular surveys have been key pathfinders in understanding the physical and chemical conditions surrounding star formation, and in infrared-dark clouds. Large-scale single-dish surveys (e.g. Ragan et al., 2006; Simon et al., 2006b; Sakai et al., 2008; Du & Yang, 2008) have helped confirm IRDC candidates from infrared studies, establish distances, and determine gross properties. Another approach has been a detailed chemical study of individual infrared-dark cloud cores (e.g. Rathborne et al., 2008), which has begun to uncover the complex chemistry and dynamics in dense, high-mass cores before and following the formation of protostars. A final approach that has been undertaken over the past few years has been the *mapping* of IRDCs in continuum emission (Rathborne et al., 2006) and molecular lines (Pillai et al., 2006a).

These studies have finally begun to help place IRDCs in a broader context examining their structure and overall internal conditions. In this study, we highlight the usefulness of molecular lines in determining the structure, kinematics, temperature and chemical composition of dense gas.

A key molecule used to trace gas in local clouds has been ammonia (Wiseman & Ho, 1998; Jijina et al., 1999; Rosolowsky et al., 2008; Friesen et al., 2009). Ammonia was the first polyatomic molecule detected in the ISM (Ho & Townes, 1983). A symmetric top molecule, NH_3 is a valuable tool in many astronomical arenas because of its sensitivity to a broad range of excitation conditions. In the case of infrared-dark clouds, ammonia has been observed in its ground state vibrational inversion transitions, mainly the lower metastable states, $(J, K) = (1,1)$ and $(2,2)$, which are excited at the characteristically low (< 20 K) temperatures of IRDCs. The splitting of the inversion transitions into hyperfine structure, due to the interaction between the N nucleus' electric quadrupole moment and the electric field of the electrons, allows for the calculation of optical depth, column density, and gas temperature.

Pillai et al. (2006a), the first to map ammonia in IRDCs, confirmed that they were cold (10 K $<$ 20 K) and dense ($n > 10^5$ cm^{-3}) objects, and noted that IRDCs are comprised of a few distinct regions. However, as shown in Chapter 4, IRDCs are comprised of many tens of clumps, typically on spatial scales of a few arcseconds, which would not have been resolved with the single-dish observations (resolution $\approx 30''$) made in Pillai et al. (2006a). In the following Chapter, we present high-resolution NH_3 (1,1) and (2,2) inversion line transition observations with the Very Large Array (VLA) (supplemented with Green Bank Telescope (GBT) maps) of six IRDCs which confirm the structure detected in our *Spitzer* observations (Ragan et al., 2009), and we characterize the gas properties on these small ($\sim 5''$) spatial scales for the first time in IRDCs.

Our VLA sample was selected to include objects of a variety of morphologies and environments (as characterized in Chapter 4), and it also spans over 2 kpc in distance, so resolution effects can be examined. Where previous surveys find general homogeny in IRDCs, the superior resolution of the VLA shows that IRDCs are a kinematically

and structurally diverse.

5.2 Observations & Data Reduction

5.2.1 Green Bank Telescope

We acquired single-dish observations of NH_3 (J, K) = (1,1) and (2,2) inversion lines using the Robert C. Byrd Green Bank Telescope (GBT) from 6 to 15 September 2006. The rest frequencies of the (1,1) and (2,2) lines are 23.6944955 and 23.7226336 GHz (Ho & Townes, 1983), respectively. These upper K-band observations were made in frequency-switching mode. The GBT spectrometer back end was configured to simultaneously observe the two transitions, using ∼32,000 spectral channels in each IF that were 50 MHz wide. The spectral resolution for the (1,1) line was 0.03 km s^{-1}, or 1.6 kHz.

We mapped the regions using a single-pointing grid with Nyquist sampling. Table 5.1 summarizes the coordinates, LSR velocities, and map sizes for each IRDC and the date on which the observation was performed. Integration times were 2-3 minutes per point, depending on the strength of the line, elevation of the source, and thus the time required to obtain the desired S/N. Pointing corrections were done toward various calibrators (see Table 5.1) every 45 to 75 minutes, weather-depending, which resulted in corrections of a few arcseconds, typically. Typical system temperatures were between 60 and 100 K over the entire run, and the elevation of the sources was between 20 and 40 throughout the run.

Data were reduced and calibrated using GBTIDL. The frequency-switched observations were reduced with the `getfs` routine, which retrieves, calibrates and plots the spectrum. We then applied `hanning` smoothing and then `boxcar` smoothing over 50 channels. Five of the spectral components of the NH_3 signature were always spectrally resolved, and we performed gaussian fitting on each hyperfine component. The data were then put into a FITS data cube using a homemade IDL-based script.

Table 5.1. GBT Observation Summary. IRDC targets, positions and dates of observation.

IRDC name	α (J2000)	δ (J2000)	v_{lsr} (km s^{-1})	Map size ($' \times '$)	Pt. Source Calibrator	Observation date
G005.85−0.23	17:59:53	−24:00:10	17.2	9 × 6	1733−1304	14 September 2006
G009.28−0.15	18:06:54	−20:58:51	41.4	9 × 7	1814−1853	15 September 2006
G009.86−0.04	18:07:40	−20:25:25	18.1	9 × 7	1733−1304	15 September 2006
G023.37−0.29	18:34:51	−08:38:58	78.5	5 × 6	1831−0949	11 September 2006
G024.05−0.22	18:35:52	−08:00:38	81.4	5 × 5	1822−0938	6 September 2006
G034.74−0.12	18:55:14	+01:33:42	79.1	7 × 5	1851+0035	7 September 2006

5.2.2 Very Large Array

Observations of the NH_3 (1,1) and (2,2) inversion transitions were undertaken of the sample in the compact D configuration of the Very Large Array (VLA) over the course of three tracks in 2007 April. Table 5.2 summarizes the observations. At this time, the array consisted of a hybrid of VLA and the updated EVLA receivers, thus improving the sensitivity.

These K-band observations were made using a four IF correlator backend configured with 3.125 MHz bandwidth containing 64 channels, yielding a spectral resolution of 48.828 kHz, or 0.6 km s^{-1}. This setup was selected as to ensure detection of relatively weak lines in IRDCs, both the (1,1) and (2,2) simultaneously, with enough spectral resolution to resolve the lines. Table 5.2 gives the target, pointing and sensitivity information for each IRDC. Bandpass and calibration were done with observations of 1331+305.

Because of the hybrid array used in these observations, it was not possible to implement Doppler tracking during the tracks, and because ammonia lines in IRDCs are so broad, we were unable to fit all of the hyperfine components in the band. In the following calculations, most quantities rely on the ration between the main line (which was always detected) and either a satellite line in the (1,1) spectrum (for optical depth) or the (2,2) main line (for temperature). For the calculation of the integrated intensity, we used the optical depth derived from the ration of the inner satellite lines to the main line to estimate the intensity of the outer satellite line, and integrated over the modeled spectrum. In cases of optically thick lines, this method breaks down, as does the subsequent calculations.

Table 5.2. VLA Observation Summary. IRDC targets, positions and dates of observation.

IRDC name	α (J2000)	δ (J2000)	v_{lsr} (km s^{-1})	Phase Calibrator	rms (mJy/bm)	Observation date
G005.85−0.23	17:59:53	−24:00:10	17.2	1833−210	2.8	16 April 2007
G009.28−0.15	18:06:54	−20:58:51	41.4	1833−210	4.8	19 April 2007
G009.86−0.04	18:07:40	−20:25:25	18.1	1833−210	4.3	19 April 2007
G023.37−0.29	18:34:51	−08:38:58	78.5	1832−105	2.5	16 April 2007
G024.05−0.22	18:35:52	−08:00:38	81.4	1832−105	4.3	11 April 2007
G034.74−0.12	18:55:14	+01:33:42	79.1	1851+005	6.8	11 April 2007

5.2.3 Single-dish and Interferometer Data Combination

The detectable size of structures has an upper limit when using an interferometer, which is set by the shortest spacing between two antennas in the array. Any flux on scales larger than this upper limit will be missing from the final image, a phenomenon known as the short-spacing problem. Because IRDCs are complex structures, with emission on all scales, it is necessary to recover any large scale emission by combining the interferometer data with single-dish observations at the same frequency. The 100-meter Green Bank Telescope offers the perfect complement to our D array observations with the Very Large Array.

First, the GBT were scaled and regridded to match the resolution of the VLA data. Using the MIRIAD task `IMMERGE`, the deconvolved interferometer images were combined in the Fourier domain with the GBT images. `IMMERGE` uses a tapering function which weights short spacings higher than long spacings. Using an annulus ranging from 30 to 70 meters, where the high and low resolution images overlap, we ensure accurate determination of the flux calibration factor. This method was applied to the (1,1) and (2,2) datasets independently, yielding images of the same spatial and velocity resolution as the VLA image.[1]

5.3 Analysis & Results

In this section, we present the spectral moment maps (i.e. the integrated NH_3 (1,1) intensity maps, centroid velocity maps, line FWHM maps) for each IRDC. We then describe the methods by which we attain physical characteristics of the IRDCs, which

[1]This method was in large part developed with the help of Rachel Friesen.

are discussed in Section 5.4. Overall, for all sources in the sample, the NH_3 intensity follows the absorption seen at 8μm with *Spitzer* extremely well. We discuss the relationship between the mid-infrared data and velocity field also in Section 5.4.

5.3.1 Optical Depth

In order to understand the physical conditions within IRDCs, we must first compute the optical depth of the NH_3 line and the column density. Optical Depth of the NH_3 (1,1) line, as given by Equation 1 in Ho & Townes (1983), is

$$\frac{\Delta T_a(J,K,m)}{\Delta T_a(J,K,s)} = \frac{1 - e^{-\tau(J,K,m)}}{1 - e^{-a\tau(J,K,m)}} \tag{5.1}$$

where the left hand side is the ratio of the intensities of the main and satellite lines in the NH_3 (1,1) signature, and a is the ratio of the intensities compared with the main line intensity. With measurements of ΔT_a for the main line and the two inner satellite lines (for which $a = 0.28$), one can solve for τ numerically. For the bulk of the IRDC, we derive a $\tau(1,1,m) > 1$, but for the most part < 10, except in G023.37−0.29, where the hyperfine lines become saturated.

5.3.2 Spectral Moments

In Figures 5.1 through 5.6 we present the moments of the NH_3 (1,1) spectrum. The sources show a wide breadth of features. In G005.85−0.23 and G024.05−0.22, the peaks in integrated intensity do not correspond to 24 μm point sources, nor do they have any enhancements in linewidth. In G023.37−0.29 and G034.74−0.12, the integrated intensity peaks are at positions where *Spitzer* MIPS 24 μm observations reveal point sources. At each of these positions (one in G023.37−0.29 and two in G034.74−0.12) the linewidth is enhanced. G009.28−0.15 has integrated intensity peaks of both types: one with a 24 μm source and linewidth enhancements, and one without either. In G009.86−0.04, the numerous 24 μm sources in the field, which appear clearly associated with the IRDC in the *Spitzer* data, do not correspond to integrated intensity peaks nor line width enhancements. We summarize the moments overall and at the integrated intensity peaks, in Table 5.3.

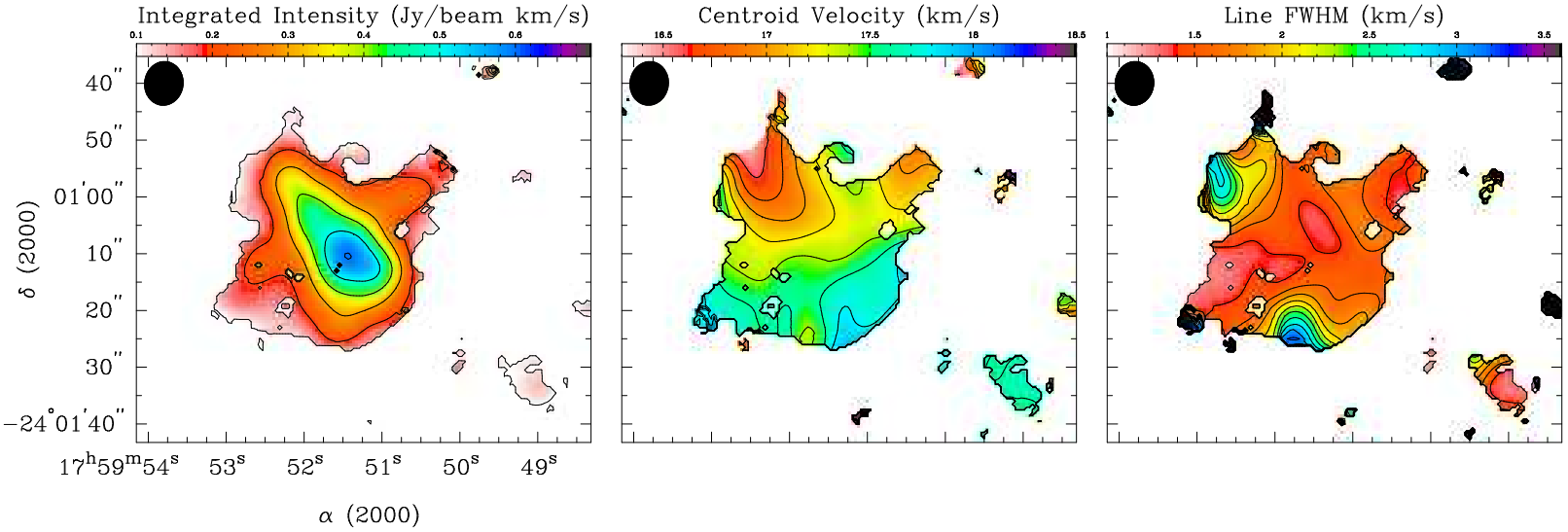

Figure 5.1. Spectral moments in G005.85−0.23. Left panel: Integrated Intensity in units of Jy beam^{-1} kms^{-1}. Center panel: Centroid Velocity in km s^{-1}. Right panel: FWHM of central line in km s^{-1}. The VLA beam for this mosaic is plotted in the upper-left corner.

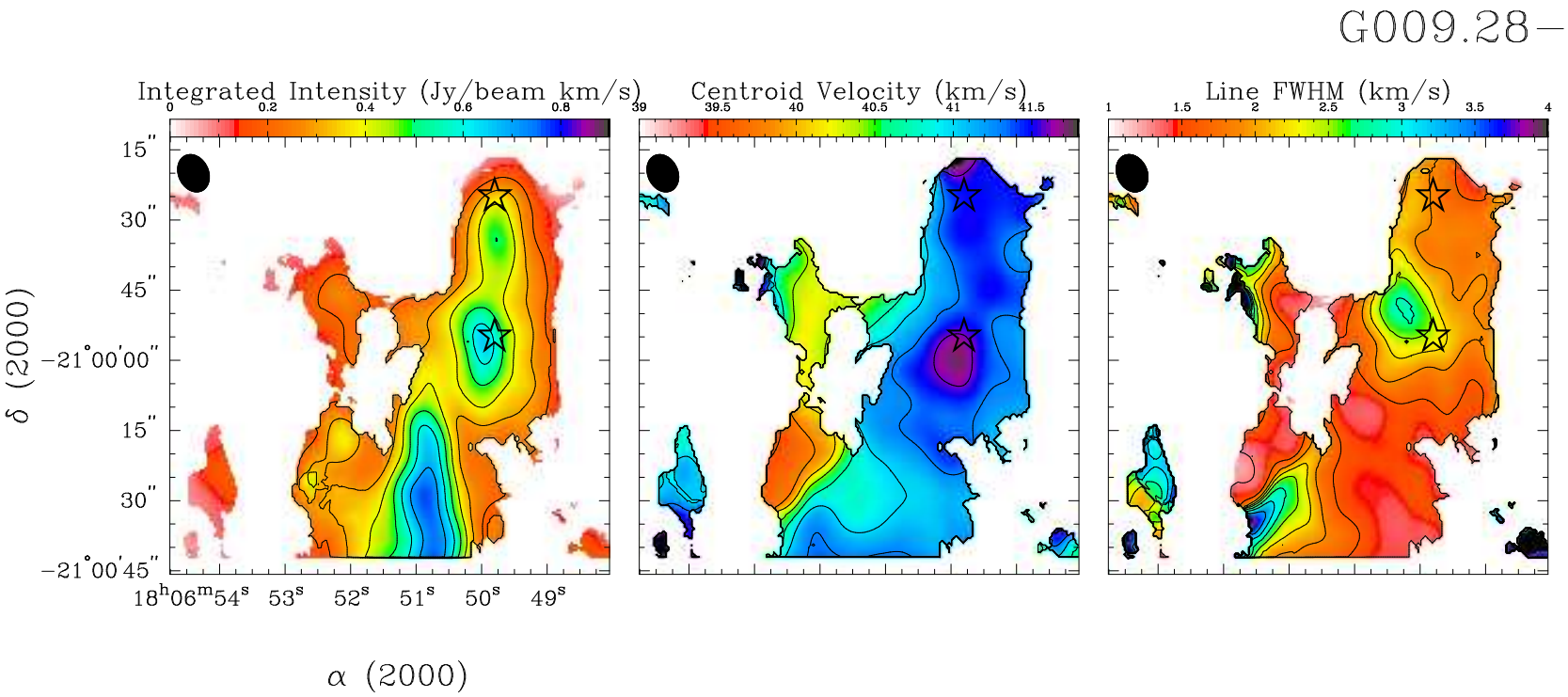

Figure 5.2. Spectral moments in G009.28−0.15. Left panel: Integrated Intensity in units of Jy beam^{-1} kms^{-1}. Center panel: Centroid Velocity in km s^{-1}. Right panel: FWHM of central line in km s^{-1}. Stars indicate where there are MIPS 24 μm sources. The VLA beam for this mosaic is plotted in the upper-left corner.

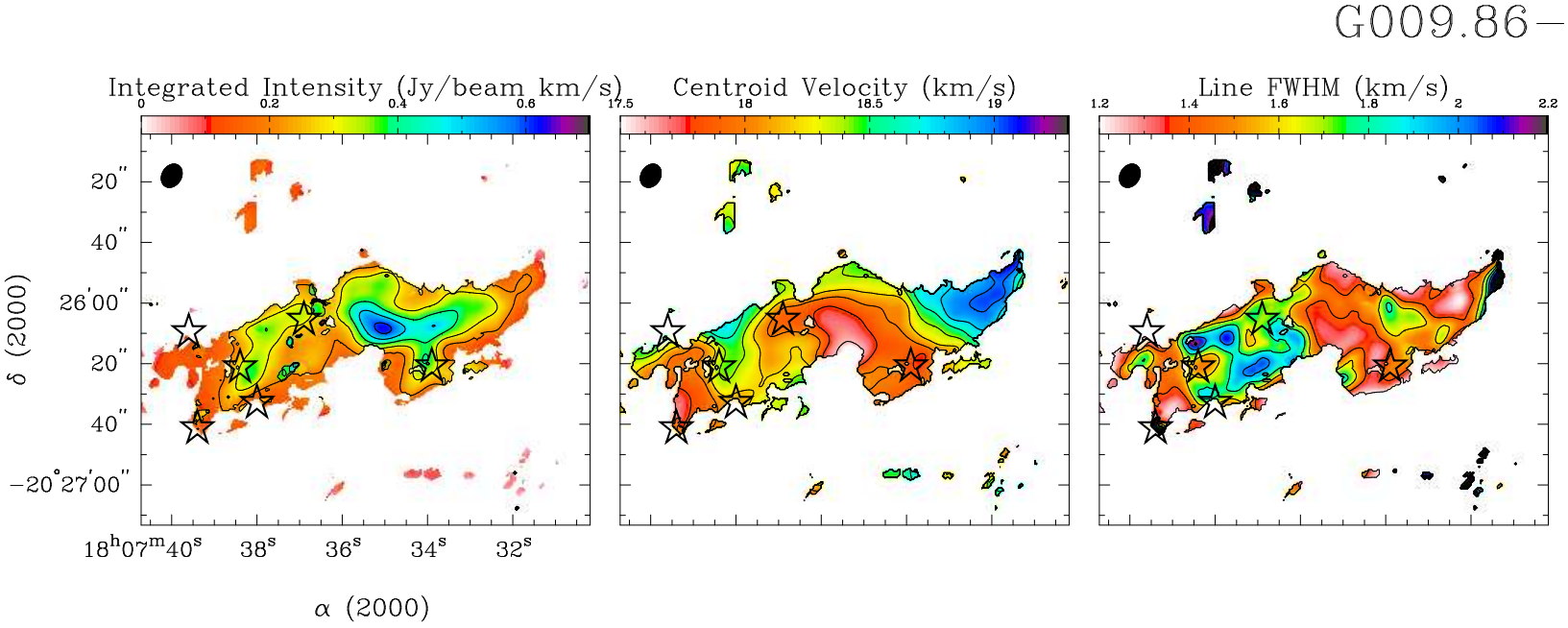

Figure 5.3. Spectral moments in G009.86−0.04. Left panel: Integrated Intensity in units of Jy beam^{-1} kms^{-1}. Center panel: Centroid Velocity in km s^{-1}. Right panel: FWHM of central line in km s^{-1}. The VLA beam for this mosaic is plotted in the upper-left corner.

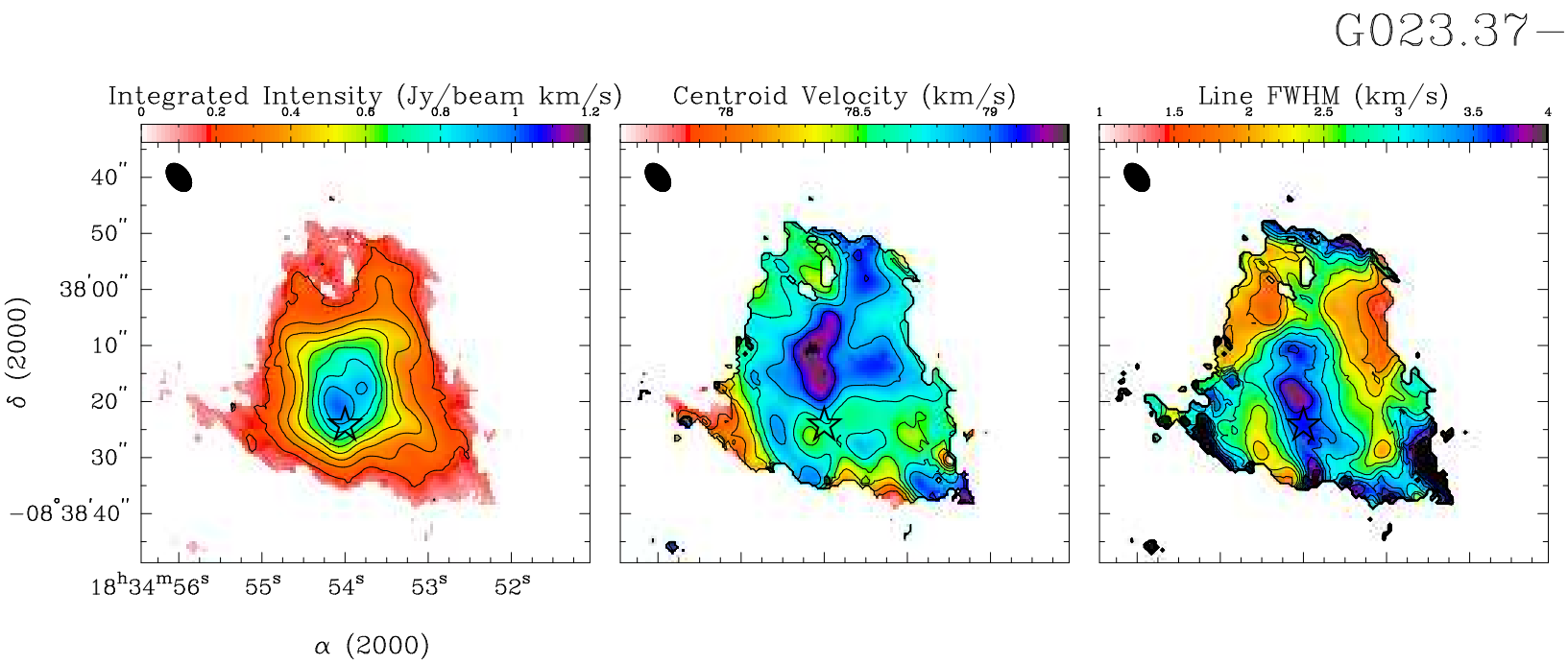

Figure 5.4. Spectral moments in G023.37−0.29. Left panel: Integrated Intensity in units of Jy beam^{-1} kms^{-1}. Center panel: Centroid Velocity in km s^{-1}. Right panel: FWHM of central line in km s^{-1}. Stars indicate where there are MIPS 24 μm sources. The VLA beam for this mosaic is plotted in the upper-left corner.

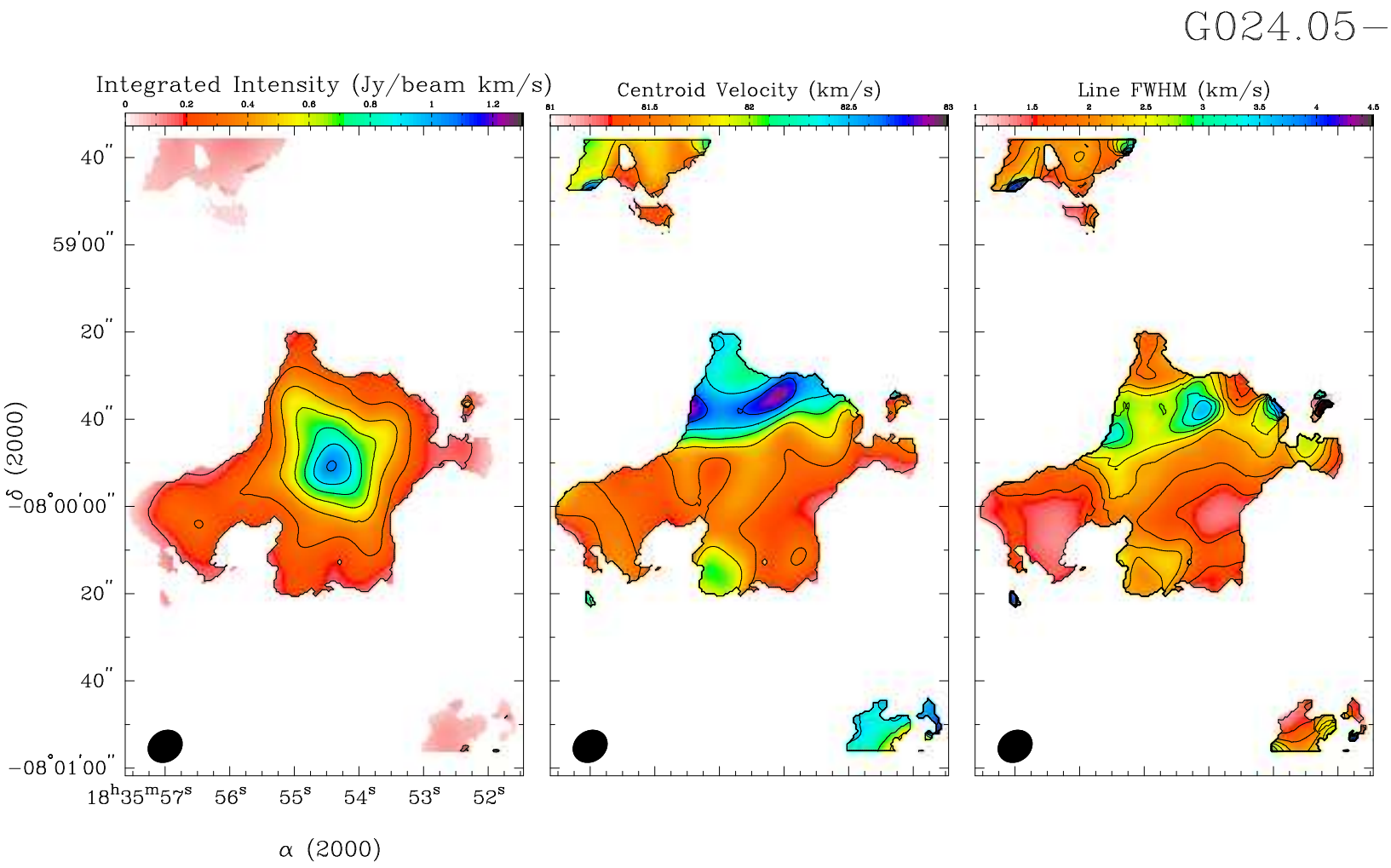

Figure 5.5. Spectral moments in G024.05−0.22. Left panel: Integrated Intensity in units of Jy beam^{-1} kms^{-1}. Center panel: Centroid Velocity in km s^{-1}. Right panel: FWHM of central line in km s^{-1}. The VLA beam for this mosaic is plotted in the lower-left corner.

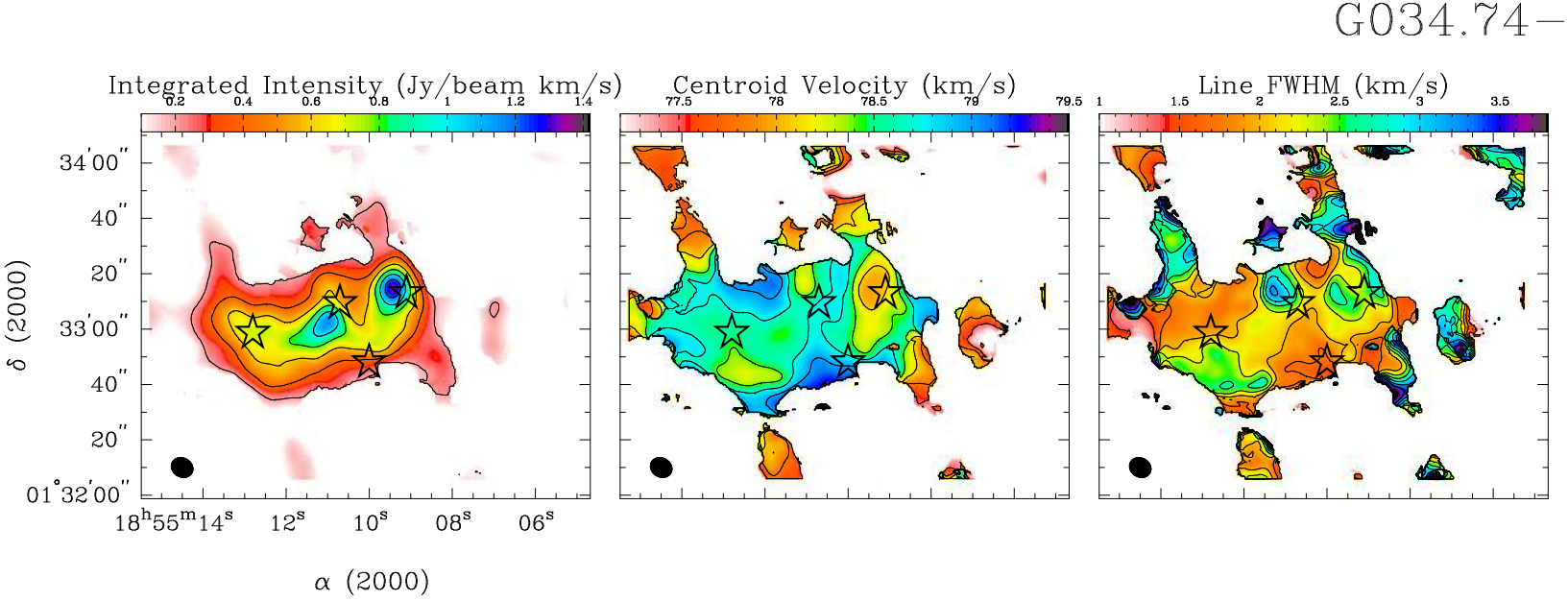

Figure 5.6. Spectral moments in G034.74−0.12. Left panel: Integrated Intensity in units of Jy beam^{-1} kms^{-1}. Center panel: Centroid Velocity in km s^{-1}. Right panel: FWHM of central line in km s^{-1}. Stars indicate where there are MIPS 24 μm sources. The VLA beam for this mosaic is plotted in the lower-left corner.

Table 5.3. Summary of IRDC Moment Analysis.

	Peak $\int Tdv$ Position				Range		
IRDC name	α (J2000)	δ (J2000)	v_{lsr} (km s^{-1})	Δv (km s^{-1})	v_{lsr} (km s^{-1})	Δv (km s^{-1})	Notes
G005.85−0.23	17:59:51.4	−24:01:10	17.4	1.4	16.6 - 17.8	1.4 - 3.0	smooth $\bigtriangledown$v
G009.28−0.15	18:06:50.8	−21:00:25	41.0	1.5	39.6 - 41.7	1.3 - 3.7	···
	18:06:49.9	−20:59:57	41.6	2.4	···	···	24 μm source
	18:06:49.8	−20:59:34	41.5	1.9	···	···	···
G009.86−0.04	18:07:35.1	−20:26:09	17.8	1.4	17.5 - 19.1	1.2 - 2.1	two filaments?
G023.37−0.29	18:34:54.1	−08:38:21	78.5	3.7	77.9 - 79.1	1.5 - 4.0	stars, optically thick
G024.05−0.22	18:35:54.4	−07:59:51	81.7	2.0	81.1 - 82.7	1.4 - 3.8	smooth $\bigtriangledown$v
G034.74−0.12	18:55:09.5	+01:33:14	78.0	2.3	77.5 - 79.6	1.1 - 3.7	24 μm source
	18:55:11.0	+01:33:02	78.7	2.1	···	···	24 μm source

5.3.3 Trends in Centroid Velocity

Of the six sources which are detectable in NH_3, three show a smooth velocity gradient (G005.85−0.23, G009.86−0.04, and G024.05−0.22) and three exhibit clumpy structure in centroid velocity (G009.28−0.15, G023.37−0.29, and G034.74−0.12), where there is more prevalent evidence for star formation activity (i.e. coincident 24 μm sources). However, in the latter case also, we tend to see a higher degree of line asymmetries and optically thick lines, thus compromising our ability to discern the effects of star formation.

Sources Showing Smooth Velocity Gradient

The following sources show simple gradients in velocity, and less structure in the linewidth across the field. With the exception of G009.86−0.04, these objects do not have 24 μm sources and therefore lack the direct evidence of disruptive, embedded star formation activity.

G005.85−0.23 This source appears sphere-like in the NH_3 (1,1) integrated intensity map, with a peak at $\alpha(2000) = 17^h59^m51.4^s$, $\delta(2000) = -24°01'10''$, which exactly corresponds to position of the peak in 8 μm optical depth. This position is not distinct in velocity space, as there is a smooth gradient across this feature from the northeast to the southwest, and we detect the lowest linewidths here, typically $\Delta v \sim 1.4$ km s^{-1}. At the extrema positions of the velocity gradient, we detect the highest linewidths ($\Delta v \sim 2.8$ km s^{-1}). There are no 24 μm sources in the mapped region.

G009.86−0.04 Despite the presence of several 24 μm point sources directly coincident with the dense, absorbing gas, they do not affect the cloud's velocity structure appreciably. Unlike the structured sources discussed in Section 5.3.3 the point sources do not have corresponding peaks in integrated intensity or line width, nor are they distinct in their centroid velocity. We detect the lowest line opacities of the sample in this object, reaching only $\tau_m \sim 3$ at the integrated intensity peak ($\alpha(2000) = 18^h07^m35.0^s$, $\delta(2000) = -20°26'09''$), where the centroid velocity is blue-shifted by $\sim$1.5 km s^{-1} compared to the outer edges. The velocity field in this object is somewhat disorga-

nized, with the centroid velocity showing two gradients in either direction from the central peak in integrated intensity, to which the linewidths show no correlation. One plausible scenario for such structure is the interface between two filaments.

G024.05−0.22 In this cloud, there are no 24 μm sources in the observed region. This source has a smooth velocity gradient approximately from north to south, starting at an east-west ridge centered on the peak of integrated intensity at $\alpha(2000) = 18^h35^m54.1^s$, $\delta(2000) = -7°59'51''$, which corresponds also to the peak in 8 μm optical depth. The "ridge" also corresponds with enhanced linewidths ($\sim$3.6 km s^{-1}). At the southern tip, there appears to be a clump with distinct blue-shifted velocity, and to the north, there is a very sharp velocity gradient (1.5 km s^{-1}), which may indicate material elongated along the line-of-sight.

Sources with Clumpy Velocity Fields

Gross clouds motions are overwhelmed by the appearance of "clumpy" structure in the line-center velocity. Star formation appears to play a large role in the kinematical signatures in IRDCs, as 24 μm point sources always coincide with peaks in integrated intensity, along with high linewidths. Our interpretation is that winds and outflows from embedded (possibly massive) stars are kinematically affecting the natal molecular gas increasing the linewidth and exciting ammonia emission, which is discussed in further detail in the following section.

One caveat in interpreting the velocity structure in these objects is the line opacity in the central region of the dark cloud, particularly in G023.37−0.29. The line opacity calculation does not converge because satellite lines in the hyperfine signature of the NH_3 exceed the intensity of the main component, which indicates that NH_3 (1,1) is completely saturated ($\tau > 10$) and the integrated intensity calculated here is a lower limit. These objects in particular would be interesting to observe with greater velocity resolution to resolve out motions along the line-of-sight.

G009.28−0.15 There are three integrated intensity peaks: the central peak ($\alpha(2000) = 18^h06^m49.9^s$, $\delta(2000) = -20°59'57''$), which has a 24 μm source associated with it, and peaks to the north (offset 25 $''$) and south (offset 30 $''$). The central peak is

near the peak in the linewidth (3.3 km s^{-1}), and is also red-shifted in centroid velocity. The southern peak has high line opacity and the highest estimated integrated intensity, the lowest linewidths detected in this object (1.4 km s^{-1}), and there is no associated 24 μm source, though there is a hint of a source (though not a significant detection) of an object at 8 μm. The northern integrated intensity peak is 10 $''$ away from a 24 μm point source, but the kinematic structure is not altered by its presence.

G023.37−0.29 Despite the simple-looking integrated intensity map, peaked at $\alpha(2000) = 18^h34^m54.1^s$, $\delta(2000) = -8°38'21''$, this object shows tremendous velocity structure. The central region has very high linewidths (highest in the sample, 4 km s^{-1}) and peak ratios uncharacteristic of NH_3. This is likely due to high line opacity ($\tau_m > 10$). The centroid velocity at the peak integrated intensity position is distinct from the surrounding material. The spectral fitting in this object should be interpreted with caution, as in the central region, the hyperfine components of NH_3 (1,1) becomes completely saturated, thus the fits to the spectra there are very uncertain, and we cannot trace deep into the object.

G034.74−0.12 There are two integrated intensity peaks in this IRDC, both in the vicinity of 24 μm sources, both coincident with high FWHM. The strong peak in the northwest portion of the cloud ($\alpha(2000) = 18^h55^m09.5^s$, $\delta(2000) = +1°33'14''$) is directly coincident with a 24 μm point source, enhanced linewidths and a slightly blue-shifted centroid velocity. The central peak ($\alpha(2000) = 18^h55^m11.0^s$, $\delta(2000) = +1°33'02''$) is offset 10 $''$ from the position of the 24 μm source and offset 15 $''$ from the nearby peak in linewidth. The centroid velocity is not distinct from the surrounding medium. There are two additional 24 μm sources coincident with the absorbing material, but they are not altering the dynamics of the gas.

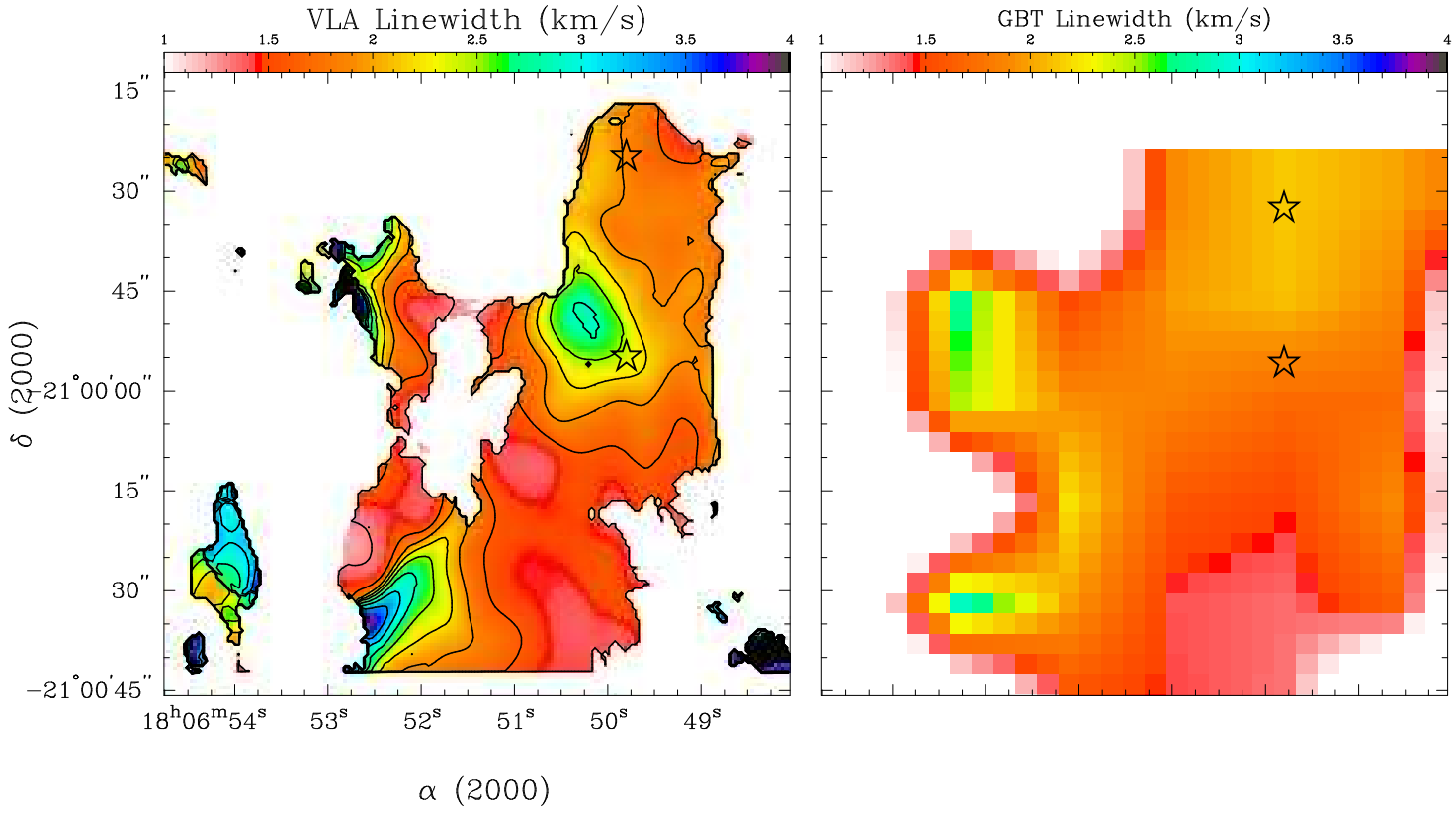

Figure 5.7. VLA and GBT linewidth maps of G009.28−0.15. *Left:* VLA+GBT combined data linewidth map. *Right:* GBT only linewidth map. Star symbols indicate the location of 24 μm point sources.

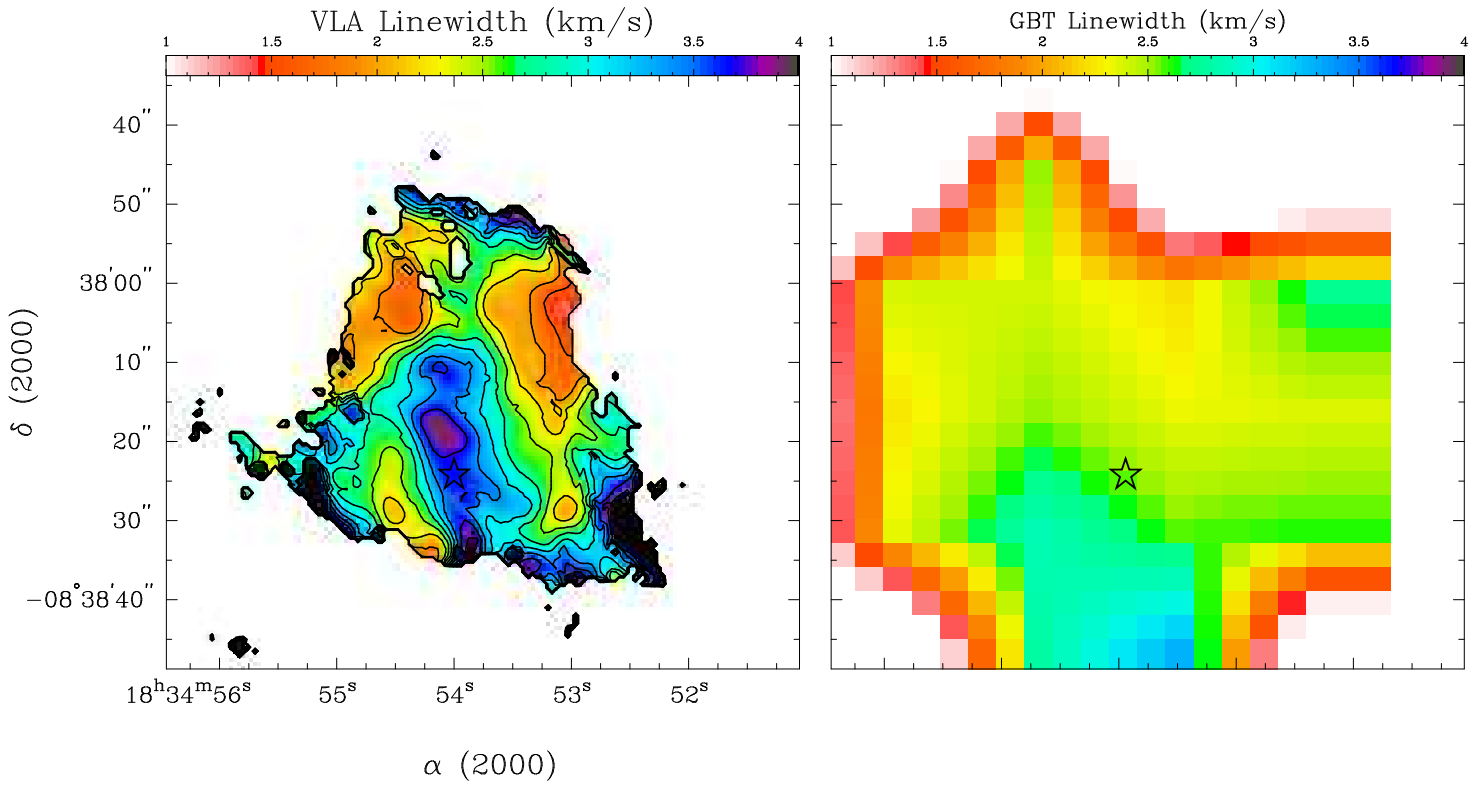

Figure 5.8. VLA and GBT linewidth maps of G023.37−0.29. *Left:* VLA+GBT combined data linewidth map. *Right:* GBT only linewidth map. Star symbols indicate the location of 24 μm point sources.

5.3.4 Linewidths

The NH_3 (1,1) linewidths in our sample of IRDCs are between 1.1 and 4 km s^{-1}, occupying the high tail of the linewidth distribution presented in the Jijina et al. (1999) survey of 264 dense cores, but on par with other ammonia studies of IRDCs: Pillai et al. (2006a), who found a slightly lower range in their single-dish study, and Wang et al. (2007), who found that different cores within an IRDC exhibited different linewidths high-resolution study.

To investigate whether linewidth enhancements are a local effect or if they are present on large scales, we plot the second moment (FWHM) of the combined VLA + GBT dataset alongside GBT-only in Figures 5.7 and 5.8. These two cases are the best examples of relatively isolated peaks in FWHM, so the effects of multiple sources or a more dynamically complex system would not likely be confused. We find that the single-dish data, which probes the large scale features of the dynamics, alone do not show a distinct linewidth enhancement at the positions of the 24 μm sources, suggesting that the enhancement is an effect local to the peak in integrated intensity.

We find that the linewidth increases with increasing distance to IRDCs, as was noted by Pillai et al. (2006a). In Figure 5.9, we show that the maximum linewidth detected in IRDCs varies directly with distance, which may be a result of clumping within the beam increasing with distance. Certainly, with *Spitzer* we do see objects on the 2 - 3″scale which would not be resolved with the beam (sometimes 6 - 8″in low-elevation sources). As noted above, the integrated intensity peaks with 24 μm point sources have a higher linewidth than those peaks without, but the apparently starless peaks typically have very low linewidths, independent of distance (Δv $\sim$ 1.4 km s^{-1}).

5.3.5 Column Density

We calculate the NH_3 (1,1) column density following Friesen et al. (2009), accounting for molecules in both parity states of the NH_3 (1,1) energy level.

$$N(1,1) = \frac{8\pi\nu_0^2}{c^2}\frac{g_1}{g_2}\frac{1}{A(1,1)}\frac{1+e^{-h\nu_0/(kT_{ex})}}{1-e^{-h\nu_0/(kT_{ex})}}\int \tau(\nu)d\nu \tag{5.2}$$

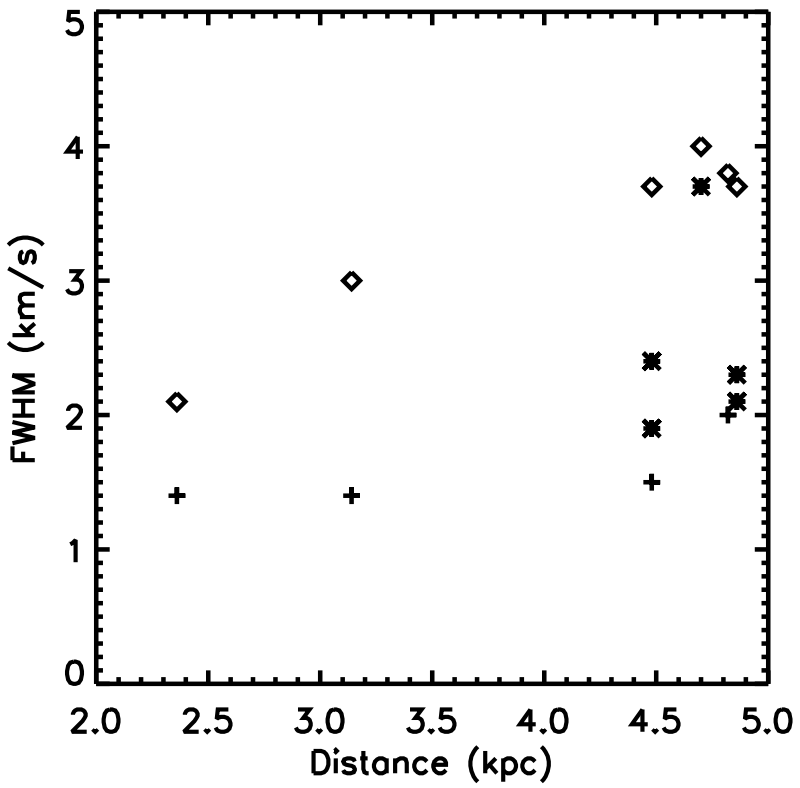

Figure 5.9. Linewidth vs. IRDC distance. The linewidth at the integrated intensity peaks (marked with asterisks where there 24 μm point sources present and + signs for those without 24 μm point sources) and the maximum detected linewidth overall in the cloud (marked with diamonds) both increase with increasing distance.

where g_1 and g_2 are the statistical weights for the upper and lower states of the NH_3 (1,1) transition, $A(1,1)$ is the Einstein spontaneous emission coefficient, 1.68 $\times 10^{-7} s^{-1}$, T_{ex} is the excitation temperature of the gas (see §5.3.6), and $\int \tau(\nu) d\nu = \sqrt{2\pi}\sigma_\nu \nu_0 \tau_{tot}/c$. The statistical weights of the inversion transition, g_1 and g_2, are equal.

5.3.6 Temperature

Ammonia has long been known to be one of the most reliable thermometers in molecular astronomy. We use the ratio of the main line intensities of the (1,1) and (2,2) main lines, as presented in Equation 4 of Ho & Townes (1983). In doing so, we assume that the (1,1) and (2,2) states are the only rotational levels populated in the system. The rotational temperature (T_{Rot}) characterizes the distribution of molecules in these two energy levels, which are separated by 41.5 K in energy, denoted as T_0.

$$T_{Rot}(2,2:1,1) = -T_0 \div ln\left[\frac{-0.282}{\tau_m(1,1)} ln\left[1 - \frac{\Delta T_a(2,2,m)}{\Delta T_a(1,1,m)} \times (1 - e^{-\tau_m(1,1)})\right]\right] \quad (5.3)$$

The two-state system assumption also implies that the kinetic temperature (T_k) is much less than the energy gap, $T_0 = 41.5$ K. Since there are no radiative transitions between the (2,2) and (1,1) levels, their population ratio, represented by T_{Rot}, probes the importance of collisions, and thus can be used to estimate T_k. This assumption has been shown to be valid in numerous studies of pre-stellar cores and IRDCs, where temperatures are typically 20 K and lower.

As Swift et al. (2005) showed, the relationship between the kinetic and rotational temperatures is as follows

$$T_{Rot} = T_k \left[1 + \frac{T_k}{T_0} ln\left(1 + 0.6 e^{-15.7/T_k}\right)\right]^{-1} \quad (5.4)$$

The above expression can be solved numerically for T_k, but Tafalla et al. (2004) find that for temperatures between 5 and 20 K, their Monte-Carlo modeled NH_3 spectra fit the following analytical solution to an accuracy of 5% or better

$$T_k = \frac{T_{Rot}}{1 - \frac{T_{Rot}}{42} ln\left[1 + 1.1e^{-16/T_{Rot}}\right]}. \quad (5.5)$$

In Figures 5.10 to 5.15, I present the results of this temperature calculation, both with kinetic temperature maps and plotted as a function of 8 μm optical depth. Temperatures range from 8 to 16 K, and the values at the integrated intensity peak locations are summarized in Table 5.4.

The temperature distribution is generally not a strong function of 8 μm optical depth ($\tau_{8\mu\mathrm{m}}$), but in G023.37−0.29, G034.74−0.12 and especially in G009.86−0.04, there are hints of a rise in temperature at low 8 μm optical depth, typically at the edges of the cloud or near radiation sources.

Table 5.4: Summary of Physical Characteristics at $\int Tdv$ peaks.

IRDC name	α (J2000)	δ (J2000)	T_{rot} (K)	T_{kin} (K)	$N(NH_3)$ (10^{14} cm^{-2})	$N(H + H_2)$ (10^{22} cm^{-2})	χ_{NH_3} (10^{-8})	σ_{NT} (km s^{-1})	R_p (10^{-3})
G005.85−0.23	17:59:51.4	−24:01:10	11.0±0.9	11.8	13.0	>4.3	<3.0	1.4	7.2
G009.28−0.15	18:06:50.8	−21:00:25	11.7±1.3	12.6	11.6	1.2	9.7	1.4	7.5
	18:06:49.9	−20:59:57	12.8±1.8	14.1	20.4	2.2	9.2	2.3	3.2
	18:06:49.8	−20:59:34	12.9±0.8	14.3	15.4	3.9	3.9	1.8	5.1
G009.86−0.04	18:07:35.1	−20:26:09	11.0±1.5	11.8	8.2	>4.3	<1.9	1.3	7.9
G023.37−0.29	18:34:54.1	−08:38:21	10.0[1]	10.6	65.3	2.2	30	3.8	0.91
G024.05−0.22	18:35:54.4	−07:59:51	11.5±1.0	12.3	10.3	>4.3	<2.4	1.9	3.9
G034.74−0.12	18:55:09.5	+01:33:14	10.0±0.7	10.6	21.9	4.1	5.3	2.4	2.2
	18:55:11.0	+01:33:02	10.0±1.2	10.5	10.7	3.3	3.2	2.1	2.9

[1]In the case of G023.37−0.29, no error was calculable for the temperature, as the lines in this region are saturated.

5.4 Discussion

5.4.1 Organized Cloud Motions

Three of the IRDCs we mapped, G005.85−0.23, G024.05−0.22, and, to a lesser extent, G009.86−0.04, exhibit smooth velocity gradients across the bulk of the IRDC. In the case of G009.86−0.04, there appear to be two gradients away from a blue-shifted velocity center. One possible interpretation of such a velocity gradient is IRDC rotation. A handful of studies in the literature have examined the rotation of dark clouds, and no such study has been done of IRDCs. For rotating dark clouds, motions are typically modeled as solid body rotation (Arquilla & Goldsmith, 1986; Goodman et al., 1993), and if we make such an assumption for our IRDCs, we find an angular velocity of ∼2.6 and 2.1 km s^{-1} pc^{-1} for G005.85−0.23 and G024.05−0.22, respectively, which is on par with low mass dense cores observed previously. The rotation interpretation is a dangerous one, Burkert & Bodenheimer (2000) point out for local clouds, as systematic line-of-sight velocity gradients can be readily produced by random motions in turbulent cores, which are likely even more prevalent in the IRDC environment.

The importance of rotation is often quantified by parameter β, which is the ratio of rotational kinetic energy to gravitational energy. For a sphere, this quantity is given as

$$\beta = \frac{\Omega^2 R^3}{3GM} \tag{5.6}$$

where Ω is the angular velocity, R is the cloud size, and M is the cloud mass. A value of $\beta = \frac{1}{3}$ is equivalent to breakup speed for a spherical cloud. In the case of G005.85−0.23 and G024.05−0.22, the projected geometry is close to round, thus a spherical approximation is probably the best one. Taking an average Ω, R from the size in the NH_3 map, and M from the corresponding area of clumps computed in Chapter 4, we find β values of 0.01 and 0.03 for G005.85−0.23 and G024.05−0.22, respectively, showing that if the clouds do indeed rotate, the rotation plays a small dynamical role in the cloud.

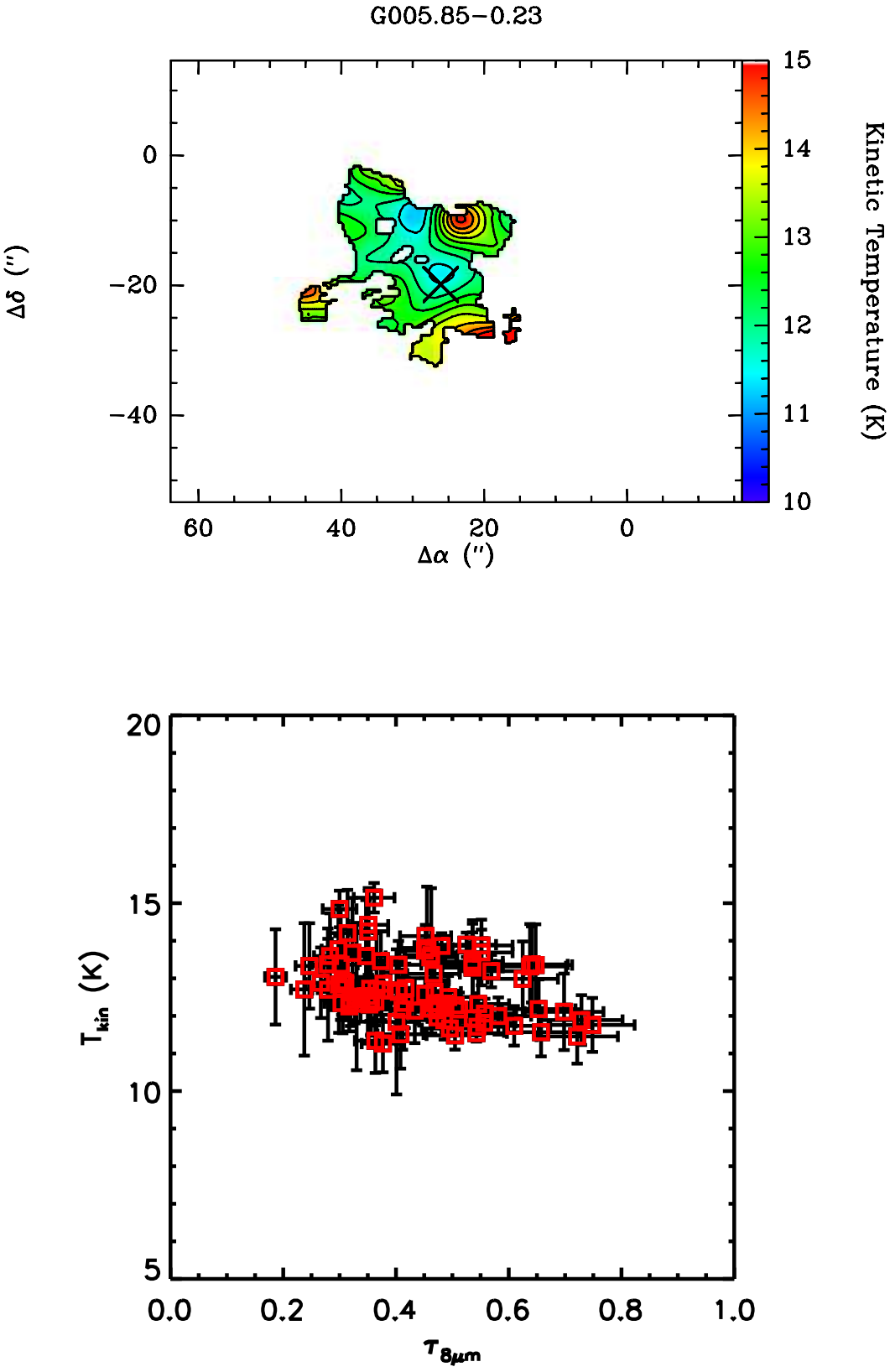

Figure 5.10. Kinetic Temperature map of G005.85−0.23. Contours are from 10 to 15K in 1K increments.

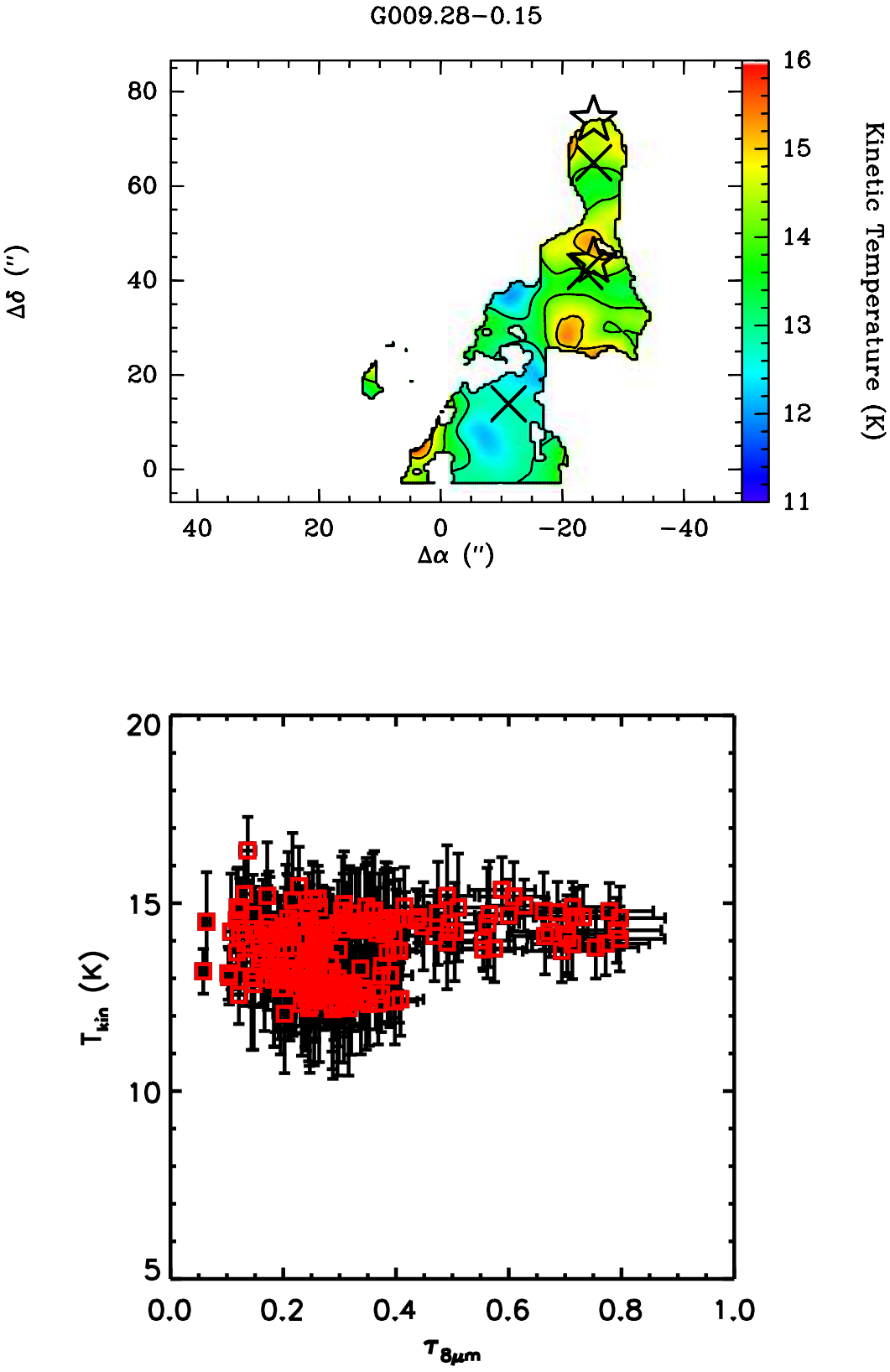

Figure 5.11. Kinetic Temperature map of G009.28−0.15. Contours are from 11 to 16 K in 0.5 K increments.

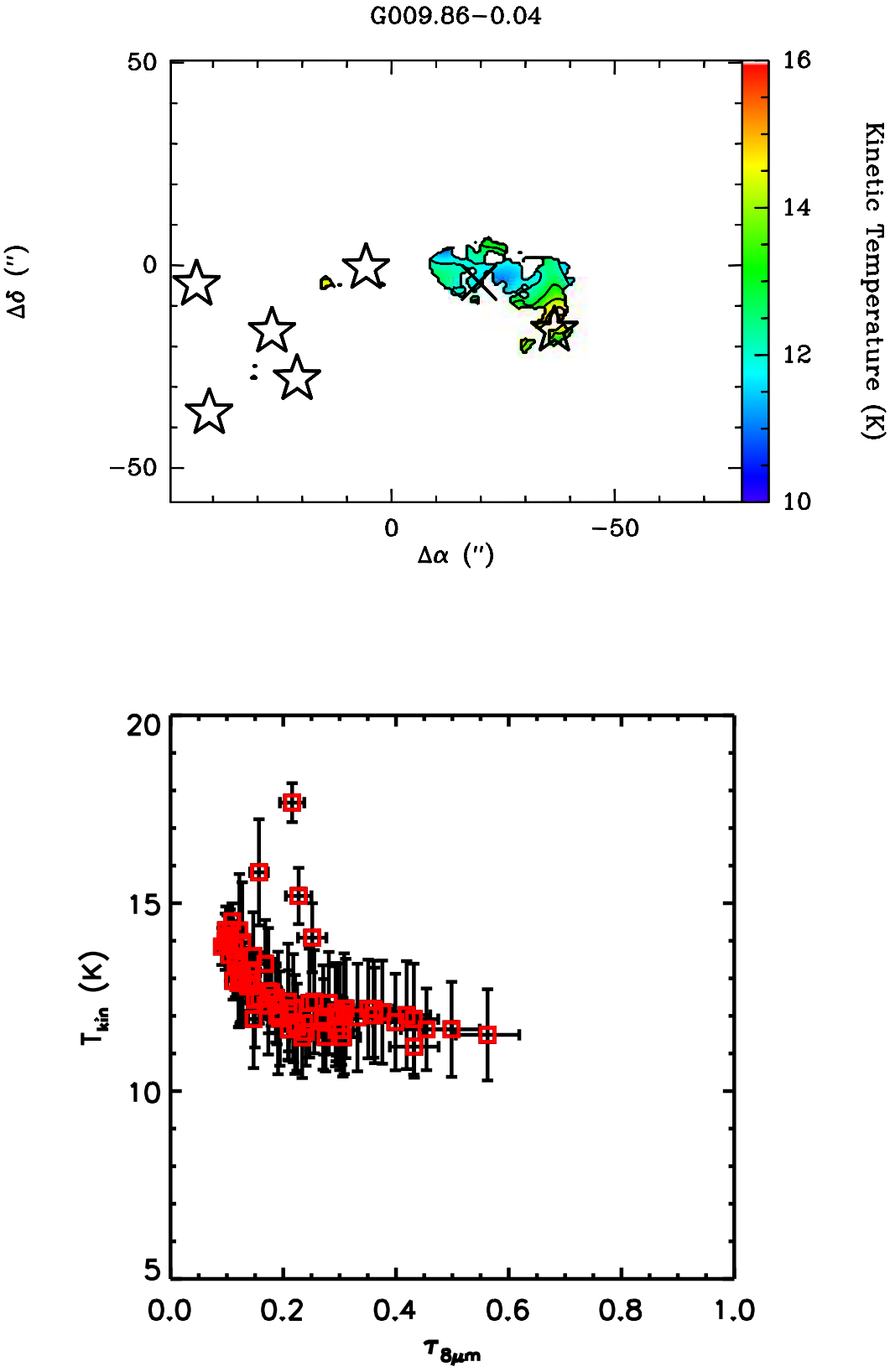

Figure 5.12. Kinetic Temperature map of G009.86−0.04. Contours are from 10 to 16 K in 1 K increments.

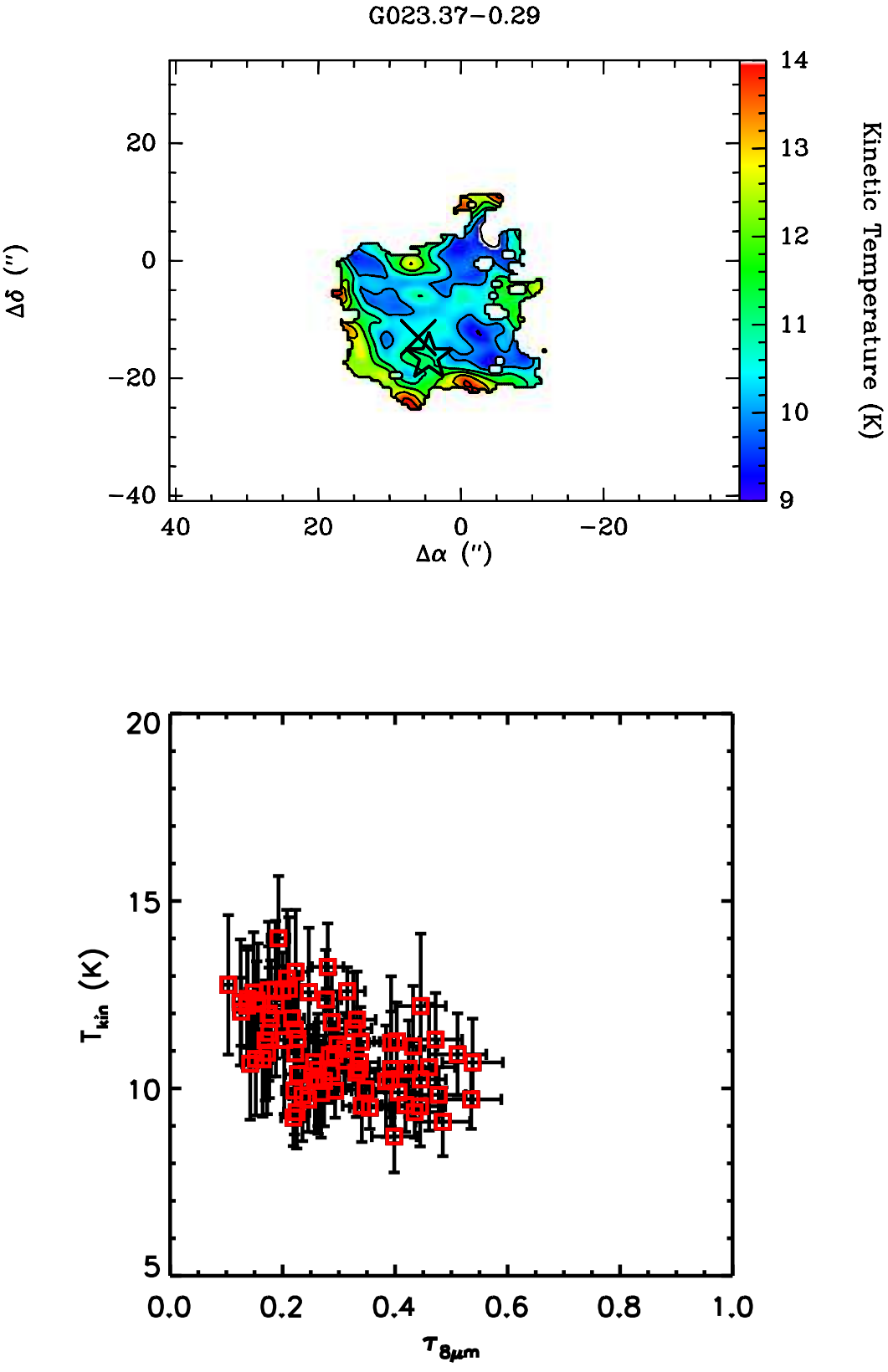

Figure 5.13. Kinetic Temperature map of G023.37−0.29. Contours are from 8 to 14 K in 1 K increments.

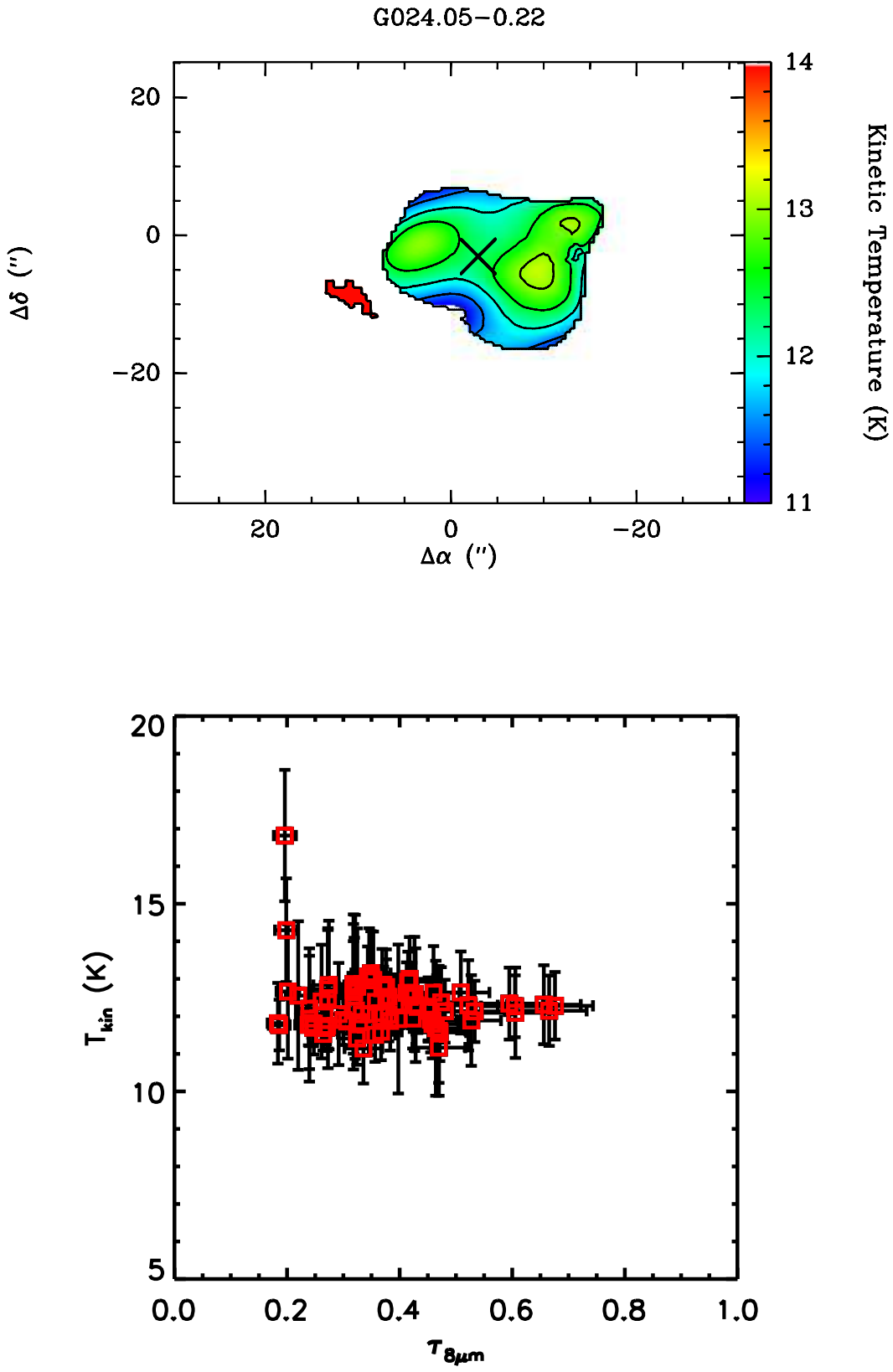

Figure 5.14. Kinetic Temperature map of G024.05−0.22. Contours are from 11 to 14 K in 0.5 K increments.

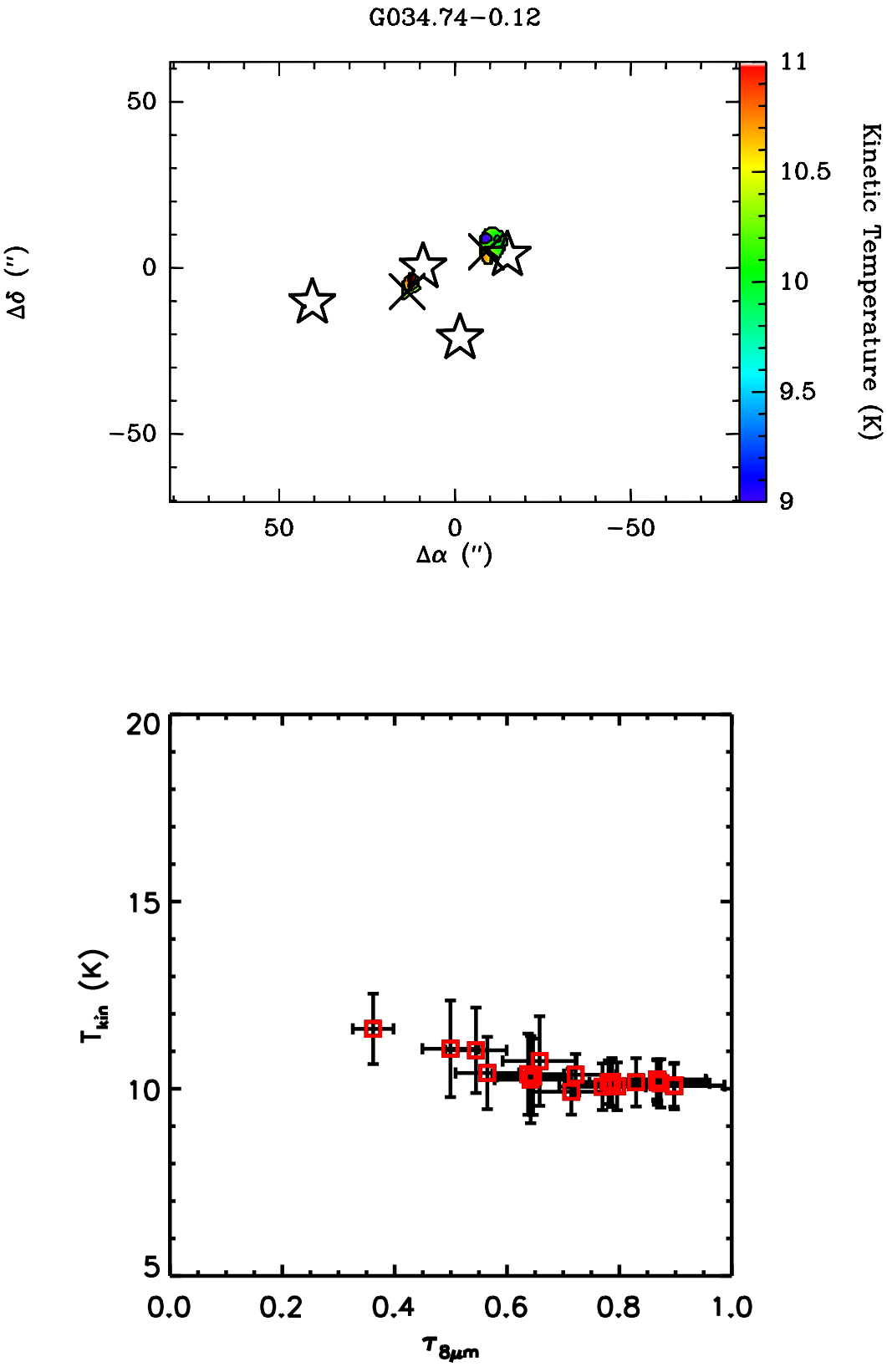

Figure 5.15. Kinetic Temperature map of G034.74−0.12. Contours are from 9 to 11 K in 0.5 K increments.

The sharp gradient in centroid velocity in the northern portion of G024.05−0.22 is the only such feature in our sample. The accompanying enhancement in linewidth and absence of star formation indicators (see §5.4.4) suggest that this feature is an interface (collision?) between distinct clouds, and could be a relic of IRDC formation.

5.4.2 Thermal / Non-thermal Support

The linewidths observed in our sample (1.1 - 4.0 km s^{-1}) are well in excess of the thermal linewidth, which at the kinetic temperatures we deduce here ($T_{kin} \sim 8 - 16$ K) would be ∼0.2 km s^{-1}. The ratio of thermal to non-thermal pressure in the cloud, as expressed by Lada et al. (2003), is

$$R_p = \frac{a^2}{\sigma_{NT}^2} \tag{5.7}$$

where a is the isothermal sound speed, and σ_{NT} is the three-dimensional non-thermal velocity dispersion. Table 5.4 displays the values of R_p at the integrated intensity peaks in each cloud, with an average value of ∼0.005, indicating that these regions are dominated by non-thermal pressure. "Non-thermal" effects can be an amalgam of motions, such as infall, ouflow, turbulence or systematic cloud motions (i.e. rotation). If it is the case that IRDCs are thermally supported (i.e. the non-thermal component of the linewidth is pure systematic motion such as infall or outflow), the masses (Chapter 4) of these object are much higher – usually by orders of magnitude – than the typical Jeans mass (Gibson et al., 2009) and thus would be prone to fragmentation. However, this ignores the possibility that turbulent motions could provide support (Arons & Max, 1975), or the potential for support via a static magnetic field (Mouschovias & Spitzer, 1976).

To examine whether the linewidth enhancements are local to particular IRDC cores or global features of the cloud, we compare the VLA (combined dataset) linewidth map with that of just the GBT, which probes the properties of extended structures. Figures 5.7 and 5.8 show two examples of clouds that exhibit a sharp rise in linewidth near peaks in integrated intensity. From this plot we see that the linewidth enhancement (near the 24 μm source) does not show a corresponding rise

in the single-dish data alone, thus the linewidth enhancement is a small scale effect.

This is the same effect Wang et al. (2007) observed in P2 of G28.34+0.06, in which they infer that the motions close to the core (probed with the interferometer) are due to infall or outflows associated with the embedded source, which are not evident in the large-scale envelope gas. The same effect could be happening in G009.28−0.15. Wang et al. (2007) attribute the difference to the presence of high-mass protostars in the core exhibiting elevated linewidth (4.3 km s^{-1}), while the another core lacked any indication of star formation activity while exhibiting a relatively low linewidth (1.2 km s^{-1}). In the following section, I discuss the correlation between linewidths and the presence of candidate embedded protostars.

5.4.3 IRDC Virial Mass

As a means of understanding the stability of the IRDCs, I compare the cloud masses (from Chapter 4) to the virial mass of the cloud, using the relation

$$M_{Virial} = \frac{5}{3}\frac{RV_{rms}^2}{G} \tag{5.8}$$

where R is the radius of the cloud, G is the gravitational constant, and $V_{rms} = 3^{\frac{1}{2}}\Delta V/2.35$ where ΔV is the average FWHM linewidth of the cloud. Virial masses for the clouds are typically $10^3 M_\odot$, which is on par with the masses in the main absorbing clumps where NH_3 was mapped. This suggests that the clouds are roughly in Virial equilibrium. But, as discussed by Ballesteros-Paredes (2006), there are limitations when applying the Virial analysis to such regions. Indeed, with the uncertainties inherent in clump identification and line-of-sight pile-up, this is not the most robust diagnostic.

5.4.4 Associated Star Formation

As addressed in Chapter 3, we find young stars in the vicinity of IRDCs, and with these VLA observations, we can look at the effect, if any, they have on the gas. We see a variety of behaviors in our small sample of IRDCs. In G009.28−0.15, G023.37−0.29 and G034.74−0.12, we detect bona fide embedded young stars (or

24 μm point sources) at or near peaks in integrated intensity. The integrated intensity peaks in G005.85−0.23 and G024.05−0.22 lack any indication of young stars and have low linewidths. This is either because any star formation activity is very deeply embedded and has not influenced the gas that we are tracing or that these cores are truly starless, making them excellent candidates for massive prestellar cores. Ammonia observations are tracing the effects of star formation, such as outflows/infall from/onto an embedded protostar, on the surrounding material.

In some cases (e.g. G009.28−0.15) there appears to be an offset between the integrated intensity peak and/or linewidth peak, which might be due to outflows oriented at an angle to the line-of-sight. However, a closer examination of the beam size and orientation prevents us from making a significant statement about the possible scales of these phenomena.

G034.74−0.12 and G009.86−0.04 have 24 μm point sources with no distinct peaks in NH_3 integrated intensity or linewidth. In these object, we suspect the young stars were at one time but are no longer kinematically associated with the cloud and the velocity field is not subject to the effects of localized star formation so much as large-scale motions of the IRDC filaments. Alternatively, these objects could be in front of the IRDCs far enough so that the dynamical effects of star formation is incapable of influencing the gas.

5.4.5 Temperature Structure

We find the gas temperatures in these IRDCs are consistently between 8 and 16 K, and its distribution is either constant with 8 μm optical depth ($\tau_{8\mu\mathrm{m}}$) or it shows a rise toward low optical depth. In G009.86−0.04, where we see the sharpest increase ($\sim$4 K) in temperature at low optical depth, we find the highest temperatures are near a bright 24μm source, where the optical depth at 8 μm is low. The marginal rise ($\sim$2 K) in G034.74−0.12 and G023.37−0.29 is also probably due to local stars. The remaining correlations between T_{kin} and $\tau_{8\mu\mathrm{m}}$ are less tight, so such modest temperature gradients do not stand out.

The temperatures here agree well with those found in Pillai et al. (2006a) and

dust temperatures derived in Carey et al. (2000) from sub-millimeter observations. Goldsmith (2001) posits that at densities greater than $10^{4.5}$ cm^{-3}, the dust and gas temperatures are coupled, which we now confirm extends to the very dense environments of IRDCs. The temperature rise we observe in several objects is likely due to external heating by massive stars in the local environment. Note that these effects are small at the low optical depth edges of the IRDCs, where $\tau_{8\mu\mathrm{m}} < 0.1$, or $\sim$2 magnitudes of extinction.

5.4.6 Chemical Abundance of NH_3 in IRDCs

We follow Friesen et al. (2009) in deriving the NH_3 column density, compare it to N(H + H_2) from our 8 μm observations, and derive a mean abundance of 7.9×10^{-8} (4.3×10^{-8} excluding the outlying value for G023.37−0.29). This is slightly higher than values reported in the local cloud Ophiuchus (Friesen et al., 2009) and in good agreement with values found previously in IRDCs (Pillai et al., 2006a). These values also agree with chemical models of pre-protostellar and protostellar cores (Bergin & Langer, 1997).

In Figure 5.16, we plot the integrated intensity of NH_3 (1,1) versus the optical depth at 8 μm. In three cases (G005.85−0.23, G024.05−0.22, G034.74−0.12), there is a clear trend well-fit with a line. In these cases, the NH_3 optical depth is low ($\tau \sim 1$), and the linear fit indicates that the NH_3 abundance is constant.

In the remaining cases (G009.28−0.15, G009.86−0.04, G023.37−0.29), the line is very optically think and sometime saturated. I correct for these effects and fit the relation with the unsaturated integrated intensity. In G023.37−0.29, the NH_3 (1,1) line is extremely optically thick in the central region (high $\tau_{8\mu\mathrm{m}}$) thus inflating the NH_3 column density considerably. In the case of G009.28−0.15 and G009.86−0.04, the correlation is weaker, and there may be two clumps along the line of sight that have different abundances or have varying depletion effects. These latter three objects will require more detailed observations and modeling to understand the nature of the NH_3 emission.

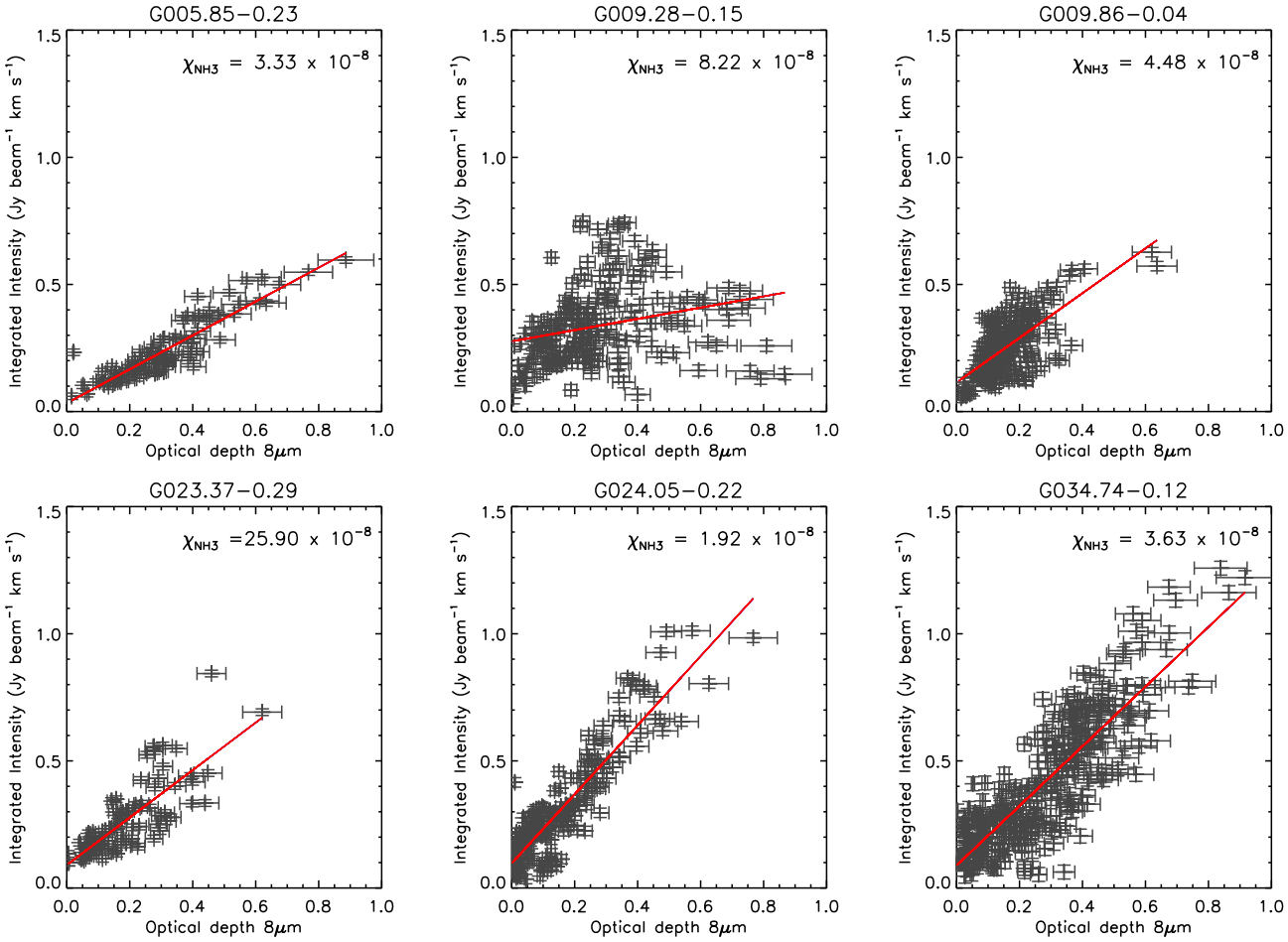

Figure 5.16. NH_3 (1,1) Integrated Intensity vs. $\tau_{8\mu m}$ with abundance. Linear fit including only optically thin lines, the ammonia abundance χ_{NH_3} is included in the plot for each object.

5.5 Summary

I present observations and analysis of NH_3 (1,1) and (2,2) inversion transition lines in six IRDCs. The sample exhibits diverse behavior in structure and kinematics. Five of the nine identified peaks in integrated intensity have 24 μm sources potentially associated with them, the remaining peaks do not. The centroid velocity fields are very complex, ranging from a rotation-like signature to "clumpy" (when associated with star formation) to random. The linewidths also show diverse behavior and are dominated by non-thermal broadening. The clouds appear to be roughly in Virial equilibrium. When there is a linewidth enhancement near a 24 μm source, it appears to always be local to the dense clump rather than a characteristic of the cloud as a whole. This supports our suggestion that these sources are embedded in the gas, and outflows or infall onto the embedded protostar(s) is traceable with these observations. The temperatures of IRDCs are constrained to a small range, between 8 and 16 K, and seem to rise slightly near cloud edges or close to nearby 24 μm sources. We detect a modest rise in gas (and dust) temperature with optical depth in half of the sample, and flat distributions in the other. We find an ammonia abundance relative to hydrogen of 4.3×10^{-8} in our sample of IRDCs, which is consistent with chemical models for dense cores.

CHAPTER 6

CONCLUSIONS AND FUTURE PROSPECTUS

6.1 Summary

6.1.1 Molecules in Infrared-dark Clouds

As in local clouds, certain species of molecules are well-suited to trace dense gas. Starting with the MSX survey, we identified 114 compact, opaque IRDC candidates and performed molecular line observations of the N_2H^+ $1 \rightarrow 0$, CS $2 \rightarrow 1$ and $C^{18}O$ $1 \rightarrow 0$ transitions in 41 of them. We successfully detected significant molecular emission in 34/41 (82%) of the observed sample. Morphologically, we find that (at least one detected velocity component) agrees well with the 8 μm absorption seen with MSX.

These observations provided us with accurate distances for use throughout this study. The average properties of the IRDCs in this sample are as follows: IRDC diameter $< D > \approx 0.9$ pc, density $< n > \approx 5000$ cm^{-3}, and mass $< M > \approx 2500$ M$_\odot$. The density estimate is likely a lower limit, as beam dilution of the clumpy structures that make up the IRDC will artificially lower the value calculated here. The mass of infrared-dark clouds is comparable to that of high-mass protostellar objects (Williams et al., 2004), but their linewidths, while higher than in local low-mass star-forming regions, are lower than active high-mass star forming regions, which suggests that these objects are prestellar.

6.1.2 Young Stars in IRDCs

Star formation in IRDCs has only been grazed in the literature, both through culling large surveys for signposts of star formation (e.g. Cyganowski et al., 2008; Chambers

et al., 2009) or pointed studies to characterize the embedded protostars detected in a handful of objects (e.g. Rathborne et al., 2005; Beuther & Steinacker, 2007). These studies, while important, have left the middle ground unexplored. I present a study of the distributed population of young stars in the vicinity of IRDCs. These deep *Spitzer* IRAC and MIPS observations are sensitive to 1 $L_{\odot}$ protostars at the fiducial 4 kpc distance. In all, there are 308 objects that qualify as YSOs according to IRAC and MIPS color criteria, but only ≈16% are directly associated with dense gas (i.e. gas identified as a "clump"). It is our contention, due to the enhanced extinction that the vast majority of the YSOs exhibit, that these young objects are likely associated with the IRDC. I detect 7 "embedded objects," though only 3 are associated with what is presumably its natal "clump" still appearing in absorption. The other four embedded objects, and possibly the remaining 269 YSOs, may be washing out neighboring absorption features of the natal cloud or perhaps have dispersed the local gas.

6.1.3 IRDC Environment

Bright, diffuse emission is present near five of the IRDCs in our Spitzer sample of eleven. In two cases, there is spatially coincident molecular emission (from the FCRAO survey), though our molecular observations cannot conclusively determine association with the IRDCs.

I also utilize molecular data to grasp the spatial extent of IRDCs. By comparing N_2H^+, $C^{18}O$, and CO emission in the vicinity of an IRDC, it is clear that IRDCs are embedded in larger molecular cloud complexes. Similar to what Bergin et al. (2002) show in B68, these chemical tracers probe different density regimes: N_2H^+ is present at high A_V, toward the "center" of clouds where CO depletes, and CO traces the more diffuse extended gas. With molecular maps from our FCRAO survey, we see that a similar thing is happening here, except on a much larger scale. N_2H^+ is strongly centered on the dark cloud, and the $C^{18}O$ (and to a greater extent, the CO) traces the weaker absorption features, and connects dark features that sometimes appear disconnected in the absorption. This lends support to the idea that IRDCs are dense condensations that are fragmenting within a much larger less dense envelope. In this

work, I tacitly define the "infrared-dark cloud" as the distinct absorbing features at 8 μm, which while true to the spirit of their discovery, is an observationally biased statement and doesn't necessarily have meaning in the large context of the molecular cloud.

6.1.4 Probing Mass with Absorption in IRDCs

The absorption of IRDCs against the Galactic background is a useful tool by which one can probe the cloud's detailed structure. First, I model the background against which the IRDC is absorbing. This model, however, contains contributions from both the foreground and background Galactic emission at 8 μm. Therefore, I use two methods of quantifying the foreground contribution. To further legitimize dust absorption at 8 μm as a mass-tracer, I compare the IRDC properties with complementary molecular observations and dust emission observations. Wavelet analysis and the `gaussclumps` fitting technique both help to understand the optical depth contribution from the more diffuse envelope surrounding the IRDC, which can be significant. IRDCs are undeniably structured hierarchically, and the following results refer to structures that make up a fraction (20-40%) of the total IRDC mass. To date, this study is the most comprehensive in its characterization of large and small scale structure in IRDCs.

6.1.5 IRDC Clump Mass Function

With dust absorption as our reliable probe of mass, I used a clump-finding algorithm to systematically decompose the IRDCs into their smallest resolvable constituent structures. With a priori knowledge of the cloud distance from the molecular survey, I calculate the mass and size of the clumps and examine the properties of the ensemble population.

The existence of substructure – from 10^3 $M_\odot$ clumps down to 0.5 $M_\odot$ "cores" – indicates that IRDCs are undergoing fragmentation and will ultimately form star clusters. The typical densities ($n > 10^5$ cm^{-3}) and temperatures ($T < 20$ K) of IRDCs are consistent with massive star forming regions, but they lack the stellar content seen

in more active massive star formation regions, such as the Orion molecular cloud or W49, for example. The mass available in the most massive clumps, however, leads us to conclude that IRDCs will eventually form multiple massive stars.

The IRDC clump mass function, with slope $\alpha = 1.76 \pm 0.05$ for masses greater than $\sim 40 M_{\odot}$, agrees with the mass function we calculate based on data from other studies of massive objects. The mass function for both IRDCs and these massive clump distributions is shallower than the Salpeter-like core mass function reported in local regions. In fact, the IRDC clump mass function is more consistent with that found when probing molecular cloud structure using CO line emission ($\alpha = 1.6 - 1.8$), again supporting the assertion that these objects are at an earlier phase of fragmentation. At the low-mass end ($M < 40 M_{\odot}$), we find a much shallower slope, $\alpha = 0.52 \pm 0.04$, which is somewhat flatter than other studies that cover the same range in masses. This could be due in part to incomplete sampling of the fields. Alternatively, the apparent flattening of the clumps mass function around 40 $M_{\odot}$ could indicate a transition between objects that will generate clustered star formation and those that give rise to more distributed star formation (Adams & Myers, 2001).

At face value, (Klessen, 2001) shows that such a shallow slope ($\alpha \sim 1.5$) is consistent with molecular cloud fragmentation simulations without turbulence. Simulations with turbulence result in steeper mass function slopes ($\alpha > 2$). This disparity is at odds with the fact that our sources should clear evidence of turbulence and thus there is inconsistency with current theory.

Infrared-dark clouds are already well-established candidates for the precursors to stellar clusters and exhibit significant structures down to 0.02 pc scales. As such, the properties of IRDCs provide powerful constraints on the initial conditions of massive and clustered star formation. We suggest that the mass function is an evolving entity, with infrared-dark clouds marking one of the earliest stages of cluster formation. The mass distribution is top-heavy, with most of the mass in the largest structures. As the massive clumps fragment further, the mass function will evolve and become steeper. The IRDC mass function is a useful benchmark for theoretical work that models molecular cloud fragmentation.

6.1.6 High-resolution Ammonia Observations in IRDCs

I present observations and analysis of NH_3 (1,1) and (2,2) inversion transition lines in six IRDCs. The correlation between line intensity and 8 μm absorption is remarkably good, even in the densest parts of the clouds. The linewidths tend to be much higher than the thermal linewidth at these low temperatures, thus these clouds are dominated either by turbulence or systematic non-thermal motions. This sample of IRDCs in not homogeneous in that the IRDCs exhibit varied and complex kinematics including signatures associated with embedded protostars. Despite these differences, the temperatures are constraint to a relatively small range of 8 to 16 K, rising slightly in areas of low optical depth either near stars or at the cloud edge. The NH_3 abundance is elevated slightly compared to local clouds and no conclusive evidence for depletion.

6.2 Understanding Galactic Star Formation

In this study, we've drawn on established techniques and models based on observations of local, low-mas star formation regions to inform our understanding of the more massive, cluster-forming regions at great distances. We have learned that IRDCs are more extreme than local regions in almost every way. Studies have shown that IRDCs reside in the molecular ring of the Galaxy, or perhaps a spiral arm in the vicinity (Jackson et al., 2008), making the IRDC environment very different from anything we see locally.

IRDCs are extremely massive, compact, and cold. The mass function of dark clumps mimics that of other massive star forming regions; the velocity fields are very complex, suggesting that IRDCs reside in a dynamic environment. In several IRDCs, massive protostars are present, yet our study shows that the bulk of the gas is devoid of star formation activity. Because of these conditions in IRDCs, we believe that IRDCs will fragment further before they become a stellar cluster. Given the masses, the clusters that IRDCs will form will be several times more massive than Orion, our nearest example of massive star formation. What becomes of the clusters that IRDCs

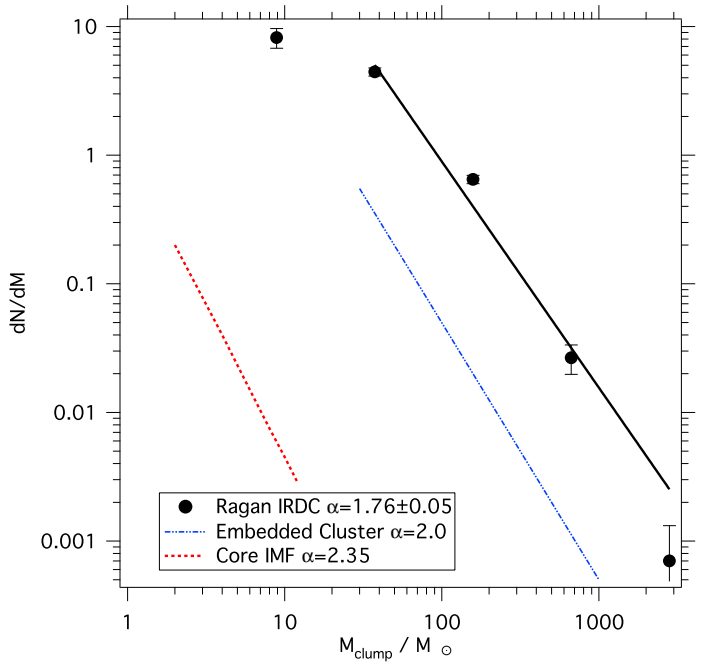

Figure 6.1. Mass Function Evolution. A schematic of the possible mass function evolution scenario: the IRDC clump mass function (black) which has a characteristic slope of $\alpha \sim 1.76 \pm 0.05$; the embedded cluster mass function (blue, $\alpha \sim 2$, Lada & Lada 2003); and the core mass function in the Pipe Nebula (red, $\alpha \sim 2.35$, Alves et al. (2007)) are plotted in their respective mass regimes.

form is an interesting question. Their dynamic environment must certainly disrupt the stars' natal environment and would possibly play a role in cluster dispersion. This question, among many others, will be interesting to pursue in the coming years.

6.3 Outlook

This work brings us to the cutting edge of IRDC surveys, from the infrared to the millimeter and radio wavebands. Our goal was to bring IRDCs to the forefront of high-resolution studies while, at the same time, keeping a broad outlook on the diversity of IRDCs in the context of Galactic star formation. We've shown that there is important physics to be understood on the smallest scales we can resolve (few $''$) and below. In addition, new instruments will open new doors in studying these objects. Below, I discuss some of the projects that I hope to pursue in the coming years.

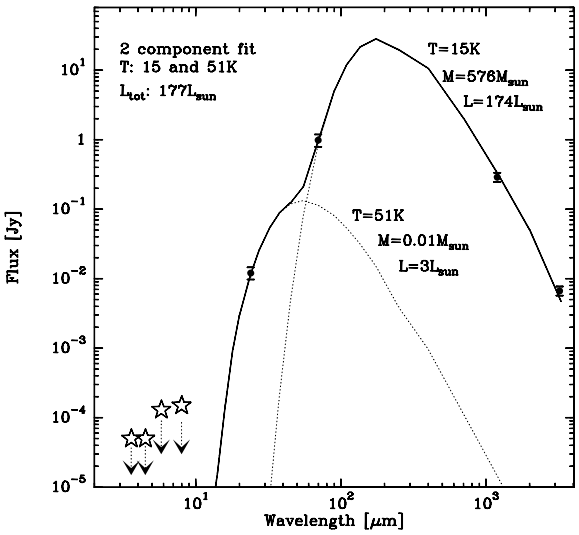

Figure 6.2. Modeled spectral energy distribution of a massive embedded protostar. From Beuther & Steinacker (2007) - the far-infrared model spectrum for a massive protostar discovered in IRDC 18223-3. The coverage offered by PACS (Herschel) is ideally suited to probe the peak of the SED and provide important constraints on the properties of the embedded protostar.

6.3.1 IRDC Chemistry

In Chapter 5, we showed that NH_3 lines become optically thick at the center of some IRDCs. Observations of higher resolution or of higher excitation energy transitions would better our chances of finding an optically thin transition and, therefore, the intensity and abundance of the molecule NH_3. Such observations would allow for a more robust test of depletion arguments at very high densities and low temperatures. We are capable of undertaking such a study today with the improvements to the Very Large Array – now the Expanded Very Large Array. With enhanced sensitivity and knowledge of strong sources, future NH_3 studies at the EVLA will be able to answer these questions.

6.3.2 Star Formation in IRDCs

To understand IRDC evolution, the associated star formation at the heart of these objects must be characterized. This work is currently underway in various groups (Beuther & Steinacker, 2007; Rathborne et al., 2007), but are conducted on a one by one basis. Figure 6.2 is taken from Beuther & Steinacker (2007) and shows the modeled spectrum of a massive protostar embedded in an IRDC. Currently, obser-

vations in the mid-infrared with *Spitzer* and millimeter observation (here, with the Plateau de Bure Interferometer) provide the only constraints on the spectral energy distribution (SED) of embedded massive protostars, but the bulk of the flux should be emitted in the far-infrared. New and imminent telescopes will have much to say about protostars in infrared-dark clouds.

In the *Spitzer* sample of 11 IRDCs, 90-100% of the clumps have no associated MIPS 24 μm sources. Is this a typical rate? To date, surveys are only beginning to answer this question. The *Spitzer* GLIMPSE and MIPSGAL legacy surveys are excellent starting points to hunt for embedded protostars, but more observations at far-infrared wavelengths are needed to characterize them. For example, with the emergence of *Herschel Space Observatory* and the eventual flight of *Stratospheric Observatory for Infrared Astronomy (SOFIA)*, the far-infrared waveband will be making sensitive observations in precisely the spectral region where massive embedded protostars emit the bulk of their radiation. These instruments give us a huge advance in understanding of how typical such protostars are in IRDCs and what their distribution of characteristics are. This is essential for understanding the evolution of IRDC and also placing them in the appropriate context of Galactic star formation.

6.3.3 Physics of IRDC Fragmentation

To investigate what led to the IRDC mass function, the natal envelope out of which the dense clumps condensed must be characterized. A reliable tool to study the diffuse envelopes is molecular line emission. Detailed chemical models of dense molecular cloud cores (Bergin & Langer, 1997) and observations of local clouds (Bergin et al., 2002; Tafalla et al., 2004) are the foundation of much of what we know of the behavior of molecules in different environments. For example, due to their chemical properties, molecules, such as CO, or the ion, C^+, are perfectly suited to probe this density regime ($A_V \sim$ 1-2). Similarly, because of molecular freeze-out, the N_2H^+ molecule can be used as a probe for high density gas ($A_V > 5$). Together, these gas probes can provide a complete, three-dimensional mass profile of IRDCs for the first time. Additionally, with special properties of select molecules, which we have shown for NH_3 in Chapter

5, a vast number of other properties are available with molecular observations.

Figure 6.3 shows that carbon-bearing molecules are abundant in low-density medium, which are characteristic of the cloud envelope and surface. With Herschel HIFI comes the ability to observe the C^+ fine structure transition at 156μm with good (10″) resolution. The C^+-to-H_2 ratio is well-known, and its chemistry confines it to the surfaces of dense clouds ($A_V < 2$ Hollenbach et al., 2009). Thus, it is a true tracer of the connection between the cloud and the HI medium. Internal to that, various isotopologues of CO are available readily with current facilities and archives (e.g. IRAM, CARMA). Deeper in the cloud ($A_V > 5$), carbon-bearing molecules freeze out onto dust grains, so the high-density gas clumps can be probed with N_2H^+, the abundance of which rises in the absence of carbon (Bergin & Langer, 1997). Chapter 5 demonstrates that NH_3 observed with the VLA (5″ resolution) traces the high-density regions in IRDCs well. The observations of the dense gas all require interferometric observations to resolve the small structures. In addition to the full mass profile, this effort will also naturally provide a full kinematic profile of infrared dark clouds and probe chemistry at the high densities characteristic of IRDCs.

6.3.4 The Future of IRDC Studies

Current plans for new observatories are advantageous for IRDC studies. Much attention is now focused on developing infrared and millimeter astronomy, which we've shown to be the ideal for studying IRDCs. Certainly the studies I mention above will present us with new and interesting pursuits in understanding these objects, and below I describe some general ideas about how the Atacama Large Millimeter Array (ALMA) and the James Webb Space Telescope (JWST) will be important to this field.

JWST will be able to probe infrared wavelengths in much the same way as we did in Chapters 3 and 4, except for an order of magnitude improvement in spatial resolution and sensitivity. If one were to conduct this project with JWST instead of *Spitzer*, one would be sensitive to the sorts of pre-stellar "cores" that are the subject to intense study in local clouds (e.g Motte et al., 1998; Lada et al., 2008) and also

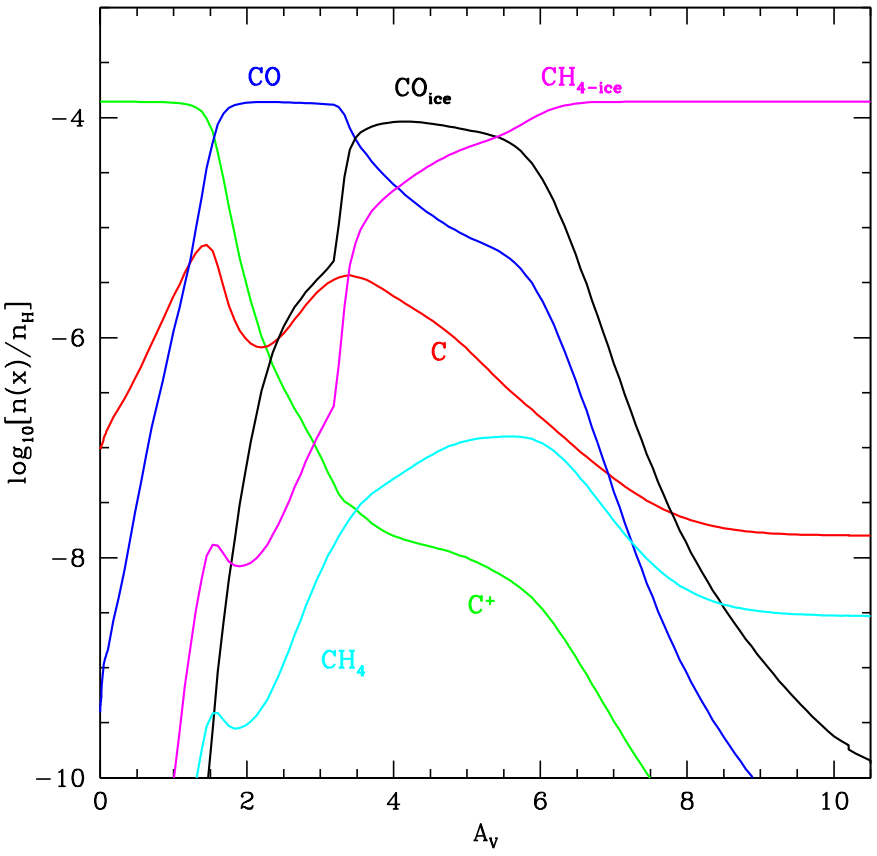

Figure 6.3. Carbon chemistry as a function of A_V. On the edge of dark cloud (where the A_V is low), C^+ has not yet reacted to form CO, making it an unambiguous tracer of the cloud surface (Hollenbach et al., 2009).

improve the sensitivity to embedded objects of lower mass and higher extinction.

ALMA is the centerpiece of numerous fields of astronomy in the coming decades, and infrared-dark clouds are no different. Any molecular study possible today can be done at least an order of magnitude better in sensitivity and resolution given the projected capabilities of the instrument. In IRDCs, the "core" spatial scale will be observable in the continuum and in molecular lines. A full profile of the hierarchical structure of IRDCs will be possible and complex chemistry straightforward to observe. The key is to lay the appropriate foundation in the coming few years to be best prepared to make maximal progress in these future observations.

I hope to address some of the lingering questions by both advancing the techniques developed in this thesis and bringing new ones into the fold. One of my immediate goals is to characterize the star formation in IRDCs with far-infrared observations, which will provide the necessary information to connect cluster formation to the evolution of the clump mass function. Another is to conduct a variety of molecular line studies of IRDCs that will probe the three-dimensional structure of IRDCs.

APPENDICES

APPENDIX A

Basic Properties of Target MSX IRDCs

Table A.1: MSX properties of IRDCs and FCRAO observational parameters

Region Name	HII IRDC	RA (J2000)	Dec (J2000)	Major Axis (′)	Minor Axis (′)	Brightnes Contrast	Bandwidth (km s^{-1})
G0589	G005.85−0.23	17:59:49.50	−24:00:50.25	0.64	0.60	0.409	−20 − 112
	G006.01−0.38	18:00:45.13	−23:57:07.10	1.90	0.78	0.427	···
	G006.26−0.51	18:01:46.57	−23:47:51.61	1.38	0.93	0.587	−25 − 107
G0867	G008.56+0.42	18:03:11.72	−21:20:37.48	0.40	0.36	0.286	···
	G008.64−0.09	18:05:13.98	−21:31:21.58	0.60	0.35	0.292	···
	G009.16+0.06	18:05:46.71	−20:59:51.77	0.80	0.46	0.340	−25 − 107
	G009.20−0.20	18:06:50.86	−21:04:56.00	0.80	0.47	0.288	···
	G009.21−0.22	18:06:56.03	−21:04:59.32	0.80	0.60	0.313	−35 − 113
	G009.28−0.15	18:06:49.96	−20:59:31.46	1.60	0.64	0.431	−38 − 116
	G009.64+0.18	18:06:17.86	−20:31:37.28	0.23	0.15	0.120	···
G1030	G009.80−0.15	18:07:54.07	−20:32:30.17	0.90	0.68	0.242	···
	G009.85−0.14	18:07:57.60	−20:29:31.81	1.20	0.80	0.254	···
	G009.86−0.04	18:07:36.47	−20:26:05.34	1.24	0.61	0.371	−35 − 113
	G009.88−0.11	18:07:55.69	−20:26:52.74	1.10	0.91	0.403	−35 − 113
	G010.27+0.19	18:07:38.17	−19:57:36.60	0.56	0.53	0.183	···
	G010.59−0.31	18:10:08.02	−19:55:34.98	1.00	0.48	0.295	−35 − 113
	G010.70−0.33	18:10:25.44	−19:49:53.70	1.00	0.84	0.367	−60 − 86
	G010.74−0.13	18:09:46.03	−19:42:06.37	5.20	1.50	0.600	···
	G010.74+0.01	18:09:16.59	−19:38:16.41	1.23	0.93	0.413	···
	G010.99−0.09	18:10:07.18	−19:27:59.72	0.80	0.58	0.593	−60 − 86
	G011.13+0.11	18:09:39.49	−19:14:59.92	0.58	0.45	0.239	···

	G011.13−0.13	18:10:34.21	−19:21:46.84	2.40	0.60	0.463	···
	G011.23+0.07	18:10:02.01	−19:11:04.88	1.22	0.27	0.202	···
	G011.24+0.07	18:10:04.30	−19:10:21.11	1.03	0.52	0.283	···
G1194	G012.22+0.14	18:11:47.79	−18:16:51.43	1.68	0.80	0.388	−35 − 113
	G012.50−0.22	18:13:41.44	−18:12:32.16	0.88	0.75	0.475	−35 − 113
	G012.58+0.27	18:12:01.49	−17:54:04.62	1.55	0.61	0.263	···
	G012.61+0.25	18:12:10.65	−17:53:13.15	0.86	0.59	0.235	···
	G012.74−0.36	18:14:41.01	−18:03:59.01	0.87	0.52	0.280	···
G1504	G014.33−0.57	18:18:37.67	−16:45:30.54	0.97	0.51	0.362	−54 − 93
	G014.38−0.46	18:18:19.32	−16:39:44.47	1.36	0.76	0.268	···
	G014.40−0.60	18:18:53.43	−16:43:10.49	1.51	1.51	0.412	···
	G014.49−0.15	18:17:23.71	−16:25:08.20	1.68	0.90	0.465	···
	G014.64−0.57	18:19:14.32	−16:29:39.47	2.25	0.90	0.568	···
	G014.65−0.18	18:17:35.72	−16:16:07.42	0.70	0.32	0.346	···
	G015.05+0.09	18:17:38.41	−15:48:52.11	1.60	0.63	0.532	···
	G015.55−0.45	18:20:34.52	−15:37:54.30	0.88	0.48	0.280	···
G1961	G019.25−0.07	18:26:20.57	−12:11:16.74	0.70	0.39	0.238	···
	G019.28−0.39	18:27:33.68	−12:18:18.35	1.08	0.78	0.417	−35 − 113
	G019.29+0.08	18:25:53.80	−12:04:46.57	2.75	1.10	0.447	···
	G019.35−0.04	18:26:25.72	−12:05:01.46	0.72	0.68	0.275	···
	G019.37−0.03	18:26:27.61	−12:03:30.32	1.01	0.80	0.375	−35 − 113
	G019.40−0.01	18:26:24.05	−12:01:33.28	1.05	0.94	0.330	−35 − 113
	G019.91−0.21	18:28:06.69	−11:39:42.83	1.39	0.98	0.346	···
	G019.97−0.11	18:27:50.94	−11:34:01.67	0.65	0.65	0.275	···
	G019.98−0.21	18:28:15.29	−11:36:20.91	1.57	0.72	0.318	···
G2371	G023.32+0.06	18:33:34.18	−08:31:19.32	2.10	0.42	0.259	···
	G023.37−0.29	18:34:53.66	−08:38:08.59	0.72	0.50	0.376	37 − 183
	G023.38−0.13	18:34:20.09	−08:33:09.71	0.77	0.40	0.321	···
	G023.38−0.51	18:35:45.56	−08:43:54.76	0.71	0.60	0.227	···
	G023.38+0.29	18:32:51.52	−08:21:26.29	0.57	0.50	0.311	···
	G023.44−0.52	18:35:52.89	−08:40:47.92	1.88	0.53	0.313	···
	G023.48+0.11	18:33:41.10	−08:21:31.62	1.22	0.54	0.378	···
	G023.48−0.53	18:35:59.52	−08:38:56.65	1.50	0.50	0.480	−35 − 113
	G023.61−0.01	18:34:21.28	−08:17:21.61	1.82	0.76	0.471	···
	G024.05−0.22	18:35:54.61	−07:59:48.07	0.81	0.51	0.368	37 − 184
	G024.16+0.08	18:35:03.29	−07:45:58.96	0.90	0.84	0.390	37 − 184

	G024.17+0.06	18:35:07.65	−07:45:43.85	0.71	0.37	0.344	···
	G024.37−0.16	18:36:17.34	−07:41:13.82	1.68	1.56	0.467	···
	G024.37−0.21	18:36:29.82	−07:42:41.72	2.10	0.96	0.258	···
	G024.44−0.23	18:36:41.36	−07:39:46.99	1.54	1.51	0.546	···
	G024.63+0.15	18:35:40.73	−07:18:57.64	2.15	0.70	0.533	···
G02572	G025.08+0.20	18:36:19.50	−06:53:44.33	0.80	0.63	0.363	···
	G025.24−0.22	18:38:07.16	−06:56:16.48	0.72	0.56	0.298	···
	G025.25−0.24	18:38:12.01	−06:56:33.53	1.00	0.50	0.283	···
	G025.61+0.24	18:37:10.53	−06:24:01.14	1.70	1.70	0.374	···
	G025.99−0.06	18:38:55.26	−06:12:20.39	1.03	0.80	0.337	−35 − 113
G2996	G030.14−0.07	18:46:34.71	−02:31:13.90	1.40	0.60	0.287	−35 − 113
	G030.31−0.28	18:47:39.31	−02:27:46.38	0.82	0.63	0.226	···
	G030.49−0.39	18:48:23.10	−02:20:54.35	0.84	0.81	0.414	22 − 168
	G030.53−0.27	18:47:42.00	−02:25:08.99	1.25	0.91	0.310	−35 − 113
	G030.58−0.25	18:48:02.48	−02:12:32.12	1.53	0.58	0.305	···
	G030.66+0.05	18:47:08.00	−01:59:53.60	1.82	0.80	0.358	···
	G030.69+0.06	18:47:08.72	−01:58:13.85	0.75	0.63	0.217	···
G3141	G030.89+0.14	18:47:14.08	−01:45:05.75	1.60	0.60	0.321	−35 − 113
	G030.98−0.15	18:48:23.97	−01:48:23.07	1.33	0.80	0.411	−35 − 113
	G031.02−0.12	18:48:22.17	−01:45:03.19	1.62	0.70	0.450	−35 − 113
	G031.23+0.02	18:50:03.85	−00:37:02.40	1.20	0.80	0.361	···
	G031.39+0.30	18:47:34.34	−01:14:10.89	2.10	1.70	0.349	···
	G031.70−0.50	18:50:57.27	−01:19:24.42	0.68	0.50	0.348	···
	G031.71−0.49	18:50:57.76	−01:17:51.09	0.63	0.60	0.336	···
	G032.01+0.05	18:49:33.70	−00:47:32.25	1.17	1.10	0.526	−35 − 113
G3350	G032.84−0.03	18:51:23.35	−00:05:37.42	1.30	0.97	0.357	···
	G033.36−0.01	18:52:14.91	00:22:49.67	1.58	0.84	0.288	···
	G033.42+0.13	18:51:52.52	00:29:24.18	0.44	0.25	0.217	···
	G033.70−0.02	18:52:53.60	00:40:31.43	1.80	0.50	0.250	···
G3426	G033.82−0.22	18:53:50.10	00:41:22.54	0.90	0.53	0.432	2 − 149
	G034.13+0.08	18:53:21.57	01:06:16.14	1.68	0.50	0.254	···
	G034.26+0.19	18:53:11.55	01:16:14.93	1.75	0.61	0.271	···
	G034.74−0.12	18:55:10.11	01:33:09.25	0.90	0.80	0.393	−15 − 131
	G034.74+0.01	18:54:43.32	01:36:55.46	0.75	0.57	0.212	···
	G035.04−0.47	18:56:58.62	01:39:44.74	0.65	0.41	0.312	···
G3520	G034.63−1.03	18:58:10.95	01:02:25.33	0.26	0.18	0.447	−29 − 117

	G034.78−0.80	18:57:40.08	01:16:33.76	0.56	0.45	0.341	−35 − 114
	G035.02−1.50	19:00:34.38	01:10:23.16	0.97	0.35	0.375	···
	G035.20−0.72	18:58:08.92	01:41:31.31	0.78	0.51	0.436	−29 − 117
G3755	G037.08−0.15	18:59:32.80	03:37:25.91	0.42	0.40	0.321	···
	G037.25+0.01	18:59:17.48	03:50:59.94	0.98	0.52	0.296	···
	G037.42+0.17	18:59:00.95	04:04:14.78	0.70	0.64	0.342	···
	G037.44+0.14	18:59:10.75	04:04:24.37	0.79	0.40	0.322	−35 − 113
	G037.89−0.15	19:01:02.00	04:20:18.23	1.03	0.58	0.325	−26 − 107
G4318	G43.19−0.16	19:10:53.01	09:02:30.58	0.42	0.20	0.304	···
	G43.32−0.20	19:11:16.78	09:08:18.83	0.50	0.42	0.165	···
	G43.78+0.05	19:11:14.38	09:39:36.89	0.92	0.91	0.377	−23 − 124
G4389	G43.64−0.82	19:14:07.05	09:08:24.64	0.60	0.21	0.577	−19 − 127
G4426	G44.29−0.09	19:12:42.25	10:03:10.40	0.71	0.46	0.219	···
G5023	G48.84+0.15	19:20:29.90	14:11:12.12	1.22	0.58	0.317	···
	G48.84+0.14	19:20:34.57	14:11:24.84	0.70	0.43	0.242	···
	G50.07+0.06	19:23:14.36	15:13:58.11	0.86	0.33	0.378	−13 − 133
G5031	G51.00−0.18	19:22:55.92	15:56:24.24	0.60	0.35	0.290	···
G5410	G53.88−0.18	19:31:42.73	18:27:55.78	1.12	0.42	0.417	−30 − 116
G6148	G61.52+0.02	19:47:09.72	25:13:00.46	0.60	0.45	0.334	···
G7578	G75.75+0.75	20:19:57.75	37:39:01.90	1.10	0.90	0.474	−33 − 113
	G76.38+0.63	20:22:17.04	38:05:50.23	0.40	0.30	0.318	−33 − 113

APPENDIX B

Sources Coincident with FCRAO IRDCs

The coordinates of each dark region were examined by the *Set of Identifications, Measurements, and Bibliography for Astronomical Data (SIMBAD)* database in search of associated objects indicative of active star formation (e.g. masers, IRAS sources, radio sources). In most cases, there are no such objects in the vicinity of the infrared absorption. However, in eight of the objects, there are indicators of active star formation nearby. To determine the likelihood of association, we compare the position and velocity data between the source and IRDC. Each signpost of active star formation within one arcminute of the central absorption peak position (given in Appendix A) is discussed below.

G009.21−0.22 There is an IRAS source (IRAS 18038-2105; $\alpha(2000) = 18^h06^m53.1^s$, $\delta(2000) = -21°04'38''$) in the vicinity of this absorbing cloud, offset by $0\farcs78$ from the center of the dark region.

G009.88−0.11 This region has an associated 1612 MHz OH maser, which is reported in Blommaert et al. (1994). This source, OH 9.878-0.127, has a position of $\alpha(2000) = 18^h07^m59\fs07$, $\delta(2000) = -20°27'34\farcs3$, which is offset from the center of the IRDC position by $1\farcs05$. This object may be associated with a circumstellar shell around an evolved star, and the velocities believed to correspond to the expanding shells of material are 79.5 and 111.3 km s^{-1}, which is not coincident with the velocity of the emission detected here (17 km s^{-1}).

G010.59−0.31 This region contains a radio source, located at $\alpha(2000) = 18^h10^m6\fs18$, $\delta(2000) = -19°55'33\farcs11$, according to Zoonematkermani et al. (1990), which is offset from the center of the IRDC by $0\farcs44$.

G012.50−0.22 There is an IRAS source (IRAS 18197-1812; $\alpha(2000) = 18^h13^m39\overset{s}{.}0$, $\delta(2000) = -18°11'46''$) offset by $0\overset{''}{.}96$ from the absorbing region.

G019.37−0.03 This region is near a known UC HII region, with a water and methanol maser (Codella & Felli, 1995; Szymczak & Kus, 2000) also identified in the vicinity ($\alpha(2000) = 18^h26^m24\overset{s}{.}3$, $\delta(2000) = -12°3'46''$, offset $0\overset{''}{.}85$ from the absorbing region. The peak velocity of this maser is 26.3 km s^{-1} Szymczak & Kus (2000), which is consistent with the velocity of our measured emission (27 km s^{-1}). Molinari et al. (1996) also observed this maser site and designated it as Mol 55.

G030.89+0.14 This region has an associated methanol maser, as noted by Szymczak & Kus (2000). The maser is located at $\alpha(2000) = 18^h47^m14\overset{s}{.}99$, $\delta(2000) = -1°44'7\overset{''}{.}99$, which is offset from the center of our region by $0\overset{''}{.}99$. Szymczak & Kus (2000), using a 6.7 GHz survey, measured the internal velocity of the maser source to be ≈ 105 km/s, the velocity of the peak to be 101.5 km/s. This is consistent with one of the velocity components we measured in this object (108 km s^{-1}).

G032.01+0.05 This region has an associated IRAS point source (18470-0050) which is offset from the center of our region by $1\overset{''}{.}00$ at $\alpha(2000) = 18^h49^m36\overset{s}{.}6$, $\delta(2000) = -00°46'51''$ which coincides with a radio source Becker et al. (1994). This was confirmed to be a methanol maser (observed in the velocity range between 91 and 102 km s^{-1}) by van der Walt et al. (1995), which is consistent with the emission we observed at 95 km s^{-1}.

G034.74−0.12 This region has an associated IRAS point source (18526+0130) which is offset from the center of our region by $0\overset{''}{.}80$ at $\alpha(2000) = 18^h55^m10^s$, $\delta(2000) = +1°33'57''$.

APPENDIX C

Spitzer Identified Young Stellar Objects: Photometry

Table C.1: YSO Photometry: 2MASS, IRAC, and MIPS photometry.

ID	α (J2000)	δ (J2000)	J	H	K_s	3.6 μm	4.5 μm	5.8 μm	8.0 μm	24 μm	A_K	class[1]
G005.85−0.23												
1	17:59:41.27	-24:03:25.8	···	···	···	···	12.13±0.06	10.88±0.04	9.08±0.02	3.58±0.02	···	EP[2]
2	17:59:49.14	-24:03:50.6	14.70±0.04	11.27±0.03	9.30±0.02	7.27±0.01	6.63±0.01	6.03±0.01	5.60±0.01	···	2.806	CII
3	17:59:49.88	-24:03:44.9	···	13.97±0.06	12.91±0.05	11.87±0.03	11.48±0.04	11.41±0.05	···	···	0.963	CII
4	17:59:51.83	-24:02:04.2	15.41±0.07	11.62±0.03	9.63±0.02	8.37±0.01	7.98±0.01	7.43±0.01	7.30±0.01	5.99±0.06	3.348	CII[2]
5	17:59:47.68	-24:01:33.0	···	···	13.16±0.06	11.71±0.02	11.02±0.01	10.52±0.01	10.09±0.05	···	···	CII
6	17:59:35.96	-24:00:43.8	14.23±0.05	10.82±0.03	8.86±0.02	6.89±0.01	6.49±0.01	6.01±0.01	5.35±0.01	···	2.777	CII
7	17:59:55.30	-24:00:39.3	15.44±0.06	14.45±0.05	13.63±0.05	12.54±0.04	12.31±0.04	12.28±0.12	···	···	···	CII
8	17:59:42.43	-24:00:29.5	10.28±0.02	7.61±0.03	6.28±0.02	5.68±0.01	5.50±0.01	5.14±0.01	4.96±0.01	3.40±0.01	2.176	CII[2]
9	17:59:46.05	-24:00:15.1	···	···	12.73±0.04	10.25±0.02	9.56±0.01	8.72±0.01	7.74±0.02	4.09±0.03	···	CII
10	17:59:48.08	-24:00:12.6	15.30±0.07	11.35±0.03	9.23±0.02	7.28±0.01	6.63±0.01	6.15±0.01	5.57±0.01	4.07±0.03	3.482	CII[2]
11	18:00:02.83	-24:00:07.7	···	···	···	12.65±0.05	12.33±0.04	11.90±0.11	11.01±0.18	···	···	CII
12	17:59:54.07	-23:59:42.9	···	14.39±0.09	11.48±0.03	8.89±0.01	8.48±0.01	7.94±0.01	7.76±0.02	5.85±0.09	4.924	CII[2]
13	18:00:02.08	-23:59:41.2	15.74±0.09	14.26±0.06	13.29±0.06	12.23±0.03	11.91±0.04	11.67±0.10	11.00±0.28	···	0.627	CII
14	18:00:02.14	-23:59:34.7	···	···	13.83±0.05	12.38±0.03	12.07±0.03	11.49±0.07	10.59±0.12	···	···	CII
15	17:59:58.51	-23:59:25.3	15.52±0.06	14.42±0.05	13.16±0.04	12.01±0.03	11.79±0.04	11.56±0.07	11.75±0.32	···	···	CII
16	17:59:57.86	-23:59:12.0	15.35±0.08	11.26±0.03	9.17±0.03	7.54±0.01	7.32±0.01	6.87±0.01	6.74±0.01	4.61±0.04	3.673	CII[2]
17	18:00:02.31	-23:58:56.1	15.85±0.09	12.86±0.04	11.43±0.03	10.40±0.01	10.22±0.01	9.76±0.01	9.50±0.03	···	2.509	CII
18	17:59:39.24	-23:58:31.8	···	···	11.99±0.05	9.77±0.01	8.95±0.01	8.29±0.01	7.45±0.01	5.33±0.04	···	CII
19	18:00:04.04	-23:58:04.8	14.58±0.03	13.78±0.05	13.35±0.06	12.72±0.05	12.54±0.04	12.57±0.14	···	···	0.059	CII
20	17:59:51.58	-23:57:42.7	15.20±0.06	13.88±0.11	12.92±0.09	11.73±0.04	11.33±0.03	11.18±0.05	10.63±0.07	···	0.400	CII
21	17:59:53.59	-23:57:40.0	14.56±0.03	13.67±0.05	13.02±0.07	12.25±0.06	12.02±0.05	12.20±0.20	···	···	0.001	CII
22	17:59:50.39	-23:56:59.8	14.07±0.07	11.13±0.05	9.23±0.03	7.55±0.01	7.30±0.01	6.71±0.01	6.17±0.01	···	2.102	CII

Continued on Next Page...

Table C.1 – YSO Photometry (Continued)

ID	α (J2000)	δ (J2000)	J	H	K_s	3.6 μm	4.5 μm	5.8 μm	8.0 μm	24 μm	A_K	class[1]
23	17:59:46.44	-23:56:53.6	15.26±0.05	11.49±0.02	9.45±0.02	7.67±0.01	7.27±0.01	6.71±0.01	6.30±0.01	···	3.278	CII
24	17:59:52.22	-23:59:03.5	···	13.83±0.05	12.00±0.04	10.51±0.01	10.13±0.01	9.77±0.02	9.66±0.06	6.90±0.13	2.849	TD
G006.26−0.51												
1	18:01:56.78	-23:48:31.4	···	···	13.92±0.07	11.96±0.03	11.17±0.02	10.43±0.08	9.55±0.19	···	···	CI
2	18:01:56.82	-23:47:33.1	···	···	···	10.68±0.01	9.46±0.01	8.44±0.01	7.66±0.03	3.60±0.04	···	CI
3	18:01:57.87	-23:47:10.0	···	14.52±0.10	13.27±0.05	9.26±0.01	7.67±0.01	6.60±0.01	5.88±0.01	2.32±0.03	···	CI
4	18:01:56.33	-23:51:09.6	14.61±0.03	13.16±0.02	12.18±0.03	10.97±0.01	10.37±0.01	···	9.39±0.16	···	0.579	CII
5	18:01:34.21	-23:50:54.0	11.93±0.03	11.17±0.03	10.57±0.03	9.48±0.01	9.03±0.01	8.42±0.01	7.35±0.03	···	···	CII
6	18:01:56.47	-23:50:30.9	···	···	12.58±0.03	10.26±0.01	10.07±0.01	9.43±0.03	9.11±0.12	···	···	CII
7	18:01:41.09	-23:50:22.4	14.29±0.05	10.88±0.03	9.08±0.03	7.42±0.01	7.12±0.01	6.59±0.01	6.41±0.01	4.87±0.13	2.923	CII[2]
8	18:01:42.11	-23:50:19.4	···	13.48±0.03	11.86±0.03	10.81±0.02	10.44±0.01	10.24±0.05	9.70±0.11	···	2.359	CII
9	18:01:43.75	-23:49:39.3	···	···	13.26±0.06	11.34±0.03	10.63±0.02	10.01±0.05	9.21±0.11	6.73±0.49	···	CII
10	18:01:57.38	-23:48:36.8	···	···	···	12.65±0.05	12.01±0.03	11.37±0.09	10.30±0.17	···	···	CII
11	18:01:36.31	-23:48:21.1	15.14±0.08	13.73±0.05	12.90±0.05	11.63±0.04	11.13±0.03	10.71±0.06	10.10±0.19	···	0.643	CII
12	18:01:35.37	-23:48:17.4	14.60±0.03	13.46±0.04	12.95±0.04	11.89±0.03	11.33±0.02	10.99±0.06	10.00±0.11	···	0.512	CII
13	18:01:56.83	-23:48:05.1	15.10±0.03	14.22±0.02	13.61±0.06	13.15±0.15	12.77±0.10	···	···	···	0.011	CII
14	18:01:38.59	-23:47:59.9	14.79±0.05	12.76±0.05	11.76±0.06	10.77±0.01	10.47±0.01	10.00±0.02	9.36±0.05	7.44±0.19	1.475	CII[2]
15	18:01:57.47	-23:47:48.9	15.02±0.06	14.31±0.07	13.54±0.06	12.75±0.07	12.55±0.07	12.17±0.09	···	···	···	CII
16	18:01:57.42	-23:47:20.5	···	···	···	12.08±0.04	11.33±0.03	10.76±0.07	9.98±0.13	···	···	CII
17	18:01:37.34	-23:47:16.9	14.12±0.02	12.47±0.03	11.18±0.03	9.84±0.01	9.26±0.01	8.59±0.01	7.18±0.01	4.41±0.04	0.598	CII
18	18:01:57.46	-23:47:02.7	···	14.46±0.12	13.13±0.05	11.32±0.02	10.57±0.02	10.13±0.06	9.46±0.14	···	0.498	CII
19	18:01:51.84	-23:46:49.7	···	12.64±0.13	···	9.34±0.01	8.72±0.01	8.24±0.01	7.57±0.02	6.23±0.23	···	CII[2]
20	18:01:55.21	-23:46:45.2	14.98±0.04	14.30±0.03	13.66±0.08	12.60±0.05	12.29±0.05	···	···	···	···	CII
21	18:02:00.43	-23:46:40.5	···	14.23±0.09	13.32±0.05	11.94±0.03	11.41±0.03	11.06±0.09	10.55±0.20	···	0.189	CII
22	18:01:55.61	-23:46:38.0	15.87±0.07	15.07±0.08	13.99±0.06	12.77±0.04	12.51±0.04	12.60±0.20	···	···	···	CII

Continued on Next Page...

Table C.1 – YSO Photometry (Continued)

ID	α (J2000)	δ (J2000)	J	H	K_s	3.6 μm	4.5 μm	5.8 μm	8.0 μm	24 μm	A_K	class[1]
23	18:01:35.94	-23:46:26.7	14.33±0.06	13.03±0.05	12.23±0.05	11.35±0.02	11.01±0.01	10.86±0.02	10.36±0.05	···	0.495	CII
24	18:01:53.26	-23:45:47.4	···	···	···	13.40±0.08	12.96±0.05	12.62±0.10	11.44±0.16	···	···	CII
25	18:01:54.11	-23:45:45.6	···	14.15±0.10	13.32±0.04	12.20±0.03	11.70±0.03	11.37±0.06	10.77±0.10	···	0.060	CII
26	18:01:53.27	-23:45:18.2	···	14.76±0.10	13.85±0.07	12.43±0.04	11.98±0.03	11.51±0.08	10.50±0.15	···	0.416	CII
27	18:01:55.61	-23:44:44.4	···	···	···	13.50±0.10	12.94±0.08	12.69±0.13	11.63±0.14	···	···	CII
28	18:01:39.39	-23:44:06.5	14.78±0.08	···	···	11.64±0.04	11.06±0.02	10.42±0.04	9.56±0.04	···	···	CII
29	18:01:37.89	-23:44:05.3	12.03±0.03	9.32±0.02	7.82±0.02	6.39±0.01	6.23±0.01	5.82±0.01	5.44±0.01	···	2.077	CII
G009.16+0.06												
1	18:05:49.67	-21:01:16.9	···	···	···	10.45±0.01	9.63±0.01	8.92±0.01	9.47±0.14	···	···	CI
2	18:05:35.30	-21:03:14.5	···	14.13±0.08	13.13±0.05	12.44±0.04	11.92±0.03	···	12.16±0.28	···	0.416	CII
3	18:05:38.19	-21:02:21.9	···	11.11±0.04	9.34±0.02	7.41±0.01	7.15±0.01	6.67±0.01	6.56±0.01	5.86±0.06	2.856	CII[2]
4	18:05:50.26	-21:00:37.4	···	···	12.79±0.05	10.93±0.02	10.63±0.02	10.07±0.05	9.63±0.15	···	···	CII
5	18:05:50.89	-20:59:31.7	···	13.29±0.04	12.72±0.04	11.99±0.04	11.77±0.04	11.81±0.12	···	···	0.359	CII
6	18:06:00.33	-20:58:24.8	···	14.30±0.08	12.73±0.04	11.48±0.03	10.87±0.02	10.91±0.06	10.64±0.22	···	1.539	CII
7	18:05:36.68	-20:58:10.6	···	···	12.41±0.05	10.33±0.01	9.60±0.01	8.99±0.01	8.27±0.01	6.21±0.07	···	CII
8	18:05:55.78	-20:57:34.1	15.88±0.09	11.47±0.02	9.38±0.02	7.74±0.01	7.53±0.01	7.05±0.01	6.69±0.01	5.37±0.09	4.016	CII[2]
9	18:05:53.18	-20:57:08.6	10.00±0.03	7.40±0.05	5.93±0.02	5.20±0.01	4.72±0.01	4.19±0.01	3.88±0.01	2.25±0.01	1.932	CII[2]
10	18:05:57.41	-20:57:01.2	12.96±0.03	9.41±0.02	7.35±0.03	5.61±0.01	5.08±0.01	4.44±0.01	3.77±0.01	1.08±0.01	2.899	CII
11	18:05:47.52	-20:56:25.0	14.82±0.05	14.00±0.07	13.27±0.07	12.28±0.04	12.05±0.04	12.08±0.14	···	···	···	CII
12	18:05:46.39	-20:55:51.8	···	···	···	12.15±0.04	11.51±0.03	10.77±0.03	10.60±0.07	···	···	CII
13	18:05:56.62	-21:00:19.2	···	···	12.65±0.05	8.25±0.01	6.50±0.01	5.22±0.01	4.44±0.01	1.96±0.01	···	CII
G009.28−0.15												
1	18:06:41.48	-20:59:32.5	···	···	···	12.89±0.07	11.32±0.02	10.28±0.03	9.65±0.04	8.24±0.43	···	CI[2]
2	18:06:53.72	-20:59:21.5	14.54±0.02	13.93±0.02	13.40±0.03	12.00±0.02	11.23±0.01	10.84±0.04	11.09±0.24	···	···	CI
3	18:06:53.75	-21:02:58.1	···	14.14±0.08	12.29±0.04	11.49±0.03	10.83±0.03	9.99±0.07	···	···	2.017	CII

Continued on Next Page...

Table C.1 – YSO Photometry (Continued)

ID	α (J2000)	δ (J2000)	J	H	K_s	3.6 μm	4.5 μm	5.8 μm	8.0 μm	24 μm	A_K	class[1]
4	18:06:50.16	-21:02:47.7	13.76±0.04	13.18±0.06	12.99±0.05	12.32±0.03	11.87±0.03	11.64±0.10	12.08±0.66	···	···	CII
5	18:06:50.38	-21:02:40.0	···	···	13.44±0.06	12.13±0.05	11.87±0.03	11.45±0.08	10.98±0.18	···	···	CII
6	18:06:54.00	-21:02:01.0	13.52±0.04	12.99±0.05	12.53±0.05	12.01±0.05	11.77±0.05	11.64±0.12	11.85±0.46	···	···	CII
7	18:06:49.53	-21:01:52.2	15.21±0.05	13.02±0.06	10.63±0.03	8.97±0.01	8.62±0.01	7.98±0.01	7.95±0.01	7.11±0.12	0.451	CII[2]
8	18:06:39.68	-21:01:47.1	···	···	···	11.84±0.03	11.08±0.02	10.46±0.02	10.21±0.07	···	···	CII
9	18:06:53.38	-21:01:41.4	13.82±0.04	13.16±0.05	12.85±0.03	12.63±0.04	12.30±0.04	12.87±0.32	···	···	···	CII
10	18:06:51.07	-21:01:12.3	14.93±0.06	14.10±0.04	13.68±0.04	12.94±0.06	12.48±0.07	12.48±0.18	···	···	0.101	CII
11	18:06:40.16	-21:00:53.3	···	···	···	12.52±0.05	12.17±0.04	11.66±0.07	11.34±0.16	···	···	CII
12	18:06:56.90	-20:59:09.0	···	13.92±0.08	12.06±0.03	10.78±0.02	10.56±0.02	9.94±0.02	9.63±0.07	···	3.027	CII
13	18:06:36.88	-20:58:40.6	7.72±0.02	6.03±0.04	5.26±0.02	5.53±0.01	5.20±0.01	4.75±0.01	4.59±0.01	···	1.137	CII
14	18:06:47.33	-20:58:07.3	14.08±0.03	13.50±0.04	13.20±0.03	12.70±0.04	12.47±0.04	12.42±0.13	···	···	···	CII
15	18:06:50.18	-20:57:52.2	15.76±0.10	14.63±0.07	13.56±0.06	12.65±0.04	12.33±0.04	···	···	···	···	CII
16	18:06:42.70	-20:56:53.7	12.19±0.02	9.01±0.02	7.25±0.02	5.74±0.01	5.45±0.01	5.04±0.01	4.77±0.01	3.09±0.01	2.591	CII[2]
17	18:06:42.07	-20:58:01.9	···	···	···	10.15±0.01	9.08±0.01	8.30±0.01	7.78±0.01	5.85±0.06	···	CII
G009.86−0.04												
1	18:07:30.41	-20:29:23.7	···	···	11.37±0.05	6.19±0.01	5.05±0.01	4.03±0.01	3.76±0.01	···	···	CI
2	18:07:39.41	-20:26:41.1	···	14.30±0.02	12.51±0.02	11.17±0.01	10.19±0.01	9.25±0.01	8.10±0.04	4.12±0.02	0.853	CI
3	18:07:38.42	-20:26:31.8	···	···	···	11.36±0.01	10.57±0.01	9.57±0.02	8.78±0.06	5.09±0.06	···	CI
4	18:07:33.91	-20:26:20.3	···	···	···	11.06±0.01	9.07±0.01	7.72±0.01	6.64±0.01	2.14±0.01	···	CI
5	18:07:39.53	-20:26:09.8	···	···	···	13.80±0.10	12.51±0.04	11.59±0.10	10.48±0.16	5.20±0.06	···	CI
6	18:07:36.99	-20:26:03.9	···	···	···	14.93±0.17	13.37±0.08	···	···	6.53±0.14	···	EP[2]
7	18:07:42.12	-20:23:34.3	···	···	···	···	12.75±0.11	11.94±0.09	9.88±0.05	4.55±0.02	···	EP[2]
8	18:07:24.28	-20:28:45.3	16.20±0.10	14.34±0.09	13.35±0.09	11.95±0.07	11.31±0.04	10.79±0.06	10.07±0.06	···	1.218	CII
9	18:07:47.77	-20:28:23.9	15.58±0.05	14.23±0.05	13.66±0.08	12.86±0.05	12.54±0.04	12.39±0.25	···	···	0.794	CII
10	18:07:30.10	-20:27:58.8	12.41±0.03	9.60±0.04	8.10±0.03	6.91±0.01	6.72±0.01	6.23±0.01	5.98±0.01	4.71±0.05	2.258	CII[2]

Continued on Next Page...

Table C.1 – YSO Photometry (Continued)

ID	α (J2000)	δ (J2000)	J	H	K_s	3.6 μm	4.5 μm	5.8 μm	8.0 μm	24 μm	A_K	class[1]
11	18:07:49.90	-20:27:50.4	15.59±0.08	14.02±0.09	13.23±0.07	12.47±0.07	12.10±0.08	12.16±0.20	···	···	0.950	CII
12	18:07:49.71	-20:27:47.7	16.20±0.09	14.38±0.04	13.52±0.05	12.62±0.03	12.29±0.04	12.72±0.33	···	···	1.287	CII
13	18:07:47.05	-20:27:45.0	···	···	···	9.91±0.01	9.46±0.01	8.97±0.01	8.78±0.04	···	···	CII
14	18:07:47.19	-20:27:44.6	14.57±0.06	12.80±0.09	11.24±0.05	9.93±0.01	9.44±0.01	···	8.80±0.04	5.85±0.08	0.547	CII
15	18:07:45.51	-20:27:26.7	12.51±0.02	9.64±0.02	8.04±0.03	6.48±0.01	6.30±0.01	5.78±0.01	5.71±0.01	4.50±0.01	2.241	CII[2]
16	18:07:44.56	-20:27:06.3	13.58±0.04	12.45±0.06	11.69±0.04	10.54±0.02	10.08±0.02	9.75±0.03	9.13±0.03	6.34±0.06	0.271	CII
17	18:07:44.23	-20:26:45.5	14.93±0.04	13.26±0.06	12.23±0.05	10.95±0.01	10.46±0.01	10.04±0.02	9.55±0.05	6.99±0.13	0.861	CII
18	18:07:23.41	-20:25:53.3	14.80±0.05	10.55±0.02	8.03±0.03	5.63±0.01	5.00±0.01	4.21±0.01	3.53±0.01	···	3.599	CII
19	18:07:30.08	-20:25:43.9	···	···	···	12.44±0.04	12.20±0.04	11.89±0.08	11.05±0.14	···	···	CII
20	18:07:32.65	-20:25:23.9	···	···	···	12.76±0.04	12.47±0.04	11.99±0.07	11.53±0.17	···	···	CII
21	18:07:49.54	-20:25:17.8	14.94±0.03	13.87±0.04	13.35±0.08	12.88±0.05	12.57±0.04	···	···	···	0.399	CII
22	18:07:41.01	-20:25:09.7	13.40±0.05	10.86±0.05	9.32±0.04	7.43±0.01	7.02±0.01	6.73±0.01	6.41±0.01	···	1.795	CII
23	18:07:45.25	-20:24:08.3	···	···	···	11.97±0.06	11.21±0.04	10.57±0.05	9.98±0.07	7.29±0.16	···	CII
24	18:07:48.21	-20:23:20.9	···	14.92±0.06	13.51±0.05	12.19±0.05	11.73±0.03	11.44±0.10	10.50±0.21	···	1.620	CII
25	18:07:36.45	-20:23:00.2	13.84±0.02	13.05±0.02	12.66±0.02	12.26±0.04	11.99±0.04	12.17±0.08	12.62±0.24	···	0.074	CII
26	18:07:41.30	-20:22:58.9	14.97±0.06	14.00±0.10	13.09±0.07	11.99±0.06	11.80±0.06	11.64±0.11	···	···	···	CII
27	18:07:37.93	-20:22:59.2	···	···	···	10.84±0.05	10.58±0.04	9.91±0.04	8.99±0.02	···	···	CII
28	18:07:29.61	-20:24:00.6	···	···	···	11.61±0.03	10.57±0.01	9.76±0.01	8.96±0.03	7.11±0.09	···	CII
29	18:07:42.65	-20:27:36.0	14.55±0.02	13.24±0.06	12.45±0.03	11.49±0.03	11.19±0.02	10.94±0.03	10.68±0.09	7.29±0.10	0.525	TD
30	18:07:41.00	-20:25:18.8	13.12±0.03	10.48±0.03	9.30±0.03	8.60±0.01	8.44±0.01	8.17±0.01	8.02±0.03	5.81±0.03	2.147	TD[2]
31	18:07:43.64	-20:23:44.3	13.30±0.04	12.32±0.06	···	11.50±0.03	11.34±0.03	11.32±0.03	11.01±0.07	6.83±0.07	···	TD
G012.50−0.22												
1	18:13:26.53	-18:15:28.5	···	···	···	11.72±0.03	10.66±0.02	9.72±0.02	9.14±0.04	···	···	CI
2	18:13:41.16	-18:12:48.6	···	···	···	11.53±0.01	9.06±0.01	7.80±0.01	7.78±0.04	6.22±0.26	···	CI
3	18:13:55.05	-18:11:37.5	···	···	···	12.75±0.09	11.18±0.02	10.10±0.02	9.31±0.03	···	···	CI

Continued on Next Page...

Table C.1 – YSO Photometry (Continued)

ID	α (J2000)	δ (J2000)	J	H	K_s	3.6 μm	4.5 μm	5.8 μm	8.0 μm	24 μm	A_K	class[1]
4	18:13:48.85	-18:09:19.4	15.95±0.09	14.74±0.13	13.40±0.10	6.10±0.01	4.77±0.01	3.50±0.01	2.78±0.01	···	···	CI
5	18:13:41.71	-18:12:29.6	···	···	···	···	12.35±0.04	10.94±0.07	10.12±0.05	4.56±0.12	···	EP[2]
6	18:13:40.99	-18:15:33.4	15.36±0.08	13.24±0.04	11.66±0.05	10.05±0.01	9.59±0.01	9.05±0.01	8.03±0.01	···	1.089	CII
7	18:13:47.88	-18:14:40.3	···	···	13.76±0.05	12.32±0.02	12.05±0.02	11.71±0.07	11.00±0.18	···	···	CII
8	18:13:30.37	-18:13:58.4	13.92±0.05	13.16±0.02	12.26±0.04	10.64±0.04	10.21±0.02	9.65±0.04	8.78±0.04	···	···	CII
9	18:13:54.54	-18:13:51.4	···	14.48±0.09	···	11.96±0.04	11.33±0.03	10.74±0.05	10.32±0.16	···	···	CII
10	18:13:28.58	-18:12:58.3	10.48±0.02	7.68±0.04	6.32±0.02	5.58±0.01	5.42±0.01	5.00±0.01	4.89±0.01	···	2.312	CII
11	18:13:48.73	-18:12:38.0	···	14.28±0.07	13.04±0.04	12.27±0.05	12.03±0.05	11.64±0.09	11.26±0.09	···	1.885	CII
12	18:13:41.65	-18:12:36.6	···	···	···	13.92±0.04	12.95±0.04	12.28±0.07	11.15±0.11	···	···	CII
13	18:13:31.59	-18:12:23.0	···	···	···	11.84±0.05	11.29±0.04	10.56±0.07	10.43±0.07	···	···	CII
14	18:13:38.38	-18:12:00.4	12.20±0.03	11.05±0.02	9.94±0.02	8.82±0.01	8.12±0.01	7.29±0.01	5.50±0.01	2.35±0.02	···	CII
15	18:13:34.99	-18:11:55.3	···	···	13.32±0.06	11.98±0.03	11.74±0.04	11.51±0.04	10.98±0.14	···	···	CII
16	18:13:51.28	-18:11:54.7	···	···	12.93±0.10	11.75±0.06	11.46±0.05	11.23±0.07	10.70±0.15	···	···	CII
17	18:13:50.82	-18:11:31.3	···	11.06±0.03	8.05±0.02	6.26±0.01	5.94±0.01	5.37±0.01	5.31±0.01	3.87±0.02	5.116	CII[2]
18	18:13:29.03	-18:11:30.2	···	14.32±0.03	11.16±0.02	8.82±0.01	8.57±0.01	8.02±0.01	7.95±0.02	···	5.393	CII
19	18:13:38.17	-18:11:29.2	11.96±0.02	8.57±0.05	6.78±0.02	5.81±0.01	5.50±0.01	5.07±0.01	4.81±0.01	2.79±0.01	2.915	CII[2]
20	18:13:33.65	-18:11:27.5	14.32±0.04	13.41±0.04	12.97±0.04	12.34±0.03	11.96±0.03	11.67±0.12	11.34±0.41	···	0.225	CII
21	18:13:34.03	-18:11:23.5	15.56±0.07	13.48±0.05	12.41±0.03	11.05±0.01	10.60±0.01	10.17±0.03	9.70±0.08	···	1.477	CII
22	18:13:27.39	-18:11:23.1	···	13.25±0.06	12.69±0.04	11.33±0.03	11.12±0.03	10.38±0.06	10.97±0.57	···	0.335	CII
23	18:13:33.71	-18:11:17.0	15.47±0.06	14.02±0.02	13.53±0.04	12.65±0.04	12.27±0.03	11.98±0.12	11.57±0.40	···	0.884	CII
24	18:13:34.43	-18:10:54.2	···	···	13.32±0.06	12.28±0.05	11.60±0.04	10.92±0.03	9.82±0.03	5.97±0.05	···	CII
25	18:13:47.41	-18:09:21.0	···	11.32±0.03	9.05±0.02	7.43±0.01	6.88±0.01	6.40±0.01	6.15±0.01	···	3.374	CII
26	18:13:39.18	-18:08:33.3	13.86±0.08	12.88±0.06	11.97±0.03	10.61±0.02	10.20±0.01	9.75±0.03	9.14±0.07	···	···	CII
27	18:13:42.91	-18:12:40.9	···	···	13.37±0.04	9.87±0.01	8.76±0.01	7.78±0.01	6.83±0.02	3.81±0.06	···	CII
28	18:13:32.00	-18:13:01.0	13.15±0.05	9.41±0.03	7.41±0.03	6.04±0.01	5.90±0.01	5.36±0.01	5.16±0.01	3.00±0.01	3.254	TD[2]

Continued on Next Page...

Table C.1 – YSO Photometry (Continued)

ID	α (J2000)	δ (J2000)	J	H	K_s	3.6 μm	4.5 μm	5.8 μm	8.0 μm	24 μm	A_K	class[1]
G023.37−0.29												
1	18:34:52.72	-08:41:51.7	···	14.03±0.12	···	8.35±0.01	7.30±0.01	6.57±0.01	6.03±0.03	···	···	CI
2	18:34:50.08	-08:40:44.1	···	···	···	13.06±0.04	10.50±0.01	8.92±0.02	8.21±0.05	4.71±0.16	···	CI
3	18:34:48.76	-08:37:29.1	···	···	···	10.62±0.01	9.60±0.01	8.78±0.01	9.09±0.05	···	···	CI
4	18:34:58.51	-08:36:11.2	15.22±0.05	14.48±0.08	12.80±0.03	10.70±0.02	10.39±0.01	9.92±0.04	10.42±0.24	···	···	CI
5	18:34:55.51	-08:35:10.0	···	···	14.09±0.08	11.84±0.03	10.87±0.02	10.09±0.05	8.60±0.05	···	···	CI
6	18:34:54.05	-08:34:57.3	···	···	···	12.37±0.02	11.45±0.01	10.63±0.05	10.26±0.12	···	···	CI
7	18:34:57.32	-08:34:53.8	···	···	···	12.27±0.04	11.29±0.03	10.50±0.04	10.53±0.14	···	···	
8	18:34:55.03	-08:34:27.2	···	···	14.11±0.08	10.41±0.01	9.42±0.01	8.67±0.03	8.62±0.12	···	···	CI
9	18:34:54.12	-08:38:25.5	···	···	···	···	12.64±0.11	10.85±0.12	10.95±0.45	4.82±0.09	···	EP[2]
10	18:35:00.04	-08:36:57.4	···	14.76±0.11	13.72±0.09	12.87±0.04	12.71±0.05	12.06±0.16	···	5.50±0.10	1.524	EP[2]
11	18:34:53.49	-08:41:15.9	···	···	10.92±0.06	9.76±0.01	9.49±0.01	9.01±0.04	8.54±0.10	···	···	CII
12	18:34:51.48	-08:41:08.1	15.68±0.10	13.89±0.07	12.96±0.05	12.16±0.04	11.72±0.05	···	···	···	1.169	CII
13	18:35:00.01	-08:40:46.1	···	14.39±0.09	13.42±0.06	12.65±0.07	12.23±0.07	···	···	···	0.699	CII
14	18:34:56.54	-08:40:36.9	···	···	13.62±0.05	11.92±0.02	11.63±0.02	11.19±0.06	10.53±0.17	···	···	CII
15	18:34:45.42	-08:40:37.3	···	···	14.15±0.08	11.81±0.02	11.30±0.02	10.70±0.07	10.06±0.17	···	···	CII
16	18:34:48.30	-08:40:21.1	15.20±0.08	14.06±0.06	13.58±0.06	13.06±0.08	12.60±0.08	12.45±0.25	···	···	0.546	CII
17	18:34:50.36	-08:40:13.5	14.71±0.04	13.86±0.05	13.27±0.05	12.73±0.04	12.54±0.07	12.47±0.34	···	···	···	CII
18	18:34:44.87	-08:40:11.9	···	···	···	12.39±0.04	11.92±0.04	11.18±0.09	10.23±0.15	···	···	CII
19	18:35:00.96	-08:40:09.9	13.75±0.04	13.36±0.04	13.14±0.05	12.95±0.06	12.33±0.09	···	···	···	···	CII
20	18:34:45.68	-08:40:07.0	15.96±0.08	14.44±0.06	13.57±0.05	12.77±0.04	12.51±0.04	12.28±0.50	···	···	0.773	CII
21	18:34:43.56	-08:39:51.5	···	···	13.29±0.05	11.55±0.02	11.21±0.02	10.76±0.06	10.33±0.16	···	···	CII
22	18:35:00.82	-08:39:41.8	···	···	···	11.82±0.05	11.51±0.05	11.10±0.13	10.26±0.17	···	···	CII
23	18:34:48.11	-08:39:34.3	14.46±0.03	13.81±0.03	13.02±0.03	12.00±0.02	11.74±0.02	11.56±0.11	···	···	···	CII
24	18:34:48.23	-08:39:24.8	15.84±0.10	14.44±0.06	13.77±0.06	12.99±0.03	12.72±0.02	···	···	···	0.783	CII

Continued on Next Page...

Table C.1 – YSO Photometry (Continued)

ID	α (J2000)	δ (J2000)	J	H	K_s	3.6 μm	4.5 μm	5.8 μm	8.0 μm	24 μm	A_K	class[1]
25	18:35:03.36	-08:39:21.6	···	···	13.10±0.06	11.41±0.02	11.12±0.02	10.80±0.05	10.49±0.06	···	···	CII
26	18:35:01.40	-08:39:15.9	14.66±0.07	13.87±0.08	13.45±0.05	12.94±0.05	12.67±0.05	12.59±0.20	···	···	0.060	CII
27	18:34:50.02	-08:39:10.3	···	···	···	12.48±0.04	11.95±0.03	11.26±0.09	10.67±0.15	···	···	CII
28	18:34:44.51	-08:39:03.7	14.87±0.05	14.24±0.02	14.04±0.06	13.86±0.10	13.35±0.17	···	···	···	···	CII
29	18:34:52.88	-08:38:56.1	···	···	13.98±0.07	11.81±0.02	11.25±0.01	10.54±0.09	9.61±0.20	···	···	CII
30	18:34:47.94	-08:38:35.6	15.88±0.09	13.88±0.05	12.90±0.05	11.88±0.05	11.33±0.06	10.90±0.22	···	···	1.458	CII
31	18:34:58.79	-08:38:21.2	···	···	14.40±0.09	12.27±0.03	11.85±0.03	11.24±0.06	10.90±0.18	···	···	CII
32	18:34:50.43	-08:38:04.6	14.95±0.04	14.29±0.06	14.11±0.08	13.48±0.06	13.16±0.06	12.80±0.28	···	···	0.064	CII
33	18:34:49.07	-08:38:03.0	···	12.03±0.02	9.13±0.02	6.80±0.01	6.41±0.01	5.80±0.01	5.67±0.01	4.17±0.05	4.907	CII[2]
34	18:34:42.06	-08:38:00.6	14.86±0.05	13.14±0.06	12.22±0.04	11.38±0.02	11.03±0.02	10.72±0.07	10.30±0.24	···	1.062	CII
35	18:35:02.67	-08:37:51.3	14.47±0.04	13.92±0.05	13.61±0.06	13.26±0.05	12.83±0.06	···	···	···	···	CII
36	18:34:55.85	-08:37:50.8	···	14.58±0.08	12.97±0.04	11.52±0.02	10.94±0.01	10.43±0.05	9.82±0.11	···	1.715	CII
37	18:35:03.81	-08:37:27.2	16.25±0.13	14.27±0.05	12.61±0.03	11.14±0.02	10.93±0.01	10.58±0.06	10.62±0.26	···	0.788	CII
38	18:35:05.07	-08:37:03.4	···	14.68±0.06	13.26±0.05	12.21±0.05	11.79±0.04	11.35±0.25	10.30±0.36	···	1.738	CII
39	18:34:49.48	-08:36:30.6	14.60±0.06	13.14±0.02	12.50±0.02	11.47±0.07	10.99±0.07	···	···	···	0.912	CII
40	18:34:55.98	-08:36:28.9	···	···	···	12.12±0.02	11.79±0.02	11.21±0.10	10.86±0.13	···	···	CII
41	18:34:43.22	-08:36:28.5	15.87±0.08	14.57±0.06	13.79±0.06	13.09±0.07	12.76±0.07	···	···	···	0.519	CII
42	18:34:59.28	-08:36:22.9	14.30±0.03	13.65±0.05	13.26±0.04	12.76±0.06	12.47±0.06	12.09±0.12	12.21±0.64	···	···	CII
43	18:35:05.36	-08:36:08.6	16.05±0.11	14.15±0.06	12.88±0.04	11.73±0.03	11.26±0.03	10.58±0.07	9.38±0.10	···	1.025	CII
44	18:34:54.85	-08:36:04.6	15.11±0.05	14.34±0.04	14.19±0.09	13.59±0.11	13.18±0.09	···	···	···	0.174	CII
45	18:34:46.61	-08:35:21.4	14.78±0.04	12.99±0.09	12.24±0.06	11.71±0.04	11.12±0.05	···	···	···	1.252	CII
46	18:34:56.72	-08:37:13.5	···	···	···	9.67±0.01	7.31±0.01	5.39±0.01	4.30±0.01	1.92±0.01	···	CII
G023.48−0.53												
1	18:35:51.33	-08:41:12.2	···	···	···	13.10±0.04	11.36±0.02	10.06±0.03	9.16±0.08	2.12±0.02	···	CI
2	18:35:50.60	-08:41:10.4	···	···	···	12.48±0.02	9.74±0.01	8.01±0.01	6.91±0.01	2.89±0.01	···	CI

Continued on Next Page...

Table C.1 – YSO Photometry (Continued)

ID	α (J2000)	δ (J2000)	J	H	K_s	3.6 μm	4.5 μm	5.8 μm	8.0 μm	24 μm	A_K	class[1]
3	18:35:50.85	-08:41:08.6	···	···	···	12.00±0.02	10.54±0.01	9.53±0.02	8.68±0.04	···	···	CI
4	18:35:59.06	-08:38:58.4	···	···	···	11.98±0.01	10.47±0.01	9.44±0.02	9.48±0.08	···	···	CI
5	18:36:10.79	-08:37:45.2	···	···	11.60±0.02	6.75±0.01	5.58±0.01	4.66±0.01	4.30±0.01	···	···	CI
6	18:35:54.47	-08:42:58.3	15.61±0.08	14.70±0.08	13.63±0.05	12.63±0.03	12.44±0.05	12.40±0.10	···	···	···	CII
7	18:35:51.23	-08:41:38.1	···	···	···	12.15±0.03	11.31±0.01	10.70±0.04	9.73±0.08	6.54±0.07	···	CII
8	18:36:08.71	-08:41:35.5	15.49±0.07	14.73±0.09	13.93±0.07	12.91±0.04	12.73±0.05	12.83±0.14	···	···	···	CII
9	18:35:48.61	-08:41:29.6	14.70±0.05	13.93±0.04	13.50±0.04	12.78±0.04	12.51±0.05	12.54±0.20	12.63±0.89	···	···	CII
10	18:35:48.14	-08:41:16.4	15.00±0.06	13.97±0.08	13.08±0.06	12.25±0.03	11.98±0.03	11.81±0.10	···	···	···	CII
11	18:35:56.19	-08:40:38.9	···	11.49±0.03	8.91±0.02	6.87±0.01	6.48±0.01	5.93±0.01	5.83±0.01	4.72±0.04	4.316	CII[2]
12	18:36:07.50	-08:40:18.9	13.33±0.03	12.76±0.03	12.31±0.03	11.76±0.01	11.61±0.01	11.51±0.05	11.42±0.26	···	···	CII
13	18:36:04.50	-08:39:40.2	···	10.63±0.02	7.49±0.02	5.81±0.01	5.30±0.01	4.76±0.01	4.62±0.01	3.05±0.01	5.336	CII[2]
14	18:36:14.10	-08:39:32.5	9.62±0.03	9.02±0.02	8.54±0.02	7.92±0.01	7.62±0.01	7.45±0.01	7.05±0.01	···	···	CII
15	18:35:56.05	-08:38:19.4	···	···	···	12.50±0.04	12.13±0.04	11.53±0.08	10.88±0.15	···	···	CII
16	18:35:58.88	-08:38:03.8	16.09±0.11	14.83±0.09	13.83±0.06	12.86±0.03	12.68±0.03	12.32±0.12	11.76±0.26	···	0.253	CI
17	18:36:10.78	-08:37:56.6	13.90±0.04	12.60±0.03	12.14±0.03	11.66±0.03	11.15±0.03	···	···	···	0.741	CII
18	18:35:49.42	-08:37:54.3	···	···	13.22±0.04	11.92±0.01	11.69±0.01	11.38±0.08	10.84±0.17	···	···	CII
19	18:36:04.83	-08:35:58.9	···	12.42±0.03	9.58±0.02	6.74±0.01	5.93±0.01	5.33±0.01	5.10±0.01	4.45±0.03	3.937	CII[2]
20	18:36:08.72	-08:35:30.0	15.11±0.05	14.33±0.06	13.71±0.06	12.76±0.05	12.50±0.04	12.64±0.11	···	···	···	CII
21	18:36:02.39	-08:39:31.6	···	···	···	10.18±0.01	8.27±0.01	7.13±0.01	7.01±0.02	5.71±0.15	···	CII[2]
G024.05−0.22												
1	18:35:54.73	-08:01:30.2	···	···	···	···	13.43±0.10	12.59±0.15	11.28±0.18	6.72±0.08	···	EP[2]
2	18:35:56.33	-08:03:05.8	14.00±0.04	13.32±0.04	12.81±0.05	12.34±0.05	12.10±0.05	11.92±0.14	···	···	···	CII
3	18:35:53.96	-08:03:05.0	···	···	13.43±0.05	11.16±0.01	10.37±0.01	9.86±0.01	9.34±0.04	···	···	CII
4	18:35:47.63	-08:02:57.1	···	···	···	11.27±0.01	10.74±0.01	10.11±0.02	9.15±0.03	···	···	CII
5	18:35:56.71	-08:02:49.2	14.50±0.05	13.85±0.07	13.27±0.07	12.71±0.08	12.47±0.07	12.57±0.13	···	···	···	CII

Continued on Next Page...

Table C.1 – YSO Photometry (Continued)

ID	α (J2000)	δ (J2000)	J	H	K_s	3.6 μm	4.5 μm	5.8 μm	8.0 μm	24 μm	A_K	class[1]
6	18:35:59.28	-08:00:50.0	···	12.07±0.03	9.74±0.02	8.09±0.01	7.84±0.01	7.36±0.01	7.25±0.01	5.62±0.08	3.867	CII[2]
7	18:35:52.59	-07:59:59.9	12.16±0.03	8.77±0.02	···	5.91±0.01	5.68±0.01	5.20±0.01	5.00±0.01	3.06±0.03	···	CII[2]
8	18:35:56.31	-07:59:42.8	···	13.91±0.05	12.49±0.05	11.57±0.02	11.34±0.03	11.11±0.07	10.59±0.18	···	2.224	CII
9	18:36:02.04	-07:59:31.7	14.74±0.05	···	···	7.54±0.01	7.31±0.01	6.83±0.01	6.64±0.01	4.36±0.05	···	CII[2]
10	18:35:54.00	-07:59:30.9	15.17±0.06	14.29±0.05	13.82±0.06	12.93±0.05	12.61±0.06	···	···	···	0.136	CII
11	18:35:51.03	-07:59:24.9	···	···	13.50±0.06	11.78±0.04	11.33±0.04	10.79±0.05	10.11±0.05	6.11±0.17	···	CII
12	18:35:58.53	-07:59:21.4	···	12.64±0.04	9.80±0.03	7.93±0.01	7.33±0.01	6.69±0.01	6.53±0.01	5.14±0.10	4.604	CII[2]
13	18:35:55.45	-07:59:14.2	13.81±0.03	13.03±0.03	12.27±0.03	11.44±0.01	11.32±0.01	11.14±0.06	11.27±0.28	···	···	CII
14	18:35:50.82	-07:58:33.1	···	···	···	12.37±0.08	11.90±0.07	11.44±0.06	10.70±0.06	···	···	CII
15	18:35:48.19	-07:58:24.8	···	11.94±0.03	9.64±0.02	7.77±0.01	7.52±0.01	6.90±0.01	6.85±0.01	5.23±0.09	3.815	CII[2]
16	18:35:49.01	-07:57:42.9	···	···	···	12.54±0.08	11.90±0.05	11.37±0.06	10.69±0.12	···	···	CII
17	18:35:47.55	-07:57:36.4	···	···	13.23±0.05	11.66±0.03	11.45±0.02	10.96±0.04	10.74±0.12	···	···	CII
18	18:36:04.10	-07:57:20.0	15.91±0.10	11.40±0.02	9.16±0.03	7.81±0.01	7.56±0.01	6.98±0.01	6.93±0.01	5.41±0.14	4.111	CII[2]
19	18:35:47.24	-07:57:18.7	···	15.06±0.20	···	12.80±0.07	12.23±0.06	11.73±0.10	10.89±0.16	···	···	CII
20	18:35:58.82	-07:56:58.4	···	···	13.58±0.08	11.71±0.01	11.51±0.03	11.06±0.07	10.62±0.19	···	···	CII
21	18:35:46.70	-07:56:50.4	12.87±0.03	12.50±0.03	11.93±0.04	11.51±0.02	11.32±0.02	···	10.66±0.22	···	···	CII
22	18:35:58.32	-07:56:34.1	15.32±0.05	14.30±0.06	13.34±0.05	12.44±0.03	12.27±0.05	12.14±0.18	···	···	···	CII
23	18:35:57.89	-08:02:31.8	···	···	12.48±0.04	9.50±0.01	8.57±0.01	7.78±0.01	7.08±0.01	4.08±0.02	···	CII
24	18:35:52.07	-08:00:39.0	···	···	···	10.85±0.02	9.70±0.01	8.66±0.01	7.76±0.01	5.58±0.09	···	CII
25	18:35:57.64	-07:57:56.8	···	···	12.75±0.03	8.99±0.01	8.11±0.01	7.33±0.01	7.10±0.02	5.33±0.07	···	CII[2]
G034.74−0.12												
1	18:55:00.99	+01:30:14.1	···	15.09±0.09	13.39±0.07	10.36±0.02	9.51±0.01	···	5.42±0.05	1.24±0.01	1.053	CI
2	18:55:01.04	+01:30:23.7	···	···	···	12.50±0.03	10.94±0.02	9.69±0.04	8.58±0.04	···	···	CI
3	18:55:12.78	+01:33:02.1	···	···	···	13.16±0.04	11.98±0.02	11.15±0.06	10.22±0.11	···	···	CI
4	18:55:18.47	+01:33:38.1	···	14.97±0.09	13.74±0.08	12.85±0.09	11.89±0.04	12.36±0.22	···	···	···	CI

Continued on Next Page...

Table C.1 – YSO Photometry (Continued)

ID	α (J2000)	δ (J2000)	J	H	K_s	3.6 μm	4.5 μm	5.8 μm	8.0 μm	24 μm	A_K	class[1]
5	18:55:05.20	+01:34:36.2	···	···	···	···	12.56±0.08	12.20±0.12	···	4.75±0.03	···	EP[2]
6	18:55:09.70	+01:29:51.8	16.42±0.11	14.10±0.06	···	12.45±0.03	12.26±0.03	11.96±0.08	11.36±0.17	···	···	CII
7	18:55:14.91	+01:30:25.0	···	···	14.19±0.08	12.46±0.02	12.27±0.03	11.72±0.07	11.19±0.15	···	···	CII
8	18:55:06.08	+01:30:51.8	···	14.72±0.07	14.26±0.07	13.43±0.04	13.16±0.04	···	···	···	···	CII
9	18:55:19.04	+01:30:55.0	16.83±0.16	15.42±0.10	14.47±0.09	13.73±0.07	13.43±0.06	···	···	···	0.538	CII
10	18:55:02.59	+01:31:11.4	···	···	14.51±0.10	13.38±0.05	13.14±0.05	12.79±0.11	11.91±0.16	···	···	CII
11	18:55:01.56	+01:31:14.7	···	···	···	12.37±0.02	11.52±0.01	10.96±0.04	10.46±0.05	9.10±0.74	···	CII[2]
12	18:55:11.50	+01:31:30.4	15.83±0.07	14.44±0.06	13.62±0.06	12.62±0.03	12.38±0.02	12.32±0.06	···	···	0.618	CII
13	18:55:11.28	+01:32:24.9	···	···	14.19±0.06	12.89±0.02	12.71±0.03	12.26±0.06	11.79±0.17	···	···	CII
14	18:55:13.05	+01:32:35.8	15.01±0.04	14.28±0.03	14.05±0.06	13.42±0.04	13.12±0.04	13.02±0.28	···	···	0.109	CII
15	18:55:18.06	+01:32:42.9	···	···	13.17±0.05	11.88±0.03	11.68±0.03	11.29±0.06	10.86±0.19	···	···	CII
16	18:55:13.06	+01:32:54.9	···	···	···	13.31±0.06	12.28±0.04	11.75±0.10	11.12±0.18	···	···	CII
17	18:55:17.34	+01:33:26.2	10.89±0.02	8.00±0.06	6.46±0.02	5.65±0.01	5.45±0.01	5.05±0.01	4.83±0.01	2.94±0.01	2.336	CII[2]
18	18:55:05.56	+01:33:41.1	16.31±0.10	14.87±0.06	14.22±0.07	13.26±0.04	12.92±0.04	···	···	···	0.866	CII
19	18:55:07.34	+01:33:44.3	15.21±0.05	13.99±0.04	12.99±0.04	12.00±0.02	11.81±0.03	10.82±0.05	···	···	0.186	CII
20	18:55:10.21	+01:33:46.1	···	···	···	11.63±0.02	11.27±0.01	10.82±0.04	10.53±0.14	···	···	CII
21	18:55:12.45	+01:34:03.7	10.70±0.02	7.67±0.03	5.79±0.02	5.20±0.01	4.67±0.01	3.82±0.01	3.16±0.01	···	2.237	CII
22	18:55:03.42	+01:34:08.3	16.81±0.16	14.45±0.05	13.31±0.04	12.17±0.03	11.85±0.03	11.13±0.07	9.93±0.12	6.56±0.18	1.845	CII
23	18:55:16.75	+01:34:39.0	16.50±0.13	14.53±0.09	13.20±0.04	11.68±0.03	11.18±0.03	10.94±0.04	10.33±0.06	6.62±0.17	1.066	CII
24	18:55:13.96	+01:35:04.3	10.07±0.02	7.46±0.02	6.16±0.02	5.54±0.01	5.33±0.01	5.00±0.01	4.76±0.01	3.10±0.01	2.123	CII[2]
25	18:55:10.50	+01:35:05.7	···	15.12±0.11	13.91±0.10	11.94±0.02	11.29±0.02	10.81±0.02	10.25±0.04	9.60±2.35	0.522	CII[2]
26	18:55:06.93	+01:35:08.9	12.03±0.03	8.82±0.02	7.02±0.03	6.10±0.01	5.45±0.01	4.95±0.01	4.64±0.01	3.44±0.01	2.601	CII[2]
27	18:55:01.86	+01:35:15.6	10.91±0.02	7.92±0.02	6.50±0.02	5.79±0.01	5.57±0.01	5.18±0.01	4.93±0.01	4.19±0.01	2.518	CII[2]
28	18:55:21.55	+01:35:21.3	···	···	···	13.61±0.07	12.89±0.06	12.43±0.08	11.69±0.08	···	···	CII
29	18:55:21.84	+01:35:30.9	···	···	···	11.53±0.02	10.79±0.01	10.30±0.01	9.77±0.03	···	···	CII

Continued on Next Page...

Table C.1 – YSO Photometry (Continued)

ID	α (J2000)	δ (J2000)	J	H	K_s	3.6 μm	4.5 μm	5.8 μm	8.0 μm	24 μm	A_K	class[1]
30	18:55:15.21	+01:35:34.3	15.95±0.07	14.79±0.05	14.04±0.07	13.06±0.05	12.83±0.05	13.33±0.28	···	···	0.329	CII
31	18:55:17.48	+01:35:41.9	···	···	···	12.40±0.03	11.74±0.02	11.33±0.05	10.89±0.16	···	···	CII
32	18:55:00.52	+01:36:02.0	14.46±0.04	10.43±0.03	8.45±0.02	6.99±0.01	6.80±0.01	6.42±0.01	6.21±0.01	···	3.608	CII
33	18:55:19.83	+01:36:27.5	14.54±0.04	13.10±0.03	12.32±0.03	11.62±0.01	11.32±0.01	11.03±0.03	10.51±0.05	···	0.746	CII
34	18:55:12.21	+01:30:37.0	···	···	···	12.88±0.03	12.31±0.02	11.89±0.05	11.73±0.09	7.56±0.08	···	TD
35	18:55:10.65	+01:32:46.2	···	···	10.99±0.03	9.00±0.01	8.69±0.01	8.13±0.01	8.19±0.03	6.14±0.15	···	TD[2]
G037.44+0.14												
1	18:59:18.21	+04:04:15.6	···	···	···	12.27±0.01	10.40±0.01	9.07±0.01	8.31±0.03	4.88±0.03	···	CI
2	18:59:12.31	+04:04:25.9	···	···	14.24±0.07	11.56±0.01	10.39±0.01	9.54±0.01	8.82±0.04	5.37±0.05	···	CI
3	18:59:00.30	+04:06:06.4	···	···	···	12.67±0.03	11.77±0.02	11.00±0.04	10.53±0.10	4.81±0.03	···	CI
4	18:59:00.07	+04:06:32.4	···	···	···	13.27±0.03	12.48±0.02	11.77±0.06	11.13±0.13	7.61±0.25	···	CI
5	18:59:22.68	+04:06:53.1	···	···	14.31±0.11	11.26±0.01	10.38±0.01	9.61±0.01	9.11±0.03	···	···	CI
6	18:59:08.86	+04:00:18.4	···	14.69±0.06	13.85±0.06	12.82±0.02	12.58±0.03	12.63±0.11	···	···	0.960	CII
7	18:59:10.40	+04:01:39.8	15.26±0.06	14.09±0.04	13.61±0.06	13.26±0.03	12.83±0.07	13.05±0.12	···	···	0.597	CII
8	18:59:01.13	+04:01:48.3	···	15.03±0.11	13.81±0.07	12.59±0.03	12.35±0.03	12.08±0.08	11.62±0.13	···	1.856	CII
9	18:59:00.03	+04:02:03.9	16.75±0.14	14.56±0.05	13.62±0.05	12.92±0.03	12.72±0.02	12.29±0.10	11.82±0.13	···	1.678	CII
10	18:59:10.75	+04:02:35.4	16.59±0.14	14.19±0.04	13.06±0.04	12.09±0.01	11.91±0.01	11.65±0.07	11.19±0.10	···	1.898	CII
11	18:59:14.02	+04:02:54.3	14.88±0.05	10.96±0.03	8.84±0.03	6.88±0.01	6.54±0.01	6.15±0.01	5.89±0.01	4.36±0.03	3.424	CII[2]
12	18:59:12.89	+04:02:56.7	···	15.13±0.08	13.08±0.03	11.57±0.03	11.16±0.03	10.93±0.07	10.39±0.08	···	3.295	CII
13	18:59:06.85	+04:03:05.7	···	···	14.43±0.09	12.90±0.03	12.69±0.03	12.34±0.10	11.73±0.19	···	···	CII
14	18:59:08.28	+04:03:08.5	···	···	···	13.73±0.06	13.49±0.06	13.05±0.15	11.87±0.19	···	···	CII
15	18:59:07.00	+04:03:11.8	···	···	···	13.23±0.06	12.85±0.06	12.47±0.11	11.79±0.20	···	···	CII
16	18:59:14.40	+04:03:26.3	···	12.46±0.03	9.47±0.02	7.35±0.01	6.85±0.01	6.21±0.01	5.90±0.01	4.24±0.02	5.065	CII[2]
17	18:59:07.94	+04:03:27.1	···	···	···	13.55±0.03	13.14±0.03	12.54±0.09	11.40±0.16	···	···	CII
18	18:59:22.40	+04:03:38.7	16.31±0.10	15.08±0.09	14.46±0.09	13.34±0.06	13.04±0.07	···	···	···	0.555	CII

Continued on Next Page...

Table C.1 – YSO Photometry (Continued)

ID	α (J2000)	δ (J2000)	J	H	K_s	3.6 μm	4.5 μm	5.8 μm	8.0 μm	24 μm	A_K	class[1]
19	18:59:25.82	+04:04:02.2	···	13.85±0.04	13.41±0.05	12.80±0.03	12.54±0.04	···	···	···	···	CII
20	18:59:11.02	+04:04:03.0	···	15.90±0.15	11.47±0.03	8.55±0.01	8.07±0.01	7.37±0.01	7.32±0.01	6.71±0.12	7.696	CII[2]
21	18:59:17.05	+04:04:15.0	16.92±0.18	15.13±0.08	14.36±0.09	13.46±0.03	13.10±0.04	13.04±0.10	13.02±0.46	···	1.247	CII
22	18:59:03.86	+04:04:22.3	···	···	14.60±0.11	13.01±0.01	12.69±0.01	12.25±0.05	11.82±0.13	···	···	CII
23	18:59:13.78	+04:04:31.8	···	15.26±0.08	13.06±0.04	11.51±0.01	11.22±0.01	10.98±0.04	10.59±0.07	···	3.644	CII
24	18:59:08.44	+04:05:17.1	16.97±0.19	15.09±0.07	14.50±0.10	13.25±0.06	12.64±0.07	···	···	···	1.345	CII
25	18:59:03.67	+04:05:57.8	···	···	···	13.59±0.11	13.01±0.07	12.48±0.12	11.78±0.14	8.19±0.18	···	CII
26	18:59:13.87	+04:05:59.3	···	···	···	14.26±0.05	13.92±0.04	13.65±0.11	12.57±0.17	···	···	CII
27	18:59:00.16	+04:06:09.5	15.26±0.04	13.66±0.04	12.84±0.05	12.10±0.02	11.84±0.02	11.49±0.06	10.92±0.11	···	0.964	CII
28	18:59:07.52	+04:06:14.6	16.27±0.10	14.42±0.04	13.49±0.05	12.37±0.01	11.82±0.01	11.26±0.02	10.45±0.04	7.23±0.09	1.259	CII
29	18:59:21.06	+04:06:22.7	···	···	14.36±0.09	12.87±0.02	12.40±0.02	11.97±0.07	11.37±0.12	···	···	CII
30	18:59:02.72	+04:06:31.4	···	···	14.68±0.12	13.32±0.03	13.02±0.03	12.59±0.07	11.86±0.13	···	···	CII
31	18:59:03.59	+04:06:43.9	16.68±0.14	14.96±0.10	13.86±0.07	12.59±0.02	12.35±0.02	···	···	···	0.879	CII
32	18:58:58.91	+04:06:48.5	···	···	13.80±0.09	12.45±0.02	12.16±0.02	12.02±0.07	11.22±0.08	···	···	CII
33	18:59:04.87	+04:07:19.6	···	···	···	12.57±0.02	11.74±0.01	11.13±0.05	10.50±0.07	···	···	CII
34	18:59:17.08	+04:07:31.8	16.99±0.21	14.88±0.06	13.60±0.04	11.93±0.01	11.29±0.01	10.74±0.03	10.03±0.08	···	0.713	CI
35	18:59:22.08	+04:07:33.5	···	···	12.86±0.06	11.65±0.01	11.03±0.01	10.30±0.03	9.30±0.04	···	···	CII
36	18:59:16.13	+04:08:03.3	···	···	···	13.54±0.03	13.09±0.03	12.52±0.08	12.17±0.19	···	···	CII
37	18:59:12.04	+04:03:00.8	···	···	11.35±0.03	8.21±0.01	6.29±0.01	4.83±0.01	3.97±0.01	1.70±0.01	···	CII
38	18:59:07.46	+04:05:19.4	···	13.50±0.04	10.16±0.03	6.55±0.01	5.55±0.01	4.77±0.01	4.43±0.01	3.41±0.01	4.485	CII[2]
39	18:59:17.84	+04:01:59.0	···	12.84±0.03	10.51±0.02	8.91±0.01	8.85±0.01	8.30±0.01	8.24±0.01	6.16±0.06	3.864	TD[2]
40	18:59:09.51	+04:04:34.3	···	14.79±0.06	13.46±0.04	11.89±0.01	11.25±0.01	10.93±0.06	10.45±0.20	6.19±0.14	0.827	TD

Continued on Next Page...

Table C.1 – YSO Photometry (Continued)

ID	α (J2000)	δ (J2000)	J	H	K_s	3.6 μm	4.5 μm	5.8 μm	8.0 μm	24 μm	A_K	class[1]

[1]CI=class I protostar, CII=class II pre-main sequence star, TD=transition disk, EP=embedded protostar

[2]denotes possible RGB star

APPENDIX D

Clump Structure in IRDCs: `clumpfind` Results

Table D.1: `clumpfind` Results.

IRDC		$\Delta\alpha$ ($''$)	$\Delta\delta$ ($''$)	Clump Mass ($M_\odot$)	τ_{max}	Clump Size (pc)	Notes[1]
G005.85−0.23							
	C1	23	-23	348.5	0.14	0.11	
	C2	-22	-75	342.5	0.55	0.09	
	C3	-33	-50	320.7	0.40	0.09	
	C4	-60	-83	305.8	0.25	0.10	
	C5	-16	-54	299.0	0.75	0.08	
	C6	-6	-61	211.8	0.46	0.08	
	C7	-42	-81	178.4	0.29	0.08	fg
	C8	-29	-63	165.3	0.93	0.07	
	C9	78	18	108.3	0.17	0.08	fg
	C10	-21	-52	72.4	0.58	0.06	
	C11	-22	-61	64.9	1.09	0.05	
	C12	-86	-93	47.1	0.23	0.07	5 - CII
	C13	15	44	32.9	0.17	0.06	12 - CII
	C14	-105	-123	3.3	0.14	0.04	
	C15	-100	-94	0.6	0.13	0.02	
G006.26−0.51							
	C1	-71	97	2226.8	0.26	0.18	
	C2	-179	-25	963.5	0.15	0.15	17 - CII
	C3	-99	93	820.9	0.15	0.15	
	C4	-51	-45	683.1	1.58	0.11	
	C5	37	-82	641.2	0.21	0.14	
	C6	-91	78	331.7	0.21	0.11	

C7	-154	-64	255.4	0.17	0.11	
C8	70	-112	240.6	0.13	0.11	
C9	-62	-64	233.8	0.55	0.10	
C10	-59	-35	221.8	0.75	0.08	
C11	-186	-52	210.7	0.17	0.10	
C12	-21	110	176.8	0.15	0.10	
C13	66	-117	175.5	0.13	0.11	
C14	47	-75	169.1	0.20	0.09	
C15	91	-80	161.1	0.36	0.10	1 - CI
C16	-67	-61	145.0	0.49	0.08	
C17	-70	-19	144.6	0.45	0.09	
C18	-58	-40	119.1	0.88	0.06	
C19	70	-77	112.5	0.18	0.09	
C20	-71	56	109.3	0.19	0.09	
C21	-70	-30	107.5	0.52	0.07	
C22	-75	-39	106.9	0.47	0.08	
C23	-173	-44	102.1	0.14	0.09	
C24	106	-53	83.8	0.14	0.09	13 - CII
C25	-207	-38	77.5	0.11	0.09	
C26	-83	-86	77.0	0.13	0.09	
C27	61	-72	71.8	0.19	0.08	
C28	-133	83	65.4	0.10	0.09	
C29	-105	-88	59.6	0.38	0.08	
C30	-61	-84	56.3	0.14	0.08	
C31	-167	-62	56.0	0.14	0.08	14 - CII
C32	-90	-173	52.7	0.48	0.07	
C33	-110	-99	49.4	0.20	0.07	
C34	-125	83	42.5	0.10	0.08	
C35	-135	-75	41.8	0.12	0.08	
C36	-110	70	37.7	0.12	0.07	
C37	-5	99	36.9	0.13	0.07	
C38	-27	117	36.6	0.15	0.07	
C39	55	102	34.0	0.14	0.07	26 - CII
C40	103	-62	32.3	0.15	0.07	
C41	-102	86	29.9	0.18	0.06	
C42	-178	-60	29.7	0.16	0.07	14 - CII

	C43	65	-75	19.8	0.16	0.06	
	C44	-25	121	18.7	0.13	0.06	
	C45	-91	-49	17.3	0.15	0.06	
	C46	-51	-84	15.6	0.11	0.06	
	C47	-154	-12	14.4	0.13	0.06	
	C48	46	-164	12.7	0.10	0.06	
	C49	-4	89	11.0	0.13	0.05	
	C50	-129	80	10.0	0.13	0.05	
	C51	-122	-86	9.5	0.12	0.05	
	C52	82	-62	8.8	0.13	0.05	
	C53	65	117	8.5	0.11	0.05	
	C54	103	-9	7.8	0.13	0.05	
	C55	-175	-58	7.6	0.15	0.04	
	C56	-159	-9	7.3	0.10	0.05	
	C57	-106	72	5.5	0.11	0.05	
	C58	-71	-177	4.0	0.18	0.04	
	C59	53	-170	1.4	0.10	0.03	
	C60	-131	-47	1.3	0.10	0.03	
	C61	77	111	1.2	0.10	0.03	
	C62	-77	-3	1.0	0.13	0.03	
	C63	-102	-63	1.0	0.10	0.03	
G009.16+0.06							
	C1	-63	-80	3732.1	0.52	0.19	
	C2	-25	-66	741.2	0.43	0.14	
	C3	-50	-82	359.0	0.76	0.10	
	C4	-180	-87	207.6	0.17	0.12	
	C5	-36	-81	162.5	0.52	0.08	
	C6	1	-97	153.6	0.23	0.10	4 - CII
	C7	-213	-96	118.6	0.09	0.10	
	C8	-106	-61	69.7	0.08	0.09	
	C9	-24	-83	68.3	0.42	0.07	
	C10	-170	17	64.1	0.08	0.09	
	C11	-20	-87	57.8	0.32	0.07	
	C12	-164	-10	54.2	0.11	0.09	
	C13	-11	-111	51.9	0.22	0.07	
	C14	-203	-1	38.0	0.11	0.08	

	C15	-185	11	36.8	0.11	0.08	
	C16	-191	10	33.2	0.11	0.08	
	C17	-123	-75	26.0	0.12	0.07	
	C18	32	-118	23.2	0.19	0.07	
	C19	-5	-130	16.3	0.16	0.06	
	C20	-194	-31	10.8	0.08	0.06	
	C21	-2	-82	10.7	0.19	0.05	4 - CII
	C22	-119	-38	4.4	0.08	0.05	
	C23	-116	-45	4.0	0.09	0.04	
	C24	87	-92	2.9	0.11	0.04	
	C25	-100	-40	1.7	0.08	0.04	
	C26	-69	-23	1.5	0.11	0.04	
	C27	-104	-39	1.3	0.08	0.03	
G009.28−0.15							
	C1	-77	1	1036.9	0.55	0.13	fg
	C2	-64	-21	636.1	0.77	0.10	fg
	C3	-59	-14	492.4	0.61	0.11	
	C4	-55	-43	343.3	0.71	0.10	
	C5	-81	-12	339.3	0.50	0.10	
	C6	-49	-56	283.5	0.49	0.09	fg
	C7	-50	-32	238.3	0.71	0.09	
	C8	-89	36	234.6	0.21	0.11	14 - CII
	C9	-127	-25	169.2	0.31	0.10	
	C10	-80	23	119.8	0.28	0.09	
	C11	-36	-125	119.3	0.29	0.09	fg
	C12	-55	-98	118.8	0.23	0.09	
	C13	-54	-38	115.2	0.67	0.07	
	C14	-37	-112	110.2	0.27	0.09	fg
	C15	-51	-70	106.8	0.40	0.08	
	C16	-43	-39	96.3	0.41	0.08	
	C17	-59	-76	87.0	0.24	0.08	
	C18	-34	-98	73.0	0.30	0.08	
	C19	-16	-147	72.5	0.20	0.08	
	C20	-139	-25	70.0	0.23	0.08	fg
	C21	-38	-104	65.5	0.29	0.07	fg
	C22	8	-34	60.8	0.20	0.08	

C23	-101	-9	60.2	0.22	0.08	
C24	-97	-20	59.0	0.21	0.07	
C25	-102	-23	58.2	0.19	0.08	fg
C26	-96	27	51.5	0.27	0.07	
C27	-34	-137	48.4	0.20	0.08	10 - CII
C28	-37	-83	46.8	0.38	0.07	
C29	-25	-65	45.8	0.23	0.07	
C30	-57	-92	45.3	0.21	0.07	
C31	-40	-90	44.2	0.38	0.06	
C32	-80	27	43.6	0.29	0.07	
C33	4	-26	41.5	0.19	0.07	2 - CI
C34	-76	-33	37.6	0.16	0.07	
C35	-26	-45	31.7	0.20	0.07	fg
C36	-41	-69	31.6	0.28	0.06	
C37	-32	-74	30.9	0.23	0.06	
C38	-36	-61	28.1	0.28	0.06	
C39	-102	-15	27.1	0.22	0.06	
C40	-53	-80	26.2	0.26	0.06	
C41	-49	-49	25.8	0.41	0.05	
C42	-32	-55	19.1	0.22	0.06	
C43	-51	-88	18.1	0.20	0.06	
C44	-19	-54	13.6	0.25	0.05	fg
C45	-20	-86	13.6	0.23	0.05	
C46	-40	-16	10.7	0.13	0.05	
C47	-76	-134	10.5	0.20	0.05	
C48	-107	-50	10.0	0.14	0.05	fg
C49	-17	-161	9.6	0.16	0.05	
C50	-4	-146	6.7	0.16	0.05	
C51	-12	31	4.6	0.13	0.04	
C52	-58	7	4.5	0.11	0.04	
C53	-110	-39	4.2	0.15	0.04	fg
C54	-12	-93	2.6	0.14	0.04	
C55	-139	12	2.6	0.16	0.04	fg
C56	-141	44	2.0	0.12	0.04	fg
C57	-32	-157	1.8	0.13	0.03	

	C58	-113	45	1.8	0.14	0.03	fg
G009.86−0.04							
	C1	-15	-68	299.0	0.42	0.08	2 - CI, 3 - CI
	C2	-62	-82	185.7	0.16	0.08	
	C3	-37	-71	174.3	0.20	0.07	fg
	C4	-101	-57	167.9	0.50	0.07	fg
	C5	-74	-44	156.9	1.57	0.06	
	C6	-92	-42	120.3	0.45	0.06	
	C7	-52	-58	117.4	0.27	0.06	
	C8	-42	-38	116.5	0.41	0.06	6 - EP
	C9	9	-67	112.3	0.32	0.07	fg
	C10	-33	-44	109.9	0.42	0.06	
	C11	-106	-35	92.4	0.52	0.05	
	C12	-85	-61	82.7	0.30	0.06	
	C13	-126	-28	80.4	0.59	0.06	
	C14	-65	-39	80.0	0.77	0.05	
	C15	-24	-11	76.3	0.18	0.06	
	C16	-114	-106	70.6	0.18	0.06	
	C17	-72	-27	65.9	0.26	0.06	
	C18	-115	-38	63.9	0.64	0.05	
	C19	-15	-40	56.1	0.17	0.06	
	C20	-26	-61	48.5	0.38	0.05	3 - CI
	C21	7	-87	43.2	0.13	0.06	
	C22	-15	-56	40.8	0.22	0.05	fg
	C23	-114	-123	36.4	0.17	0.05	
	C24	-139	-7	35.9	0.24	0.05	19 - CII
	C25	-137	-121	27.7	0.25	0.05	fg
	C26	-163	-122	26.6	0.22	0.05	
	C27	-121	-31	23.8	0.56	0.04	
	C28	27	-65	21.9	0.32	0.05	fg
	C29	-5	-39	19.1	0.15	0.04	5 - CI
	C30	-52	-45	18.0	0.28	0.04	
	C31	-45	-52	17.8	0.26	0.04	
	C32	-184	-125	12.9	0.17	0.04	
	C33	-160	-131	6.5	0.13	0.04	
	C34	-157	-1	4.7	0.12	0.03	

	C35	-3	-116	0.7	0.12	0.02	
	C36	-201	-7	0.4	0.11	0.02	
G012.50−0.22							
	C1	-70	-30	1418.6	0.39	0.14	
	C2	-51	-61	1293.3	0.44	0.14	2 - CI
	C3	-41	-59	838.6	0.62	0.12	
	C4	-50	-41	488.8	0.98	0.09	5 - EP, 12 - CII
	C5	-196	39	385.4	0.46	0.10	
	C6	-104	-31	373.2	0.23	0.11	fg
	C7	-51	-50	333.5	0.95	0.08	2 - CI
	C8	-78	-12	204.6	0.40	0.09	14 - CII
	C9	-42	-43	179.0	1.16	0.07	5 - EP, 12 - CII
	C10	-190	49	165.1	0.32	0.08	
	C11	-131	-47	99.9	0.26	0.08	
	C12	80	-146	36.2	0.21	0.07	fg
	C13	-32	-43	31.1	0.25	0.06	
	C14	-32	-112	21.9	0.22	0.06	
	C15	-35	-101	3.6	0.20	0.04	
G023.37−0.29							
	C1	45	43	5199.6	1.64	0.18	
	C2	45	37	3143.6	1.28	0.17	9 - EP
	C3	-18	183	417.3	0.32	0.13	
	C4	-44	139	317.3	0.82	0.10	
	C5	-16	197	231.2	0.58	0.11	
	C6	-44	153	188.9	0.28	0.10	
	C7	87	24	188.2	0.21	0.11	
	C8	48	70	167.5	0.24	0.10	
	C9	-79	107	128.0	0.18	0.10	
	C10	192	209	127.5	1.19	0.09	fg
	C11	-50	167	94.0	0.26	0.09	fg
	C12	-18	191	81.4	0.31	0.08	
	C13	39	112	78.8	0.27	0.08	
	C14	7	-86	78.2	0.33	0.08	
	C15	-26	206	67.3	0.17	0.09	
	C16	0	151	63.4	0.20	0.09	39 - CII
	C17	-36	194	61.0	0.18	0.08	

	C18	124	-13	30.8	0.14	0.07	
	C19	-39	126	29.3	0.21	0.07	
	C20	171	131	28.0	0.28	0.06	
	C21	10	104	27.7	0.24	0.07	
	C22	-52	186	24.6	0.28	0.06	fg
	C23	44	102	24.2	0.21	0.06	
	C24	5	-64	22.2	0.21	0.06	fg
	C25	48	122	21.1	0.22	0.06	
	C26	-76	118	20.3	0.17	0.06	
	C27	192	202	18.6	1.40	0.05	fg
	C28	0	-64	18.2	0.20	0.06	
	C29	-39	115	15.9	0.21	0.06	
	C30	-47	199	15.1	0.18	0.06	
	C31	74	-65	14.9	0.16	0.06	
	C32	-34	211	14.7	0.18	0.06	
	C33	49	98	13.9	0.25	0.05	9 - EP
	C34	53	88	13.7	0.20	0.06	
	C35	15	114	12.4	0.18	0.06	fg
	C36	-100	172	12.1	0.16	0.06	
	C37	26	114	12.0	0.15	0.06	fg
	C38	196	133	10.6	0.15	0.06	
	C39	36	-70	8.2	0.17	0.05	
	C40	71	-43	8.1	0.19	0.05	
	C41	-62	188	6.2	0.17	0.05	
	C42	-63	199	6.0	0.16	0.05	
	C43	164	140	5.4	0.16	0.05	
	C44	58	86	5.4	0.13	0.05	fg
	C45	-83	185	4.3	0.15	0.04	
	C46	-109	70	4.2	0.14	0.04	
	C47	50	-58	4.0	0.15	0.04	
	C48	-29	38	3.8	0.18	0.04	33 - CII
	C49	-77	81	2.6	0.13	0.04	fg
	C50	-56	202	1.8	0.14	0.04	
G023.48−0.53							
	C1	78	26	1274.2	0.82	0.13	
	C2	68	32	775.0	0.71	0.12	

C3	104	29	436.3	0.33	0.12	
C4	52	37	363.6	0.76	0.09	
C5	43	33	249.7	0.91	0.08	4 - CI
C6	50	56	247.5	0.58	0.09	
C7	-43	-45	206.2	0.41	0.09	
C8	33	40	204.1	0.72	0.08	4 - CI
C9	12	42	202.3	0.58	0.09	
C10	60	51	186.1	0.37	0.09	
C11	-79	-72	182.4	0.31	0.09	1 - CI, 2 - CI, 3 - CI
C12	19	59	178.0	0.45	0.09	
C13	-62	-62	154.1	0.36	0.09	
C14	91	0	142.7	0.20	0.09	
C15	-45	-57	129.6	0.49	0.08	
C16	-34	-30	129.0	0.31	0.09	
C17	23	51	101.2	0.61	0.06	
C18	-12	-24	96.7	0.28	0.08	
C19	34	59	96.6	0.46	0.07	
C20	8	75	91.3	0.28	0.08	
C21	44	44	83.3	0.59	0.06	4 - CI
C22	-24	-29	79.2	0.26	0.08	
C23	-54	-64	69.7	0.38	0.07	
C24	116	30	64.0	0.19	0.08	
C25	-1	57	47.5	0.26	0.07	
C26	28	54	46.4	0.52	0.05	
C27	4	37	40.4	0.46	0.06	
C28	-91	101	39.0	0.23	0.07	
C29	-9	-12	38.6	0.19	0.07	
C30	105	-10	38.0	0.29	0.07	
C31	36	40	27.1	0.72	0.04	4 - CI
C32	68	68	18.0	0.25	0.06	
C33	123	42	14.5	0.17	0.05	
C34	52	80	12.9	0.17	0.05	
C35	59	70	9.6	0.21	0.05	fg
C36	-59	-44	5.0	0.16	0.04	fg
C37	66	3	4.5	0.17	0.04	

	C38	-21	89	2.4	0.17	0.03	
G024.05−0.22							
	C1	44	55	598.9	0.70	0.12	
	C2	32	37	411.5	0.58	0.11	7 - CII
	C3	26	56	363.0	0.37	0.12	
	C4	31	83	343.8	0.29	0.13	fg
	C5	44	20	277.8	0.28	0.12	
	C6	40	84	217.8	0.21	0.12	fg
	C7	36	183	192.1	0.10	0.13	13 - CII
	C8	38	46	184.5	1.10	0.08	10 - CII
	C9	47	128	181.7	0.14	0.12	
	C10	40	165	179.6	0.14	0.12	
	C11	173	181	131.7	0.17	0.11	
	C12	52	42	122.2	0.36	0.09	
	C13	56	119	118.1	0.19	0.10	
	C14	45	73	99.4	0.23	0.09	fg
	C15	69	124	71.9	0.16	0.09	
	C16	28	160	70.7	0.11	0.10	
	C17	66	113	61.5	0.20	0.09	
	C18	44	45	54.0	0.44	0.06	
	C19	144	205	53.6	0.11	0.09	
	C20	59	37	47.4	0.23	0.08	
	C21	130	208	45.2	0.13	0.09	fg
	C22	152	173	33.5	0.12	0.08	
	C23	136	177	27.6	0.11	0.08	
	C24	28	45	27.1	0.31	0.06	
	C25	-90	173	23.9	0.19	0.07	fg
	C26	128	186	19.3	0.11	0.07	fg
	C27	184	172	15.6	0.11	0.07	
	C28	24	127	15.1	0.13	0.07	8 - CII
	C29	71	59	14.6	0.13	0.07	8 - CII
	C30	191	179	14.1	0.10	0.07	
	C31	68	32	12.8	0.19	0.06	
	C32	148	175	8.9	0.10	0.06	
	C33	-83	-24	7.8	0.14	0.05	
	C34	-94	173	4.8	0.19	0.05	fg

	C35	-100	167	4.4	0.14	0.05	fg
	C36	76	37	3.8	0.14	0.05	
	C37	-106	176	3.7	0.11	0.05	fg
	C38	-75	-42	2.0	0.10	0.04	
	C39	7	184	1.8	0.09	0.04	
G034.74−0.12							
	C1	-62	-26	1411.1	0.66	0.14	
	C2	-59	-49	353.2	0.42	0.11	
	C3	-58	-39	309.7	0.42	0.10	
	C4	-5	-83	282.1	0.19	0.13	14 - CII
	C5	-23	-60	223.0	0.49	0.10	
	C6	-11	-62	185.3	0.32	0.10	14 - CII
	C7	0	-108	157.0	0.09	0.12	
	C8	-36	-54	150.8	0.35	0.10	35 - TD
	C9	-39	-40	147.7	0.50	0.08	
	C10	-19	-40	146.8	0.35	0.09	
	C11	-26	-76	144.9	0.26	0.10	
	C12	-59	-10	134.7	0.22	0.10	
	C13	-37	-17	113.7	0.22	0.10	
	C14	-47	-26	92.3	0.29	0.08	
	C15	-89	-24	89.8	0.14	0.10	fg
	C16	-39	-83	86.6	0.12	0.10	
	C17	-44	-5	83.4	0.21	0.09	fg
	C18	-32	-39	74.7	0.29	0.08	
	C19	-42	-28	69.4	0.27	0.08	
	C20	7	-59	63.1	0.16	0.09	
	C21	-6	-38	57.6	0.42	0.07	3 - CI
	C22	-15	-89	54.6	0.15	0.09	fg
	C23	-122	0	54.4	0.19	0.09	18 - CII
	C24	-26	-48	54.3	0.34	0.07	
	C25	-108	-15	52.5	0.17	0.09	
	C26	-48	-15	50.2	0.22	0.07	
	C27	-28	-106	46.2	0.11	0.09	fg
	C28	-8	-43	42.6	0.38	0.06	3 - CI, 16 - CII
	C29	-5	-55	41.7	0.26	0.07	
	C30	-36	-44	41.0	0.50	0.06	

	C31	-40	5	40.5	0.12	0.08	
	C32	-8	-33	34.3	0.22	0.07	
	C33	-28	-91	34.0	0.15	0.08	
	C34	-14	-49	32.8	0.30	0.06	16 - CII
	C35	18	-73	30.5	0.09	0.08	
	C36	-81	-114	29.8	0.13	0.08	
	C37	-141	19	28.6	0.17	0.07	22 - CII
	C38	-29	-113	28.3	0.09	0.08	
	C39	1	-53	28.0	0.20	0.07	
	C40	12	-103	25.7	0.14	0.07	
	C41	-12	-83	25.2	0.14	0.07	
	C42	-84	-106	23.5	0.16	0.07	fg
	C43	-42	63	23.4	0.15	0.07	fg
	C44	-127	-60	18.1	0.16	0.07	
	C45	-56	10	16.7	0.13	0.07	
	C46	-92	-16	15.4	0.12	0.06	fg
	C47	-60	-62	13.8	0.14	0.06	
	C48	-47	-94	13.0	0.11	0.06	
	C49	-130	9	12.4	0.11	0.06	
	C50	-21	-86	11.4	0.13	0.06	
	C51	6	-113	8.7	0.10	0.06	
	C52	-48	57	8.6	0.13	0.06	
	C53	-25	-92	5.8	0.14	0.05	fg
	C54	-131	-81	2.8	0.09	0.04	
	C55	-110	-5	2.1	0.09	0.04	
G037.44+0.14							
	C1	52	159	352.7	0.19	0.10	
	C2	64	48	258.3	0.45	0.08	2 - CII
	C3	77	43	218.6	0.40	0.08	
	C4	-86	36	203.7	0.30	0.08	
	C5	45	141	170.1	0.17	0.08	
	C6	70	196	130.4	0.17	0.08	fg
	C7	35	206	119.3	0.14	0.08	
	C8	61	211	117.1	0.29	0.07	fg
	C9	30	47	116.4	0.80	0.06	
	C10	-101	23	110.0	0.35	0.07	

C11	18	203	95.7	0.16	0.07	
C12	24	58	89.8	0.92	0.06	40 - TD
C13	51	56	88.6	0.59	0.06	
C14	47	205	68.6	0.23	0.06	
C15	52	210	60.4	0.25	0.06	
C16	-111	31	53.4	0.81	0.05	
C17	-102	38	52.7	0.38	0.05	
C18	51	72	44.8	0.59	0.05	
C19	44	16	35.4	0.15	0.06	
C20	5	16	34.6	0.32	0.05	
C21	42	56	26.8	0.60	0.04	
C22	-114	40	25.5	0.98	0.04	
C23	17	42	24.7	0.23	0.05	
C24	41	77	22.5	0.64	0.04	
C25	91	39	20.9	0.18	0.05	
C26	33	131	17.8	0.13	0.05	
C27	28	14	17.5	0.16	0.05	
C28	97	33	16.2	0.42	0.04	
C29	42	23	15.8	0.13	0.05	20 - CII
C30	13	48	15.3	0.13	0.05	
C31	36	61	14.2	0.60	0.03	
C32	105	34	13.3	0.32	0.04	
C33	31	60	13.0	0.87	0.03	
C34	34	3	12.6	0.14	0.04	
C35	11	18	11.3	0.23	0.04	
C36	37	55	10.3	0.55	0.03	
C37	5	34	10.0	0.13	0.04	
C38	112	33	10.0	0.28	0.04	
C39	53	82	8.7	0.21	0.04	
C40	33	105	7.2	0.13	0.04	fg
C41	29	29	6.7	0.14	0.04	
C42	-52	88	5.9	0.83	0.03	
C43	37	20	5.0	0.15	0.03	
C44	-108	-19	4.4	0.12	0.03	fg
C45	68	66	3.7	0.12	0.03	
C46	-112	37	2.4	0.96	0.02	

C47	85	54	1.9	0.12	0.03	
C48	8	37	1.8	0.13	0.03	
C49	-111	134	1.7	0.26	0.03	
C50	-46	82	1.7	0.27	0.02	
C51	-59	88	1.1	0.19	0.02	
C52	110	39	1.0	0.30	0.02	
C53	136	-6	0.9	0.15	0.02	
C54	-103	121	0.9	0.21	0.02	fg
C55	90	16	0.5	0.11	0.02	

[1]Numbers indicate which stars from Table C.1 are associated with a given clump. The YSO type (CI = Class I; CII = Class II; EP = Embedded Protostar; TD = Transition Disk) is also listed. The "fg" denotation indicates that a foreground (or background) star in the field may contaminate the properties listed for that clump.

BIBLIOGRAPHY

Adams, F. C. & Myers, P. C. 2001, ApJ, 553, 744

Aikawa, Y., Herbst, E., Roberts, H., & Caselli, P. 2005a, ApJ, 620, 330

Aikawa, Y., Herbst, E., Roberts, H., & Caselli, P. 2005b, ApJ, 620, 330

Allen, L. E., et al. 2004, ApJS, 154, 363

Alves, J., Lombardi, M., & Lada, C. J. 2007, A&A, 462, L17

Alves, J. F., Lada, C. J., & Lada, E. A. 2001, Nature, 409, 159

André, P., Ward-Thompson, D., & Barsony, M. 2000, Protostars and Planets IV, 59

Arons, J. & Max, C. E. 1975, ApJ, 196, L77+

Arquilla, R. & Goldsmith, P. F. 1986, ApJ, 303, 356

Bacmann, A., André, P., Puget, J.-L., Abergel, A., Bontemps, S., & Ward-Thompson, D. 2000, A&A, 361, 555

Ballesteros-Paredes, J. 2006, MNRAS, 372, 443

Baraffe, I., Chabrier, G., Allard, F., & Hauschildt, P. H. 1998, A&A, 337, 403

Becker, R. H., White, R. L., Helfand, D. J., & Zoonematkermani, S. 1994, ApJS, 91, 347

Beichman, C. A., Myers, P. C., Emerson, J. P., Harris, S., Mathieu, R., Benson, P. J., & Jennings, R. E. 1986, ApJ, 307, 337

Bergin, E. A., Alves, J., Huard, T., & Lada, C. J. 2002, ApJ, 570, L101

Bergin, E. A. & Langer, W. D. 1997, ApJ, 486, 316

Bergin, E. A. & Tafalla, M. 2007, ARA&A, 45, 339

Beuther, H. & Sridharan, T. K. 2007, ApJ, 668, 348

Beuther, H. & Steinacker, J. 2007, ApJ, 656, L85

Beuther, H., Walsh, A., Schilke, P., Sridharan, T. K., Menten, K. M., & Wyrowski, F. 2002, A&A, 390, 289

Beuther, H., Zhang, Q., Bergin, E. A., & Sridharan, T. K. 2009, AJ, 137, 406

Binney, J. & Merrifield, M. 1998, Galactic astronomy (Princeton University Press), 133–138

Blommaert, J. A. D. L., van Langevelde, H. J., & Michiels, W. F. P. 1994, A&A, 287, 479

Bonnell, I. A., Bate, M. R., Clarke, C. J., & Pringle, J. E. 1997, MNRAS, 285, 201

Burkert, A. & Bodenheimer, P. 2000, ApJ, 543, 822

Burton, W. B. 1976, ARA&A, 14, 275

Burton, W. B., Gordon, M. A., Bania, T. M., & Lockman, F. J. 1975, ApJ, 202, 30

Butler, M. J. & Tan, J. C. 2009, ApJ, 696, 484

Carey, S. J., Clark, F. O., Egan, M. P., Price, S. D., Shipman, R. F., & Kuchar, T. A. 1998, ApJ, 508, 721

Carey, S. J., Feldman, P. A., Redman, R. O., Egan, M. P., MacLeod, J. M., & Price, S. D. 2000, ApJ, 543, L157

Carpenter, J. M. 2000, AJ, 120, 3139

Caselli, P., Benson, P. J., Myers, P. C., & Tafalla, M. 2002, ApJ, 572, 238

Chambers, E. T., Jackson, J. M., Rathborne, J. M., & Simon, R. 2009, ApJS, 181, 360

Churchwell, E., et al. 2009, PASP, 121, 213

Clemens, D. P., Sanders, D. B., & Scoville, N. Z. 1988, ApJ, 327, 139

Codella, C. & Felli, M. 1995, A&A, 302, 521

Cyganowski, C. J., Brogan, C. L., Hunter, T. R., & Churchwell, E. 2009, ApJ, 702, 1615

Cyganowski, C. J., et al. 2008, AJ, 136, 2391

Di Francesco, J., Johnstone, D., Kirk, H., MacKenzie, T., & Ledwosinska, E. 2008, ApJS, 175, 277

Draine, B. T. 2003, ARA&A, 41, 241

Du, F. & Yang, J. 2008, ApJ, 686, 384

Egan, M. P., Shipman, R. F., Price, S. D., Carey, S. J., Clark, F. O., & Cohen, M. 1998, ApJ, 494, L199+

Espaillat, C., et al. 2007, ApJ, 664, L111

Fich, M., Blitz, L., & Stark, A. A. 1989, ApJ, 342, 272

Flaherty, K. M., Pipher, J. L., Megeath, S. T., Winston, E. M., Gutermuth, R. A., Muzerolle, J., Allen, L. E., & Fazio, G. G. 2007, ApJ, 663, 1069

Friesen, R. K., Di Francesco, J., Shirley, Y. L., & Myers, P. C. 2009, ApJ, 697, 1457

Gibson, D., Plume, R., Bergin, E., Ragan, S., & Evans, N. 2009, ArXiv e-prints

Goldsmith, P. F. 1987, in ASSL Vol. 134: Interstellar Processes, ed. D. J. Hollenbach & H. A. Thronson, 51–70

Goldsmith, P. F. 2001, ApJ, 557, 736

Goldsmith, P. F., Heyer, M., Narayanan, G., Snell, R., Li, D., & Brunt, C. 2008, ApJ, 680, 428

Goodman, A. A., Benson, P. J., Fuller, G. A., & Myers, P. C. 1993, ApJ, 406, 528

Goodman, A. A., Pineda, J. E., & Schnee, S. L. 2009, ApJ, 692, 91

Gutermuth, R. A., Megeath, S. T., Muzerolle, J., Allen, L. E., Pipher, J. L., Myers, P. C., & Fazio, G. G. 2004, ApJS, 154, 374

Gutermuth, R. A., Myers, P. C., Megeath, S. T., Allen, L. E., Pipher, J. L., Muzerolle, J., Porras, A., Winston, E., & Fazio, G. 2008, ApJ, 674, 336

Harju, J., Walmsley, C. M., & Wouterloot, J. G. A. 1993, A&AS, 98, 51

Hennebelle, P., Pérault, M., Teyssier, D., & Ganesh, S. 2001, A&A, 365, 598

Ho, P. T. P. & Townes, C. H. 1983, ARA&A, 21, 239

Hollenbach, D., Kaufman, M. J., Bergin, E. A., & Melnick, G. J. 2009, ApJ, 690, 1497

Hora, J. L., et al. 2004, in Society of Photo-Optical Instrumentation Engineers (SPIE) Conference Series, Vol. 5487, Society of Photo-Optical Instrumentation Engineers (SPIE) Conference Series, ed. J. C. Mather, 77–92

Hunter, D. A., Elmegreen, B. G., Dupuy, T. J., & Mortonson, M. 2003, AJ, 126, 1836

Indebetouw, R., et al. 2005, ApJ, 619, 931

Jackson, J. M., Finn, S. C., Rathborne, J. M., Chambers, E. T., & Simon, R. 2008, ApJ, 680, 349

Jackson, J. M., et al. 2006, ApJS, 163, 145

Jijina, J., Myers, P. C., & Adams, F. C. 1999, ApJS, 125, 161

Johnstone, D., Fich, M., Mitchell, G. F., & Moriarty-Schieven, G. 2001, ApJ, 559, 307

Johnstone, D., Fiege, J. D., Redman, R. O., Feldman, P. A., & Carey, S. J. 2003, ApJ, 588, L37

Johnstone, D., Wilson, C. D., Moriarty-Schieven, G., Giannakopoulou-Creighton, J., & Gregersen, E. 2000a, ApJS, 131, 505

Johnstone, D., Wilson, C. D., Moriarty-Schieven, G., Joncas, G., Smith, G., Gregersen, E., & Fich, M. 2000b, ApJ, 545, 327

Klessen, R. S. 2001, ApJ, 556, 837

Kramer, C., Stutzki, J., Rohrig, R., & Corneliussen, U. 1998, A&A, 329, 249

Kramer, C., Stutzki, J., & Winnewisser, G. 1996, A&A, 307, 915

Kroupa, P. 2001, MNRAS, 322, 231

Krumholz, M. R., McKee, C. F., & Klein, R. I. 2005, Nature, 438, 332

Lada, C. J., Bergin, E. A., Alves, J. F., & Huard, T. L. 2003, ApJ, 586, 286

Lada, C. J. & Lada, E. A. 2003, ARA&A, 41, 57

Lada, C. J., Muench, A. A., Rathborne, J., Alves, J. F., & Lombardi, M. 2008, ApJ, 672, 410

Landsman, W. B. 1993, in Astronomical Society of the Pacific Conference Series, Vol. 52, Astronomical Data Analysis Software and Systems II, ed. R. J. Hanisch, R. J. V. Brissenden, & J. Barnes, 246–+

Lee, C. W. & Myers, P. C. 1999, ApJS, 123, 233

Lee, J., Bergin, E. A., & Evans, N. J. 2004, ApJ, 617, 360

Li, D., Velusamy, T., Goldsmith, P. F., & Langer, W. D. 2007, ApJ, 655, 351

Lombardi, M. & Alves, J. 2001, A&A, 377, 1023

Lombardi, M., Alves, J., & Lada, C. J. 2006, A&A, 454, 781

Maret, S., Bergin, E. A., & Lada, C. J. 2006, Nature, 442, 425

Meixner, M., et al. 2006, AJ, 132, 2268

Menten, K. M., Pillai, T., & Wyrowski, F. 2005, in IAU Symposium, Vol. 227, Massive Star Birth: A Crossroads of Astrophysics, ed. R. Cesaroni, M. Felli, E. Churchwell, & M. Walmsley, 23–34

Molinari, S., Brand, J., Cesaroni, R., & Palla, F. 1996, A&A, 308, 573

Mookerjea, B., Kramer, C., Nielbock, M., & Nyman, L.-Å. 2004, A&A, 426, 119

Motte, F., Andre, P., & Neri, R. 1998, A&A, 336, 150

Motte, F., Schilke, P., & Lis, D. C. 2003, ApJ, 582, 277

Mouschovias, T. C. & Spitzer, L. 1976, ApJ, 210, 326

Muñoz, D. J., Mardones, D., Garay, G., Rebolledo, D., Brooks, K., & Bontemps, S. 2007, ApJ, 668, 906

Myers, P. C. & Benson, P. J. 1983, ApJ, 266, 309

Neufeld, D. A. & Yuan, Y. 2008, ApJ, 678, 974

Ossenkopf, V. & Henning, T. 1994, A&A, 291, 943

Pagani, L., Bacmann, A., Cabrit, S., & Vastel, C. 2007, A&A, 467, 179

Parsons, H., Thompson, M. A., & Chrysostomou, A. 2009, MNRAS, 1235

Pavlyuchenkov, Y., Henning, T., & Wiebe, D. 2007, ApJ, 669, L101

Pillai, T., Wyrowski, F., Carey, S. J., & Menten, K. M. 2006a, A&A, 450, 569

Pillai, T., Wyrowski, F., Menten, K. M., & Krügel, E. 2006b, A&A, 447, 929

Pipher, J. L., et al. 2004, in Society of Photo-Optical Instrumentation Engineers (SPIE) Conference Series, Vol. 5487, Society of Photo-Optical Instrumentation Engineers (SPIE) Conference Series, ed. J. C. Mather, 234–243

Plume, R., Jaffe, D. T., Evans, N. J., Martin-Pintado, J., & Gomez-Gonzalez, J. 1997, ApJ, 476, 730

Ragan, S. E., Bergin, E. A., & Gutermuth, R. A. 2009, ApJ, 698, 324

Ragan, S. E., Bergin, E. A., Plume, R., Gibson, D. L., Wilner, D. J., O'Brien, S., & Hails, E. 2006, ApJS, 166, 567

Rathborne, J. M., Jackson, J. M., Chambers, E. T., Simon, R., Shipman, R., & Frieswijk, W. 2005, ApJ, 630, L181

Rathborne, J. M., Jackson, J. M., & Simon, R. 2006, ApJ, 641, 389

Rathborne, J. M., Jackson, J. M., Zhang, Q., & Simon, R. 2008, ApJ, 689, 1141

Rathborne, J. M., Simon, R., & Jackson, J. M. 2007, ApJ, 662, 1082

Reid, M. A. & Wilson, C. D. 2005, ApJ, 625, 891

Reid, M. A. & Wilson, C. D. 2006, ApJ, 644, 990

Robinson, B. J., Manchester, R. N., Whiteoak, J. B., Sanders, D. B., Scoville, N. Z., Clemens, D. P., McCutcheon, W. H., & Solomon, P. M. 1984, ApJ, 283, L31

Robitaille, T. P., et al. 2008, AJ, 136, 2413

Robitaille, T. P., Whitney, B. A., Indebetouw, R., Wood, K., & Denzmore, P. 2006, ApJS, 167, 256

Rosolowsky, E. W., Pineda, J. E., Foster, J. B., Borkin, M. A., Kauffmann, J., Caselli, P., Myers, P. C., & Goodman, A. A. 2008, ApJS, 175, 509

Sakai, T., Sakai, N., Kamegai, K., Hirota, T., Yamaguchi, N., Shiba, S., & Yamamoto, S. 2008, ApJ, 678, 1049

Salpeter, E. E. 1955, ApJ, 121, 161

Sault, R. J., Teuben, P. J., & Wright, M. C. H. 1995, in Astronomical Society of the Pacific Conference Series, Vol. 77, Astronomical Data Analysis Software and Systems IV, ed. R. A. Shaw, H. E. Payne, & J. J. E. Hayes, 433–+

Shirley, Y. L., Evans, N. J., Young, K. E., Knez, C., & Jaffe, D. T. 2003, ApJS, 149, 375

Simon, R., Jackson, J. M., Rathborne, J. M., & Chambers, E. T. 2006a, ApJ, 639, 227

Simon, R., Rathborne, J. M., Shah, R. Y., Jackson, J. M., & Chambers, E. T. 2006b, ApJ, 653, 1325

Sridharan, T. K., Beuther, H., Saito, M., Wyrowski, F., & Schilke, P. 2005, ApJ, 634, L57

Stutzki, J. & Guesten, R. 1990, ApJ, 356, 513

Swift, J. J., Welch, W. J., & Di Francesco, J. 2005, ApJ, 620, 823

Szymczak, M. & Kus, A. J. 2000, A&AS, 147, 181

Tafalla, M., Myers, P. C., Caselli, P., & Walmsley, C. M. 2004, A&A, 416, 191

Tafalla, M., Myers, P. C., Caselli, P., Walmsley, C. M., & Comito, C. 2002, ApJ, 569, 815

van der Wiel, M. H. D. & Shipman, R. F. 2008, A&A, 490, 655

Walsh, A. J., Myers, P. C., & Burton, M. G. 2004, ApJ, 614, 194

Wang, Y., Zhang, Q., Pillai, T., Wyrowski, F., & Wu, Y. 2007, ArXiv e-prints, 711

Weingartner, J. C. & Draine, B. T. 2001, ApJ, 548, 296

Whitney, B. A., Wood, K., Bjorkman, J. E., & Cohen, M. 2003, ApJ, 598, 1079

Williams, J. P., de Geus, E. J., & Blitz, L. 1994, ApJ, 428, 693

Williams, J. P., Lee, C. W., & Myers, P. C. 2006, ApJ, 636, 952

Williams, S. J., Fuller, G. A., & Sridharan, T. K. 2004, A&A, 417, 115

Wiseman, J. J. & Ho, P. T. P. 1998, ApJ, 502, 676

Wood, D. O. S. & Churchwell, E. 1989, ApJS, 69, 831

Zinnecker, H., McCaughrean, M. J., & Wilking, B. A. 1993, in Protostars and Planets III, ed. E. H. Levy & J. I. Lunine, 429–495

Zoonematkermani, S., Helfand, D. J., Becker, R. H., White, R. L., & Perley, R. A. 1990, ApJS, 74, 181